University of Alberta

Probing Electronic Structure and Chemical Bonding with X-ray Spectroscopy

by

Astrid Jürgensen ©

A thesis submitted to the Faculty of Graduate Studies and Research in partial fulfillment of the requirements for the degree of Doctor of Philosophy

Department of Chemistry

Edmonton, Alberta

Fall 1999

National Library of Canada
Acquisitions and Bibliographic Services
395 Wellington Street
Ottawa ON K1A 0N4
Canada

Bibliothèque nationale du Canada
Acquisitions et services bibliographiques
395, rue Wellington
Ottawa ON K1A 0N4
Canada

Your file Votre référence

Our file Notre référence

The author has granted a non-exclusive licence allowing the National Library of Canada to reproduce, loan, distribute or sell copies of this thesis in microform, paper or electronic formats.

The author retains ownership of the copyright in this thesis. Neither the thesis nor substantial extracts from it may be printed or otherwise reproduced without the author's permission.

L'auteur a accordé une licence non exclusive permettant à la Bibliothèque nationale du Canada de reproduire, prêter, distribuer ou vendre des copies de cette thèse sous la forme de microfiche/film, de reproduction sur papier ou sur format électronique.

L'auteur conserve la propriété du droit d'auteur qui protège cette thèse. Ni la thèse ni des extraits substantiels de celle-ci ne doivent être imprimés ou autrement reproduits sans son autorisation.

0-612-46862-3

Canada

University of Alberta

Library Release Form

Name of Author: Astrid Jürgensen

Title of Thesis: Probing Electronic Structure and Chemical Bonding with X-ray Spectroscopy

Degree: Doctor of Philosophy

Year this Degree Granted: 1999

Permission is hereby granted to the University of Alberta Library to reproduce single copies of this thesis and to lend or sell such copies for private, scholarly, or scientific purposes only.

The author reserves all other publication and other rights in association with the copyright in the thesis, and except as hereinbefore provided, neither the thesis nor any substantial portion thereof may be printed or otherwise reproduced in any material form whatever without the author's prior written permission.

Astrid Jürgensen

Astrid Jürgensen
95 Clarendon Cres.
London, Ont.
Canada, N6C 5B7

1. October. 1999

University of Alberta

Faculty of Graduate Studies and Research

The undersigned certify that they have read, and recommend to the Faculty of Graduate Studies and Research for acceptance, a thesis entitled “Probing Electronic Structure and Chemical Bonding with X-ray Spectroscopy” submitted by Astrid Jürgensen in partial fulfillment of the requirements for the degree of Doctor of Philosophy.

Dr. Ronald G. Cavell

R.F. Egerton

Dr. Raymond F. Egerton

Dr. Wolfgang Jäger

Dr. Robert B. Jordan (Chair)

Dr. Mariusz Klobukowski

Dr. Dennis W. Lindle

30. Sept. 1999

To my parents

Dr. Reinhild and Dr. Helmut Jürgensen

and my sister

Frauke Jürgensen

Abstract

The availability of synchrotron sources has expanded significantly the use of x-ray photoelectron (PE) and photoabsorption (PA) spectroscopy to probe the molecular electronic structure and to test the various bonding models the understanding of which is central to all aspects of chemistry. All features observed in x-ray spectra result from electronic transitions within the molecule, which are in turn determined by the molecular electronic structure.

For this Ph.D. thesis, x-ray Photoelectron and photoabsorption spectra were measured for a variety of small model molecules. Of particular interest were simple compounds containing nitrogen, oxygen, chlorine and fluorine bound to phosphorus and sulphur wherein these latter elements exist in a highly oxidized valence state, because the state of bonding in these molecules is not well understood.

The experiments were conducted at the Canadian Synchrotron Radiation Facility (CSRF) located at the Synchrotron Radiation Center (SRC), University of Wisconsin, Madison, Wisconsin. A synchrotron light source displays several unique features ideal for x-ray spectroscopy. The light produced has a continuous frequency distribution ranging from the ultraviolet to the x-ray region. Specific frequencies can be selected with a monochromator; and finally, the light produced is intense, collimated and polarized. All of these properties contribute to the measurement of very high resolution x-ray spectra.

The research program involved the collection of experimental spectra of carefully selected compounds in the gas phase, which simplified analysis because all the observed spectral structure results from the electronic structure of the molecule without crystal

lattice or intermolecular interaction effects. The experimental spectra were compared with the results of electronic structure calculations done with MS-Xα and Gaussian-94 programs. This comparison with experimental results allows the evaluation of the theory and refinement of the bonding model.

Acknowledgements

I thank my supervisor Dr. R.G. Cavell for giving the opportunity to conduct research in the field of electron spectroscopy and for his guidance and support in the work. I also thank him for providing me with the experience of working at a Synchrotron Light Source. I also thank Dr. P.A. Cavell for all her help.

I thank M. Bissen (SRC), Dr. E. Hallin (CSRF), Dr. G.Retzlaff (CSRF), Dr. K. Tan (CSRF), D. Wallace (SRC) and Dr. B. Yates for their assistance with beamline operation and the setup of the experimental apparatus. I further thank our collaborators Dr. A.P. Hitchcock and Dr. T. Tyliszczak at McMaster University, Dr. J.J. Neville at the University of New Brunswick (Fredericton) and Dr. N. Kosugi at the Institute for Molecular Sciences in Okazaki, Japan.

All experimental work was conducted at the Synchrotron Radiation Center (SRC) of the University of Wisconsin, Madison, which is funded by NSF grant No. DMR-95-31009. The Canadian Synchrotron Radiation Facility (CSRF) at SRC is funded by NSERC. The MS-Xα program used for theoretical calculations of the spectra was provided by Dr. J. Tse from NRC, Ottawa. I thank NSERC and the University of Alberta for scholarship and financial support.

I thank S. Drummond, T. Oosterhuis and R. Reimer (Chaplains at the University of Alberta) and the members of the Lutheran Students movement for their friendship and spiritual support, and I thank my parents and my sister for their encouragement, help and moral support.

Table of Contents

1. THE SPECTROSCOPIC STUDY OF MOLECULAR BONDING........................ 1

1.1. PHOTOELECTRON SPECTROSCOPY 2

1.2. PHOTOABSORPTION SPECTROSCOPY 7

1.3. EXCITED STATE DECAY PROCESSES: AUGER, X-RAY FLUORESCENCE, AND FRAGMENTATION OF THE MOLECULE 8

2. THE GENERAL EXPERIMENTAL PROCEDURES... 15

2.1. AN ELECTRON STORAGE RING, A SYNCHROTRON 15

2.2. BEAMLINES AND MONOCHROMATORS: 19

2.2.1. The Mark IV "Grasshopper" Monochromator beamline of CSRF............ 20

2.2.2. The HERMON Beamline of SRC.. 21

2.2.3. Double Crystal Monochromator (DCM) beamline of CSRF 22

2.3. ENDSTATIONS: PHOTOELECTRON SPECTROMETER, GAS CELLS 23

2.3.1. Electron Energy Analyzer 23

2.3.2. Photoabsorption Gas Cell.. 25

3. ELECTRONIC STRUCTURE AND BONDING THEORY.................................. 30

3.1. THE PRINCIPLES OF MOLECULAR ORBITAL THEORY 30

3.1.1. Hartree-Fock Theory 31

3.2. MOLECULAR BONDING THEORY APPLIED TO PHOTOELECTRON AND PHOTOABSORPTION SPECTROSCOPY 33

3.2.1. Potential-at-the-nucleus model.. 34

3.2.2. The ΔE_{SCF} Method.. 38

3.2.3. Koopmans' Theorem Value 38

3.2.4. Direct Calculation of the Transition Energies with MS-Xα and Gaussian 94 39

3.3. MOLECULAR FIELD SPLITTING OF CORE ORBITALS 40

3.4. PHOTOABSORPTION CROSS-SECTION: 42

3.5. MS-Xα CALCULATIONS.. 45

3.6. MOLECULAR ORBITAL COMPOSITIONS WITH AB INITIO METHODS 50
3.7. ENERGY ESTIMATION FOR RYDBERG SERIES 52

4. AN OUTLINE OF THE CONCEPT OF HYPERVALENT MOLECULES 62

4.1. DUODECET RULE 62
4.2. THE THREE-CENTRE-FOUR-ELECTRON BOND MODEL AND PARTIAL IONIC BONDING 64
4.3. BOND ORDER AND VALENCES 66
4.4. NATURAL POPULATION ANALYSIS 69

5. P(1S) PHOTOABSORPTION EDGES AND THE CHEMICAL SHIFT TRENDS FOR A SERIES OF GASEOUS PHOSPHORUS COMPOUNDS 73

5.1. INTRODUCTION 73
5.2. EXPERIMENTAL 73
5.3. CALCULATIONS 74
5.4. RESULTS 75
5.5. DISCUSSION 77
  5.5.1. Trends and Relationships 77
  5.5.2. Electronegativity 79
  5.5.3. Potential at the nucleus method 81
  5.5.4. ΔE_{SCF} method for Photoelectron and Photoabsorption spectroscopy 83
  5.5.5. Excited states with $X\alpha$ and ab initio methods 84
  5.5.6. The role of d-orbitals 85
5.6. SUMMARY 85

6. CHEMICAL SHIFTS OF OXYGEN (1S) AND SULPHUR (2P) CORE BINDING ENERGIES OF VOLATILE SULPHUR COMPOUNDS: A SYNCHROTRON PHOTOELECTRON STUDY 105

6.1. INTRODUCTION 105
6.2. EXPERIMENTAL 106
6.3. RESULTS 107

6.4. DISCUSSION 107
6.4.1. Analysis based upon the Electronegativity of the Ligands *109*
6.4.2. Potential at the Nucleus *111*
6.4.3. Absolute Ionization Potentials *113*
6.5. SUMMARY 118
7. THE SULPHUR 2P PHOTOABSORPTION SPECTRUM OF NSF$_3$ 149
7.1. INTRODUCTION 149
7.2. EXPERIMENTAL 149
7.3. CALCULATIONS 150
7.4. RESULTS AND DISCUSSION 151
7.4.1. Valence shell antibonding orbitals *152*
7.4.2. Rydberg orbitals *153*
7.4.3. Post-edge resonances *153*
7.4.4. NSF$_3$ versus OPF$_3$ *155*
7.5. SUMMARY 156
8. NITROGEN, OXYGEN, PHOSPHORUS AND SULFUR K-SHELL PHOTOABSORPTION SPECTRA OF NSF$_3$ AND YPF$_3$ (Y = O, S, NOTHING) MOLECULES 169
8.1. INTRODUCTION 169
8.2. EXPERIMENTAL 169
8.3. CALCULATIONS 170
8.4. RESULTS AND DISCUSSION 171
8.4.1. PF$_3$, OPF$_3$ and SPF$_3$ *172*
8.4.2. The NSF$_3$ Molecule *178*
8.4.3. NSF$_3$ versus OPF$_3$ *180*
8.5. SUMMARY 181

9. COMPARATIVE OXYGEN 1S PHOTOABSORPTION SPECTRA OF SO_2 AND NO_2 195

9.1. INTRODUCTION 195
9.2. EXPERIMENTAL 195
9.3. CALCULATIONS 196
9.4. RESULTS AND DISCUSSION: 198
    9.4.1. Molecular Structure 198
    9.4.2. Experimental Spectra and Assignment 201
9.5. SUMMARY 203

10. A SYNCHROTRON STUDY OF THE OXYGEN 1S PHOTOABSORPTION SPECTRA OF SULPHURYL HALIDES AND THEIR METHYLATED DERIVATIVES SO_2XY (X, Y = F, CL, CH_3, CF_3) 214

10.1. INTRODUCTION 214
10.2. EXPERIMENTAL 214
10.3. CALCULATIONS 214
10.4. RESULTS 216
    10.4.1. SO_2Cl_2 216
    10.4.2. SO_2FCl 217
    10.4.3. SO_2F_2 217
    10.4.4. CH_3SO_2F 218
    10.4.5. CH_3SO_2Cl 218
    10.4.6. CF_3SO_2Cl 219
10.5. DISCUSSION 219
    10.5.1. Pre–edge Peaks 219
    10.5.2. Post Edge shape resonances 222
10.6. SUMMARY 224

11. THE VALENCE SHELL PHOTOIONIZATION ENERGIES CROSS-SECTIONS OF NF_3 AND PF_3 237

11.1. INTRODUCTION 237

11.2. EXPERIMENTAL 237

11.3. CALCULATIONS 238

11.4. RESULTS AND DISCUSSION 240

11.4.1. Experimental Results *240*

11.4.2. Identity of the molecular orbitals *240*

11.4.3. Comparison of Experiment and Theory *242*

11.5. SUMMARY 244

12. OVERVIEW AND GENERAL DISCUSSION 257

12.1. THE MS-Xα TECHNIQUE FOR THE CALCULATION OF X-RAY SPECTRA 257

12.1.1. The Effect of the Molecular Symmetry on the Ionization Potentials *257*

12.1.2. The Chemical Shift of the Hydrides H_2S and PH_3 .... *258*

12.1.3. Radicals and the Inclusion of Electron Spin *260*

12.1.4. The Role of the Watson Sphere in the Calculation of the Pre-Edge Photoabsorption Peaks *261*

12.2. AB INITIO GAUSSIAN 94 METHODS FOR THE CALCULATION OF IONIZATION POTENTIALS AND X-RAY SPECTRA 264

12.2.1. Molecular excited states with CIS *265*

12.3. THE OCCURRENCE OF LS STATES. IS THIS A GENERAL PHENOMENON? 267

12.4. BOND COVALENCY DEDUCED FROM THE P-CHARACTER OF MOLECULAR ANTIBONDING ORBITALS 269

12.5. CONCLUSION 274

13. REFERENCES 284

List of Figures

Figure 1-1: The photoelectron and photoabsorption processes. 12
Figure 1-2: Potential curves for ground state and excited state. 13
Figure 1-3: The valence shell photoelectron spectra of SO_2 and NO_2. 14
Figure 2-1: Diagram of a synchrotron ring. 27
Figure 2-2: A Hemispherical Analyzer. 28
Figure 2-3: Gas cell assembly and illustration of the cell parameters. 29
Figure 3-1: The arrangement of potential spheres in SO_2 54
Figure 3-2: Muffin tin potential for N_2 55
Figure 4-1: Resonance structures of PF_5. 71
Figure 4-2: The traditional three-centre-four-electron bonding model (left) and Ángyán's bonding modification [134] involving the central atom d_{z^2} orbital (right). 72
Figure 5-1: P(1s) Photoabsorption Spectra of PH_3 , PF_5, $OPCl_3$ and PCl_3. 86
Figure 5-2: The correlation between the P(1s)$\rightarrow$ 1e* transition energy shifts and the P(1s) ionization potential (IP) and KL_2L_3 ($^1D_2$) Auger shifts (eV) (relative to PH_3). 87
Figure 5-3: Correlation between the chemical shift (eV) and the sum of the ligand electronegativities, $\Sigma\chi_l$. 88
Figure 5-4: Correlation of the P(1s) Ionization Potential chemical shift (eV) with the Potential at the Nucleus shifts calculated from *ab initio* natural charges (Gaussian 94, D95* basis set). 89
Figure 5-5: Correlation between the calculated charge on the phosphorus atom (Gaussian 94, D95* basis set) and $\Sigma\chi_l$. 90
Figure 5-6: Correlation between the chemical shift (eV) and the calculated charge on the phosphorus atom (Gaussian 94, D95* basis set). 91
Figure 5-7: Correlation between the experimental P(1s)$\rightarrow$ 1e* transition energy chemical shift (eV) and the Potential at the Nucleus shifts calculated from *ab initio* charges. . 92
Figure 5-8: The correlation between the experimental chemical shifts and calculated values: ΔE_{SCF} method. 93
Figure 5-9: The correlation between the P(1s)$\rightarrow$ 1e* experimental transition energy chemical shifts (eV) and the calculated values: CIS method. 94

Figure 5-10: The correlation P(1s)→ 1e* experimental transition energy chemical shifts (eV) and calculated values: Xα method. 95

Figure 6-1: Experimental chemical shifts (eV), O(1s) *versus* S($2p_{3/2}$). 119

Figure 6-2: Experimental chemical shifts (eV) *versus* ligand electronegativity 120

Figure 6-3: S($2p_{3/2}$) chemical shifts (eV), calculated *versus* experimental: Potential at the Nucleus model. 122

Figure 6-4: O(1s) chemical shifts (eV), calculated *versus* experimental: Potential at the nucleus model. 123

Figure 6-5: O(1s) chemical shifts (eV), calculated *versus* experimental: ΔE_{SCF} model. 124

Figure 6-6: S($2p_{3/2}$) chemical shifts (eV), calculated *versus* experimental: ΔE_{SCF} model. 125

Figure 6-7: Chemical shifts (eV), calculated *versus* experimental: Xα method. 126

Figure 6-8: Chemical shift (eV), calculated *versus* experimental: Koopmans' value, ground state model. 127

Figure 6-9: Chemical shifts (eV), calculated *versus* experimental: Koopmans' value, transition state model. 128

Figure 7-1: The sulphur 2p photoabsorption spectrum of NSF_3. 158

Figure 7-2: Comparison of the experimental S(2p) pre edge spectrum with the results from the GSCF3 calculation. 159

Figure 7-3: The sulphur 2p photoionization cross-section calculated with Xα. 160

Figure 7-4: Central atom 2p photoabsorption spectra of NSF_3 and OPF_3. 161

Figure 7-5: The contour plots of the valence shell antibonding orbitals for NSF_3 and OPF_3. 162

Figure 8-1: Central atom—phosphorus or sulphur—K shell spectra calculated with the Xα technique. 182

Figure 8-2: Terminal atom—nitrogen, oxygen or sulphur—K shell spectra calculated with the Xα technique. 183

Figure 8-3: Experimental spectra of central atom—phosphorus or sulphur—K shell. 184

Figure 8-4: Experimental spectra of terminal atom—nitrogen, oxygen or sulphur—K shell. 185

Figure 9-1: The calculated (Xα) oxygen 1s spectra 205
Figure 9-2: The experimental oxygen 1s spectra 206
Figure 9-3: The molecular orbital energy diagrams of NO_2 and SO_2, showing the relative positions of the valence and virtual orbitals in the initial electronic state ($^2A_1$ for NO_2 and $^1A_1$ for SO_2) 207
Figure 10-1: Experimental O(1s) photoabsorption spectra, pre-edge peaks 225
Figure 10-2: Calculated O(1s) spectra, pre-edge peaks 226
Figure 10-3: Decomposition of SO_2Cl_2 as evidenced from the O(1s) photoabsorption spectrum and the O(1s) spectrum of SO_2, the reaction product 227
Figure 10-4: Experimental O(1s) Spectra, pre-edge peaks and all post-edge resonances 228
Figure 10-5: Calculated Oxygen 1s Photoionization Cross-Sections 229
Figure 11-1: The experimental valence shell photoelectron spectra of NF_3 and PF_3. 246
Figure 11-2: The orbital energy diagrams of NF_3 and PF_3. 247
Figure 11-3: The calculated (MS-Xα) valence shell photoelectron spectra of NF_3 and PF_3. 248
Figure 11-4: The valence shell photoionization branching ratios of NF_3 249
Figure 11-5: The valence shell photoionization branching ratios of PF_3. 250

List of Tables

Table 3-1: The valence shell ionization potentials of PF_3 (eV) 56
Table 3-2: Character Table for the K point group 57
Table 3-3: Character Table of the C_{3v} double group 58
Table 3-4: Character Table of the C_{2v} double group 59
Table 3-5: Character Table of the D_{3h} Double Group 60
Table 3-6: Character Table for the C_s Double Group 61
Table 5-1: P(1s) and P(2p) ionization potentials (eV) of PBr_3 and $CH_3P(O)Cl_2$ 96
Table 5-2: Experimental P(1s)→1e* transition energies ($E_{1s\rightarrow 1e^*}$), the experimental transition energy shifts ($\Delta E_{1s\rightarrow 1e^*}$), and calculated chemical shifts: Potential at the Nucleus Method. 97
Table 5-3: The line of best-fit parameters for the correlation between calculated and experimental chemical shifts 98
Table 5-4: Atom and group electronegativities (Pauling Scale) 100
Table 5-5: Ligand electronegativities and charge (NPA method) on the phosphorus nucleus. 101
Table 5-6: Experimental and calculated P(1s)→1e* ($\Delta E_{1s\rightarrow 1e^*}$) and P(1s) ionization potential (ΔE_{IP}) chemical shifts(eV): ΔE_{SCF} method. 102
Table 5-7: Calculated P(1s)→1e* transition energy ($E_{1s\rightarrow 1e^*}$) and the corresponding chemical shift (eV): CIS method. 103
Table 5-8: Calculated P(1s) ionization potential (E_{IP}) and P(1s)→1e* transition energy ($E_{1s\rightarrow 1e^*}$) and the corresponding chemical shifts (eV): Xα method 104
Table 6-1: Oxygen 1s ionization potentials (eV). 129
Table 6-2: Sulphur 2p ionization potentials (eV). 130
Table 6-3: Sulphur compound groups. 131
Table 6-4: Oxygen compound groups. 132
Table 6-5: Experimental ionization potentials and chemical shifts (eV). 133
Table 6-6: Group electronegativities. 135
Table 6-7: Ligand electronegativities. 136

Table 6-8: Calculated O(1s) ionization potential chemical shifts (ΔIP): Potential at the Nucleus method. 138

Table 6-9: Calculated $S(2p_{3/2})$ ionization potential chemical shifts (ΔIP): Potential at the Nucleus method. 139

Table 6-10: The line of best-fit parameters for the correlation between calculated and experimental chemical shifts 141

Table 6-11: Calculated $S(2p_{3/2})$ ionization potential chemical shifts (eV): ΔE_{SCF} method. 143

Table 6-12: Calculated O(1s) ionization potential chemical shifts (eV): ΔE_{SCF} method. 144

Table 6-13: Calculated ionization potentials and chemical shifts (eV): Xα method. 145

Table 6-14: O(1s) ionization potentials (eV), symmetry effects: Xα method 146

Table 6-15: Calculated $S(2p_{3/2})$ chemical shifts (eV): Koopmans' value 147

Table 6-16: Calculated O(1s) chemical shifts (eV): Koopmans' value 148

Table 7-1: Molecular geometry of NSF_3 163

Table 7-2: Calculated relative energies (eV) for the electronic transitions from the S(2p) core to the valence shell antibonding orbitals of NSF_3. 164

Table 7-3: Calculated S(2p)→Rydberg transition energies and term values (eV) of NSF_3. 165

Table 7-4: Experimental peak energies and term values (eV) of the S(2p) spectrum of NSF_3 166

Table 7-5: Transitions to valence shell antibonding orbitals in NSF_3 and OPF_3. The LS coupled states are highlighted in bold type 167

Table 7-6: Singlet-Triplet splitting (eV) for the LS states in NSF_3 and OPF_3 168

Table 8-1: Core ionization potentials (eV) 186

Table 8-2: Molecular geometry 187

Table 8-3: alpha parameters and sphere radii 188

Table 8-4: Assignment of the virtual orbitals 189

Table 8-5: Central atom K shell photoabsorption peaks 190

Table 8-6: Terminal oxygen or sulphur K shell photoabsorption peaks 192

Table 8-7: Calculated Atomic Charges with Gaussian 94 (HF, D95* basis set, experimental geometry, natural charges) 194

Table 9-1: The parameters employed for the $X\alpha$ calculations of NO_2 and SO_2 208

Table 9-2: The valence shell and virtual molecular orbitals of SO_2 and NO_2 as determined by Gaussian-94. 209

Table 9-3: Experimental oxygen 1s photoabsorption peaks and their assignments based upon the $X\alpha$ calculation results. 210

Table 9-4: The vibrational modes of SO_2 and NO_2, experiment and Gaussian 94 calculations (optimized geometry, 6-31G* basis set) for the ground state and the $(O(1s)^3\ 1b_1{}^{*1})$ excited state. 212

Table 9-5: Calculated transition energies (eV) and term values (eV) from the O(1s) core to virtual orbitals, using the MS-$X\alpha$ method. 213

Table 10-1: Experimental Transition Energies (eV) and Assignments. 230

Table 10-2: O(1s)→LUMO transition and p–character of the LUMO. 234

Table 10-3: p–character of the other sulphur–"halogen" σ^* orbital. 235

Table 10-4: p–character of the other sulphur–oxygen σ^* orbitals. 236

Table 11-1: The molecular geometries, experiment and theory (Gaussian 94, B3LYP, 6-31G*). 251

Table 11-2: The valence shell ionization potentials (eV) of NF_3 and PF_3 and their assignment. 252

Table 11-3: The molecular orbital compositions as calculated from the LCAO molecular orbital coefficients (G-94, 6-31G*). 253

Table 11-4: The calculated valence shell ionization potentials obtained with Koopmans' theorem (Gaussian 94 *ab initio* calculations) (eV). 254

Table 11-5: The calculated valence shell ionization potentials obtained from the difference in total energy between the initial and final sates (eV). 255

Table 11-6: The calculated valence shell ionization potentials obtained from the CIS excited states of NF_3^+ and PF_3^+ (Gaussian 94 *ab initio* calculations) (eV). 256

Table 12-1: The effects of molecular point group on the O(1s) ionization potentials calculated with $X\alpha$. 275

Table 12-2: The Ionization Potentials (eV) of the NO_2 Molecule. 276

Table 12-3: The stabilization effect by the Watson Sphere on the virtual orbitals of SO_2. At a constant sphere radius (R = 4.035 a.u.) an increased Sphere charge Q leads to increased stabilization. 277

Table 12-4: The effect of the Watson Sphere charge Q on the calculated O(1s)→mo* transition energies (E) and oscillator strengths (f) of SO_2 at a constant Sphere radius (R = 4.035 a.u.). 278

Table 12-5: The effect of the Watson Sphere radius on the calculated O(1s)→mo* transition energies (E) and oscillator strengths (f) of SO_2 at a constant Sphere charge (Q = 0.5). 279

Table 12-6: The O(1s)→mo* transitions of SO_2, calculated with the CIS method of Gaussian 94. 280

Table 12-7: The central atom $L_{2,3}$ shell excited state, which displays LS coupling......... 281

Table 12-8: The O(1s)→π* transition energies and cross-sections, and the experimental and calculated O(2p) character of the π* orbital. 282

Table 12-9: The P(1s)→1e* transition energies and cross-sections, and the experimental and calculated P(3p) character of the 1e* orbital. 283

1. The Spectroscopic Study of Molecular Bonding

Understanding the chemical bond is central to all aspects of chemistry. Atoms combine in many different ways to form molecules, each with a unique set of physical and chemical properties. These properties are determined by the molecular electronic structure, which in turn is determined by the laws of physics [1], in particular electrostatics. Knowledge of the electronic structure is thus essential to understand and predict the chemical behaviour of individual molecules. An insight into how the electronic structure and the molecular properties vary within groups of related molecules is required as well [1]. Numerous theoretical methods [1-7] have been developed to model the electronic structure of atoms and molecules, and to calculate their physical and chemical properties. In order to use these theoretical models to explain the electronic structure and to predict unknown properties of atoms and molecules, these models need to be thoroughly tested to answer the question: how well do the calculations reproduce known properties, determined experimentally? Recent advances in x-ray spectroscopy using synchrotron sources have provided the means of probing the molecular electronic structure and testing the theoretical models. All features observed in the x-ray spectra result from electronic transitions within the molecule, and these are determined by its electronic structure.

Electronic spectroscopic studies can reveal substantial information about the electronic structure of a molecule. The binding energies of all molecular orbitals can be determined with photoelectron spectroscopy [8]. With appropriate resolution, vibrational and rotational states of the ionized molecule can be revealed [8]. The energies required to excite core electrons to unoccupied molecular orbitals in the valence shell and to Rydberg orbitals fall within the x-ray region (soft to very hard, depending on the atom involved), and this process is labeled x-ray absorption near edge spectroscopy (XANES). The position and intensity of peaks in K-shell XANES spectra reveal both the identity of the atom and its valence state in the molecule. Electronically excited states created with x-rays undergo de-excitation processes, which yield fluorescence (x-ray fluorescence) [9] and Auger electron spectroscopies [10]. Additional detail may be revealed through the use of photoelectron-photoion-coincidence techniques [11, 12]. All the electronic processes observed are chemically sensitive and also sensitive to the structure of the molecule. The fullest information is provided by high quality x-ray spectra, which are readily obtained with a synchrotron light source [13].

In this project, x-ray photoelectron and photoabsorption spectra were measured and combined with *ab initio* calculations to determine the electronic structure and chemical bonding of a variety of small molecules. Of particular interest are simple compounds containing nitrogen, oxygen, fluorine, and chlorine bound to phosphorus and/or sulphur, especially species wherein these latter elements exist in a highly oxidized valence state. In the cases of these highly oxidized valence states, the actual nature of the chemical bonds formed is not well understood [14, 15]. Comparing the theoretical calculations with experimental results derived from the x-ray spectroscopic measurements will allow the evaluation of the theory, and whether it provides an appropriate description of the bond.

1.1. Photoelectron Spectroscopy

Photoelectron spectroscopy yields both a measurement of the specific electron binding energy of each molecular orbital and the photoionization cross-section $\sigma(h\nu)$ (relative intensity) for each photoionization process. The photoelectron process is illustrated in Figure 1-1. A photon with energy $h\nu$ interacts with the initial state of a molecule, ionizing the molecule (i.e. creating an ionic state of the molecule with a vacancy in molecular orbital ϕ_i). All of the input energy is used to promote and eject an electron from the molecule and, because the energy of the photon is greater than the ionization potential, this photoelectron has a measurable kinetic energy, E_k. The energy difference between that of the initial molecular state (Ψ_i) and the final state of the ion (Ψ_f) can be deduced through measurement of E_k at a known fixed photon energy $h\nu$, and by applying equation (1-1), which is based on the Conservation of Energy Principle. This energy difference is called the binding energy (E_B) of the electron [16].

$$E_B = h\nu - E_k - E_c \tag{1-1}$$

The term E_c is a correction term which accounts for the recoil energy of the ion, negligibly small in most applications [16], and the work function W, which can have a significant effect in solids [16]. In a gas system, W arises from charging effects of the cell and the charge buildup in the ionization region. The former can be minimized by grounding the gas cell and the latter by effective pumping. Since E_c is difficult to measure, it is eliminated through calibration of the instrument with a gas with well known electron binding energies, for example noble gases. Equation (1-1) hence simplifies to equation (1-2) where $E(\Psi_f)$ and $E(\Psi_i)$ are the total energies of the final and initial states [8].

$$E_B = h\nu - E_k = E(\Psi_f) - E(\Psi_i) \tag{1-2}$$

Both the molecule and the ion are polyatomic species; hence both have electronic, vibrational and rotational excited states. At room temperature, given the energy differences between these states (rotational: < 0.1 eV, vibrational: 0.3 eV, electronic: 3 to 10 eV), the vast majority of molecules will be in the electronic and vibrational ground states (Boltzman distribution: ground state population > 99.99% for $E_{vib} \geq 0.24$ eV and $E_{rot} \geq 0.12$ eV). However, transitions to electronically and vibrationally excited states can, and do, occur. Both have been observed experimentally [17-20]. Transitions to rotationally excited states are also expected, but these energy differences are so small (a few meV) that in most photoelectron experiments they are not resolved. Their contribution is omitted in further discussion. As the resolution of photoelectron spectrometers continues to improve (at present, the state of the art instruments have a resolution of about 5 meV), resolution of rotational structure for small molecules will likely become routine in the near future. Recently there have been investigations of rotationally excited states of N_2^+ [21, 22] and H_2^+ [23].

The potential energy curves for the initial and final states are shown schematically in Figure 1-2. The photoelectron process for the molecule thus involves a transition from the ground electronic state X and ground vibrational state v_0 to an ion in an electronic state Y and with a vibrational state v'_n [8].

$$M(X, v_0) + h\nu \rightarrow M^+(Y = X,A,B,C,\ldots, v'_{n=0,1,2,\ldots}) + e^- \qquad (1\text{-}3)$$

For this photoexcitation process the transition probability per unit time, P_{if}, is given by equation (1-4) [24], where E_0 is the magnitude of the electric field vector of the incident radiation, $\omega = 2\pi\nu$ is the angular frequency and $\rho_f(E)$ is the density of states at $h\nu = E$, **p** is the sum of the linear momentum operators of the electrons, and **e** is a unit vector in direction of the electric field vector of the incident radiation.

$$P_{if} = \frac{\pi e^2 E_0^{\ 2}}{2\hbar m^2 \omega^2} \rho_f(E) \mid \langle \Psi_f (Y, v_n') | \, e^{i\mathbf{k}\cdot\mathbf{x}} \, \mathbf{e}\cdot\mathbf{p} \, |\Psi_i(X, v_0)\rangle \mid^2 \qquad (1\text{-}4)$$

Application of the Born-Oppenheimer approximation [25] and the dipole approximation [26] allows the last term of equation (1-4) to be separated into three components, which describe the electronic state, the vibrational motion, and the electron spin configuration, respectively.

$$P_{if} = \frac{\pi e^2 E_0^{\ 2}}{2\hbar m^2 \omega^2} \rho_f(E) \mid \langle \psi_f^e \mid \mathbf{e}\cdot\mathbf{p} \mid \psi_i^e \rangle \mid^2 \mid \langle \psi_f^{v'} \mid \psi_i^{v_0} \rangle \mid^2 \mid \langle \psi_f^s \mid \psi_i^s \rangle \mid^2 \qquad (1\text{-}5)$$

The existence of an unbound electron in the final state guarantees that P_{if} will be non-zero for all transitions, provided that $\psi_f^s = \psi_i^s$; hence, the photoelectron process is restricted only by the spin selection rule $\Delta s = 0$ [8]. As a result, if there is minimal lifetime broadening, there can be a multitude of vibrational peaks for each electronic transition. Of these, two are most commonly considered [8]:

1. Adiabatic ionization energy E_{Ba}: the energy corresponding to the transition

   $$M(X, v_0) + h\nu \rightarrow M^+(Y, v' = v_0') + e^-, \qquad (1\text{-}6)$$

2. Vertical ionization energy E_{Bv}: the energy corresponding to the transition

   $$M(X, v_0) + h\nu \rightarrow M^+(Y, v' = v_n') + e^-, \qquad (1\text{-}7)$$

   where n is the quantum number of the vibrational state whose wavefunction gives the largest overlap with the wavefunction of the initial state.

For many molecules, these two ionization energies are identical or indistinguishable within the limits of the spectral resolution.

Analysis of photoelectron spectra must also include the concept of multiplet splitting. The two most important types of multiplet splitting arise from Russell-Saunders (LS) coupling and from spin-orbit (jj) coupling of the orbital angular momenta and electron spins. The former is caused by electrostatic repulsion of the electrons in an atom or molecule [27]. This repulsion is greater for electrons occupying the same orbital than for electrons in different orbitals. The electron spin is connected to electrostatic repulsion, because electrons with parallel spins must of necessity occupy different orbitals. To determine the electronic states in the Russell-Saunders coupling scheme, the orbital angular momenta and spins of all electrons are coupled separately to give an overall angular momentum L and spin S. These then couple to give the total angular momentum $J = L+S, L+S-1, \ldots, |L-S|$ of the state [27]. These three quantum numbers are then combined to obtain the term value ($^{2S+1}L_J$) [27]. Just as the atomic orbitals with different angular momentum are designated by letters (s, p, d, f…), so are the electronic states. The angular momentum L is indicated by the corresponding capital letter (S, P, D, F…). A state with $L = 1$, $S = {}^1/_2$ and $J = {}^3/_2$ is written as $^2P_{3/2}$, for example. Various theoretical [28] inorganic and physical chemistry textbooks [27, 29, 30] describe the methodology of assembling the proper description of LS coupled states of atoms or molecules.

Spin-orbit coupling (jj) arises from the relativistic interaction of electron spin and orbital angular momentum [27]. As the electron moves about the nucleus with velocity **v** at a distance **r**, it creates a magnetic field **B** given by equation (1-8)[31]. The magnetic moment inherent in the electron spin aligns itself with this field in either parallel or opposite directions. Of these, the latter alignment has lower energy.

$$\mathbf{B} = \frac{Ze}{r^3 c}\,\mathbf{r} \times \mathbf{v} \qquad (1\text{-}8)$$

To determine the electronic states, first the orbital angular momentum l and the spin s of each individual electron are coupled to give a combined moment j, and these are then coupled to give a combined momentum J [27].

Both Russell-Saunders and spin-orbit coupling represent extreme cases of the coupling between orbital angular momentum and electron spin. Many states of intermediate coupling exist. It is, however, difficult to calculate these states of intermediate coupling. Features in photoelectron spectra are usually described in terms of either Russell-Saunders or spin-orbit coupling, and the decision on which scheme to use is based upon relative energetics. If the electrostatic electron-electron repulsion energy exceeds the magnetic spin-orbit energy, then Russell-Saunders coupling is the correct scheme. Otherwise, spin-orbit coupling applies. For most molecules the former coupling scheme dominates for valence shell excitations, while for core excitations the latter scheme is more important. The magnitude of spin-orbit coupling increases with atomic number Z of the excited atom.

Most molecules have a singlet ground state configuration, that is, all electrons are paired. Upon valence-shell photoionization, an unpaired electron remains in the molecular orbital ϕ_i, which leads to a doublet final electronic state. A single peak is observed for the transition because the spin-orbit coupling within the valence shell is generally not large. A few molecules, for example NO_2, are radicals, which already have at least one unpaired electron in the ground state configuration. Photoionization in these cases leads to a final ion state, which has at least two unpaired electrons. These spins interact, creating several distinct electronic states of the ion and photoelectron. In general, the transition energies to these states will be different; and hence a photoelectron peak is observed for each. These contrasting situations are illustrated in Figure 1-3 with the valence shell photoelectron spectra of SO_2 (closed shell) and NO_2 (open shell). Photoionization of the former molecule leads to an ion with one unpaired electron. The final state of the ion is—in the LS coupling scheme—always a doublet, so each valence shell ionization gives rise to a single photoelectron peak (Figure 1-3). In the case of NO_2, however, the photoelectron process leads to ions with two unpaired electrons unless the original unpaired electron in the outermost orbital is ejected. With two unpaired electrons there exist two possible electronic states for the ion, a singlet and a triplet (LS coupling scheme). Each gives rise to a photoelectron peak, as seen in Figure 1-3. In cases where the spin-orbit coupling is large even in the (outermost) valence shell, for example, the 5p shell of xenon, a large spin-orbit component is observed. The valence shell photoelectron spectrum of xenon shows three peaks corresponding to the $^2P_{3/2}$, $^2P_{1/2}$ (electron ejected from the valence shell p orbitals) and $^2S_{1/2}$ (electron ejected from the valence shell s orbital) final electronic states of the ion.

1.2. Photoabsorption Spectroscopy

If the photon energy is less than that required for photoionization, the interaction between photons and molecules leads to electronically excited molecular states. The absorption of the photon promotes an electron into one of the unoccupied orbitals, which may be of non- or anti-bonding character. In contrast to the photoelectric effect, which occurs at all photon energies exceeding the ionization threshold, this process requires matching of the incident photon energy to the transition energy, since there is no photoelectron to carry away the excess energy. The photoabsorption spectrum of a molecule therefore displays peaks at energies corresponding to the transition energies between occupied and empty orbitals.

The photoabsorption transition probability to excited molecular states is given by equation (1-5). However, in this case the final state does not contain any free electrons; all electrons are in molecular orbitals, which have specified angular momentum. Hence, the dipole selection rule ($\Delta l = \pm 1$) applies to the photoabsorption process in addition to the spin selection rule $\Delta s = 0$.

Most molecules do not belong to a high symmetry point group. In consequence, the molecular field created by the presence of the other atoms removes the degeneracy of atomic p, d, f etc. orbitals. For example, in PF_3, a C_{3v} molecule, the triply degenerate p orbitals of phosphorus split into a_1 and e symmetry components, and the five-fold degenerate d-orbitals split into an a_1 and two e components. Under these lower symmetry conditions the electronic transition term $|\langle\psi_f^e|\mathbf{e}\cdot\mathbf{p}|\psi_i^e\rangle|^2$ in equation (1-5) is only non-zero if and only if the triple product $\Gamma(\psi_f^e) \times \Gamma(\mathbf{p}) \times \Gamma(\psi_i^e)$ of the irreducible representations of

ψ_f^e, **p** and ψ_i^e, respectively, contains the totally symmetric irreducible representation of the molecular point group [28]. Or, more simply, the direct product $\Gamma(\psi_f^e) \times \Gamma(\psi_i^e)$ must contain at least one component of $\Gamma(\mathbf{p})$. Since the dipole operator has components in each coordinate ($p_x\mathbf{x}$) etc., $\mathbf{p} = p_x\,\mathbf{x} + p_y\,\mathbf{y} + p_z\,\mathbf{z}$, it will always transform as x, y and z (the unit vectors in the Cartesian coordinate system) in any point group. That is, $\Gamma(\mathbf{p}) = (\Gamma(\mathbf{x}), \Gamma(\mathbf{y}), \Gamma(\mathbf{z}))$. The character of the wavefunctions $\Gamma(\psi_f^e) \times \Gamma(\psi_i^e)$ must contain at least one of these three irreducible representations [28]. Both $\Gamma(\psi_f^e)$ and $\Gamma(\psi_i^e)$ are determined from the electron configurations of the final and initial states, respectively. A detailed method for determination of $\Gamma(\psi_f^e)$ and $\Gamma(\psi_i^e)$ is presented by Harris and Bertolucci [28]. The overall effect of the lower molecular symmetries is to increase the number of allowed transitions.

1.3. *Excited State Decay Processes: Auger, X-ray Fluorescence, and Fragmentation of the Molecule*

Both photoabsorption and photoelectron processes leave the molecule or ion in an excited electronic state. This state, being unstable, will decay to a lower energy electronic state through rearrangement of the electron configuration. Several paths exist to achieve this de-excitation.

The major competing processes for decay of a core hole state are x-ray fluorescence and the ejection of an Auger electron. In both processes, a transition of an outer shell electron into the core hole takes place. The energy released is either converted into an x-ray photon (x-ray fluorescence) or it is given to another electron in an outer shell orbital, which is then ejected from the ion—the Auger electron. Of these two de-excitation processes, the Auger effect is dominant for low binding energies of the core level initially ionized, up to about the 1s ionization potential of arsenic ($Z = 33$) [32] (11.8 keV [33]).

X-ray fluorescence is essentially the reverse process of photoabsorption: an electronic transition to fill an inner shell hole leads to the emission of a photon [9]. It is, therefore, subject to the same selection rules: $\Delta l = \pm 1$, $\Delta s = 0$, and $\Delta j = \pm 1$ or 0. In a few instances the first and the last rule are broken (e.g. $\Delta l = -2$ or 0, $\Delta j = -2$), and low intensity forbidden lines are observed [9]. The energy of the x-ray produced corresponds to the difference in binding energy between the two levels involved in the electronic transition. The widely accepted notation for x-ray emission lines indicates the final level of the electronic transition by a capital letter, e.g. K for the 1s shell. This is then followed by a lower case Greek letter and a number subscript to differentiate each line based upon its relative intensity, for example $K\alpha_1$ and $L\beta_2$ [9].

In the non-relativistic limit the Auger process involves a two-electron electrostatic interaction [34]. Under Russell-Saunders coupling conditions the selection rules are $\Delta S = \Delta L = \Delta M_S = \Delta M_L = \Delta J = 0$ and parity is conserved. Similarly, in the spin-orbit coupling scheme, $\Delta M = \Delta J = 0$, and parity is conserved. For low Z atoms, the Auger transitions are best described in terms of Russell-Saunders coupling. Spin-orbit interactions become more important as the atomic number Z increases, but even for Z = 80 the electrostatic interactions between electrons cannot be ignored, and the observed transitions are best described by an intermediate coupling scheme [34].

When a vacancy in an inner shell V is filled by an electron from the outer shell X, the energy E_{VX} released by this transition equals the difference between the ionization potentials of the two levels. This energy is acquired by a second electron in the outer shell Y, which then escapes from the ion. Its measurable kinetic energy E_{Aug} equals the difference between E_{VX} and the binding energy of shell Y in an ion with a vacancy in shell X—i.e. E_Y'. This radiationless rearrangement of electrons is only allowed if E_{VX} exceeds E_Y'. The kinetic energy of the Auger electron is independent of the energy of the incident particles. It depends only on the energy levels involved in species that undergo Auger de-excitation.

The Auger transitions resulting in the de-excitation of ions are labeled using the energy levels involved, usually in the form of $V_pX_qY_r$ [34]. V is the energy level of the original vacancy; X and Y are the levels where vacancies occur after de-excitation. The subscripts p, q and r are subshell indices. For example, K-series transitions have the original vacancy in the K or 1s shell. They are denoted by KX_qY_r or $1sX_qY_r$. Possible K-series transitions include KL_1L_2=$1s2s2p_{1/2}$ and KL_2L_3=$1s2p_{1/2}2p_{3/2}$. A special type of Auger transition is the Coster-Kronig transition [34]. In this process, the primary vacancy is filled by an electron from a different subshell of the same major shell, for example $L_1L_2M_4$. However, the overall process is similar to the Auger process.

A special case of the Auger process is the resonance Auger transition [10]. This may occur when absorption of the photon leads to the excitation of a core electron into an antibonding orbital, forming an excited molecular state with a hole in an inner shell rather than the ion formed in the continuum Auger process. The normal Auger process then occurs, with the final result that an ion with charge +1 and the Auger electron are produced, in contrast to the continuum Auger process, in which the initial state is an ion of +1 charge, and the final state an ion of +2 charge. Resonant Auger processes are commonly divided into two groups [10]:

1. Spectator resonant Auger transition: The excited electron is a spectator in the Auger decay process.
2. Participator resonant Auger transition: The excited electron is one of the participating electrons in the Auger decay process. This transition is also referred to as autoionization as it is identical to the autoionization process [8] observed for valence shell excitation [10].

Of these two decay mechanisms, the spectator resonant Auger transition is the dominant method for core hole states [10], but decay by participator resonant Auger transitions is prominent in cases where the other mechanism is forbidden, for example valence shell excited states [10]. Participator resonant Auger transitions are an important decay mechanism in some core excited states (e.g. $Ba(4d^9 4f)$ [35]) as well [10]. Energies and peak intensities of the resonance Auger spectrum are expected to differ from the continuum Auger spectrum observed when the initial excitation energy exceeds the ionization potential of the core level with the primary vacancy [10]. Unlike the continuum Auger, the resonance Auger process is only observed when the photon energy matches the core→mo* transition energy, and so, it is necessary to have a tunable excitation source (such as is provided by an electron synchrotron).

Another de-excitation path for electronically excited molecules or ions is fragmentation. One or more of the chemical bonds break to produce various charged and neutral fragment species. Core excitation usually leads to the complete breakup of the molecule [11] into its component atoms, which often have a high positive charge due to multiple Auger transitions. In contrast, polyatomic fragment ions are often observed at lower photon energies following valence shell ionization, see for example [36-43]. The study of these fragmentation processes to gain information about electronic structure and chemical bonding is the object of the emerging field of photoelectron-photoion coincidence spectroscopy.

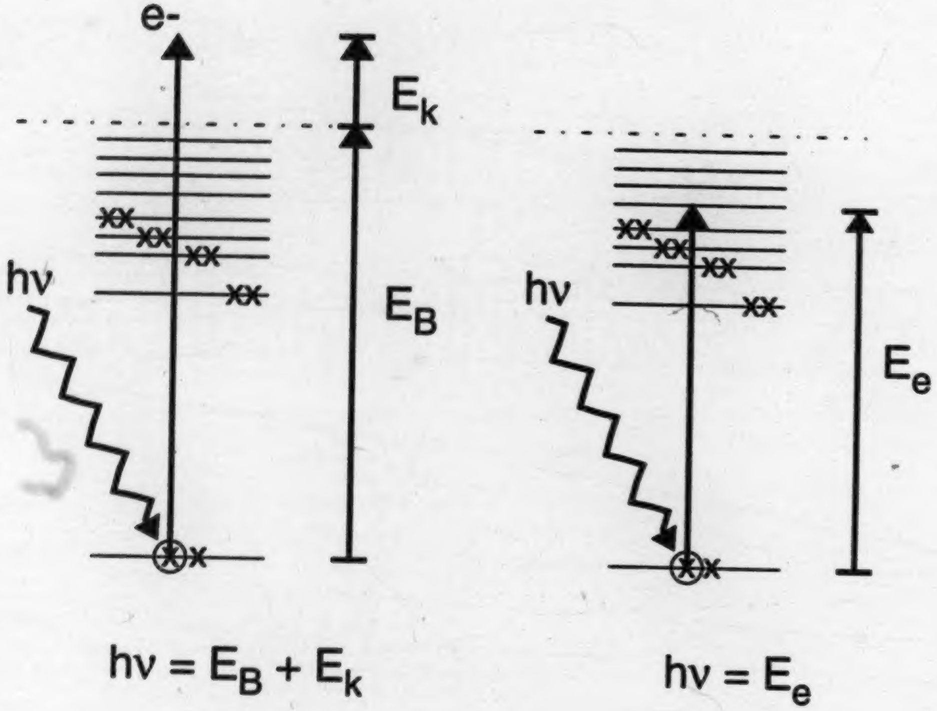
e-
E_k
hν
E_B
hν
E_e
$h\nu = E_B + E_k$
$h\nu = E_e$

Figure 1-1: The photoelectron and photoabsorption processes.

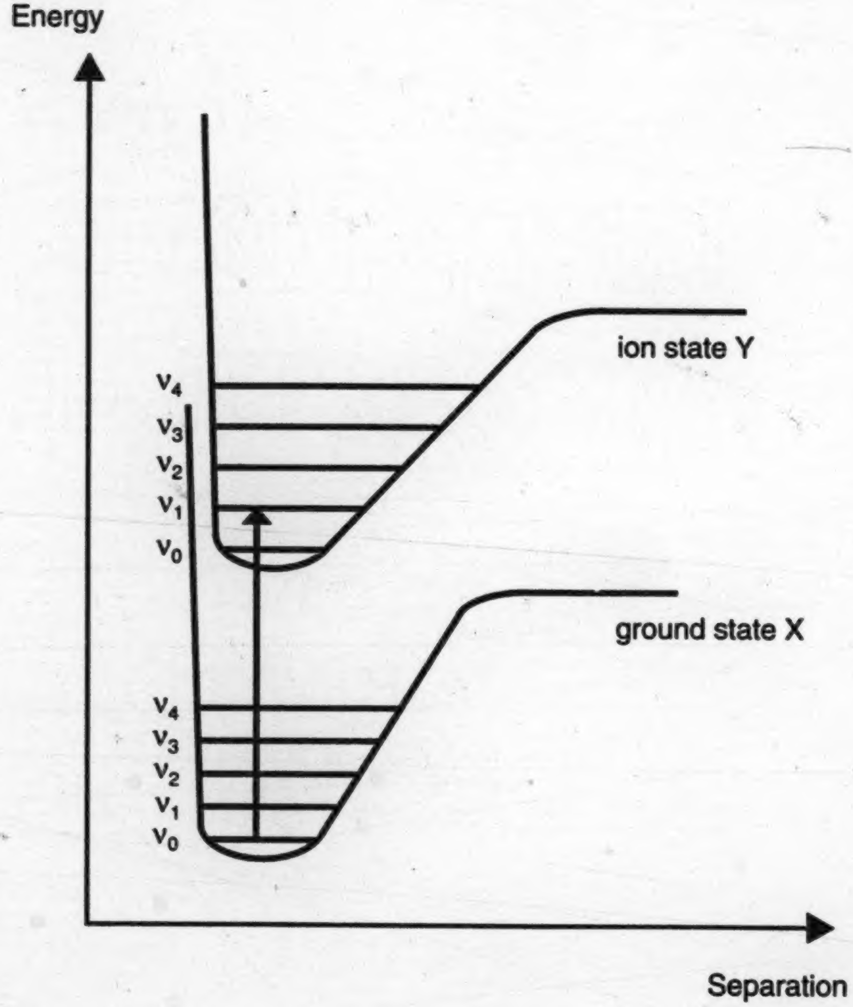
Energy
ion state Y
v_4
v_3
v_2
v_1
v_0
ground state X
v_4
v_3
v_2
v_1
v_0
Separation

Figure 1-2: Potential curves for ground state and excited state.

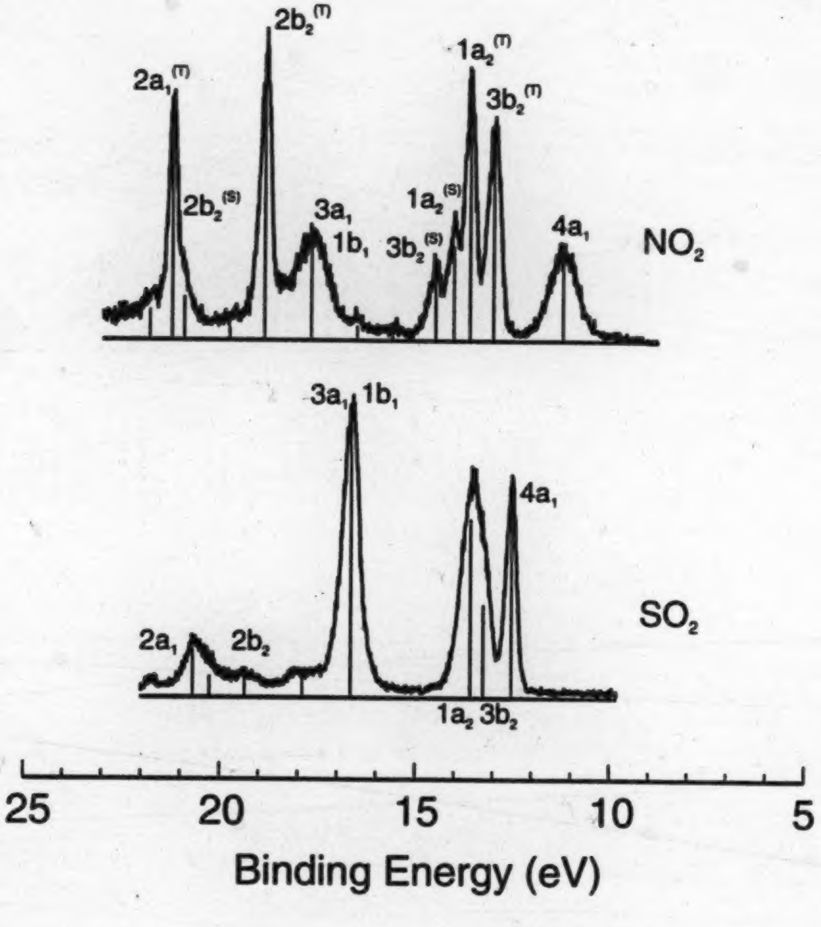

Figure 1-3: The valence shell photoelectron spectra of SO_2 and NO_2. The labels specify the orbital from which the photoelectron was ejected. (S) = singlet and (T) = triplet final state.

2. The General Experimental Procedures

As explained in the previous Chapter, the molecular structure greatly influences all intra-molecular interactions between photons and electrons. Thus, the various types of electron spectroscopy can be used to probe the molecular electronic structure and to test the various bonding models, the understanding of which is central to all aspects of chemistry. To accomplish this, high quality spectra are a necessity. This requires an x-ray photon source having both high intensity and high energy resolution. In addition, for photoabsorption experiments the photon source must supply a continuous spectrum from which the desired energies can be selected with a monochromator. The detection mechanisms used to analyze the resulting photoelectrons also require high resolution. The former is readily achieved with a synchrotron light source.

During the last three decades the availability of synchrotron light sources has greatly expanded the fields of photoelectron and photoabsorption spectroscopy, as the photons from such a source posses the qualities necessary for high resolution x-ray spectra. Synchrotron light is intense, collimated, polarized, and in general has a continuous frequency distribution [13]. Specific frequencies can be selected with a monochromator without extreme losses in radiation intensity.

2.1. An Electron Storage Ring, a Synchrotron

Synchrotron radiation is generated with a ring in which energetic particles, such as electrons, are stored. A diagram of a typical synchrotron ring is shown in Figure 2-1. The curvature of the particle trajectory introduces acceleration at relativistic speeds, which in turn causes the emission of synchrotron radiation. Although all charged particles, when accelerated, emit synchrotron radiation, the intensity of emission is inversely proportional to the fourth power of the particle mass (intensity $\propto 1/m^4$) [13]. Therefore, only very light particles, such as electrons and positrons, give off light with useful intensities [13, 44].

Synchrotron radiation is intense, collimated and plane polarized radiation ranging from the infrared (ir) to x-ray regions. It has found innumerable applications in physics, chemistry, biology, materials science, and other fields [44].

In the electron storage ring, such as the one used in this study, the electrons are kept in a circular path by a series of bending (dipole) magnets spaced around the ring. The centripetal acceleration thus created in these dipole magnets yields the synchrotron radiation. The electrons, however, lose energy in the process. This lost energy is resupplied by an accelerating voltage, which is applied *via* an oscillating electric field at a radio frequency (rf) ω, i.e. a microwave resonance cavity [45]. The required frequency is determined by the field strength of the bending magnets (B) and the rest mass (m_0) and the charge (q) of the electrons [46]. This rf-cavity is inserted into the ring and the oscillating nature of this potential allows transfer of energy only to electrons traveling in phase with the rf ω [46]. In consequence, ω must be a whole number multiple of the revolution frequency f_0 of the electrons [45]. The ring and its radiation take their name from this synchronous nature of the accelerating process, which is essential for maintaining the electron beam in the ring over several hours [46].

When viewed from alongside the ring, the electrons oscillate in a similar fashion as those on a radio antenna. So the expected frequency of the emitted light should equal the revolution frequency f_0 [44].

$$f_0 = \frac{qB}{2\pi m_0 c} \qquad (2\text{-}1)$$

If the electrons in the ring have low kinetic energies, the classical dipole pattern of light having that frequency is observed [44]. However, when the electrons travel at relativistic energies, the Lorentz transformations change the radiation pattern, so that the light is emitted in a very narrow ray with its maximum intensity in the forward direction tangential to the electron travel path. There will also be two side lobes. These result from the backward radiation, which is bent forward by the Lorentz transformations. The angular width θ of the main ray is [13, 44]:

$$\theta \cong \gamma^{-1} = \frac{m_0 c^2}{E} \qquad (2\text{-}2)$$

Similarly the frequency is transformed from f_0 into a pseudocontinuum. This is composed of many harmonics of f_0. These range from f_0 itself, a rf, into the UV, x-ray or even the γ-ray regions of the electromagnetic spectrum. The spectrum is characterized by a critical energy ε_c given by

$$\varepsilon_c = \frac{3hc\gamma^3}{4\pi R}$$

and the corresponding wavelength is

$$\lambda_c = \frac{4\pi R}{3\gamma^3}, \tag{2-3}$$

where R is the radius of the ring, and γ is defined in equation (2-2) [44]. The maximum photon flux occurs at about $\lambda_c/2$. Flux declines rapidly with decreasing wavelength (increasing energies), but there is only slow variation at longer wavelengths. Thus, the synchrotron light spans a large section of the electromagnetic spectrum from the far ir to the x-ray regions in a smooth continuum. The electron bunch structure imparted by the rf phasing requirement means that the electrons travel in bunches or buckets around the ring, and therefore the emitted radiation is pulsed. The frequency and length of these pulses are determined by R, ω, and the number and length of the bunches [44].

In addition to the bending dipole magnets, "wigglers" and "undulators" can be used to alter and control the electron trajectories, and so produce radiation [44]. These so-called insertion devices are positioned on straight sections of the ring. They consist of a series of closely spaced and oppositely orientated magnets. The field reversals cause the electrons to travel in a zigzag path. The radiation from each pole adds constructively, resulting in much higher beam intensity. The magnetic fields of wigglers are strong, and the resulting deviation angle of the electrons is large compared to the width of the radiation cone. This results in a uniform gain in intensity over the whole spectral range. Undulators, in contrast, have small magnetic fields, so that the deviation of the electron path is small compared to the cone width. Here, interference effects dominate and only specific frequencies are enhanced. Undulator radiation is quasimonochromatic with a very small solid angle. Its high brightness and coherence make it an excellent radiation source for x-ray microscopy and x-ray holography applications [44]. Both wigglers and undulators are characterized by the dimensionless wiggler parameter [44]

$$K = \frac{e\lambda_0 B_0}{2\pi mc} \qquad (2\text{-}4)$$

and the magnetic period length λ_0 [44]. If K is small ($K \leq 1$), the motion of the electrons creates a dipole radiation pattern. Upon transformation to the lab frame of reference this pattern gives the first undulator maximum with wavelength λ_1. For a symmetric device only the odd harmonics of this fundamental wavelength are produced. The magnitude of the wavelengths depends upon K and λ_0 according to equation (2-5) [44].

$$\lambda_n = \frac{1}{n}\frac{\lambda_0}{2\gamma^2}(1 + \frac{K^2}{2})$$

$$E_n = n\frac{hc}{\lambda_0}\frac{2\gamma^2}{1 + K^2/2} \qquad (2\text{-}5)$$

Different sets of wavelengths can be selected through variation of K by changing the gap between the poles of the permanent magnets in the undulator.

At large values of K the radiation pattern produced by the electrons becomes increasingly more complex creating significant intensity in higher order harmonics. The peaks broaden to create an intensity increase over the whole spectral range. An undulator is an insertion device with a small value for K, usually $K \leq 1$ [44], while wigglers have very large values for K, $K >> 1$ [44].

The experimental work for this thesis was conducted at the Synchrotron Radiation Center (SRC) which is operated by the University of Wisconsin, Madison in Stoughton, Wisconsin. This particular ring (Aladdin) has a 50.582 MHz resonance cavity [47] and an average radius of 14.1 m [47]. The revolution period for each bunch of electrons is 297 ns

(f_0 = 3.37 MHz) [47] and there are 15 bunches in the ring [47]. There are two operating modes for electron kinetic energies: 800 MeV and 1 GeV. For the former the critical wavelength λ_c is 22.7 Å (ε_c = 545 eV) [47] while for the latter λ_c is 11.6 Å (ε_c = 1065 eV) [47]. Further information about the Aladdin ring can be obtained from the SRC website [48].

2.2. Beamlines and Monochromators:

As explained above, a synchrotron produces a wide spectral range of light, from the ir to the hard x-ray region. However, for most experiments specific frequencies are needed, so it is necessary to select the required wavelength (energy) of the radiation [49]. This is achieved with the use of a monochromator device. The monochromator has three main optical elements: an entrance slit, an exit slit, and the diffraction element, which is typically an appropriate crystal or a ruled grating operating under the Bragg diffraction law [50] $n\lambda = 2d \sin\theta$ (where d is the spacing of the diffraction centres, and θ is the angle of incidence). The type of diffraction element used is dependent upon the photon energy region to be accessed [49]. Crystals are often used for the x-ray region above approximately 1000 eV, for example [51-57], but they can be used for energies as low as 500 eV, for example Beamline 6.3.1 at the Advanced Light Source [58]. Hard x-rays (3.5-25 keV) are typically diffracted with Si(111), Si(220) or Si(311) crystals [53-56]. InSb(111) crystals cover the energy range from the Si K-edge (1840 eV) up to about 4000 eV. Lower photon energies can be obtained with Quartz ($10\underline{1}0$), Beryl ($10\underline{1}0$) and YB_{66} crystals. Energies in the vacuum ultraviolet and soft x-ray regions can be selected with a spherical grating monochromator [59-61] and a plane grating monochromator [62-64]. Normal Incidence Monochromators [65] and Toroidal Grating [66] monochromators are used in the vacuum ultra-violet region as well.

The grating typically consists of a plane or spherically concave mirror surface with many parallel grooves. The spacing of these grooves depends on the desired photon energy range, and can vary from 20 to 6000 lines/mm. The interference pattern created by a diffraction grating is highly dependent upon the wavelength of the light; thus, there exists a unique pattern for each photon energy.

Other methods for energy selection exist as well, for example zone plates [67] which focus x-rays of specific wavelengths determined by the width-spacing of the zones. This form of energy selection is often used in x-ray microscopy beamlines, for example Beamline 6.1.2 at the Advanced Light Source [68].

The experimental spectra presented herein were collected using three different beamlines at the SRC depending upon the photon energy range required. Each of these three beamlines will now be described in some detail.

2.2.1. The Mark IV "Grasshopper" Monochromator beamline of CSRF

The Mark IV Grasshopper beamline of the Canadian Synchrotron Radiation Facility (CSRF) located at the SRC in Stoughton, WI was employed for the valence-shell photoelectron work and the phosphorus and sulphur L-shell photoabsorption spectra. In this monochromator the energy selection is achieved through employment of a concave grating and a Rowland circle geometry [69].

The focusing conditions of a concave grating are described with the aid of the Rowland circle. This circle, having a diameter equal to the radius of curvature of the grating, is placed tangential to the grating so that the grating centre lies on the circumference. Then the diffraction spectrum of a point source lying on this circle will be focused on the circle as well [70]. So, to achieve the optimal focal conditions of the monochromator, both entrance and exit slit are positioned on the Rowland circle of the diffraction grating with the grating centre lying on its circumference.

The total beam of synchrotron light enters the monochromator at the entrance slit, but only light at one specific frequency and its harmonics exits through the exit slit. This frequency is determined by the positions of both slits on the Rowland circle. In order to select different frequencies and still maintain focus, at least one monochromator element must be movable. The focal conditions can be maintained in one of two ways [70]:

1. One element moves along the Rowland circle.
2. The Rowland circle rotates about one element and the other two move accordingly to remain on the circle.

In the Grasshopper beamline of CSRF the exit slit is kept at a fixed position to obtain a constant exit beam direction. The other elements move so that the Rowland circle (radius r = 1m [69]) rotates about the exit slit. A cylindrical mirror, M_1, focuses the synchrotron radiation in the vertical plane onto the entrance mirror-slit S_1 which then directs the beam onto the spherical grating (radius of curvature R = 2m [69]). To keep the Rowland circle focusing conditions at the exit slit, the grating pivots about S_1, while S_1 itself rotates at half the angular velocity of the grating [69]. Both grating and M_1 also translate parallel to the incoming radiation [69]. In theory this beamline covers an energy range between 40 and 1000 eV (12-300 Å) [71]. In practice, the energy range of photons with useful intensity is much smaller, and is somewhat dependent upon the grating installed. The 1200 lines/mm grating has a low energy cut-off at approximately 38 eV, while the higher resolution 1800 lines/mm grating cuts off at approximately 67 eV. At higher energies, the light intensity decreases significantly above the carbon 1s edge at 284 eV; thus, the actual useful energy range for this beamline is between 40 and 300 eV. The minimum bandpass is 0.05 Å [71], so the best attainable energy resolution varies between 0.007 eV (at 40 eV) and 0.4 eV at (300 eV). The focused spot is 7 mm wide and 1 mm high [71].

2.2.2. The HERMON Beamline of SRC

The photoabsorption and photoelectron oxygen 1s measurements in this thesis were done with the High Energy and high Resolution Monochromator beamline (HERMON) of SRC. This monochromator has a unique and new design feature, a grating with variable spacing [72]. The optics for this type of beamline were developed to achieve beam focus to the first power over a large range of wavelengths while keeping the position of the entrance and exit slits fixed [73]. A Rowland circle monochromator, such as the "Grasshopper" described earlier (Section 2.2.1), requires movable slits to maintain focus conditions, and a plane grating monochromator employs auxiliary mirrors to do this. The additional mirrors greatly reduce throughput and introduce additional difficulties in figuring and alignment. The new optical design described for HERMON uses a variable spacing grating [73] which can eliminate all these limitations. If the motion of such a grating is constrained to rotation only, very high resolution is achieved at two wavelengths, but not elsewhere, largely due to defocusing of the beam. These defocusing aberrations are removed by the introduction of a translation of the grating at all other wavelengths. This translation motion, executed along the tangent plane of its centre and in direction of its ruled width, has the effect of bringing all wavelengths into focus at the fixed exit slit, leaving only spherical aberration as the new limit for optical resolution. Thus, this design has the potential to achieve very high spectral resolution of the order of 0.003 Å (0.06 eV at 500 eV)[73].

In addition to a variable-grating fixed-slit monochromator design, the HERMON beamline employs a Kirkpatrick-Baez mirror system for both pre- and postfocusing optics [72]. SiC spherical mirrors are used for vertical focusing, and bent-glass cylindrical mirrors for horizontal focusing, which occurs at the grating.

The high-energy varied-groove-density spherical grating installed for the experiments presented herein covers an energy range between 500 and 1100 eV [74]. The best attainable photon resolution is of the order of 0.002 Å (slit = 0.01 mm, $\Delta\lambda(\text{Å}) = 0.2 \times \text{slit(mm)}$) [74]. This corresponds to 0.05 eV in the oxygen 1s absorption region (530 eV). The focused spot size is 1 mm by twice the width of the exit slit [74].

2.2.3. Double Crystal Monochromator (DCM) beamline of CSRF

The Canadian DCM beamline was used for measurement of phosphorus and sulphur K shell spectra. This beamline employs crystal lattice diffraction to monochromatize the synchrotron radiation. To keep the exit beam position fixed as the photon energy is scanned, two crystals with linked rotation and translation motions are used. This synchronized motion is achieved with a Golovchenko type of Boomerang mechanism [75, 76]. Both crystals rotate as the Bragg angle [50] is scanned to keep them parallel. The second crystal also translates to intercept the diffracted x-ray from the first crystal and to maintain a fixed vertical position of the exit beam. A focusing mirror is installed downstream of the crystals. This mirror should ideally be ellipsoidal; however, such a design was impractical when the beamline was built. Instead, a cylindrical mirror with a unique mirror bender, which distributes the bending moment along the length of the mirror, is employed [75]. The optical surface of the mirror has a nickel coating, giving good reflection in the 1500-5000 eV range [75, 76]. Two sets of crystals are available: InSb (111) and Quartz (10$\underline{1}$0). With these, the beamline covers an energy range from 1500 to 4000 eV (3-8 Å) [51]. However, the light intensity provided by the Madison storage ring decreases rapidly above the chlorine edge at approximately 2800 eV. The photon energy resolution is about 1.0 eV [74]. The spectra of the phosphorus and sulphur K shell regions presented in this thesis were obtained with the InSb crystals installed.

2.3. Endstations: Photoelectron Spectrometer, Gas Cells

2.3.1. Electron Energy Analyzer

The photoelectron spectra were measured with a hemispherical spherical sector analyzer built at the University of Alberta using hemispherical section spheres manufactured originally by the McPherson Instrument Company [17]. In a spherical analyzer, the entering photoelectrons, which exit from the gas cell (ionization chamber) through a slot, traverse an electric field established between two concentric spheres to reach the detector. This spherically symmetric electric field causes the electrons to traverse the analyzer along a circular path. The central ray is shown by the dotted line in Figure 2-2. The path traveled is determined by the relationship between the voltage applied across the spherical plates and the radius of the plates. Thus, a specific voltage allows a certain set of kinetic energies to traverse the internal paths between the plates, equation (2-6).

$$-\frac{eR_1R_2}{2(R_2-R_1)} \times \frac{V}{r} = E_k \tag{2-6}$$

Only electrons with kinetic energies corresponding to a path radius between R_1 and R_2 will be able to traverse the analyzer.

For a spherical analyzer the first-order focal point of the electron current occurs at 180° [77]. However, according to Barber's Rule, for spherical segments less than 180°, object, image point and centre of curvature lie on a straight line [77]. This allows the ionization region and the detector to be outside the field. The analyzer is able to accept a wide range of azimuthal angles, giving it very good sensitivity for a quasi-point source [77]. Also, it is possible to simultaneously measure a range of kinetic energies through the use of a multidetector array [77]. A range of kinetic energies, given by equation (2-6), is focused at the detector plane by the analyzer. A subset of this energy range can be selected through the use of an analyzer exit slit. The central kinetic pass energy of the analyzer can be altered by changing the potential difference V between the spheres.

Our analyzer is a hemispherical section, which spans a horizontal angle of 154° and a vertical angle of 60°. The inner and outer sphere radii R_1 and R_2 are 320 mm and 400 mm, respectively, with a central radius of 360 mm [17]. A multi-channel plate detector assembly was installed at the exit focal plane to count the electrons. The width of the detector range of kinetic energies is determined by the dispersion equation (reduced to eliminate trap fields). Electrons with a range of kinetic energies given by equation (2-7) were detected simultaneously.

$$\Delta E = \frac{\text{KE at centre}}{2 \times R_{\text{mean}}} = \frac{\text{KE at centre}}{2 \times \frac{R_1+R_2}{2}} \qquad (2\text{-}7)$$

The photoelectron spectra were obtained by scanning the analyzer voltage and measuring the electron counts as a function of the pass energy at a fixed photon energy hv. To avoid asymmetry contributions to the peak intensities, the exit slit of the gas cell and the entrance slit of the analyzer were mounted at the pseudo-magic angle [17] to the incident photon beam.

The ionization region was located inside a small gas cell to prevent the gas from dispersing too quickly, and so, a localized high-pressure area was created. Effective pumping kept the rest of the spectrometer at operating pressures of 10^{-7} to 10^{-5} torr [17]. A window and a differential pumping section were mounted between the monochromator and the spectrometer to prevent gas flow into the UHV (10^{-10} torr) monochromator region. The window material was aluminum for O(1s), or carbon or polyimide for the S(2p), P(2p), and valence shell studies.

For the oxygen 1s photoelectron spectra, differential pumping and monochromator protection requirements necessitated the use of a windowed cell, which was constructed in the form of a copper block 5.6 cm long with an inner diameter of 0.95 cm, with an exit slit of width 0.2 mm × 10 mm that was coupled to the entrance of the analyzer. The cell was electrically isolated from the spectrometer to allow application of a retardation potential. A thin (1500 Å Al) window separated the sample chamber containing the cell from the monochromator chamber, and similar windows capped each end of the gas cell to minimize gas egress into the chamber. Thus, the monochromatized synchrotron radiation passed through two windows before exciting the gas contained within the cell.

Monochromator protection requirements were not as stringent on the Grasshopper compared to HERMON, so a more open gas cell design was used for the S(2p), P(2p) and valence shell spectra. Rectangular capillaries guided the light into and out of the cell, which was grounded to avoid charge buildup.

2.3.2. Photoabsorption Gas Cell

The photoabsorption spectra were measured using a double gas cell assembly as shown in Figure 2-3. The type of window at the cell entrance depended upon the energy region probed (carbon for the sulphur and phosphorus L shell and the oxygen K shell, and beryllium for the sulphur and phosphorus K shell regions). To avoid contamination of the monochromator due to possible gas leaks, a differential pumping section was established between the monochromator and the window. Furthermore, as described above, monochromator protection requirements of HRMON necessitated the employment of two carbon windows between the monochromator and the gas cells. On the DCM, an in-line gas cell containing 1.2 torr N_2 and closed off by beryllium windows was located between the monochromator and the main gas cells. The i_0 current from this cell was collected simultaneously with the experimental spectra and used for normalization purposes.

Each of the two gas cells of the main assembly (Figure 2-3) was 21.0 cm (8¼") long, with an inner diameter of 3.5 cm ($1^3/_8$"), separated by an intervening distance of 21.0 cm (8¼"). A potential of 200 V was applied to one electrode in each cell to create a photoelectron current, i_1 and i_2, in each cell. The absorption spectra were generated by scanning through the energy region of interest and measuring the electron currents i_1 and i_2 as a function of photon energy. To obtain optimal spectral resolution, the monochromator exit slits were set at the most narrow values (10 μm for HRMON and 20 μm for the Grasshopper).

The total electron yield spectrum thus obtained was normalized by taking the ratio of these two current signals: i_1/i_2. Alternatively, the spectrum can be normalized by simultaneous measurement of a standard, for example N_2, and then taking the ratio of the experimental spectrum to the standard. In either, the dependence of the electron yield signal upon photon intensity is eliminated. The experimental peak energies were obtained by fitting the experimental spectra with Gaussian/Lorentzian (Voigt) curves. A step in the baseline was put at the approximate position of the ionization edge.

The gas cell used is based upon the double ion chamber design developed by Samson [78]. When filled with a gas at a number density n and having a photoabsorption cross-section σ(hν), the ionization yield (η) as a function of photon energy is given by equation (2-8) [78]:

$$\text{cell 1:} \qquad \eta = \frac{i_1/e}{I_0\, e\text{-}\sigma n L_1\, (1-e^{-\sigma n d})} \qquad \text{(2-8a)}$$

$$\text{cell 2:} \qquad \eta = \frac{i_2/e}{I_0\, e\text{-}\sigma n L_2\, (1-e^{-\sigma n d})} \qquad \text{(2-8b)}$$

where q is the charge of the species collected and the cell parameters L_1, L_2 and d are as shown in Figure 2-3. An expression, given by equation (2-9), for the photoabsorption cross-section σ(hν) is obtained from the ratios of equations (2-8a) and (2-8b) [78].

$$\sigma = \frac{\ln(i_1/i_2)}{n(L_2-L_1)} \qquad \text{(2-9)}$$

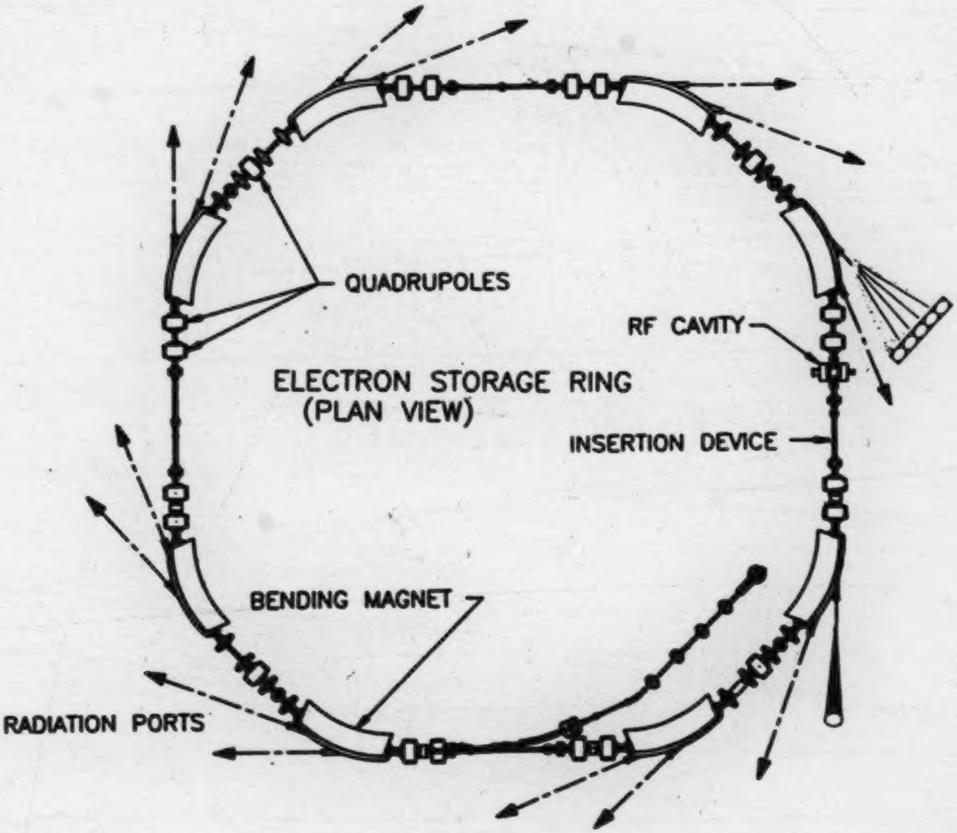
QUADRUPOLES
RF CAVITY
ELECTRON STORAGE RING
(PLAN VIEW)
INSERTION DEVICE
BENDING MAGNET
RADIATION PORTS

Figure 2-1: Diagram of a synchrotron ring, adapted from a brochure of the Maxwell Brobeck company.

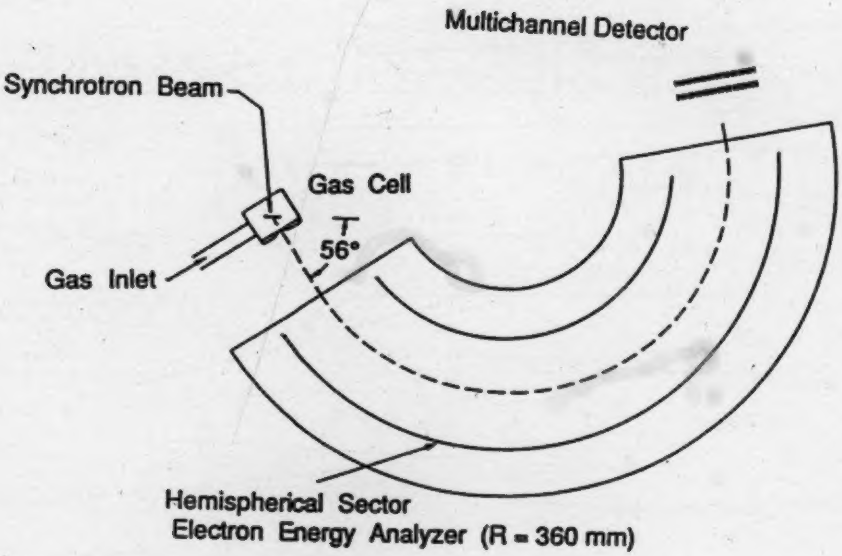
Multichannel Detector
Synchrotron Beam
Gas Cell
56°
Gas Inlet
Hemispherical Sector
Electron Energy Analyzer (R = 360 mm)

Figure 2-2: A Hemispherical Analyzer, adapted from [17].

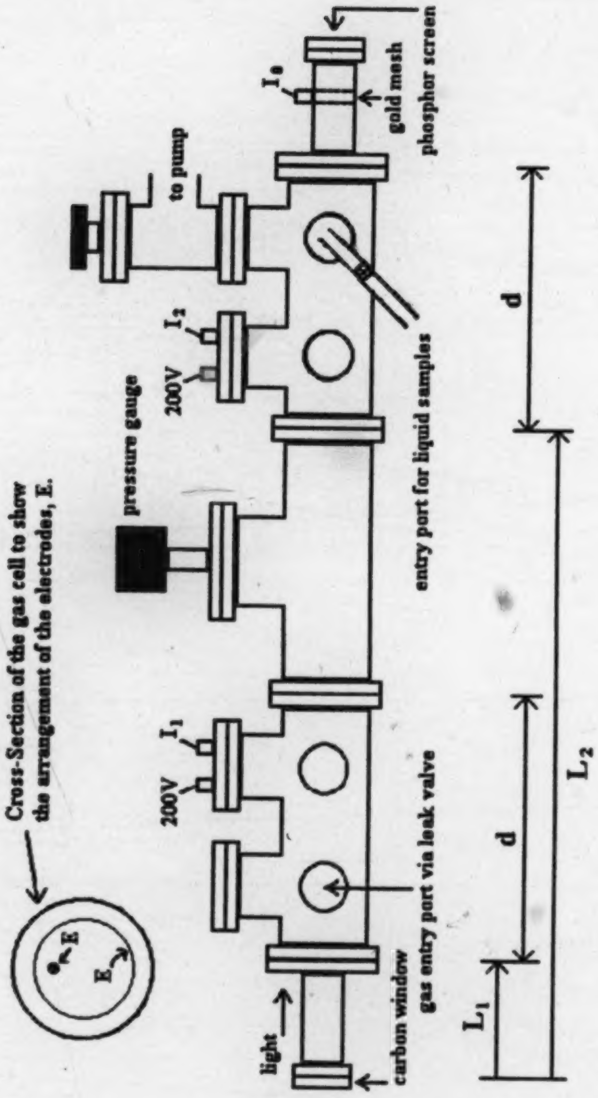
Cross-Section of the gas cell to show the arrangement of the electrodes, E.
E
E
light
carbon window
gas entry port via leak valve
200V
I1
L1
d
L2
pressure gauge
entry port for liquid samples
200V
I2
d
to pump
I3
gold mesh
phosphor screen

Figure 2-3: Gas cell assembly and illustration of the cell parameters.

3. Electronic Structure and Bonding Theory

The interaction of the positive nuclei and negative electrons of the constituent atoms of molecules gives rise to interatomic bonding. Atoms can be arranged in many ways to form molecules. For each of these arrangements, there exists only one stable electronic structure describing the movement of the electrons within the molecule. This electronic structure is commonly described in terms of a molecular orbital bonding theory. Since all chemical and physical properties are ultimately dictated by the electronic structure, an accurate and reliable bonding model is required.

3.1. The Principles of Molecular Orbital Theory

The analysis of bonding in molecules has advanced immensely during the last 70 years. The basic molecular orbital theory dates back to the 1920's [25], but major advances have been driven by the development of mathematical methods for the solution of the very complex equations and the ever-increasing power of computers [7, 14]. In all modern bonding theories, the behaviour of electrons in atoms and molecules is determined by the Schrödinger equation [79, 80]

$$\hat{H}\ \Psi = (KE_n + KE_e + V_{nn} + V_{ne} + V_{ee})\ \Psi = E \qquad (3\text{-}1)$$

where

$\hat{H}$ = Hamiltonian operator

KE_n = Kinetic energy of the nuclei = $\sum_{\mu} \frac{-\hbar^2}{2\ m_\mu} \nabla_\mu^2$

KE_e = Kinetic energy of the electrons = $\sum_{i} \frac{-\hbar^2}{2\ m_e} \nabla_i^2$

V_{ne} = potential energy due to the interaction between the nuclei (μ) and the electrons (i)

$= -\sum_{i,\mu} \frac{Z_\mu\ e^2}{r_{i\mu}}$

$V_{ee}(i,j)$ = potential energy due to the interaction between the electrons

$$= \sum_{i>j} \sum_{j} \frac{e^2}{r_{ij}}$$

$V_{nn}(\mu,\nu)$ = potential energy due to the interaction between the nuclei

$$= \sum_{\nu>\mu} \sum_{\mu} \frac{Z_\mu Z_\nu e^2}{r_{\mu\nu}}$$

E = total energy of the system.

The application of the Born-Oppenheimer approximation [25, 80] simplifies equation (3-1) through the elimination of the nuclear motion (KE_n terms) [79]. The remaining terms comprise the electronic Hamiltonian $\hat{H}_{el}$:

$$\hat{H}_{el} = KE_e + V_{ne} + V_{ee} \tag{3-2}$$

and the nuclear repulsion term V_{nn} [79], which is a constant for each nuclear configuration and independent of the electron coordinates, the variables in the electronic Schrödinger equation (3-2). V_{nn} decreases all eigenvalues by a uniform amount, but otherwise it has no effect on the eigenfunctions [79].

3.1.1. Hartree-Fock Theory

In a multi-electron system, the term V_{ee} in equations (3-1) and (3-2) links the coordinates of all electrons into a system of unseparable partial differential equations; hence the Schrödinger equation cannot be solved exactly [79]. An approximate solution of the Schrödinger equation is achieved by substituting for the wavefunction Ψ, another function Φ of known form. A very convenient and meaningful choice for this function is a molecular orbital wave function which is an antisymmetric linear combination of products of one-electron spin-orbitals (Slater determinant) [7, 79, 80].

$$\Phi_{MO} = (N!)^{-1/2} \det|\phi_1(1)\, \phi_2(2) \ldots \phi_N(N)| \tag{3-3}$$

where N is the number of electrons in the molecule. The individual molecular orbitals ϕ_i are functions of the coordinates of the electrons. In general these molecular orbitals are not localized on any individual atom or within a specific bond, but are spread over the whole molecule; thus, the electrons are delocalized [7].

Each molecular orbital $\phi_i(i)$ is an eigenfunction of an effective one-electron Hamiltonian $\hat{F}_i$ (the Hartree-Fock Hamiltonian operator) [79]:

$$\hat{F}_i\,\phi_i(i) = KE_e + V_{ne} + \sum_j [\,2 \times \hat{J}_j(i) - \hat{K}_j(i)] \tag{3-4}$$

where the electron-electron interaction energy V_{ee} is approximated by the Coulomb operator $\hat{J}_j(i)$ and the exchange operator $\hat{K}_j(i)$[79]. The Hartree-Fock operator depends on its eigenfunctions, so the solution has to be obtained by an iterative process until self-consistency is achieved [79]. The molecular orbital function Φ_{MO} is the solution of the Hamiltonian $\hat{H}_{eff}$ (equation (3-5)) [79].

$$\hat{H}_{eff}\,\Phi = E_{HF}\,\Phi \quad \text{where} \quad E_{HF} = 2\sum_i \varepsilon_i - \sum_i \sum_j (2\,\hat{J}_{ij} - \hat{K}_{ij}) + V_{nn} \tag{3-5}$$

According to the variation theorem [7], $E_{HF} \geq E$. Therefore, to determine the best approximation of Ψ, E_{HF} is minimized through the use of a self-consistent-field method of energy minimization [81].

A common method of forming the molecular orbitals ϕ_l is to construct a linear combination of a complete set of basis functions χ_r, first proposed by Roothaan in 1951 [79].

$$\phi_l = \sum_r c_{rl}\,\chi_r \tag{3-6}$$

which follow the normalization rules [1]:

$$\int \chi_r^2\, dv = 1, \int \chi_r \chi_s\, dv = s_{rs} \neq 0 \quad \text{but} \quad \int \phi_l^2\, dv = 1, \int \phi_k \phi_l\, dv = 0 \qquad (3\text{-}7)$$

If the initial basis set used is not orthonormal ($s_{rs} \neq 0$), then an orthonormalization procedure should be undertaken before the solution of the Hartree-Fock equation is attempted [7]. The electron indistinguishability principle and the electron density interpretation of the wavefunction make all molecular orbitals ϕ_l either symmetric or antisymmetric with respect to the symmetry operations of the molecule. This requirement restricts the numbers and types of basis functions χ_r that may be combined to form a particular molecular orbital ϕ_l. Hence, symmetry considerations greatly simplify the task of forming the molecular orbitals [1, 7].

The Hartree-Fock method of approximating the Schrödinger equation has limitations in accuracy, as it models the electronic motion as a set of one-electron functions [79]. For each electron it approximates the electron-electron interaction as a potential due to a charge density distribution of all other electrons, rather than treating each interaction individually [7, 79]. This ignores any electron correlation effects, which can contribute significantly to the overall energy of the system. To address this deficiency of the Hartree-Fock theory, numerous post Hartree-Fock methods have been devised. These include Møller-Plesset perturbation theory for correlation energy correction [7, 82, 83], configuration interaction methods [7, 84, 85] and density functional theory [7, 86, 87].

3.2. *Molecular Bonding Theory applied to Photoelectron and Photoabsorption Spectroscopy*

Solution of the Hartree-Fock equation gives a set of molecular orbitals, each with a unique energy, thus creating a system of energy levels into which the electrons are placed. The lower-lying members of these levels correspond to the localized core orbitals, which are mainly atomic in character. The valence shell orbitals that correspond to the high energy levels are often delocalized over the whole molecule. The removal of an electron from one of these orbitals using photoelectron spectroscopy causes small perturbations to the system. In particular, photoionization perturbs not only the energy level probed, but also all those orbitals corresponding to higher energy levels. The rearrangement of the orbitals following such a perturbation is a collective response property, and is unique to each compound. This "relaxation" process is an integral component of photoionization; it contributes the larger portion to the so-called "chemical shifts" in the binding energy of electrons in core orbitals. The magnitude of these shifts is determined by several factors. These include the chemical environment of the photoionized atom, the extent by which other electrons shield the electron in question from the nucleus, and the forms of orbital rearrangement occurring following photoionization. Thus, the "chemical shifts", i.e. small changes in the core level ionization potentials between different molecular systems, reflect the chemical bonding in the molecule, and they can be used to deduce information about the molecular structure. Several theoretical methods with varying degree of complexity were applied to interpret the experimental values for both core level ionization and bound core→mo* transitions.

3.2.1. Potential-at-the-nucleus model

A quite simple and successful method used previously [88-92] for the calculation of the chemical shifts is the potential-at-the-nucleus method.

Koopmans' theorem [8] relates the binding energy (E_b^i) of an electron in molecular orbital i to the energy of that orbital (ε_i) by equation (3-8). Hence, binding energy shifts are related to orbital energy shifts [92].

$$E_b^i = -\varepsilon_i \quad \text{and} \quad \Delta E_b^i = -\Delta\varepsilon_i \tag{3-8}$$

These shifts in orbital energy of the molecular orbital i can be approximated by shifts in the potential energy of an electron in that orbital (ΔV_i), which in turn is approximated by shifts in the potential energy of an electron located at the nucleus (ΔV_N^e).

The total potential V_A^e at the nucleus of atom A in a molecule is given by the general expression shown in equation (3-9) [92]. The wavefunction Φ is the antisymmetric product of the molecular orbitals ϕ_j, and the sum is over all electrons (i) in the molecule.

$$V_A^e = \langle \Phi | \sum_i^n \frac{e^2}{r_i^A} | \Phi \rangle \tag{3-9}$$

The molecular orbitals are orthogonal and $\frac{1}{r_{iA}}$ is a one-electron operator, therefore equation (3-9) can be written as [92]:

$$V_A^e = \sum_i^n \int \phi_i(i) \frac{e^2}{r_{iA}} \phi_i(i)\, d\tau_i \tag{3-10}$$

Expansion of the molecular orbitals in terms of the atomic orbitals ($\phi_i = \sum_j c_{ij}\, \chi_j$) reduces expression for V_A^e to three terms shown in equation (3-11) [92].

$$V_A^e = e^2 \left\langle \frac{1}{r_A} \right\rangle \sum_{i,j} (c_{ij}{}^A)^2 + \sum_{i,j} c_{ij}{}^B \langle \chi_j{}^B(i) | \frac{e^2}{r_A} | \chi_j{}^B(i) \rangle + \sum_{i\neq k,\, j\neq k} (c_{ij}{}^B c_{ik}{}^C) \langle \chi_j{}^B(i) | \frac{e^2}{r_A} | \chi_k{}^C(i) \rangle \tag{3-11}$$

The first of these terms is V_A, the potential due to the nucleus of atom A and the electrons formally assigned to it. As a consequence of the normalization conditions for the molecular orbitals, the term $\sum_{ij}(c_{ij}{}^A)^2$ equals the net valence shell electron population of atom A = $Z_A'-q_A$, where Z_A' is the core charge of atom A and is equal to Z_A–(# of core electrons). This definition of $\sum_{ij}(c_{ij}{}^A)^2$ assumes that the core orbitals are atomic in character. The value of $\langle \frac{1}{r_A} \rangle$, the average value of $\frac{1}{r_A}$, where r_A is the distance from the nucleus for electrons in atom A, is provided by $\frac{\xi}{n}$, where ξ is the Slater exponent for the valence shell of atom A, and n the principal quantum number of that valence shell [88]. A weighted average, calculated according to equation (3-12), was used for ξ, because the s and p orbitals in the valence shell have slightly different ξ values. The values of these Slater exponents used were those given by Clementi [93].

$$\xi(\text{ave}) = \frac{\xi(s) + 3\,\xi(p)}{4} \tag{3-12}$$

The off-atom potential created by the interaction of the ionized atom A with all other atoms in the molecule, V_{AB}, was obtained in the simplest model by treating all the other atoms as point charges as represented in equation (3-13) [92], where q_B is the charge on atom B and R_{AB} the distance between atoms A and B.

$$V_{AB} = \sum_{B \neq A} \frac{q_B e}{R_{AB}} \tag{3-13}$$

This point-charge model for the off-atom potential neglects a group of integrals which are in principle not small [92]; however, the studies by Sodhi and Cavell [88, 89] have shown that the point-charge model suffices for the assessment of the chemical shifts.

The binding energy shifts are equated to the shift in atomic potential, defined as the difference between the potential V_A^e of the compound of interest and that of a reference compound.

$$V_A^e = V_A + V_{AB} = e\,(Z'_A - q_A)\frac{\xi}{n} + \sum_{B} \frac{q_B e}{R_{AB}} \tag{3-14}$$

If evaluations are carried out for the ground state of the molecule, the ground potential model (GPM) is obtained, equation (3-15).

$$\Delta E_b^A = -\left(V_A^e(\text{cmpd}) - V_a^e(\text{ref.})\right) \tag{3-15}$$

In actuality, a significant contribution to the observed shift arises from the adiabatic relaxation following photoexcitation. This is easily accommodated as described by Davis and Shirley in the relaxation-potential model (RPM) [92], wherein the excited (core ionized) centre is represented by the equivalent core Z+1 atom lacking one valence shell electron. That is, the final state of the molecule is mimicked by replacement of the Z atom with a $(Z+1)^+$ ion.

$$\Delta E_B = -{}^1\!/_2(\Delta V_Z + \Delta V_{Z+1}^{ion}) = -\Delta\left(\frac{V_Z + V_{Z+1}^{ion}}{2}\right) \qquad (3\text{-}16)$$

Similar calculations were done for the photoabsorption transition energies. In this case, however, the final state of the electronic transition possesses, in addition to the core hole, an unpaired electron in an antibonding orbital. Thus, the retained antibonding electron will influence the relaxation process. The final excited state for a bound electronic transition was represented by the equivalent core + 1 radical rather than the equivalent core +1 ion. That is, Z is replaced by a (Z+1) atom instead of a $(Z+1)^+$ ion. As in the photoionized equivalent-core approach, the strategy is to maintain the proper number of electrons in the final state system.

$$\Delta E_B = -{}^1\!/_2(\Delta V_Z + \Delta V_{Z+1}^{radical}) = -\Delta\left(\frac{V_Z + V_{Z+1}^{radical}}{2}\right) \qquad (3\text{-}17)$$

Since relaxation is to some degree determined by the electronic state of the photoexcited molecule, the unpaired electron of the radical was placed in the antibonding orbital involved in the transition leading to the main pre-edge peak. This, however, does not always correspond to the calculated ground state of the radical.

The formal charges q of the atoms in each molecule used for equation (3-14) were calculated with Gaussian 94 [94], using the experimental bond lengths and angles [95-97] as input. Since these charges are highly dependent upon the calculation method employed, several different schemes were explored to ascertain the most appropriate one for explaining the experimental results. Details about these calculation methods are described later in Chapters 5 and 6.

3.2.2. The ΔE_{SCF} Method

A second method for estimation of the chemical shifts involves the calculation of the difference in total energy between the initial and final states of the molecule and its ion [98, 99]. This method has been used recently for the calculation of chemical shifts in the C-1s binding energy of alkenes [98, 99] and benzenes [100]. The total energy, E_{SCF}, of the molecule was calculated with Gaussian 94 [94] for both the initial and final states. The latter was simulated by the equivalent core model as described previously (Section 3.2.1). The energy difference (ΔE_{SCF}) between the initial and final states represents the transition energy [98, 99]. The chemical shift is given by the change in ΔE_{SCF} with respect to a reference molecule. As with the potential at the nucleus method, the calculations were done using different energy calculation methods. Details are given in Chapters 5 and 6.

As will be shown in detail below, the ΔE_{SCF} method does not predict the absolute values of the ionization potentials accurately. However, in general, chemical shifts are represented quite well by the ΔE_{SCF} model. The degree of correlation is highly dependent upon the calculation method used. Better correlation with experiment is achieved for K-shell excitation than L-shell excitation. This is not surprising, since the equivalent-core model neglects shielding effects by lower lying core orbitals. The ΔE_{SCF} model provides improvement over the potential at the nucleus model, as it does not treat atoms as point charges, and so gives a better picture of the changes of electron distribution within the molecule.

3.2.3. Koopmans' Theorem Value

As already mentioned, the binding energy of an electron in a molecular orbital ϕ_i is in the simplest, Koopmans' Theorem [8, 101] picture related to the energy of that orbital, equation (3-8). These orbital energies can be readily calculated with Gaussian 94 [94]. Again, several different calculation methods were employed, which are discussed in detail in Chapters 5 and 6. As expected, the values obtained are dependent upon the calculation method.

The use of Koopmans' value does not consider relaxation effects, relativistic correction to the core energies or electron correlation [8]; hence, the absolute value of the ionization potentials are often overestimated by this method [8]. Inclusion of adiabatic relaxation by the use of the transition state method (equivalent-core model) improved the correlation for ionization potential shifts between calculated and experimental data (Chapter 6). The absolute values, however, are not improved. In the same way as the ΔE_{SCF} method, the use of Koopmans' theorem does not treat the atoms as point charges, and it provides an improvement over ΔE_{SCF}, in that it models the shielding effects due to other core electrons to a better degree.

3.2.4. Direct Calculation of the Transition Energies with MS-Xα and Gaussian 94

Direct calculation methods of the photoabsorption transition energies and the photoionization potentials account for both orbital relaxation and shielding effects, giving an improved model of the electronic transitions involved; hence improved chemical shift correlations are anticipated. They also give fairly accurate predictions of the absolute energies. See, for example, Chapters 5 and 6.

Calculation of the excited electronic states of a molecule with Gaussian 94 [94] is achieved with the single-excitation CI method described by Foresman et al. [102], but because of a size restriction of the Davidson Matrix to 2000 diagonal elements in the program, only a limited number of excited states can be computed. To obtain the core excited states for most molecules, it is necessary to freeze most virtual orbitals in the calculation for even the smallest basis sets, STO-3G and STO-3G*. Thus the analysis by this method is not extended to the ultimate power of the method at this stage.

Ideally, calculation of the ionization potentials and the transition energies would involve the computation of the total energy at optimized geometry of the initial and the final electronic state, where the latter has a core hole in the proper orbital and, if required, an electron in an antibonding orbital. The energy difference between these two states then represents the transition energy. This process is, unfortunately, not possible with the Gaussian 94 program package [94], as the final state electron configuration is automatically rearranged to obtain the lowest energy stable state (the state with the hole in the HOMO).

This problem did not arise with the MS-Xα [103] code. Any electronic state of the molecule can be computed, as the originally specified electron configuration is retained. Optimization of the molecular geometry is, however, not possible. Furthermore, the transition energies are not computed as total energy differences between the initial and final states, but rather a transition state method is employed wherein ½ an electron is removed from the core orbital and, if required, placed in an antibonding orbital. The transition energy then equals the energy difference between the two orbitals containing $^{(2n+1)}/_2$ electrons. For the ionization potential of the core orbital, Koopmans' theorem [8, 101] is applied to the transition state.

3.3. Molecular Field Splitting of Core Orbitals

An isolated atom has spherical symmetry, and belongs to the spherical group K_h [28], but to determine the symmetry transformations of the atomic orbitals in this group it is sufficient to use the rotation subgroup K given in Table 3-2. The electric field generated by nucleus and electrons is completely isotropic. Thus, although p and d orbitals are orientated differently in space, their electrons are subjected to the same electric field. As a result, the p-subshells are triply degenerate and d-subshells have five-fold degeneracy. They transform as P and D, respectively, under K symmetry. Photoionization of a closed shell atom, for example Xe, creates an unpaired electron in one of these levels. This introduces spin-orbit coupling. Consequently, there are two final states, giving rise to two peaks in the photoelectron spectrum. Open shell atoms such as nitrogen, oxygen or chlorine already have unpaired p electrons in their ground electronic state. Photoionization of these atoms can lead to an increase or a reduction of unpaired p electrons. The combined effect of spin-orbit and Russell-Saunders coupling (Section 1.1) in final states with multiple vacancies in p (or d) orbitals leads to a multitude of peaks in the valence shell photoelectron spectrum. Photoionization of a core orbital also leads to

Russell-Saunders and spin-orbit coupling in the final state. The spin-orbit interaction, however, tends to dominate in this case, so only two photoelectron peaks are observed.

Combining several atoms to form a molecule alters the valence shell through establishment of the molecular orbitals and, except in the special cases of radicals, electrons are maximally paired to create singlet ground states. In molecules, the core orbitals remain essentially atomic in nature. The altered valence orbitals and the presence of the other nuclei change the electric field seen by the core electrons of the central atom. It becomes anisotropic and depends upon the molecular structure and symmetry. The p- and d-orbitals have different orientations in space; hence, their electrons are subjected to different electric fields. This results in a loss of degeneracy for these core orbitals. They split into different levels given by the molecular symmetry. The energy difference between these levels is called the molecular field split (MFS) [104].

The strength of the molecular field depends upon the electronegativity of the atoms in the molecule. A ligand with high electronegativity relative to the central atom tends to pull the valence electrons away from the central atom, and thereby increases the magnitude of the molecular field experienced by the core electrons. In lower symmetry environments, the field is anisotropic; it will increase more in some directions than in others, and thus, the molecular field splitting will increase. Both PH_3 and PF_3 are molecules with C_{3v} symmetry. In this point group, the 2p level of phosphorus will split into an a_1 orbital and a doubly degenerate e orbital due to the molecular field. However, the Pauling electronegativity of hydrogen is 2.20 [105], the same as that of phosphorus, while that of fluorine is 3.98 [105]. Thus, fluorine will pull electrons away from the phosphorus centre and increase the molecular field. The molecular structure and geometry of PF_3 causes the field to increase mainly in the x- and y-directions, but not in the z-direction. Hence, the MFS between the a_1 ($2p_z$) and e ($2p_x$ and $2p_y$) orbitals will increase. *Ab initio* calculations have given an MFS of 120 meV for the P-2p level of PF_3, compared to 60 meV for PH_3 [106].

Core level photoionization will again result in an unpaired electron, introducing spin-orbit coupling. The effect due to spin-orbit coupling will dominate because the spin-orbit splitting is much larger than the molecular field splitting. Traditionally, the effect of the molecular field has been ignored; the core orbitals were treated in the same manner as in the atomic case. This results in two final electronic states for the ion, giving two peaks separated by the spin-orbit energy, just as in the atomic spectrum. However, with improved spectrometer resolution, the molecular field splitting becomes observable [104].

The spin-orbit interaction dominates, so J, rather than L and S, remains a good quantum number. Thus, the actual splitting of the final ionic states in the molecular field has to be determined using the double point-group corresponding to the molecular symmetry [107, 108] (Table 3-3 to Table 3-6). In a C_{3v} molecular field the $2p_{3/2}$ final state splits into Γ_4, Γ_5 and Γ_6. However, because of time reversal (Kramer's theorem) [107], Γ_4 and Γ_5 form a doubly degenerate E_2 state. So, the combined effect of the molecular field and spin-orbit coupling will result in three possible final electronic states following P-2p photoionization of PF_3: $E_2(2p_{3/2})$, $E_3(2p_{3/2})$ and $E_3(2p_{1/2})$. Time reversal also makes the Γ_3 and Γ_4 states of the C_s double group form one doubly degenerate E state. Hence, there will be three final states possible for SOF_2^+ with an S-2p core hole, all with E symmetry. The combined effect of the molecular field and spin-orbit splitting will give three P-2p photoelectron peaks for PF_5: $E_3(2p_{3/2})$, $E_5(2p_{3/2})$ and $E_3(2p_{1/2})$. Similarly, the C_{2v} symmetry of H_2S and SO_2 will give three possible final states for S-2p ionization, all having E symmetry. The only molecular fields which will not split the $np_{3/2}$ photoelectron peaks into two are the cubic fields of T_d, O and O_h symmetry, because in these double groups, a four-fold degenerate irreducible representation exists [107]. The $nd_{5/2}$ final states, however, will split even in these groups.

3.4. Photoabsorption Cross-Section:

The peak intensities of x-ray photoabsorption spectra represent σ, the absorption cross-section. This is defined as the number of electrons excited per unit time divided by the photon flux (photon per unit time per unit area) [24].

$$\sigma = \frac{P_{if}}{F_{ph}} \tag{3-18}$$

For any time dependent perturbation $V(t) = V\,e^{-i\omega t}$, the transition probability per unit time, P_{if}, is given by Fermi's "Golden Rule" [26], where $\rho_f(E)$ is the density of final states, Ψ_f is a particular final state, and Ψ_i is the initial state [24].

$$P_{if} = \frac{2\pi}{\hbar}\,|\langle\Psi_f|V|\Psi_i\rangle|^2\,\rho_f(E) \qquad (3\text{-}19)$$

For an electronic excitation caused by electromagnetic radiation of wavelength λ and frequency ω, P_{if} is represented by equation (3-20) [24], where E_0 is the magnitude of the electric field vector of the incident radiation.

$$P_{if} = \frac{\pi e^2}{2\hbar m^2 \omega^2}\,E_0^2\,|\langle\Psi_f|\,e^{ik\cdot x}\,\hat{\mathbf{e}}\cdot\mathbf{p}\,|\Psi_i\rangle|^2\,\rho_f(E) \qquad (3\text{-}20)$$

The photon flux for electromagnetic radiation with frequency ω is given by equation (3-21) [24].

$$F_{ph} = \frac{E_0^2\,c}{8\pi\hbar\omega} \qquad (3\text{-}21)$$

Substitution of equations (3-20) and (3-21) plus employment of the dipole approximation [26] yields equation (3-22) [24] as an expression for the x-ray photoabsorption cross-section σ.

$$\sigma = \frac{4\pi e^2}{m^2 c\,\omega}\,|\langle\Psi_f|\,\hat{\mathbf{e}}\cdot\mathbf{p}\,|\Psi_i\rangle|^2\,\rho_f(E) \qquad (3\text{-}22)$$

The expression for the density of states $\rho_f(E)$ depends upon the normalization conditions of the wavefunctions involved [24]. In the case of the bound states, this is unit normalization, and for continuum states the wavefunctions are normalized to the Dirac delta function in the kinetic energy of the photoelectron. As the photon energy approaches the ionization energy, the bound state cross-section merges into the continuum cross-section: $\rho_f^c(IP) = \rho_f^b(IP)$ ($\rho_f^c(E)$ = continuum density of states, $\rho_f^b(E)$ = bound density of states) [24]. The plane wave approximation is often used for the wavefunctions in the continuum. Although this gives a practical and simple expression for $\rho_f(E)$, it does not represent an accurate description of the wavefunctions, especially near the ionization threshold, leading to incorrect values for σ [24].

Intensities for bound state transitions are typically quoted in terms of oscillator strength f rather than cross-section σ. The two values are related according to equation (3-23). [24]

$$\sigma(E) = \frac{2\,\pi^2\, e^2\, \hbar}{m\, c}\frac{df}{dE}$$

$$f = \frac{2}{m\,\hbar\,\omega}\,|\langle\Psi_f|\,\hat{e}\cdot\mathbf{p}\,|\Psi_i\rangle|^2 \tag{3-23}$$

The oscillator strength represents the area of the pre-edge photoabsorption peak. The width of the peak represents $1/\rho_f^b(E)$ and the height σ.

The interaction of the electric field vector of the incident radiation with the anisotropic molecular field of the species ionized imparts an angular dependence onto the photoionization cross-section. When the incident radiation is polarized, pronounced asymmetry is expected. This angular dependence is given by the differential cross-section [8]

$$\frac{d\sigma}{d\Omega} = \frac{\sigma}{4\pi}\left[1 + \frac{\beta}{2}(3\cos^2\theta - 1)\right] \tag{3-24}$$

where β is the asymmetry parameter, dependent on the molecular geometry and the symmetry of the orbital ionized, and θ is the angle between the polarization vector of the light and the electron travel path. This angular dependence of the cross-section does not influence the total electron yield spectra measured with a gas cell, because all electrons are collected and counted, regardless of their travel path. In a photoelectron experiment, however, only a fraction of the electrons generated are actually analyzed, namely those that pass through the analyzer entrance slit. Hence, the angular distribution of the cross-section can have a significant effect on the photoelectron peak intensities. The asymmetry contribution can be eliminated by positioning the analyzer entrance slit at the magic angle of 54.74° to the polarization of the light. At this angle, the term $3\cos^2\theta$ equals 1 and equation (3-24) reduces to $\frac{\delta\sigma}{\delta\Omega} = \frac{\sigma}{4\pi}$.

3.5. MS-Xα calculations

A popular and quite successful method for calculating x-ray photoabsorption spectra is the Xα Multiple Scattering Method. The method was developed by Slater and Johnson in the late 1960's [24]. Originally employed only for the bound electronic states, it was expanded for the calculation of continuum final states by Dill, Dehmer and Davenport in the mid 1970's [24]. A detailed description of the technique is given by Johnson [103], along with examples for gaseous molecules (SF_6), complex ions in salts ($KMnO_4$), impurities in semiconductors (Mn in ZnS), and metal bonding in enzymes and proteins. Here, we will give only a short summary of the main aspects of the method. Two approximations form the basis of the Xα technique:

1. The exchange potential in the Hartree-Fock Hamiltonian is approximated by an average potential determined by the total charge density. The one-electron Hartree-Fock equation is solved for each atom of the molecule in turn. To avoid the calculation of numerous two-electron integrals, the Coulomb and exchange potentials caused by electron-electron interactions are expressed in terms of the total charge density of all other electrons, a simple matter for the Coulomb term, but somewhat problematic for the exchange potential. It is approximated by the Xα potential, where $\rho(\mathbf{r})$ is the local electron density [24].

$$V_{X\alpha}(\mathbf{r}) = 3\, e^2\, \alpha \sqrt[3]{\frac{3}{8\pi}\rho(\mathbf{r})} \tag{3-25}$$

The scaling parameter α has been calculated by Schwarz [109, 110] for atoms up to Z = 86 (Radon), and is typically of the order of 0.75. At large distances from the molecular centre these averaged potentials are insufficient to describe the Coulomb interaction between electron and positive ion correctly. This shortfall can be amended by the introduction of a "Latter tail": the simple Coulomb potential between electron and ion e^2/r replaces the calculated molecular potential at distances when the former exceeds the latter in magnitude.

2. The overall cluster potential is approximated by a potential in the form of a muffin tin. The molecule under study is partitioned into three main regions. This is illustrated for SO_2 in Figure 3-1. Each atom is represented by a sphere with radius a_i, and the entire molecule is surrounded by an outer sphere. The sphere radii employed in the calculation influence the accuracy of the transition energies and ionization potentials obtained. This is shown in Table 3-1, where our results for the binding energies of the valence shell orbitals of PF_3 are compared to those obtained by Powis [111]. However, although the sphere radii are of importance to the Xα calculation, their choice is a somewhat arbitrary and intuitive process. To put consistency into this choice, the atomic sphere radii a_i are determined according to the procedure suggested by Norman [112]. The ratios of these radii are chosen to be proportional to volumes containing the atomic number of electrons based upon the initial atomic charge distribution. Keeping this ratio fixed, the actual radii are chosen to satisfy the virial theorem at self-consistency. Overlapping atomic spheres are employed, as this improves the agreement between the calculations and experimental results compared to touching spheres [112]. Position and radius of this outer sphere are chosen so that it encompasses all atomic spheres and minimizes the intersphere region II, the region with the

least well-defined potential. The potential at any arbitrary point **r** is then calculated as a superposition of the potentials stemming from each atom [24].

$$V(\mathbf{r}) = \sum_i [V_C^i(\mathbf{r}_i) + V_{X\alpha}^i(\mathbf{r}_i)] \tag{3-26}$$

$V_C^i(\mathbf{r}_i)$ and $V_{X\alpha}^i(\mathbf{r}_i)$ are the Coulomb and Exchange potentials of atom i, respectively. In the atomic regions I_i, the potentials are expressed in terms of spherical harmonics. The potential is averaged to a constant value in the intersphere region II, and a spherical average with respect to the centre of the outer sphere is used in the outer region III to give the potentials V_{II} and $V_{III}(\mathbf{r})$, respectively. By retention of only the l=m=0 spherically symmetric term for the atomic potentials $V_I(\mathbf{r}_i)$, the overall molecular potential takes on a "muffin tin" form, as illustrated for N_2 in Figure 3-2 [24].

Calculation of ionization potentials and transition energies to bound excited states are performed in the transition state mode. Half an electron is removed from the initial orbital and placed into the final orbital state. For the photoelectron process, then, wherein the electron is completely removed from the molecule, a final state has one half unit of charge. For the photoabsorption process, wherein the electron in transition is moved from the inner-core level to an unoccupied level within the molecule, half an electron is placed in the receiving antibonding orbital, and the molecule retains electroneutrality. A positively charged Watson sphere [103] was employed to stabilize the final states of the bound transitions [113].

The oscillator strengths for the bound transitions are obtained using the method developed by Noodleman [114]. In presence of an electromagnetic field $\mathbf{A}(t) = \mathbf{A}_0\, e^{-i\omega t}$, a Hamiltonian of the form

$$H = H_{SCF} + \frac{e}{mc}\mathbf{A}_0 \cdot \mathbf{p}\, e^{-i\omega t} \tag{3-27}$$

describes the system, where H_{SCF} is the one-electron ground state Xα self-consistent-field Hamiltonian for the system. H_{SCF} is not uniquely defined throughout the entire excitation process, so approximations are required [114]:

1. H_{SCF} is replaced by an average self-consistent-field Hamiltonian. For this purpose, the one-electron transition-state Hamiltonian is used, appropriate for the configurational average between initial and final state.
2. The ground state density operator ρ_0 is assumed to be diagonal in the basis of this average Hamiltonian, achieved by expansion of ρ_0 in terms of transition state orbitals.

The accuracy of the second approximation is, of course, dependent upon the magnitude of the perturbation resulting from photoexcitation [114]. Through application of time-dependent perturbation theory, the oscillator strength equation is obtained. Because of the nature of the potentials used in Xα theory, the acceleration form of the oscillator strength, given in equation (3-28), is most convenient [114].

$$f = \frac{2\hbar^2}{3m(\Delta E)} \sum_{s=1,2} [n_1(s)-n_2(s)] \sum_{p1,\, p2} \left| \langle \mu_1^T(\Gamma_1,p_1,s) | -\nabla V_T | \mu_2^T(\Gamma_2,p_2,s) \rangle \right|^2 \delta[\varepsilon_2^T(s)-\varepsilon_1^T(s)-\hbar\omega] \tag{3-28}$$

where

ΔE = excitation energy = $\varepsilon_2^T - \varepsilon_1^T$
σ = spin index
p_1, p_2 = initial and final orbitals, respectively
Γ_1, Γ_2 = initial and final irreducible representations
$n_1(s)$, $n_2(s)$ = orbital occupation numbers
ε_1^T, ε_2^T = orbital eigenvalues

The advantage of the acceleration method for calculation is the behaviour of the potential gradient ∇V in the Xα scattered wave method [114]. Since the potential is constant in region II, its gradient will be zero in that region. Further, the potential is radially symmetric in regions I_i and III, giving the gradient the simple form shown in equation (3-29) in those regions [114].

$$\nabla V_T = [\sin\theta \cos\phi \, \mathbf{i} + \sin\theta \sin\phi \, \mathbf{j} + \cos\theta \, \mathbf{k}] \frac{\delta Vr}{\delta r} \tag{3-29}$$

The photoionization cross-section as a function of excitation energy was calculated using the method developed by Dill and Dehmer [115] and Davenport [116]. Following photoionization, the free electron moves in a pure Coulomb field. Thus, at long range the final state electronic wavefunction takes on an asymptotic form of an incoming-wave normalized Coulomb function combined with incoming Coulomb spherical waves, caused by scattering from the non-Coulomb part of the potential. Photoionization of a molecule is a dipole process to the first approximation; thus, the differential cross-section is given by

$$\frac{\delta\sigma}{\delta\Omega} = \frac{e^2 a_0{}^2}{\hbar c \pi} \frac{k}{\omega} \left| \langle f | \hat{\mathbf{A}} \cdot \mathbf{p} | i \rangle \right|^2 \tag{3-30}$$

[115] where

k^2 = kinetic energy of the photoelectron

ω = photon energy

$\hat{\mathbf{A}}$ = polarization of the incident radiation

$\mathbf{p}$ = momentum operator

As with the oscillator strength for bound transitions [114], the acceleration method is used to simplify the calculation of the transition dipole moment [115].

$$\left| \langle f | \hat{\mathbf{A}} \cdot \mathbf{p} | i \rangle \right| = \frac{\left| \langle f | \hat{\mathbf{A}} \cdot \nabla V | i \rangle \right|}{k^2 - \varepsilon_i} \tag{3-31}$$

where

ε_i = initial state energy of the orbital ionized

V = potential

The cross-section is calculated in the molecular frame of reference [115]. For gas phase species, this is then averaged over all possible orientations to obtain the overall differential cross-section, equation (3-24). The total cross-section can be determined through integration over all spatial angles Ω [115].

For these calculations, the default settings of the Xα program were used. The alpha parameters were the α_{HF} values from the tables compiled by Schwarz [109, 110]. The alpha parameters for the outer sphere (region III) and the intersphere region (region II) were set equal to the same value, the average of the atomic alpha parameters. The atomic sphere radii were calculated according to the Norman procedure [112], with a ratio of actual radius to atomic radius of 0.88, and the atomic charge densities are used for all atoms, including H, to calculate the initial potentials. Frozen core orbitals were not used. Electron spins were considered only for open-shell molecules (e.g. NO_2). The spin-orbit splitting of P-2p orbitals (0.9 eV) and S-2p orbitals (1.2 eV) was added manually by assuming that the calculated value is a weighted average of the two spin-orbit partners. Relativistic core corrections were not made. The experimental bond lengths and angles [95-97] were used to determine the atom positions, and the ground state molecular point group was employed in the calculation.

The natural peak shape of the transitions in electronic spectra is a Lorentzian distribution; however, instrumental resolution of the detection system and energy resolution of the photon source add Gaussian components to the peak shape. Often these instrumental effects dominate, leading to an essentially Gaussian envelope for the experimental peaks.

The calculated spectra were generated using pure Gaussian or pure Lorentzian curves, as described in detail later (Chapters 5 to 11). The peak area was given by the oscillator strength or the photoionization cross-section.

3.6. Molecular orbital compositions with ab initio *methods*

To determine the identity of the molecular orbitals (e.g. S-O σ or Rydberg-d), the compositions of all valence and virtual orbitals were calculated for the ground state configuration of the molecule, using the Gaussian 94 package. The molecular geometry was optimized, and the LCAO coefficients of the molecular orbitals were calculated at the optimized geometry. The atomic orbital basis functions were orthonormalized according to the symmetric orthogonalization procedure proposed by Löwdin [117] and outlined in [80], using $\mathbf{S}^{-1/2}$—the inverse square root of the overlap matrix **S**, equation (3-32)—as the transformation matrix of the atomic orbital basis functions χ_i ,equation (3-33), where χ'_i are the new orthonormal basis functions:

1. The overlap matrix **S** was diagonalized by the unitary matrix **U**, whose columns were the eigenvectors of **S**.
2. The inverse square root $\mathbf{s}^{-1/2}$ of this diagonal matrix **s** was obtained by taking the inverse square root of each of the non-zero elements of **s**, the eigenvalues of **S**.
3. $\mathbf{S}^{-1/2}$ is obtained by undiagonalizing $\mathbf{s}^{-1/2}$.

$$\mathbf{S} = \begin{bmatrix} \langle\chi_1|\chi_1\rangle & \langle\chi_1|\chi_2\rangle & \langle\chi_1|\chi_3\rangle & \cdots & \langle\chi_1|c_n\rangle \\ \langle\chi_2|\chi_1\rangle & \langle\chi_2|\chi_2\rangle & \langle\chi_2|\chi_3\rangle & \cdots & \langle\chi_2|\chi_n\rangle \\ \langle\chi_3|\chi_1\rangle & \langle\chi_3|\chi_2\rangle & \langle\chi_3|\chi_3\rangle & \cdots & \langle\chi_3|\chi_n\rangle \\ \vdots & \vdots & \vdots & \ddots & \vdots \\ \langle\chi_n|\chi_1\rangle & \langle\chi_n|\chi_2\rangle & \langle\chi_n|\chi_3\rangle & \cdots & \langle\chi_n|\chi_n\rangle \end{bmatrix} \tag{3-32}$$

$$\begin{bmatrix} \chi'_1 \\ \chi'_2 \\ \chi'_3 \\ \vdots \\ \chi'_n \end{bmatrix} = \mathbf{S}^{-1/2} \times \begin{bmatrix} \chi_1 \\ \chi_2 \\ \chi_3 \\ \vdots \\ \chi_n \end{bmatrix} \tag{3-33}$$

$$\begin{bmatrix} c'_1 \\ c'_2 \\ c'_3 \\ \vdots \\ c'_n \end{bmatrix} = \mathbf{S}^{1/2} \times \begin{bmatrix} c_1 \\ c_2 \\ c_3 \\ \vdots \\ c_n \end{bmatrix} \tag{3-34}$$

The molecular orbital coefficients, c'_i, of this orthonormal basis are related to the original coefficients by equation (3-34), where the matrix $S^{1/2}$ is the inverse of $S^{-1/2}$ [80]. The new atomic orbital basis functions obtained from this transformation are orthonormal:

$$\langle \phi_1 | \phi_1 \rangle = \sum_i \sum_j c'^*_j c'_i \langle \chi'_j | \chi'_i \rangle = \sum_i |c'_i|^2 \langle \chi'_i | \chi'_i \rangle = \sum_i |c'_i|^2 = 1 \qquad (3\text{-}35)$$

The contribution in % to the molecular orbital by the atomic orbital χ'_i is given by $|c'_i|^2 \times 100$. Valence shell orbitals that are mainly (over 90%) composed of one particular type of atomic orbital are assigned as localized lone pairs, while those with contributions from many different types of atomic orbitals are either bonding orbitals or delocalized lone pairs. Of these, the σ-type bonding orbitals tend to have the lowest orbital energy, followed by the delocalized lone pairs. The π-type bonding orbitals generally have the highest orbital energy.

Orbital compositions of the virtual orbitals follow a comparable pattern. Rydberg-type orbitals are usually localized and composed of one particular type of atomic orbital, while molecular antibonding orbitals tend to be delocalized, with many different types of atomic orbital contributing.

For example, in an HF calculation of SO_2 with the 6-311G* basis set, the $1a_2$ orbital of SO_2 was found to be 6.6% S-d, 93.2% O-p, and 0.2% O-d in character. This orbital is dominated by O-p character, and thus classified as an O(2p) non-bonding (lone pair) orbital. The $1b_1^*$ orbital of the same molecule has 56.7% S-p, 2.5% S-d, 41.9% O-p and 0.3% O-d character; thus, it represents a π-type molecular antibonding orbital.

3.7. Energy estimation for Rydberg Series

Transition energies (E_n) to Rydberg orbitals can be estimated using the modified Rydberg formula [118]:

$$E_n = IP - \frac{R}{(n - \delta)^2} \qquad (3\text{-}36)$$

where IP is the ionization potential to which the series converges, R is the Rydberg constant, n is the principal quantum number of the Rydberg level and δ is the quantum defect, the term introduced to account for the presence of the other nuclei and electrons in the molecule. The applicable value depends on the penetration of the Rydberg orbital, because it reflects the shielding. Thus, each subshell has a different value of δ, leading to distinct s, p, d,... Rydberg series. Furthermore, the existence of an anisotropic molecular field removes the degeneracy of the p, d, f,... orbitals giving multiple peaks in the corresponding series.

Estimated values for these quantum defects, without consideration of the molecular field effects, are obtained from the experimental term values of valence shell→Rydberg transitions of many different molecules [118]. These data show that the quantum defect for the p and d Rydberg series remains fairly constant regardless of chemical environment, but the quantum defect for the s series varies significantly from molecule to molecule. In the present work equation (3-36) has been used to estimate the term values of Rydberg transitions in the phosphorus and oxygen K shell spectra (Chapters 8 and 9) and in sulphur L shell spectra (Chapter 7). Details about the quantum defect employed are given in the relevant sections.

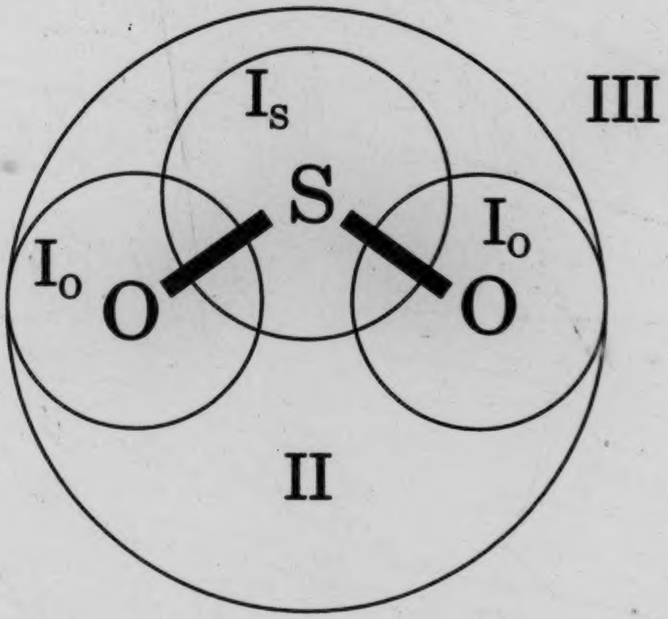
I$_S$
III
S
I$_O$
I$_O$
O
O
II

Figure 3-1: The arrangement of potential spheres in SO_2.

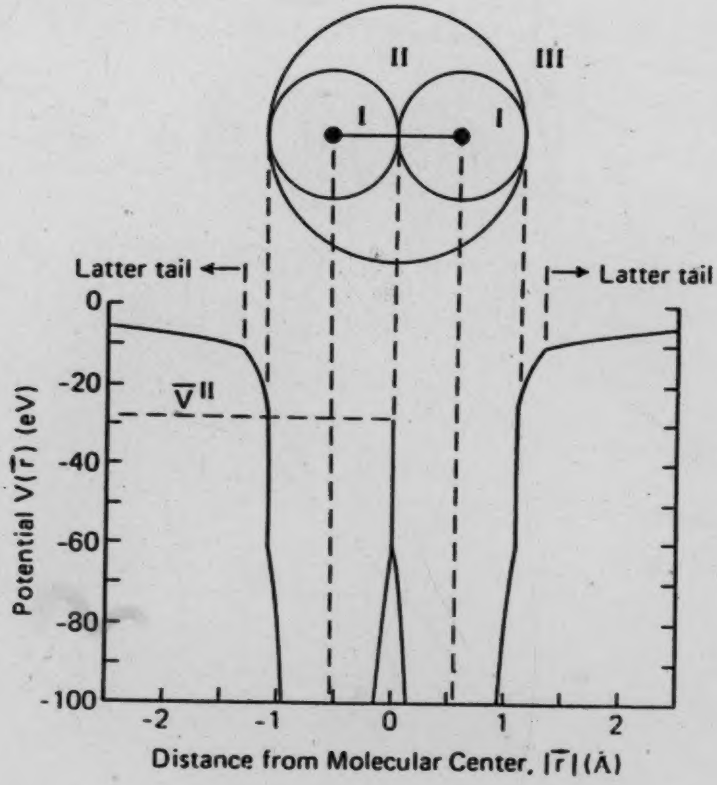

Figure 3-2: Muffin tin potential for N_2 [24].

Table 3-1: The valence shell ionization potentials of PF_3 (eV)

orbital	Experiment[(a)]	Xα calculations	
	[119]	present	literature [111]
$5a_1$	40.85	36.25	36.47
$6a_1$	22.44	21.79	22.04
$7a_1$	18.60	16.67	17.34
$8a_1$	12.27	10.81	12.05
$1a_2$	15.88	14.88	15.64
3e	38.76	35.16	35.48
4e	19.45	18.83	18.80
5e	17.47	16.10	16.75
6e	16.44	15.14	15.85

(a): experimental uncertainty ±0.06 eV

Table 3-2: Character Table for the K point group [28]

C_{3v}	E	$\infty C_\infty^{\varphi}$	$\infty C_\infty^{2\varphi}$	…	
S	1	1	1		$x^2+y^2+z^2$
P	3	$1+2\cos\varphi$	$1+2\cos(2\varphi)$		(x,y,z), (R_x,R_y,R_z)
D	5	$1+2\cos\varphi+2\cos(2\varphi)$	$1+2\cos(2\varphi)+2\cos(4\varphi)$		$(2z^2-x^2-y^2,xz,yz,xy,x^2-y^2)$
F	7	$1+2\cos\varphi+2\cos(2\varphi)+$ $2\cos(3\varphi)$	$1+2\cos(2\varphi)+2\cos(4\varphi)+$ $2\cos(6\varphi)$		$[z^3,xz^2,yz^2,xyz,z(x^2-y^2),$ $x(x^2-3y^2),y(3x^2-y^2)]$
G	9	$1+2\cos\varphi+2\cos(2\varphi)+$ $2\cos(3\varphi)+2\cos(4\varphi)$	$1+2\cos(2\varphi)+2\cos(4\varphi)+$ $2\cos(6\varphi)+2\cos(8\varphi)$		
.					
.					
.					

Table 3-3: Character Table of the C_{3v} double group [a]

C_{3v}	E	$\bar{E}$	$2C_3$	$2\bar{C}_3$	$3\sigma_v$	$3\bar{\sigma}_v$
A_1 (Γ_1)	1	1	1	1	1	1
A_2 (Γ_2)	1	1	1	1	-1	-1
E_1 (Γ_3)	2	2	-1	-1	0	0
E_2 (Γ_4)	1	-1	-1	1	i	-i
(Γ_5)	1	-1	-1	1	-i	i
E_3 (Γ_6)	2	-2	1	-1	0	0

(a): This character table was determined as described in [107, 108].

Table 3-4: Character Table of the C_{2v} double group [a]

C_{2v}	E	E	$C_2, \bar{C}_2$	$\sigma_v, \bar{\sigma}_v$	$\sigma_v', \bar{\sigma}_v'$
A_1 (Γ_1)	1	1	1	1	1
A_2 (Γ_2)	1	1	1	-1	-1
B_1 (Γ_3)	1	1	-1	1	-1
B_2 (Γ_4)	1	1	-1	-1	1
E (Γ_5)	2	-2	0	0	0

(a): This character table was determined as described in [107, 108].

Table 3-5: Character Table of the D_{3h} Double Group [(a)]

D_{3h}	E	E	$2C_3$	$2\bar{C}_3$	$3C_2,3\bar{C}_2$	$\sigma_h,\bar{\sigma}_h$	$2S_3$	$2\bar{S}_3$	$3\sigma_v,3\bar{\sigma}_v$
A_1' (Γ_1)	1	1	1	1	1	1	1	1	1
A_2' (Γ_2)	1	1	1	1	-1	1	1	1	-1
E' (Γ_3)	2	2	-1	-1	0	2	-1	-1	0
A_1'' (Γ_4)	1	1	1	1	1	-1	-1	-1	-1
A_2'' (Γ_5)	1	1	1	1	-1	-1	-1	-1	1
E'' (Γ_6)	2	2	-1	-1	0	-2	1	1	0
E_3 (Γ_7)	2	-2	1	-1	0	0	$\sqrt{3}$	$-\sqrt{3}$	0
E_4 (Γ_8)	2	-2	1	-1	0	0	$-\sqrt{3}$	$\sqrt{3}$	0
E_5 (Γ_9)	2	-2	-2	2	0	0	0	0	0

(a): This character table was determined as described in [107, 108].

Table 3-6: Character Table for the C_s Double Group (a)

C_{2v}	E	$\bar{E}$	σ	$\bar{\sigma}$
A′ (Γ_1)	1	1	1	1
A″ (Γ_2)	1	1	-1	-1
E (Γ_3)	1	-1	i	i
(Γ_4)	1	-1	-i	-i

(a): This character table was determined as described in [107, 108].

4. An Outline of the Concept of Hypervalent Molecules

The modern concept of the chemical bond as the formation of an electron pair linkage between atoms was first described in the Lewis-Langmuir theory of molecular bonding [120, 121], which predates molecular orbital theory. In this description, molecular stability is achieved through the formation of octets; each atom in the molecule is surrounded by eight electrons, or four electron pairs. These electron pairs can be considered to correspond to the doubly occupied molecular orbitals obtained from the solution of the Schrödinger equation. While the application of the Lewis-Langmuir theory [120, 121] explained the chemical bonding of second row elements (C, N, O and F) in a satisfactory way, it broke down for compounds containing third and higher row elements (P, S, Cl, As, Se, Br, Kr, Sb, Te, I and Xe) in valencies other than their lowest stable valence [14]. To explain the existence of these hypervalent compounds and ions, that is, compounds which violate the octet rule by having more than eight electrons in the valence shell (e.g. OPF_3, SO_2F_2 and ClO_4^-), one of two modifications is required to the Lewis rules [14]:

1. allow the violation of the octet rule by promotion of electrons into vacant d-orbitals, or
2. modify the rule of localized bonding pairs to allow 50% or more ionic character.

The traditional method of dealing with hypervalency employed the first modification treating these molecules as exceptions to the Lewis rule [14].

4.1. Duodecet Rule

Robinson [122] proposed a duodecet rule for Si(IV), P(V), S(VI) and Cl(VII) compounds, based on the overall bond order of the central atom. In general, X-O and X-N (X = central atom) bond lengths in hypervalent compounds are significantly shorter than single bond lengths calculated from Pauling's covalent radii, r_p. Furthermore, bonds of similar bond order have a constant value for r/r_p. The value of r/r_p decreases with increasing bond order [122].

$$\log(k_{XO}) + A \log(r_{XO}) = \text{constant}$$
$$n_{XO} = B\, k_{XO} + \text{constant} \qquad (4\text{-}1)$$

Application of the relationship between bond lengths (r_{XO}), stretching force constants (k_{XO}) and bond orders (n_{XO}), shown in equation (4-1) [122], established X-O and X-N bond orders as well as an overall bond order of the central atom X for a variety of Si(IV), P(V), S(VI), and Cl(VII) molecules. In all cases the total bond order of the central atom was approximately 6, giving credence to a duodecet rule for third period elements in their maximum oxidation state [122].

Experimental evidence for an expanded octet, which led to the concept of involvement of d-orbitals in bonding, comes, for example, from the stability of phosphine oxides which do not reduce even when heated with metallic sodium [123]. In contrast, the corresponding amine oxides are thermally unstable [123]. This difference has been rationalized by invoking the possibility of P(3d)-O(2p) π bonding in the phosphorus compounds. The resulting double bond character strengthens the P-O bond leading to the overall stability of the species. Since corresponding d-orbitals are unavailable in the amines, the N-O bond is restricted to a weaker dative N→O single bond [123]. Support for P(3d)-O(2p) π bonding is given by the relative dissociation energies of P-O (500-600 kJ/mol) in phosphine oxides and N-O (200-300 kJ/mol) in amine oxides [123]. Also, the P=O bond lengths of phosphoryl compounds correspond to values expected for a double bond—shorter than the sum of covalent radii, and the P-O stretching frequency correlates to the electronegativity of the other ligands [123]. These also give supporting evidence for the π bonding model.

A second example is provided by NSF_3 [123]. Here, the S-N bond length of 1.416 Å [123], the shortest known between these two atoms, is consistent with the formation of a triple bond. Also, the F-S-F bond angle of 94° [123] is compatible with the presence of four sp^3 σ bonds and two S(3d)-N(2p) π bonds [123].

4.2. The Three-Centre-Four-Electron Bond Model and Partial Ionic Bonding

The first modification of the Lewis rules has, however, a serious drawback [14]: it requires the promotion of electrons into empty d-orbitals and the formulation of sp^3d or sp^3d^2 hybridization combinations. Consequently, the discovery of Xe compounds in the early 1960's led to a renewed search for the proper bonding model for hypervalent compounds, because the Xe 5p→5d transition energy is prohibitively large [14] (of the order of 10 eV [124]). The second modification to the Lewis rules therefore gained popularity and a general theory of hypervalency was developed by Rundle [125] and Musher [15], based upon a linear three-centre-four-electron bond model developed by Pimentel [126], and by Hach and Rundle [127]. Musher [15] divided hypervalent compounds into four groups:

1. HV_I^m – hypervalent compounds of the first class with monovalent ligands, for example: SF_4, BrF_3, IF_5 and XeF_2
2. HV_I^d – hypervalent compounds of the first class with divalent ligands, for example: OSF_2, $HOClO$, $HOClO_2$, XeO_3, and $OXeF_4$
3. HV_{II}^m – hypervalent compounds of the second class with monovalent ligands, for example: SF_6, PF_5, and IF_7
4. HV_{II}^d – hypervalent compounds of the second class with divalent ligands, for example: SO_2F_2, SO_4^{2-}, XeO_4, OIF_5, $FClO_3$, OPF_3, $HOClO_3$, and NSF_3.

It should be noted that the central atom in HV_I compounds invariably belongs to Group VI (S, Se, Te), Group VII (Cl, Br, I) or Group VIII (Kr, Xe) [15]. The ground state electronic configuration for atoms in these groups is $s^2p_x^2p_y^1p_z^1$, $s^2p_x^2p_y^2p_z^1$ and $s^2p_x^2p_y^2p_z^2$, respectively. All have at least one doubly occupied p-orbital.

When comparing hypervalent molecules with ordinary covalent molecules having the same central atom, several characteristics of the former are observed [15]:

1. The ligands of the hypervalent molecules always include atoms with high electronegativity (F, Cl, O, N),
2. Only HV molecules can have co-linear single bonds,

3. Only HV molecules can have two different types of single bond on an atom so that this species can undergo unimolecular geometric isomerization.

In a simple quantum mechanical picture, normal covalent bonds in molecules are formed as a result of the overlap of a singly occupied atomic orbital of the central atom with a singly occupied atomic orbital from the ligand [15]. The two orbitals combine to form molecular orbitals—a doubly occupied bonding orbital and an empty antibonding orbital. A thermodynamically stable species is obtained when all singly occupied atomic orbitals of the central atom are employed in the bonding (e.g. PF_3, SF_2, and ClF). The HV_I^m compounds can be viewed as forming through the addition of two extra ligands to a stable covalent molecule ($SF_2+F_2 \rightarrow SF_4$, $ClF+F_2 \rightarrow ClF_3$ etc.) [15]. These additional ligands are added on opposite sides of the central atom along the axis of a lone pair p-orbital forming two co-linear single bonds, leaving the structure of the original molecule essentially intact [15] (SF_2 [128]: S-F = 1.589Å, F-S-F = 98°16′; SF_4 [95]: $S\text{-}F_{eq}$ = 1.545Å, $S\text{-}F_{ax}$ = 1.646Å, $F_{eq}\text{-}S\text{-}F_{eq}$ = 101.6°, $F_{ax}\text{-}S\text{-}F_{ax}$ = 173.1°). Similarly, HV_I^d compounds are formed by the interaction of the two singly occupied orbitals on the ligand with a lone pair p-orbital of the central atom (SOF_2 [95]: S-F = 1.5854Å, S-O = 1.4127Å, F-S-F = 92.83°, F-S-O 106.82°). In both cases, three orbitals containing a total of four electrons combine to form molecular orbitals: an occupied bonding orbital ($2e^-$), an occupied non-bonding orbital ($2e^-$), and an empty antibonding orbital [15].

However, HV_{II} compounds have more ligands than p-electrons on the central atom [15]. This requires the use of the spherical symmetric s-orbital in bonding. The arrangement of ligands in HV_{II} molecules invariably has a highly symmetric geometry [15]: tetrahedral (SO_2F_2, OPF_3), octahedral (SF_6, OIF_5), trigonal bipyramidal (PF_5) and pentagonal bipyramidal (IF_7). Given these observations, formation of HV_{II} can be described as the addition of extra ligands to an existing molecule to bring the central atom to its maximum valence. The geometry of the product species is dictated by steric factors. The electronic structure is completely rearranged through some form of sp^x hybridization on the central atom to obtain the necessary bonding orbitals [15].

A second model that may be used to describe the bonding in hypervalent molecules allows partial ionic bonding in combination with resonance structures. This was first proposed by Pauling [129] and is illustrated in Figure 4-1 for PF_5. Of these six structures, only the central one violates the octet rule, necessitating the employment of a d-orbital in bonding. The other structures all contain an ionic bond, avoiding the involvement of d-orbitals. Assuming equal contribution from each resonance structure to the overall molecular structure, this scheme predicts 16.7% ionic character for each P-F bond. Similarly, because of the resonance structure contributions, the phosphorus d-character of the bonding orbitals is small (3.3%).

The advancement of computers during the last 30 years has made it possible to perform theoretical molecular orbital calculations using wave-functions of sufficient quality to obtain reasonably accurate molecular properties [14]. The bonding in hypervalent molecules has been analyzed with a variety of theoretical methods: shared electron number and occupation number analysis, electron density analysis, and natural population analysis [14], for example. The general conclusion from these analyses is that, although central atom d-orbitals in hypervalent species frequently contribute significantly to the molecular energy (for example, the inclusion of d-functions in the basis set lowers the total energy of the SF_6 molecule by 0.4 Hartree or 250 kcal/mol [130]) the overall d-orbital population is small (≤ 0.3 electrons) [14]. This supports the partial ionic bonding model (modification 2 of the Lewis rules), rather than the covalent sp^3d and sp^3d^2 hybridization models (modification 1 of the Lewis rules) [14]. However, the d-orbital functions are required to obtain reasonably correct molecular properties, even for many non-hypervalent species [14]. This suggests that central atom d-orbitals in hypervalent molecules serve as electron acceptor orbitals for back-bonding from the ligands, leading to an overall energy stabilization which negates ligand-ligand repulsion [14]. The d-orbital functions also act as polarization functions [14]. These are functions added to the basis set to describe the distortion or polarization of the atomic orbitals in a molecular environment [131], in part because Gaussians do not fully describe the wavefunction.

4.3. Bond Order and Valences

The d-polarization functions are generally introduced in *ab initio* calculations even for non-hypervalent molecules containing only first row atoms (C, N, O, F) which do not posses d-orbitals in their atomic valence shell [14]. Mayer [132] therefore proposed an extra criterion to determine if the d-orbitals have actual chemical significance. For this purpose he calculated bond order and valencies for a variety of sulphur compounds, including both hypervalent and non-hypervalent molecules. Three different basis sets were employed: STO-3G, 3-21G and STO-3G*. From these calculations, Mayer [132] concluded that for divalent sulphur the d-orbitals play only a role as polarization functions, whereas the tetra- and hexavalent sulphur compounds (classed as hypervalent molecules) require d-orbitals as valence orbitals which cannot be replaced by a more flexible s-p basis set (3-21G). The d-orbitals are essential for full descriptions of the bonding features including the molecular geometry, p-character of S=O double bonds and the charge of the sulphur atom [132].

To summarize, Mayer proposed the traditional valence shell expansion model for formation of hypervalent sulphur compounds [132]. In later papers Mayer [133] and Ángyán [134] investigated the three-centre-four-electron bond model of Musher [15] and Rundle [125] and the role of central atom d-orbitals therein. First, the bond order of the two occupied orbitals was investigated using the sp bonding model of Musher [15]. The bond order for each hypervalent bond was ½ (overall bond order of 1 for the bonding orbital), and the ligand-ligand bond order was ¼ (the non-bonding orbital) [133] for compounds with symmetric hypervalent ligands. This reduced bond order explains the differing bond lengths in HV_1 compounds (e.g. SF_4 [95]: $S\text{-}F_{eq} = 1.545$ Å, $S\text{-}F_{ax} = 1.646$ Å). Furthermore, the hypervalent three-centre-four-electron bond is sensitive to the ligand electronegativity [133]. In molecules with unequal ligands, the increased electronegativity of one ligand atom leads to a stronger hypervalent bond between the central atom and the other ligand [133]. Although the reduced bond order of the hypervalent bond in the three-centre-four-electron bond model predicts increased bond lengths for the hypervalent bonds, this increase is significantly overestimated [134]. The model also requires a relatively large charge on the central atom, and *ab initio* calculations predict a bond order less than ¼ between the two ligands. These shortfalls led Ángyán [134] to propose an extended model where the non-bonding orbital gains some bonding character through involvement of a central atom d-orbital with the appropriate symmetry (Figure 4-2).

Inclusion of the d-orbital reduces both the charge on the central atom and the long bond order between the ligand atoms [134]. It should be noted that this model allows for partial d-orbital participation ($0 \leq$ d-orbital population ≤ 1). The extreme cases will give the sp^3d hybridization model (d-orbital population = 1) and the sp three-centre-four-electron bond model (d-orbital population = 0).

These models proposed by Mayer and Ángyán [132-134] have several serious shortfalls. The calculation method for bond orders proposed by Mayer [135] is highly dependent upon the basis set employed [136], in similar fashion as the Mulliken population analysis method. Furthermore, because atomic orbitals from different centres overlap, the point charge approximation is invalid [14]. Higher order terms in the Taylor expansion of the Coulomb potential have significant values and should not be ignored. As a result, it is possible for bond orders calculated by Mayer's method to have negative values [14, 136]. Baker [136] investigated calculated bond orders obtained in two different ways: Mayer's method based upon Mulliken population analysis [135], and an alternative method proposed by Natiello and Medrano based upon Löwdin population analysis [137]. In general, he found that the latter method gave more accurate results [136]. He also gave an example of the instability of the Mulliken population analysis method using the negative ion $C_3H_3^-$. The calculations were performed with the 3-21G and 3-21G+G basis sets. The latter has diffuse s and p functions on the carbon atoms. While the Löwdin population analysis gave reasonable occupancies and bond orders for both basis sets, the Mulliken analysis predicted occupancies of +2.2012 and −1.9809 for diffuse orbitals when the latter basis set was employed. Mayer's bond order analysis gave C-C bond orders of −1.76 and −4.26 with this basis set [136].

In a molecular environment, the valence shell atomic orbitals of each species combine to form molecular orbitals. Thus, atomic orbitals *per se* do not exist in molecules. However, it is convenient to discuss the molecular electronic structure in term of its atomic building blocks and to connect it to the electronic structure of the isolated atoms. Hence, the logical way to populate orbitals is to fill the lower energy valence shell of all component atoms first, before placing electrons in the higher energy extra valence d-orbitals of the central atom. Both Mulliken population analysis and Mayer's bond order analysis tend to populate high energy Rydberg orbitals (in particular central atom d-orbitals) at the expense of non-bonding valence shell orbitals on ligand atoms, a phenomenon which makes these analysis methods vulnerable to basis set effects [14].

4.4. Natural Population Analysis

The first popular method for evaluation of the atomic orbital composition of molecular orbitals was developed in the mid 1950's by Mulliken [138-141]. However, this method has significant drawbacks: it is possible to have orbitals with negative populations, it gives unreasonable charge distributions in molecules with significant ionic bonding character, and it is highly sensitive to the basis set used. To overcome these shortcomings of the Mulliken population analysis, the natural population analysis (NPA) method was developed [142]. Here, the atomic orbitals are constructed from linear combination of the available basis functions, and the electrons are first assigned to valence shell orbitals before any are placed in extra-valence central atom d-orbitals. This makes the NPA method relatively immune to basis set effects. The natural atomic orbitals converge smoothly towards well-defined limits upon expansion of the basis set, with stable electron populations. The natural atomic orbitals obtained by NPA neatly divide into a set of core and valence shell orbitals with high occupancy (> 1.95 electrons) and a set of Rydberg orbitals with low occupancy (< 0.05 electrons). The molecular orbitals are constructed from these through formation of an optimal orthonormal set of hybrids, the natural bond orbitals (NBO). These NBO's have maximum occupancy which similar to the natural orbitals proposed by Löwdin [143]. However, in contrast to the Löwdin model, they are localized on one (lone pair) or two (bond pair) atomic centres.

Reed and von Ragué Schleyer [14] investigated the electronic structure of X_3AY species using the NPA method. They concluded that hypervalent bonding in these molecules occurs through "negative hyperconjugation" by which they mean that electrons from ligand p-orbitals delocalize into σ^* orbitals, a process which provides π bonding character to orbitals with nominal σ character. This process also weakens adjoining σ bonds through the population of σ^* orbitals. The d-orbitals of the central atom A act as polarization functions. Their interaction with σ_{AX}* improves the overlap of σ_{AX}* and the valence shell p-orbitals of Y, but also decreases the antibonding character of σ_{AX}*.

The NPA method is, however, not infallible. In this thesis, the NPA method was used to evaluate the covalency of chemical bonds, including π bonds between oxygen and other atoms belonging to Group IV, V or VI (Section 12.4). Optimized geometries were calculated with Gaussian 94 using the HF method and the 6-311G* basis set. Both Mulliken and Natural Population Analysis were performed at this optimized geometry. CO_2, a linear molecule with two equivalent C=O double bonds, was among the compounds studied. Rather than the expected structure of O=C=O, the NPA method predicted a structure involving a C−O single bond and a C≡O triple bond, O−C≡O.

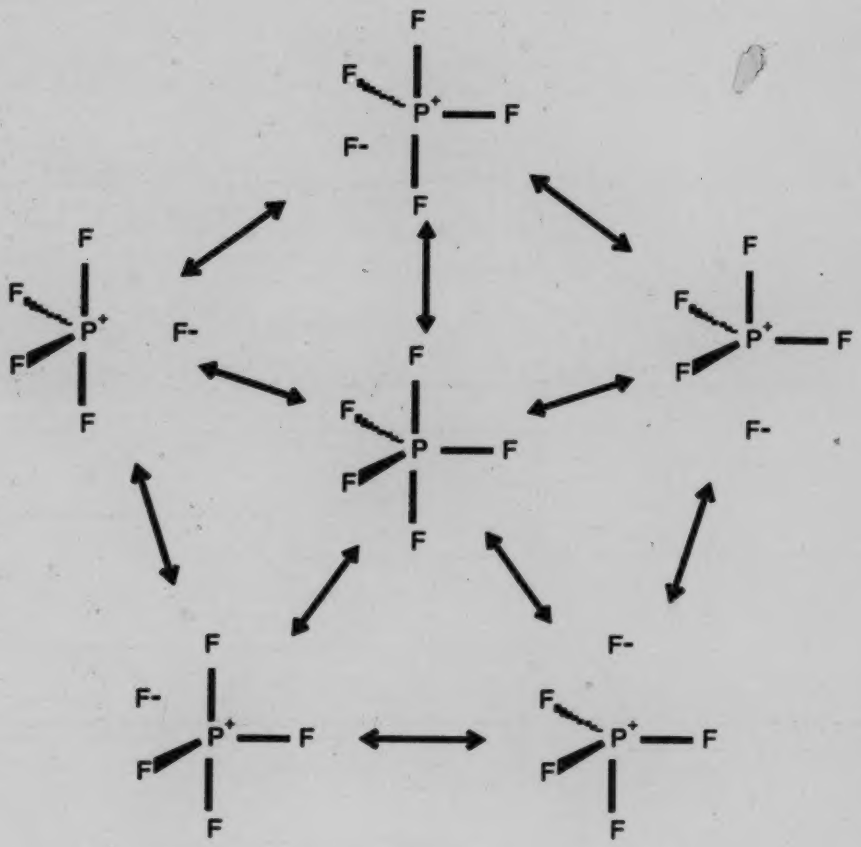
F
F
P+
F
F-
F
F
F
P+
F-
F
F
F
F
P+
F
F
F-
F
F
P
F
F
F
F
F-
P+
F
F
F
F-
F
F
P+
F
F
F

Figure 4-1: Resonance structures of PF_5.

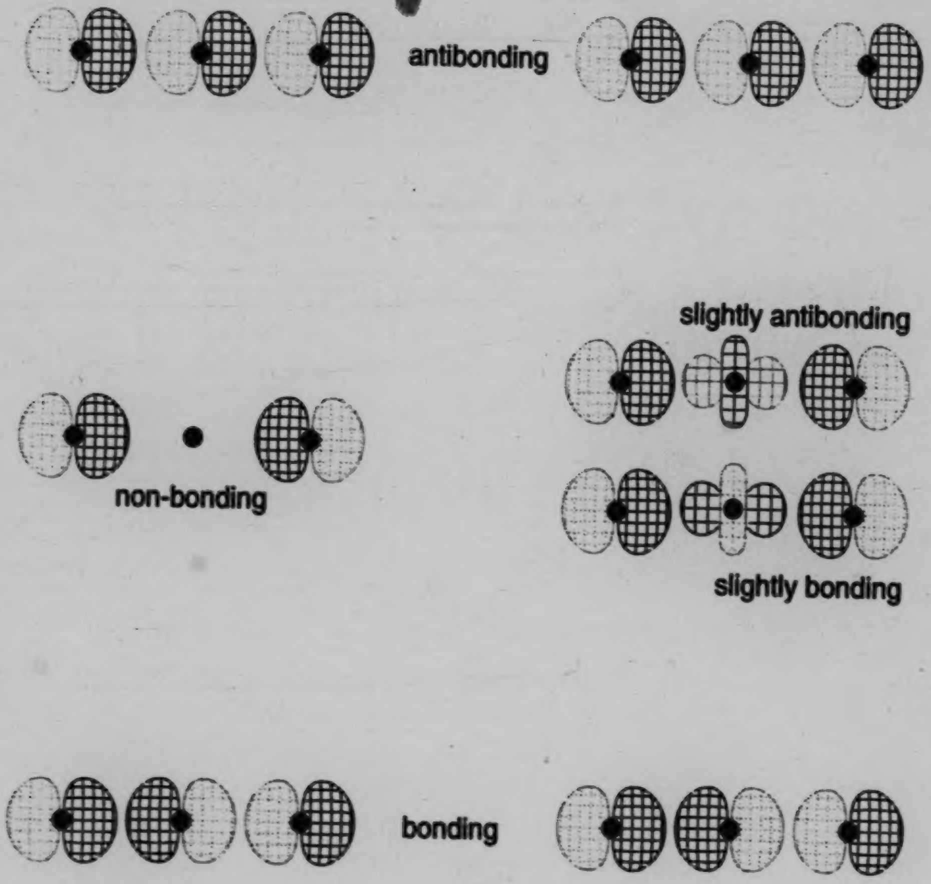
antibonding
slightly antibonding
non-bonding
slightly bonding
bonding

Figure 4-2: The traditional three-centre-four-electron bonding model (left) and Ángyán' s bonding modification [134] involving the central atom d_{z^2} orbital (right).

5. P(1s) Photoabsorption Edges and the Chemical Shift Trends for a Series of Gaseous Phosphorus Compounds [1]

5.1. Introduction

Binding energies of core atomic orbitals in molecules are influenced by the valence shell electron distribution in the molecule. The differences within a series of molecules can be represented as chemical shifts—the differences in the binding energies or transition energies of the atomic core orbital transitions from one molecule to the next, generally assessed relative to one reference compound for the element. The magnitude of these shifts thus reflects the chemical environment of the excited atom. As such these shifts reflect the chemical bonding in a molecule and can be used to extract information about the molecular electronic structure. Herein we describe the exploration of the P(1s) absorption feature in a series of 19 gaseous phosphorus compounds, which span the trivalent to pentavalent valence state and coordination environments ranging from 3 to 5. The P(1s) and P(2p) core photoionization chemical shifts of this same series of molecules as well as the shifts of the KL_2L_3 ($^1D_2$) Auger lines have been previously reported [88-91]; and the absorption edge behaviour is herein compared. Our absorption edge results were analyzed by various methods ranging from simple electronegativity, atomic charge and potential-at-the-nucleus models (with molecular relaxation effects included) to semiempirical and *ab initio* calculations. The experimental peaks were assigned with the results from Xα [103] calculations and more complete *ab initio* calculations used to verify and support the assignments.

5.2. Experimental

The phosphorus K shell spectra were obtained according to the procedure outlined in Chapter 2. The spectra were normalized with the I_0 current from the nitrogen cell. PF_3 was used as an internal calibrant. The energy scales for the spectra of all other gases were referenced to a P(1s) spectrum of PF_3 measured during the same experimental session. The overall photon energy scale was calibrated using the main peak of $Na_4P_2O_7$ at 2152.40eV [144]. The P(1s) spectrum of PF_3 was referenced to the P(1s) spectrum of solid $Na_4P_2O_7$ in a separate experiment in which both solid samples and the gas cell were assembled as a contiguous unit. The gas pressure in the cells was between 0.2 and 1.0 torr. Several spectra were measured for each compound and the resulting peak energies were averaged. For $(CH_3O)_2P(S)Cl$ the standard deviation of the P(1s)→1e* peak energy was 0.12 eV, and for all other compounds it was less than 0.06 eV. The chemical shift values are estimated to be precise within 0.12 eV.

---

[1] A version of this chapter has been published:
R.G. Cavell, A. Jürgensen; *J. Elec. Spec.* 101-103 (1999) 125-129

OPF_3 was prepared by Dr. J. Nielson at Los Alamos National Laboratories, and SPF_3 was prepared at the University of Alberta by Dr. D. Kennepohl. All other compounds were obtained commercially, $(CH_3)_3P{\cdot}AgI$ and most liquids from Aldrich, $(CH_3O)_3PS$ from Hooker, PF_3 from Ozark Mahoning and PH_3 and PF_5 from Matheson. All chemicals were used as received from the supplier. However, the solid and liquid samples were vacuum-sealed into small glass tubings prior to use for transportation purposes. These tubings were connected to the gas entry port of the cell apparatus while still sealed, and then opened under vacuum. The $(CH_3)_3P{\cdot}AgI$ complex was heated to 200 °C in vacuo, to obtain $P(CH_3)_3$ gas, a decomposition product.

5.3. Calculations

Assignment of the experimental peaks was accomplished by calculating the transition energies and their oscillator strengths for transitions to the first few symmetry allowed antibonding orbitals using the Xα technique [103] as explained in Section 3.5 above. Experimental molecular geometries [95-97] were used wherever possible for the calculations. As molecular geometries of $P(C_2H_5)_3$, $SP(OCH_3)_3$ and $CH_3P(S)Cl_2$ were not available, bond lengths and angles were approximated based on the data of structurally related compounds. Thus $CH_3P(S)Cl_2$ was given P–Cl (2.055 Å), P–C(1.815 Å), P–S (1.914 Å), C–H (1.10 Å) and angles (for a staggered structure) $\angle$ C–P–Cl (104.1°), $\angle$ Cl–P–S (115.95°), $\angle$ C–P–S (115.2°), $\angle$ P–C–H (110°) estimated primarily from the parameters for $OPCl_3$, $SPCl_3$ and $CH_3P(O)Cl_2$. For $P(C_2H_5)_3$ the molecular structural parameters are: P-C (1.844 Å), C–H (1.070 Å), C-C_{II} (1.5351 Å), C_{II}-H (1.0940 Å), ∠ P–C–H and ∠ P–C–C_{II} both (111.4°), ∠ C–P–C (98.8°), ∠ C–C_{II}-H (111.17°) using parameters derived from $P(CH_3)_3$ and C_2H_6. For $SP(OCH_3)_3$ the parameters are: P–O (1.580 Å,) P–S (1.936 Å), C–H (1.10 Å), C–O (1.432 Å) and angles ∠ P–O–C (118°), ∠ O–P–O (105°), and ∠ O–C–H (105.7°) as estimated from $P(CH_3)_3$, $SP(CH_3)_3$, $OP(CH_3)_3$, $P(OCH_3)_3$ and $OP(OCH_3)_3$.

Transition energies were calculated by means of the transition state method (Section 3.5). A Watson sphere with a charge of +5.0 and a radius slightly larger than the outer sphere was added in order to lower all orbital energies and thus allow the calculation of the transition energies to virtual orbitals. The P(1s) ionization potential was calculated in the same manner but without the imposition of the Watson sphere.

5.4. Results

Selected spectra are illustrated in Figure 5-1. Spectra of PH_3, PCl_3, and $OPCl_3$ represent typical spectra obtained for the pyramidal compounds: one high intensity pre-edge peak followed by some low intensity structure below the ionization edge and a shape resonance in the continuum. The strong peak corresponds to the P(1s)→1e* transition. This 1e* orbital corresponds to a phosphorus-halide σ*.

The spectrum of PF_5 differs significantly from the pattern displayed by all other compounds in that there are two high intensity pre-edge peaks instead of the single dominant peak demonstrated by the pyramidal molecules. The D_{3h} trigonal bipyramidal structure of PF_5 leads to two P(1s)→mo* transition energies, both with similar oscillator strengths assigned to P(1s)→2e'*(P-F_{eq} σ*) and P(1s)→2a''*(P-F_{ax} σ*) transitions, respectively. The three fluorines in the equatorial plane of PF_5 correlate to a flattened PF_3 pyramid; hence, the 2e'* component correlates to 1e* in the pyramidal molecules.

All the other differentially substituted compounds in the series are either trigonal pyramids or symmetric tops with C_{3v} or C_s symmetry. In the lower C_s symmetry the 1e* antibonding orbital splits into two (1a'* and 1a''*) but the same behaviour prevails; one strong peak arises from the transition into one of the two orbitals resulting from the split of the 1e*. Because this strong peak originates from an overlap of transitions to the two components of the 1e* and therefore correlates to this feature in the more symmetric molecules, we will henceforth refer to this peak as the 1e* peak even in these lower symmetry environments.

To facilitate comparison with related previous photoelectron and Auger studies on these compounds [88, 90] the numbering scheme previously employed for compound identification is used. In two cases, PBr_3 and $CH_3P(O)Cl_2$, the P(1s) ionization energy had not been measured. They were estimated using the previously established correlation between 1s and 2p binding energies [88, 90] and a weighted average P(2p) ionization potential measured by us in another study [145] (Table 5-1).

Experimental transition energies for the main pre-edge peak (1e* or 2e′* for PF_5) and the chemical shift values relative to PH_3 are listed in Table 5-2. The shifts, defined according to equation 5-1,

$$\text{shift} = \text{photoabsorption edge of compound} - \text{photoabsorption edge of reference.} \qquad (5\text{-}1)$$

were compared to the previously reported P(1s) photoelectron shifts and the KL_2L_3 ($^1D_2$) Auger line shifts of the same compounds [88, 90]. The relationships are shown in Figure 5-2.

These photoabsorption shifts were also correlated with the sum of the electronegativity values of the ligands, as illustrated in Figure 5-3 and compared with similar correlations of the P(1s) ionization potential (IP) shifts with the same electronegativity assessment.

The simple charge and potential models used previously [88-92] can also be applied with various levels of calculational detail being used to determine the on-and off-atom charges. The success of this approach, discussed below, is very dependent on the resultant charges. To compare the molecular calculation strategies used herein (Xα and *ab initio*) with those used earlier (Potential at the nucleus using Hückel and CNDO calculations) [88, 90, 91] we have calculated and illustrate (Figure 5-4) the P(1s) IP shifts obtained with the potential at the nucleus method (Gaussian 94, [94], Hartree-Fock (HF) theory, experimental molecular geometry [95-97], D95* basis set, natural charges) to compare with the reported experimental P(1s) shifts [88-91]. As the studies on the effect of the basis sets on the photoabsorption transition discussed below are mirrored in the P(1s) photoionization results, we herein illustrate only the best of the set, the Natural populations obtained with the D95* basis set. Finally we tested the ability of the Xα [146] and Gaussian 94 [94] program sets to calculate directly the photoionization (1s) and photoabsorption transition energies using the transition state method in the former case, the ΔE_{SCF} [99] strategy in the latter case and also, with Gaussian 94 [94], the excited state approach [102]. Numerical results are given in Table 5-2 and Table 5-5 to Table 5-8. Assessment of these theoretical methods was achieved through comparison with the experimental data (Table 5-2). The correlation was evaluated based upon the scatter parameter χ^2, equation (5-2), the slope and the intercept (in that order) of the best-fit line (Table 5-3).

$$\chi^2 = \sum_n [\Delta IP_n(calc) - F(\Delta IP_n(exp))]^2, \quad F(\Delta IP_n(exp)) = slope \times \Delta IP_n(exp) + intercept \qquad (5\text{-}2)$$

A perfect correlation is achieved when the slope equals 1 and the intercept and χ^2 both equal 0.

5.5. Discussion

5.5.1. Trends and Relationships

All of the processes analyzed herein derive from the photon excitation of the P(1s) orbital and so in some respects the trends and responses of the system should be comparable. There is however a considerable difference in the final state accessed by the transition in each case, and thus, the detailed behaviour of each system is likely to be different, reflecting the different chemical environment of the phosphorus atom and its response to the perturbation.

We correlate the processes by plotting the shift values for the Photoabsorption *vs.* Photoelectron (1s) and Auger processes. As Figure 5-2a and Figure 5-2b show, all of the spectroscopies do indeed follow the same overall trend but the detailed fit is not particularly good; molecules with bulkier ligands tend to lie above the fit line, while those with smaller ligands tend to lie below the line. There is a considerable amount of scatter, especially in the correlation of the photoabsorption peak shifts with the Auger shifts. However, this might be expected in view of the highly charged final state developed in the Auger transition, which contrasts to the maintenance of a neutral molecule in the photoabsorption process. Figure 5-2c emphasizes that within a limited structural and substitutional series, quite good correlation between the photoabsorption transition energy and the P(1s) ionization potential exists. The extension to the Auger shifts is only effective in the limited case of the YPF_3 molecules (Figure 5-2d), but again the correlation is very good.

The phosphorus-1s ionization potential represents the transition energy for the ejection of an electron from the P(1s) orbital into the continuum. The initial state is the electronic ground state of the molecule and the final state is composed of a singly charged ion with a localized P(1s) core hole ($^2S_{1/2}$ state) and a photoelectron. The same electronic states are involved for all molecules studied, so the chemical shift of the P(1s) ionization potential is dominated by the adiabatic relaxation [92, 147, 148] of the system in response to the creation of the core hole. In the KL_2L_3 ($^1D_2$) Auger transition this initially created (1s) core hole ($^2S_{1/2}$ state) is filled and two (2p) core holes (nominally equivalent in a simple electrostatic picture) are created. The final state consists of a doubly charged ion ($^1D_2$ state) and an Auger electron. The doubly charged nature of the final ion state induces a larger relaxation contribution to the energy shifts [147, 148]. Again, the initial and final electron states are the same for all molecules and the shift behaviour reflects the magnified relaxation contributions induced by the larger charge and the shielding differences between 1s and 2p holes. The differences between IP and Auger trends were analyzed to isolate the relaxation contributions [88-91, 147, 148].

In photoabsorption spectra, the transitions connect the inner core level to outer bound excited states beyond the valence shell. The electron remains bound in the neutral molecule. These transitions are therefore sensitive to the molecular structure because the character of the final state, the antibonding orbital connected, may differ from one compound to another. This is exemplified in the relative position of the $1a_1^*$ peak in YPX_3 compounds compared to PX_3 compounds. For example $OPCl_3$ and PCl_3 (Figure 5-1) each show a strong peak corresponding to the $P(1s)\rightarrow 1e^*$ transition (which is the basis of the chemical shift comparisons). Detailed spectral assignments show that in the former case the companion weak $1a_1^*$ (P-Cl σ^*) peak occurs at a lower energy than the $1e^*$, but in the latter case the weak $1a_1^*$ (P-Cl σ^*) peak occurs at a higher energy than the $1e^*$. In the case of this series of phosphorus compounds however, the common transition to $1e^*$ ($2e'^*$ for PF_5) is dominant in all cases and can be readily used for a chemical shift analysis. In other systems we have examined, we have found that the final electronic state can differ dramatically [149].

Hence, structural and electronic effects contribute significantly to the relaxation processes involved in each of the three different electronic transitions and it is not possible to relate the shifts of all the compounds by simple functions of the form:

$$\Delta E_{P(1s)\rightarrow 1e^*} = -k\,\Delta E_B + c \qquad \Delta E_{P(1s)\rightarrow 1e^*} = -k\,\Delta E_{Auger} + c \qquad (5\text{-}3)$$

However, as illustrated in Figure 5-2c and Figure 5-2d, simple shift relationships exist for subsets of similar compounds. This agrees with earlier results [88] displaying a rough correlation between the P(1s) binding energy and KL_2L_3 Auger shifts. Of note is the correlation between binding energy and $P(1s)\rightarrow 1e^*$ chemical shifts for the trihalides and dihalides (Figure 5-2c), suggesting similar relaxation processes and very closely related environments exist.

5.5.2. Electronegativity

A simple, chemically satisfying, relationship between the photoabsorption shifts values and the overall chemical environment of the excited atom which emphasizes that there is a substantial "chemical shift" to the photoabsorption transition peak is given by the correlation of the shifts with the total electronegativities of the ligand atoms (Figure 5-3a).

Electronegativities of all ligands on the phosphorus were added to allow for the differential substitutional members of the system. The Pauling electronegativities [105] of all simple atomic ligands used are listed in Table 5-4 and the group electronegativities of C_2H_5, CF_3 and CH_3 were calculated using the orbital method described by Huheey [150] (Table 5-4). Although there is some scatter, the P(1s)→1e* shifts vary approximately linearly with the sum of the ligand electronegativities (Figure 5-3a). All compounds correlate in a manner comparable to the correlation of the (1s) photoelectron binding energy shift (Figure 5-3b) with electronegativity. Overall, the P(1s) ionization potential shifts correlate better with the ligand electronegativities, χ^2 equals 12.0 compared to 21.5 for the P(1s)→1e* chemical shift. This is caused by the differences in the respective final states for these two electronic transitions. The final state of the P(1s)→1e* transition has an additional electron in the outermost shell which influences the distribution of the valence shell electrons. P(1s) photoionization does not add extra valence shell electrons to the system, so changes of the electron distribution within the molecule are only caused by relaxation effects due to the core hole.

Qualitatively, in molecules with atoms of comparable electronegativity—e.g. PH_3—the electrons in bonding orbitals are shared more or less equally by the central phosphorus and the ligand atoms. The valence shell population for phosphorus is expected to be close to five, the formal charge on phosphorus will be low and the phosphorus-ligand bonds are dominantly covalent. As the electronegativity of the ligands increases, valence electron population is delocalized to the ligands thereby decreasing the valence population on the phosphorus. The phosphorus atom becomes positively charged and the bonds become more ionic in character. This decreases the phosphorus core electron-valence electron repulsion leading to a stabilization of the P(1s) orbital and an increase in the ionization potential or the absorption transition energy.

This simple picture is certainly supported by the calculated charges on the phosphorus atom (Gaussian 94 [94], HF theory, experimental molecular geometry [95-97], Natural Population Analysis (NPA) method [151]), Table 5-5. Although there is a considerable amount of scatter, the general trend is an increased charge on phosphorus with increasing ligand electronegativity (Figure 5-5). The same trend is observed for the correlation between P(1s)→1e* and P(1s) ionization potential (IP) chemical shifts and the calculated charge on phosphorus. While there is some scatter for the ionization potential shifts (χ^2 = 41.5), the chemical shifts for the P(1s)→1e* transition correlate nicely (χ^2 = 10.0) (Figure 5-6). Again, these observations can be explained by differences in the final electronic state. In the P(1s)→1e* transition process the final state involves a neutral molecule, all electrons are still bound. The excited electron is in the 1e* orbital, which is centered on phosphorus. So, the overall atomic charges do not change significantly. In contrast, photoionization creates a +1 ion; the electron is removed from the molecule. Since the P(1s) orbital is localized on the phosphorus atom, the photoelectron process leads to a substantial change in the charge on the phosphorus atom ($\Delta q = +1$).

While this ligand electronegativity model does an adequate job in explaining the influence of the initial electronic state upon the chemical shifts, it does not consider orbital relaxation processes, which contribute significantly to ionization potentials and transition energies. A proper calculation method for the chemical shifts has to accommodate these relaxation processes. The following sections investigate several different methods for calculation of the chemical shifts and correlate the results to the experimental data.

5.5.3. Potential at the nucleus method

In this method, the transition or ionization energies (as chemical shifts) are fitted to a simple linear equation connecting the potential at the nucleus of the atom undergoing that transition. The simplest model [92], which was found sufficient in the earlier work [88, 89], has been described in detail in Section 3.2.1 above.

The previous analyses used CNDO and similar semiempirical methods to evaluate the charges and potentials [88-91]. In the present case, the formal charges q of the atoms in each molecule were calculated with Gaussian 94 [94] at the Hartree-Fock [79] (HF) level of theory using experimental bond lengths and angles [95-97]. The resultant charges are highly dependent upon the calculation method and basis set employed. We evaluate the performance by determining the best fit to the experimental data. Only the transition (or RPM) correlations are illustrated and listed as these have been long recognized as the most appropriate [88, 89, 92]. To investigate the effect of d-polarization effects on the calculations, the HF charges were calculated using two different basis sets: D95 and D95*, the latter being the case wherein d polarization functions are added. The population analysis was done using both Mulliken [138-141] and Natural [151] population analysis, again because each approach gives different values of the charges. The calculated chemical shift for the main P(1s) photoabsorption spectrum peak energy relative to PH_3, determined for all compounds and the different strategies used is listed in Table 5-2. Correlations of experimental and predicted shifts are illustrated in Figure 5-7 and summarized in Table 5-3. The slope and intercept of the best fit line are closer to the ideal values of 1 and 0, respectively, for the Mulliken charges, but the parameter χ^2 has a lower value for the Natural charges. The Mulliken charge set demonstrates more scatter, leading to an increased value of χ^2. The effect of d-polarization functions is minimal in the case of Natural charges, the two plots being almost superimposable. The d polarization functions increase all calculated chemical shifts relative to PH_3. This effect, however, is not uniform. It is largest in the chlorides, increasing the predicted chemical shift by as much as 1 eV for $SPCl_3$ and $CH_3P(S)Cl_2$. In contrast, the fluorides experience only a minor increase in chemical shift, the largest value being 0.17 eV for PF_5. Overall these effects of the d polarization functions slightly decrease the slope of the fit line (1.87 for D95, 1.86 for D95*) and slightly increase the intercept and χ^2. In the case of Mulliken charges, however, the inclusion of d-functions has a discernible effect on the relative positions of the points and brings about some improvement to the correlation; χ^2 and the slope both decrease, but the intercept increases (Table 5-3). Overall, the Mulliken charge set gives best fit lines with slope and intercept closer to the ideal values of 1 and 0 (Table 5-3), but there is more scatter (larger χ^2). So, the Mulliken charge set does not correlate as well as the Natural charge set. These same natural charge values (calculated with d-polarization functions) predict the P(1s) ionization potential chemical shifts very well as illustrated in Figure 5-4. Comparable agreement is obtained by determining natural charges without d-functions. For the Mulliken charges only the set obtained with the D95* basis set gives comparably good predictions (Table 5-3).

5.5.4. ΔE_{SCF} method [99] for Photoelectron and Photoabsorption spectroscopy

The total energy E_{SCF} of each molecule was calculated with Gaussian 94 [94] (HF theory, experimental molecular geometry) for both the initial and final state as described in Section 3.2.2 of this thesis. To evaluate the involvement, if any, of the d-functions these calculations were done using both the D95 and D95* basis set.

The results of these calculations for the P(1s) photoionization process are listed in Table 5-6 and illustrated in Figure 5-8. The correlation results are summarized in Table 5-3. While the absolute P(1s) ionization energies are very different from the experimental values, being far too low, the shifts of these ionization energies relative to PH_3 are quite reasonable and correlate well to the experimental values (Table 5-3). The D95 basis set gives a steeper slope (1.47) than the D95* set (1.18) suggesting that the polarization functions are important in improving the energy spread of the system.

Table 5-6 also lists the calculation results for the P(1s)→1e* photoabsorption process. The correlation with the experimental data is shown in Figure 5-8 and summarized in Table 5-3. Again, the absolute values are far too low, but the predicted and experimental shifts correlate well (Table 5-3). The slope of this correlation is greater without d-functions (slope = 1.24) (Figure 5-8c) than with d-functions (slope = 1.09) (Figure 5-8d). The predicted transition energy shifts are of similar quality as those obtained for P(1s) photoionization. Again, the different slopes observed for the two basis sets arise from changes in the calculated chemical shifts. The d polarization functions increase the shifts of the chlorides (maximum +0.4 eV for $SPCl_3$ and $CH_3P(S)Cl_2$) and decrease the shifts for all other compounds. The net effect is an improvement in the correlation; the slope of the fit line is closer to 1. The use of d-polarization functions also decrease the amount of scatter in the data (lower χ^2 as seen in Table 5-3); hence, d-polarization functions are required for an accurate prediction of the energy spread of the system.

5.5.5. Excited states with Xα and *ab initio* methods

Direct calculations of the photoabsorption transition energies yield fairly accurate predictions of the absolute transition energies (Table 5-7 and Table 5-8). Calculation of the excited states with the Gaussian 94 [94] program package tends to predict larger P(1s)→1e* chemical shifts than observed experimentally Table 5-7. The excited electronic states were calculated using the single-excitation configuration interaction (CIS) method described by Foresman et al. [102], but because of a size restriction of the Davidson Matrix to 2000 diagonal elements, only the STO-3G and STO-3G* basis sets were employed and only three virtual orbitals were kept in the calculation; all others were frozen. Thus the analysis by this method is not full at this stage. The results of this limited analysis are shown in Figure 5-9. The method tends to overestimate chemical shift differences. This over-estimation decreases if d-polarization functions are employed (slope = 1.567 for STO-3G, slope = 1.454 for STO-3G*). However, the inclusion of d-polarization functions also increases the amount of scatter (greater χ^2). The theoretical chemical shifts obtained by the ΔE_{SCF} method (Section 5.5.4) compare favourably to the CIS method giving better agreement with experiment (Table 5-3). The poorer performance of the CIS method is at least partially explained by basis set effects. Future work should include a re-evaluation of the CIS chemical shifts using a larger basis set, for example D95*.

The transition state calculations done with the Xα method [103] (Figure 5-10a) give a good correlation (Table 5-3) for the most part with chemical shift differences being estimated correctly (slope = 0.925). However, there is a significant deviation from the main fit line, PH_3. The reason for this deviation of PH_3 is not clear but this discrepancy has the effect of shifting all predictions away from the unit slope and zero intercept line. Were this not so, the predictions deriving from Xα would be very impressive. Excluding PH_3 from the correlation results in a slope of 1.00 and a χ^2 of 2.17 for the main fit line. The simple hydride is the most obvious reference molecule for chemical shift analysis so the reason for the deviation should be explored. The chemical shifts for the P(1s) ionization potential calculated with the Xα method are of slightly poorer quality (Figure 5-10b).

There is a bit more scatter to the points (greater χ^2, Table 5-3). PH_3 still deviates from the main fit line, but not as significantly as for the P(1s)→1e* transition.

5.5.6. The role of d-orbitals

As already mentioned, the inclusion of d-polarization functions improves the correlation between the calculated and experimental chemical shift values. This arises from non-uniform changes in the calculated shifts. Although these changes are unique for each molecule, there are some general trends.

1. ΔE_{SCF} method: The chemical shift increases for the chlorides and decreases for all other compounds. The phosphorus atom in thiohalides has a more positive charge than that in the corresponding oxyhalide. The halide falls in between.
2. Excited state method: The chemical shift increases for most compounds; the exceptions are PF_3, $P(OCH_3)_3$ and $P(C_2H_5)_3$. As with the ΔE_{SCF} method these changes in chemical shift are not uniform. Greater increases are observed for chlorides than fluorides.

For both methods the inclusion of d-polarization functions in the basis set decrease the slope of the fit line between calculated and experimental values. Hence, the model gives a better description of reality with d-functions in the basis set.

5.6. Summary

Photoabsorption shifts of the P(1s) peak in phosphorus compounds reflect the chemical environment of the phosphorus atom in the compounds. The trends can be successfully analyzed in terms of simple electronegativity relations and simple transition-state potential calculations with appropriate assessment of the atomic charge profile. Natural charges give better agreement with experimental shifts suggesting that these natural charges are probably more appropriate for the realistic evaluation of atomic character than Mulliken charges. The Xα method [103] is quite successful at predicting the photoabsorption transition energy whereas the *ab initio* Gaussian 94 excited state methodology [102] does not fare as well. The newer calculation methods used herein provide good predictions of the P(1s) photoionization behaviour in these same compounds.

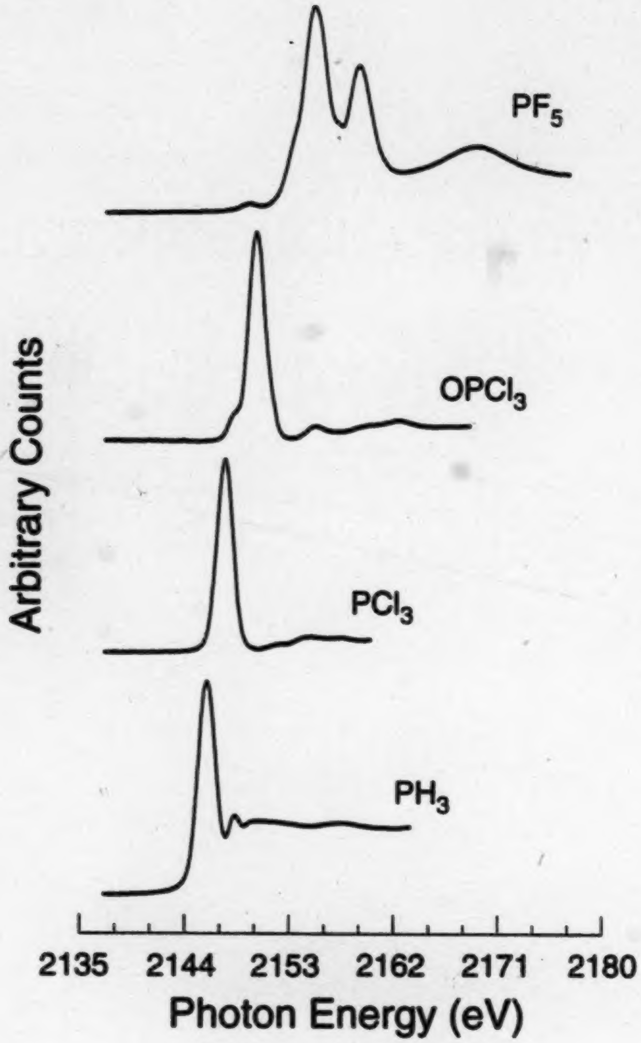

Figure 5-1: P(1s) Photoabsorption Spectra of PH_3 , PF_5, $OPCl_3$ and PCl_3.

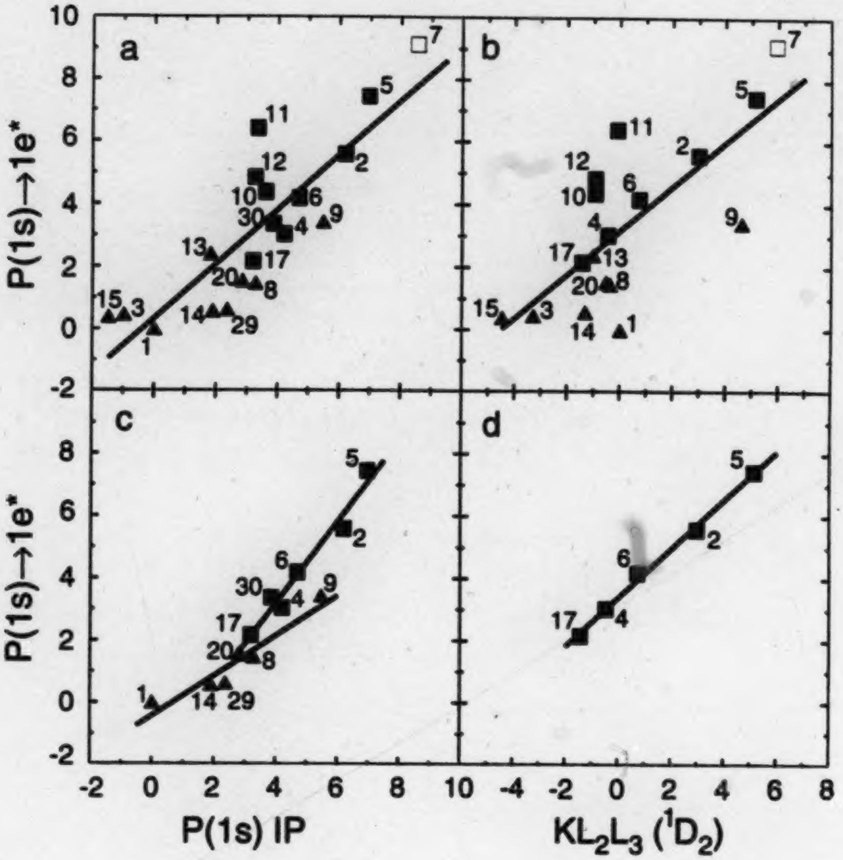

Figure 5-2: The correlation between the P(1s)→ 1e* transition energy shifts and the P(1s) ionization potential (IP) [88, 90] and KL_2L_3 ($^1D_2$) Auger shifts [88, 90] (eV) (relative to PH_3). Compound numbers are given in Table 5-8. In all cases, the numbering scheme corresponds to that used previously [88, 90].

The symbols are: ▲ = coordination No. 3, ■ = CN. 4 and ☐ = CN 5.

a: P(1s)→1e* *vs.* P(1s)IP   b: P(1s)→1e* *vs.* KL_2L_3($^1D_2$)

c: P(1s)→1e* *vs.* P(1s)IP   d: P(1s)→1e* *vs.* KL_2L_3($^1D_2$).

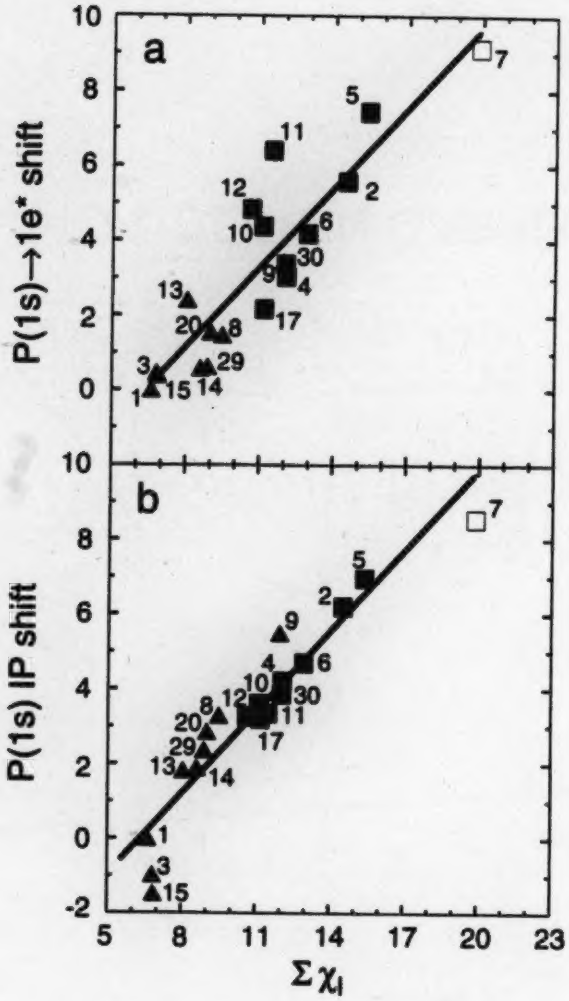

Figure 5-3: Correlation between the chemical shift (eV) and the sum of the ligand electronegativities, $\Sigma\chi_l$.

a: P(1s)→1e* *vs.* $\Sigma\chi_l$ b: P(1s)IP [88, 90] *vs.* $\Sigma\chi_l$.

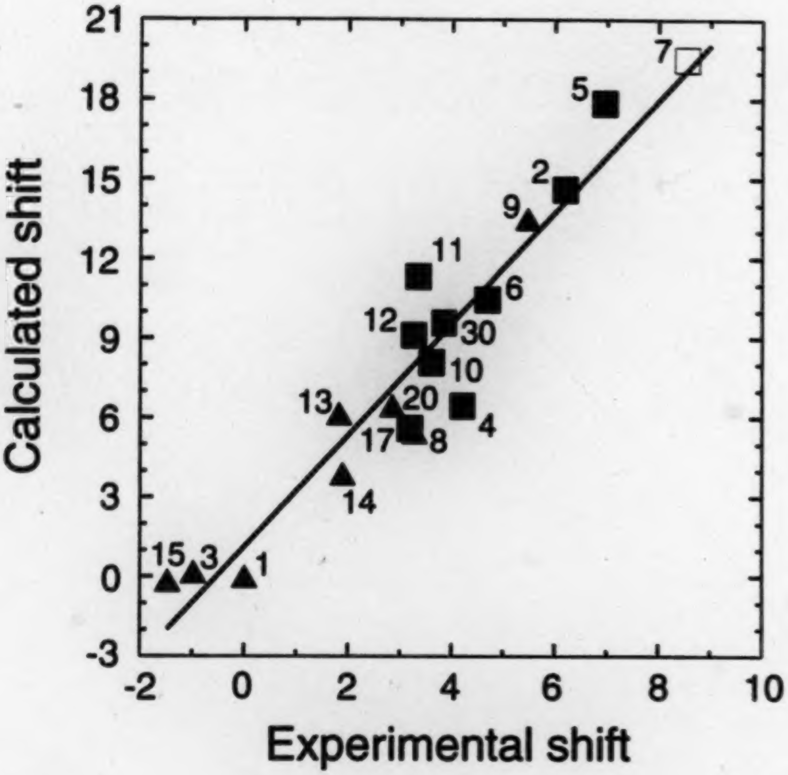

Figure 5-4: Correlation of the P(1s) Ionization Potential chemical shift [88, 90] (eV) with the Potential at the Nucleus shifts calculated from *ab initio* natural charges (Gaussian 94, D95* basis set).

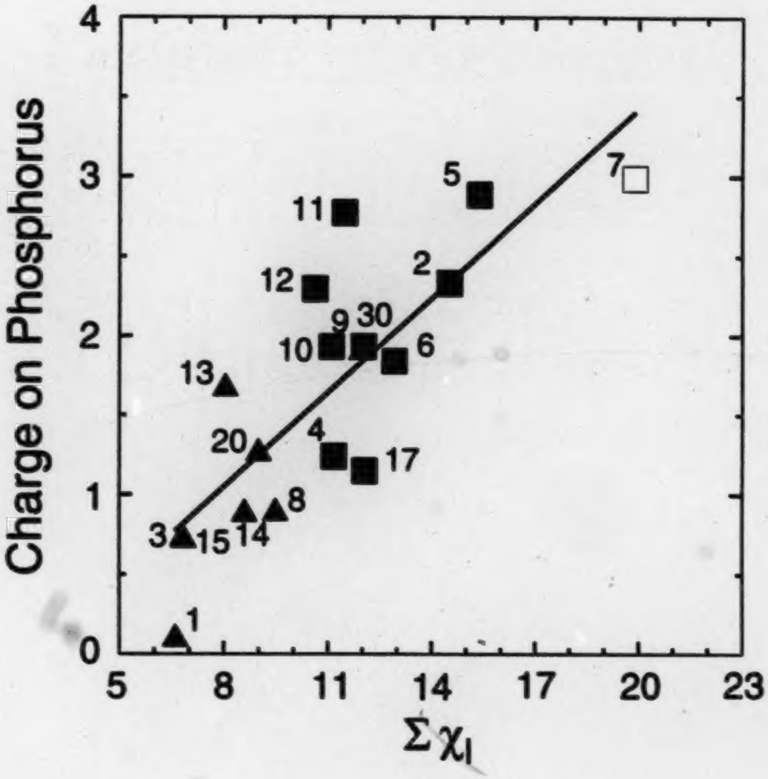

Figure 5-5: Correlation between the calculated charge on the phosphorus atom (Gaussian 94, D95* basis set) and $\Sigma\chi_I$.

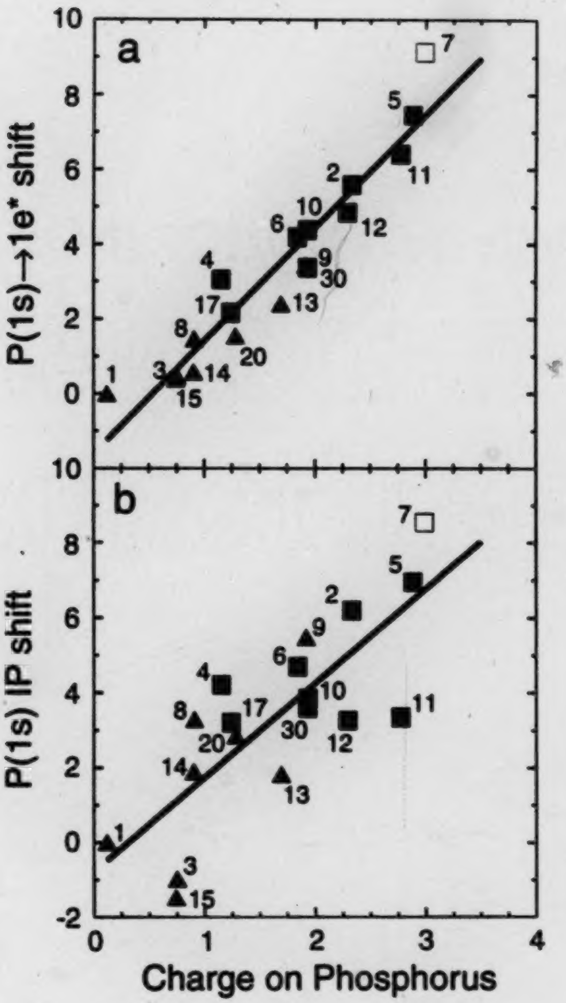

Figure 5-6: Correlation between the chemical shift (eV) and the calculated charge on the phosphorus atom (Gaussian 94, D95* basis set).

a: P(1s)→1e* *vs.* charge on P b: P(1s)IP [88, 90] *vs.* charge on P.

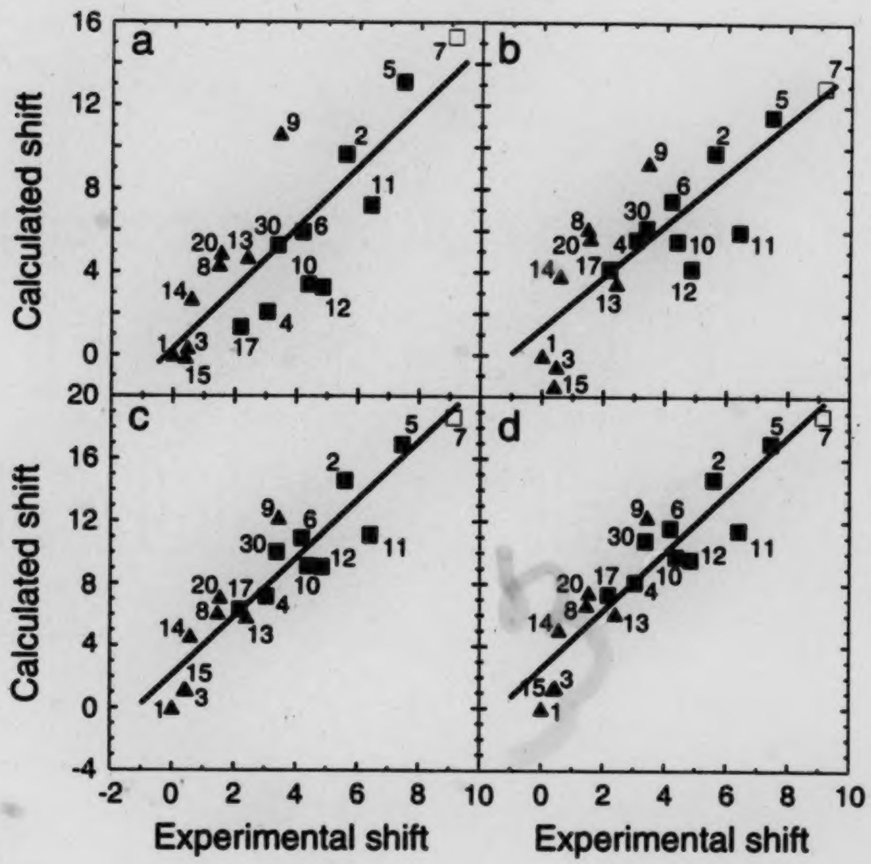

Figure 5-7: Correlation between the experimental P(1s)→ 1e* transition energy chemical shift (eV) and the Potential at the Nucleus shifts calculated from *ab initio* charges.

a: D95 basis set and Mulliken charges b: D95* basis set and Mulliken charges

c: D95 basis set and Natural charges d: D95 basis set and Natural charges.

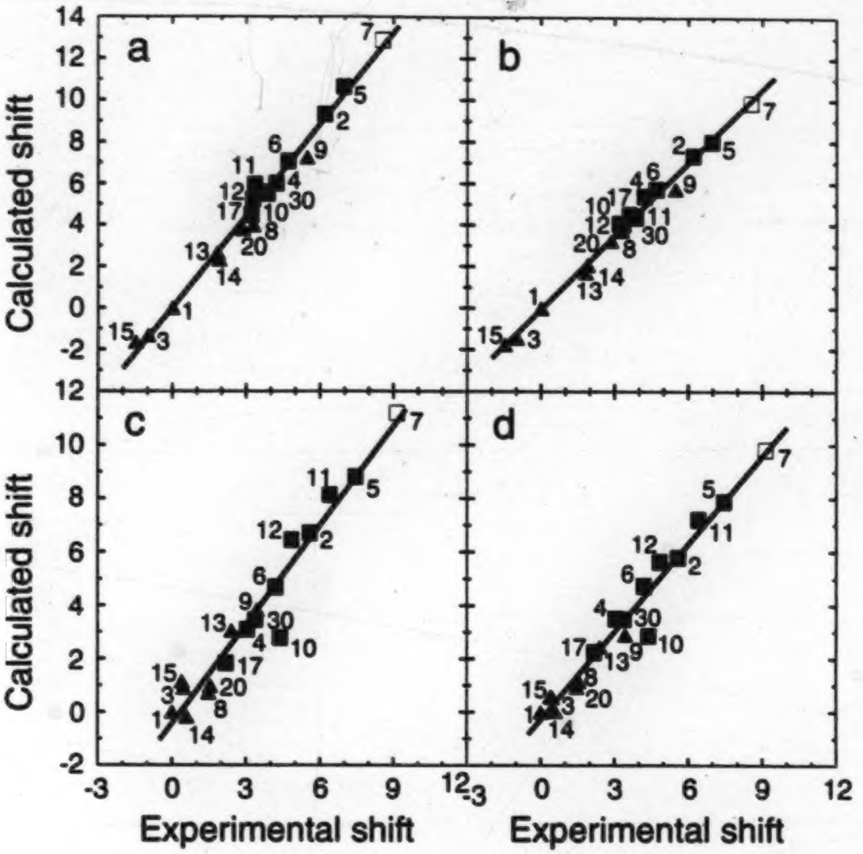

Figure 5-8: The correlation between the experimental chemical shifts and calculated values: ΔE_{SCF} method [99].

a: P(1s)IP [88, 90], D95 basis set b: P(1s)IP [88, 90], D95* basis set

c: P(1s)→1e*, D95 basis set d: P(1s)→1e*, D95* basis set.

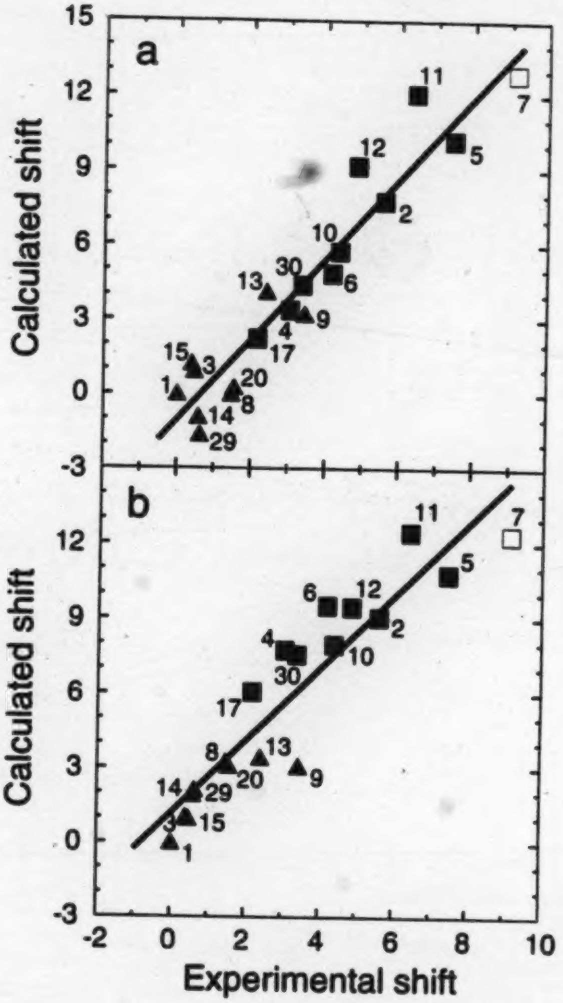

Figure 5-9: The correlation between the P(1s)→ 1e* experimental transition energy chemical shifts (eV) and the calculated values: CIS method [102].

a: STO-3G basis set b: STO-3G* basis set.

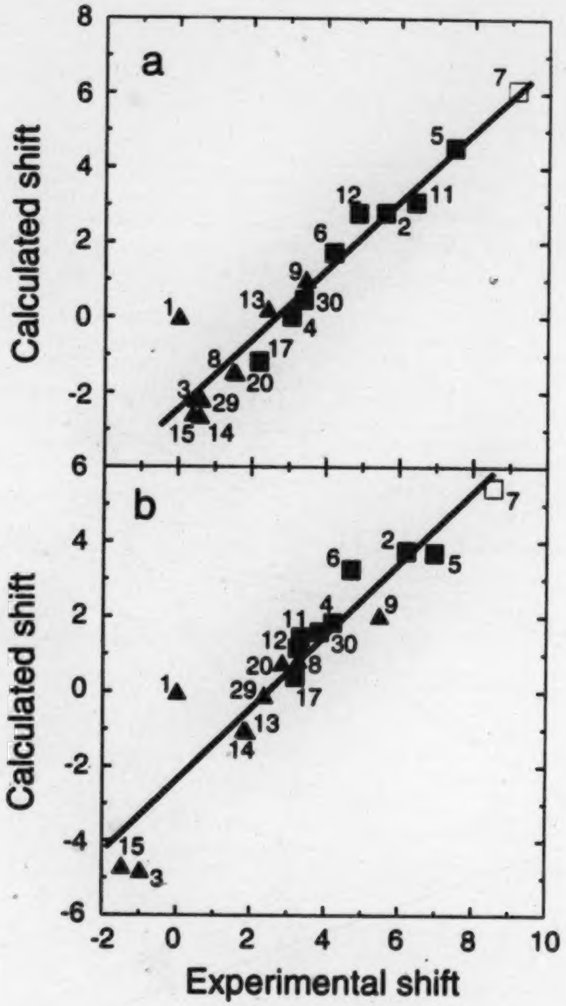

Figure 5-10: The correlation P(1s)→ 1e* experimental transition energy chemical shifts (eV) and calculated values: Xα method [103].

a: P(1s)→1e* b: P(1s)IP[88, 90].

Table 5-1: P(1s) and P(2p) ionization potentials (eV) of PBr_3 and $CH_3P(O)Cl_2$

Compound	$P(2p_{3/2})^{(a)}$	$P(2p_{1/2})^{(a)}$	$P(2p)^{(b)}$	$\Delta(P(1s))^{(c)}$	$P(1s)^{(d)}$
PBr_3	138.81	139.65	139.09	2.36	2153.20
$CH_3P(O)Cl_2$	140.13	140.97	140.41	3.85	2154.69

(a) [145], standard deviation: ±0.08 eV

(b) weighted average, standard deviation: ±0.16 eV

(c) $\Delta IP_{P(1s)} = 1.129\ \Delta IP_{P(2p)} + 0.396$, standard deviation: ±0.16 eV

(d) Reference compound: PH_3; standard deviation: ±0.26 eV

Table 5-2: Experimental P(1s)→1e* transition energies ($E_{1s\rightarrow 1e^*}$), the experimental transition energy shifts ($\Delta E_{1s\rightarrow 1e^*}$), and calculated chemical shifts: Potential at the Nucleus Method [92].

		$E_{1s\rightarrow 1e^*}$	$\Delta E_{1s\rightarrow 1e^*}$	Calculated $\Delta E_{1s\rightarrow 1e^*}$ (eV)			
No.	compound	(eV)	(eV)	(c)	(d)	(e)	(f)
1	$PH_3^{(g)}$	2145.84	0.0	0	0	0	0
2	SPF_3	2151.43	5.59	9.66	14.58	9.78	14.71
3	$P(CH_3)_3$	2146.30	0.46	0.35	1.16	-0.53	1.39
4	$SPCl_3$	2148.88	3.04	2.07	7.16	5.60	8.14
5	OPF_3	2153.29	7.45	13.12	16.92	11.52	17.04
6	$OPCl_3$	2150.03	4.19	5.94	10.92	7.48	11.61
7	PF_5	2154.98	9.14	15.30	18.65	12.94	18.82
8	PCl_3	2147.31	1.47	4.36	6.12	6.11	6.69
9	PF_3	2149.27	3.43	10.66	12.23	9.29	12.34
10	$(CH_3O)_2P(S)Cl$	2150.22	4.38	(h)	(h)	(h)	(h)
11	$OP(OCH_3)_3$	2152.25	6.41	7.23	11.13	5.97	11.46
12	$SP(OCH_3)_3$	2150.69	4.85	3.27	9.10	4.19	9.59
13	$P(OCH_3)_3$	2148.24	2.40	4.73	5.86	3.49	6.12
14	CH_3PCl_2	2146.42	0.58	2.71	4.62	3.84	5.08
15	$P(C_2H_5)_3$	2146.23	0.39	-0.12	1.17	-1.47	1.29
17	$CH_3P(S)Cl_2$	2148.01	2.17	1.34	6.33	4.17	7.34
20	CH_3OPCl_2	2147.38	1.54	4.92	7.13	5.68	7.49
29	PBr_3	2146.46	0.62	(i)	(i)	(i)	(i)
30	$CH_3P(O)Cl_2$	2149.21	3.37	5.30	10.03	6.14	10.80

(a) standard deviation: ±0.06 eV (b) standard deviation: ±0.12 eV

(c) D95 Mulliken Charges (d) D95 Natural Charges (e) D95* Mulliken Charges

(f) D95* Natural Charges (g) reference compound

(h) The C_1 symmetry of the molecule did not allow unambiguous identification of the 1e* component orbitals (i) the basis set is not defined for bromine.

Table 5-3: The line of best-fit parameters for the correlation between calculated and experimental chemical shifts

P(1s)→1e* transition				
Method		slope	intercept	χ^2
Potential at the Nucleus [92]				
D95, Mulliken[(a)]	(Figure 5-7a)	1.45	0.32	95.99
D95*, Mulliken[(a)]	(Figure 5-7b)	1.24	1.33	78.10
D95, Natural[(a)]	(Figure 5-7c)	1.87	2.12	56.62
D95*, Natural[(a)]	(Figure 5-7d)	1.86	2.57	59.22
ΔE_{SCF} [99]				
D95[(b)]	(Figure 5-8c)	1.24	-0.44	9.64
D95*[(b)]	(Figure 5-8d)	1.09	-0.27	4.80
CIS [102]				
STO-3G[(b)]	(Figure 5-9a)	1.62	-1.06	30.60
STO-3G*[(b)]	(Figure 5-9b)	1.45	1.18	39.98
$X\alpha$ [103]				
	(Figure 5-10a)	0.92	-2.43	9.05

Table 5-3, continued from the previous page.

P(1s) ionization potential				
Method		slope	intercept	χ^2
Potential at the Nucleus [92]				
D95, Mulliken(a)		1.72	-1.49	143.37
D95*, Mulliken(a)		1.66	-0.86	29.83
D95, Natural(a)		2.08	0.56	64.46
D95*, Natural(a)	(Figure 5-4)	2.10	1.13	51.03
ΔE_{SCF} [99]				
D95(b)	(Figure 5-8a)	1.47	0.03	3.83
D95*(b)	(Figure 5-8b)	1.18	-0.05	1.31
$X\alpha$ [103]				
	(Figure 5-10a)	0.96	-2.36	12.44

(a): basis set, and charge analysis method (b): basis set

Table 5-4: Atom and group electronegativities (Pauling Scale)

Atom	Electronegativity	Group	Electronegativity
P	2.19	CH_3	2.27(a)
H	2.20	CH_3CH_2	2.28(a)
C	2.55	OCH_3	2.68(a)
S	2.58		
Br	2.96		
N	3.04		
Cl	3.16		
O	3.44		
F	3.98		

(a) Calculated according to [150]

Table 5-5: Ligand electronegativities and charge (NPA method [151]) on the phosphorus nucleus.

No	Compound	$\Sigma\chi_I$	Natural Charge (q) on P	
			D95 basis set	D95* basis set
1	PH_3	6.60	0.07	0.12
2	SPF_3	14.52	2.27	2.33
3	PMe_3	6.81	0.72	0.75
4	$SPCl_3$	12.06	1.00	1.15
5	OPF_3	15.38	2.81	2.89
6	$OPCl_3$	12.92	1.71	1.84
7	PF_5	19.9	2.93	2.99
8	PCl_3	9.48	0.81	0.91
9	PF_3	11.94	1.87	1.92
10	$(CH_3O)_2P(S)Cl$	11.10	1.84	1.93
11	$OP(OCH_3)_3$	11.48	2.71	2.77
12	$SP(OCH_3)_3$	10.62	2.20	2.30
13	$P(OCH_3)_3$	8.04	1.63	1.69
14	CH_3PCl_2	8.59	0.84	0.90
15	$P(C_2H_5)_3$	6.84	0.71	0.74
17	$CH_3P(S)Cl_2$	11.17	1.10	1.24
20	CH_3OPCl_2	9.00	1.22	1.28
29	PBr_3	8.88	(a)	(a)
30	$CH_3P(O)Cl_2$	12.03	1.82	1.93

(a) the basis set is not defined for bromine

Table 5-6: Experimental and calculated P(1s)→1e* ($\Delta E_{1s\rightarrow1e^*}$) and P(1s) ionization potential (ΔE_{IP}) chemical shifts(eV): ΔE_{SCF} method [99].

No.	Compound	Experiment(a)		Calculation			
		$\Delta E_{1s\rightarrow1e^*}$	ΔE_{IP}	$\Delta E_{1s\rightarrow1e^*}$		ΔE_{IP}	
				(b)	(c)	(b)	(c)
1	PH_3(d)	0.0	0.00(e)	0.00	0.00	0.00	0.00
2	SPF_3	5.59	6.20(e)	6.70	5.80	9.31	7.35
3	$P(CH_3)_3$	0.46	-0.98(e)	0.90	0.55	-1.33	-1.45
4	$SPCl_3$	3.04	4.21(e)	3.09	3.50	6.00	5.40
5	OPF_3	7.45	6.96(e)	8.81	7.88	10.63	8.01
6	$OPCl_3$	4.19	4.70(e)	4.67	4.73	7.07	5.75
7	PF_5	9.14	8.55(e)	11.19	9.83	12.88	9.89
8	PCl_3	1.47	3.28(e)	0.72	0.94	3.97	3.71
9	PF_3	3.43	5.48(e)	3.81	2.89	7.25	5.75
10	$(CH_3O)_2P(S)Cl$	4.38	3.60(e)	(f)	(f)	5.57	4.50
11	$OP(OCH_3)_3$	6.41	3.34(e)	8.12	7.21	5.95	4.06
12	$SP(OCH_3)_3$	4.85	3.26(e)	6.44	5.64	5.25	3.95
13	$P(OCH_3)_3$	2.40	1.82(e)	3.04	2.44	2.64	1.72
14	CH_3PCl_2	0.58	1.89(e)	-0.19	0.03	2.32	2.08
15	$P(C_2H_5)_3$	0.39	-1.48(e)	1.13	0.58	-1.64	-1.76
17	$CH_3P(S)Cl_2$	2.17	3.19(e)	1.82	2.24	4.47	4.07
20	CH_3OPCl_2	1.54	2.85(g)	0.98	1.15	3.79	3.23
29	PBr_3	0.62	2.36(h)	(i)	(i)	(i)	(i)
30	$CH_3P(O)Cl_2$	3.37	3.85(h)	3.45	3.48	5.50	4.36

(a) standard deviation: ±0.12 eV for $\Delta E_{P(1s)\rightarrow1e^*}$ and ±0.10 eV for ΔE_{IP}

(b) D95 basis set (c) D95* basis set (d) reference compound

(e) from [88] (f) The C_1 symmetry of the molecule did not allow unambiguous identification of the 1e* component orbitals. (g) from [91]

(h) from Table 5-1 (i) the basis set is not defined for bromine.

Table 5-7: Calculated P(1s)→1e* transition energy ($E_{1s\rightarrow1e^*}$) and the corresponding chemical shift (eV): CIS method [102].

No.	Compound	STO-3G		STO-3G*	
		$E_{1s\rightarrow1e^*}$	$\Delta E_{1s\rightarrow1e^*}$	$E_{1s\rightarrow1e^*}$	$\Delta E_{1s\rightarrow1e^*}$
1	PH_3(a)	2145.10	0	2143.15	0
2	SPF_3	2152.85	7.75	2152.20	9.05
3	$P(CH_3)_3$	2146.03	0.93	2144.12	0.97
4	$SPCl_3$	2148.47	3.36	2150.87	7.72
5	OPF_3	2155.29	10.19	2153.92	10.78
6	$OPCl_3$	2149.93	4.82	2152.66	9.51
7	PF_5	2157.98	12.88	2155.50	12.35
8	PCl_3	2145.09	-0.02	2146.39	3.24
9	PF_3	2148.32	3.22	2146.23	3.08
10	$(CH_3O)_2P(S)Cl$	2150.81	5.71	2151.10	7.95
11	$OP(OCH_3)_3$	2157.15	12.05	2155.61	12.46
12	$SP(OCH_3)_3$	2154.25	9.15	2152.60	9.45
13	$P(OCH_3)_3$	2149.20	4.10	2146.58	3.43
14	CH_3PCl_2	2144.17	-0.93	2145.07	1.92
15	$P(C_2H_5)_3$	2146.31	1.21	2144.18	1.03
17	$CH_3P(S)Cl_2$	2147.31	2.21	2149.20	6.05
20	CH_3OPCl_2	2145.36	0.26	2146.24	3.09
29	PBr_3	2143.46	-1.64	2145.28	2.12
30	$CH_3P(O)Cl_2$	2149.47	4.36	2150.69	7.54

(a) reference compound

Table 5-8: Calculated P(1s) ionization potential (E_{IP}) and P(1s)→1e* transition energy ($E_{1s\rightarrow1e^*}$) and the corresponding chemical shifts (eV): Xα method [103].

No.	Compound(a)	E_{IP}	$E_{1s\rightarrow1e^*}$	ΔE_{IP}	$\Delta E_{1s\rightarrow1e^*}$
1	PH_3(b)	2157.69	2153.08	0.00	0.00
2	SPF_3	2161.45	2155.88	3.76	2.80
3	$P(CH_3)_3$	2152.89	2150.89	-4.80	-2.19
4	$SPCl_3$	2159.53	2153.10	1.84	0.02
5	OPF_3	2161.40	2157.62	3.72	4.54
6	$OPCl_3$	2160.95	2154.80	3.26	1.72
7	PF_5	2163.15	2159.18	5.46	6.10
8	PCl_3	2158.55	2151.63	0.86	-1.45
9	PF_3	2159.73	2154.09	2.20	1.01
11	$OP(OCH_3)_3$	2159.15	2156.16	1.46	3.08
12	$SP(OCH_3)_3$	2158.86	2155.86	1.17	2.78
13	$P(OCH_3)_3$	2156.68	2153.30	-1.01	0.22
14	CH_3PCl_2	2156.64	2150.44	-1.05	-2.64
15	$P(C_2H_5)_3$	2153.01	2150.51	-4.68	-2.57
17	$CH_3P(S)Cl_2$	2158.10	2151.89	0.41	-1.19
20	CH_3OPCl_2	2158.47	2151.60	0.78	-1.48
29	PBr_3	2157.60	2150.88	-0.09	-2.20
30	$CH_3P(O)Cl_2$	2159.28	2153.55	1.59	0.47

(a) $(CH_3O)_2P(S)Cl$ (No. 10) was not included because its low symmetry (C_1) did not allow proper calculation with the Xα code.

(b) reference compound

6. Chemical Shifts of Oxygen (1s) and Sulphur (2p) Core Binding Energies of Volatile Sulphur Compounds: A Synchrotron Photoelectron Study

6.1. Introduction

Chemical shift effects on the core level ionization potentials of phosphorus and sulphur have been studied previously [88-91]. The 1s and 2p binding energy shifts were recorded and compared to each other as well as to shifts in the KL_2L_3 ($^1D_2$) principal Auger line. Simple semi-empirical calculations were used to evaluate various charge and potential at the nucleus models which can be applied to evaluate the changes associated with chemical valence and structure.

The present study expands on this earlier work. As part of a study on the photoabsorption spectra of sulphuryl halides (Chapter 10) we had occasion to measure the oxygen 1s ionization potentials of many of these compounds plus a variety of related species, which are all characterized by a formally multiply bonded terminal oxygen, sulphur or nitrogen atom. We used this opportunity to explore the binding energy chemical shift of the peripheral oxygen or sulphur atom. This property had not been extensively evaluated, previously because it has been generally regarded as insensitive to the variations of substituents on the central atom.

Core level photoelectron and photoabsorption spectroscopy has been revolutionized in recent years by the availability of synchrotron radiation. In particular, core level photoelectron spectra can be measured with a resolution unattainable by most laboratory photon sources with the exception of the very expensive and elaborate monochromatized x-ray sources developed for specialized laboratory instruments. The synchrotron sources routinely allow clean separation of the spin-orbit splitting of the S(2p) levels. Vibrational structure has been observed and molecular field splitting features have been measured for some sulphur compounds [18, 104]. In this study we have measured both the O(1s) and the S(2p) ionization potentials for all compounds of interest using a synchrotron light source with a variety of monochromators, according to the energy requirements, and the best attainable resolution of our photoelectron spectrometer. Several of these molecules had not been studied previously. In addition we have applied alternate up-to-date *ab initio* calculations to the analysis of the ionization energy and chemical shifts.

The ionization potential shifts of the S($2p_{3/2}$) level of thionyl and sulphuryl halides were correlated to the 1s orbital ionization potential shifts for the terminal oxygen atom. This revealed a difference in relaxation effect introduced by the presence of the lone pair of electrons on sulphur in the thionyl compounds. To determine the role of these lone pair electrons, the S($2p_{3/2}$) chemical shifts of a variety of compounds, representing all three valencies of sulphur, were correlated to theoretical values obtained from ab initio calculations. Similarly, a series of oxygen compounds having a different central atom was investigated. With the exception of the thionyl species, this central atom was always in its maximum oxidation state.

6.2. Experimental

The photoelectron spectra were measured according to the procedure described earlier in Chapter 2. The O(1s) ionization potentials of SO_2, SO_2F_2, SO_2FCl and SO_2Cl_2 were measured using an excitation energy of 570.0 ± 0.3 eV. The photon energy for all other spectra was 900.0 ± 2.0 eV, with a 200 eV retardation potential applied to the gas cell. The monochromator exit slit width was set at 50 μm for the 570.0 eV photons. However, at higher photon energies a wider monochromator exit slit setting (150 μm) was required with concomitant reduction in resolution. Excitation energies of 190 ± 0.2 eV, 195 ± 0.2 eV, 200 ± 0.2 eV and 210 ± 0.2 eV were used to collect the S(2p) spectra.

On average, five spectra were collected for each compound in each energy region. The standard deviation of the experimental peak energies was ±0.10 eV or less, so the chemical shifts are precise within ±0.20 eV. The measured binding energies were calibrated against O(1s) ionization potential of CO_2 [152] and S($2p_{3/2}$) ionization potential of SO_2 [153]. All spectra were fitted with a combined Gaussian/Lorentzian curve. No relativistic corrections were made in the kinetic energy to binding energy conversion.

SF_5Cl and OSF_4 were obtained from Dr. J. Thrasher at the University of Alabama, OPF_3 from Dr. J. Nielson at the Los Alamos National Laboratory and SPF_3 from Dr. D.

Kennepohl at the University of Alberta. All other compounds were obtained commercially, the liquids from Aldrich, SO_2 and SF_6 from Matheson and the other gases from Ozark Mahoning. Liquid samples were degassed *via* a freeze-thaw procedure in vacuum at liquid nitrogen temperatures. Otherwise the compounds were used as received from the supplier without further purification.

6.3. Results

All measured O(1s) binding energies are referenced to the accepted value for the O(1s) ionization potential of CO_2 at 541.32 ± 0.05eV [152]. The measured S(2p) binding energies are referenced to the $S(2p_{3/2})$ ionization potential of SO_2 at 174.78 ± 0.03eV [153]. The resultant O(1s) and S(2p) ionization potentials are listed in Table 6-1 and Table 6-2, respectively and therein also compared to literature values where available. Agreement with those literature values is, in general, good.

The sulphur compounds studied can be divided into three groups, (Table 6-3) according to the oxidation state of the sulphur atom. All compounds containing oxygen have only sulphur-oxygen double bonds. They are, thus, thionyl or sulphuryl compounds, belonging to groups S-IV and S-VI, respectively.

Comparison of the O(1s) and $S(2p_{3/2})$ chemical shifts of these compounds suggests two separate correlations (Figure 6-1a), one for each group. This becomes even more apparent (Figure 6-1b) when the O(1s) data for $SOCl_2$, $(CH_3)_2SO$ and $(CH_3)_2SO_2$ [154] are added. Each group correlates separately with a slope of 0.51 in the case of the S-VI compounds, and a larger slope of 0.84 in the case of the S-IV group. These non-unity slopes reflect differences in chemical environment, shielding from the nucleus and differential relaxation between the two levels. It is clear, however, that both peripheral and central atoms reflect the overall chemical environment found in each compound with the central atom showing larger effects than the peripheral atoms, as would be expected.

6.4. Discussion

Changes in ligand character and number alter the chemical environment of the central sulphur atom leading to different $S(2p_{3/2})$ binding energies (herein expressed as shifts relative to the reference compound, SO_2). These changes also cause—although to a lesser degree—binding energy chemical shifts of the terminal oxygen 1s orbital. Its neighbours collectively determine the overall chemical environment of each atom in a molecule. The combination of the valence shell electron distribution about a typical atom and the field created by the surrounding nuclei creates a unique chemical environment for each atom, which is specific for a particular molecule. The binding energy of the core electrons of the atomic center samples this environment and hence the variations in binding energy are a source of chemical information. The central atom is of course the most strongly affected by the character of the surrounding atom set. The present results, however, illustrate that the binding energies of peripheral atoms also sample the total environment and should not be regarded as non-participants. Valence shell electron distributions within a molecule vary according to the collective action of the constituent atoms. More electronegative atoms attract electrons towards themselves and large electronegativity differences between neighbouring atoms in a molecule result in a polarized electron distribution described as ionic bond character. Small electronegativity differences yield a less polarized distribution within the molecule described as a more covalent type of bonding. In the latter case the atoms possess smaller effective charges. It is therefore possible to describe the environment of any particular atom by means of atomic charges, which in simple or classical models can be treated as point charges at the nuclear center. The molecular field is assembled from the on-atom (or local) charges and the off-atom (or remote) charges distributed according to the molecular geometry.

In the following discussion the various phenomena contributing to the chemical shift effects are investigated. In order to obtain a relatively complete picture of all aspects involved some literature data [89, 153, 154] was added to the measured set. Except for SPF_3 and SCl_2 the formal oxidation state of sulphur in the compounds we studied is either IV or VI. To provide a set of molecules representing all three possible oxidation states and all six possible coordination numbers of sulphur, the $S(2p_{3/2})$ ionization potential data set was augmented by seven molecules containing sulphur with oxidation state II (Table 6-3).

In all of the compounds studied the oxygen is a terminal atom and may be represented as a formally doubly bonded substituent. For comparison, we have included a number of similar M=O compounds of phosphorus, vanadium, chromium and carbon. These compounds can be divided into five groups according to the identity of the central atom. The sulphur compounds are further divided into thionyls (S-IV) and sulphuryls (S-VI), resulting in a total of six groups. These groups are listed in Table 6-4. With exception of the thionyl compounds (group S-IV), the central atom in all cases is in its maximum oxidation state and there are no lone pairs on the central atom.

All molecules investigated are listed in Table 6-5 along with their $S(2p_{3/2})$ and O(1s) ionization potentials and their corresponding chemical shifts relative to SO_2, a molecule which provides a convenient reference standard for both oxygen and sulphur. This allows for easy comparison of the O(1s) and $S(2p_{3/2})$ chemical shift behaviour, since both are referenced to the same standard. Table 6-5 also gives the numbering scheme employed in all figures and subsequent tables.

It is clear from the variation in the core ionization potentials in this system that the chemical environment affects the binding energies. The environment is defined by the core oxidation state of the element in question and this oxidation state may be represented by the charge on that atom. The potential field created by the surrounding atoms in the molecule also modulates the binding energy. Because of the localized nature of the chemical environment, replacement of second and third neighbours has less effect than replacement of a first neighbour. As a result, the chemical shifts for the $S(2p_{3/2})$ level are larger than their O(1s) counterparts. It is therefore important to analyze these variations for their chemical information content. The methodology available for such analyses varies from the simplest semiquantitative level, which is easily applied, to detailed and therefore more complex molecular orbital calculations for each system. The latter occasionally present technical difficulties due to inadequacies of the code and/or the computing platform available. The agreement between experiment and theory serves to evaluate the efficacy of the theoretical strategy.

6.4.1. Analysis based upon the Electronegativity of the Ligands

The overall chemical environment provided by the ligand groups around the central sulphur atom can be represented at the simplest level by summation of the electronegativities (Table 6-6) of the substituent groups ($\Sigma\chi_l$). For the S($2p_{3/2}$) ionization potential there is a general trend of increasing chemical shift as $\Sigma\chi_l$ on the sulphur increases. The overall correlation is reasonable but there is significant scatter in the points (Figure 6-2a) and occasional anomalous deviations hence the predictability of the relationship is wanting. If we separate subgroups of molecules with similar molecular structure there is an improved correlation, which indicates that the molecules with a lone pair on the sulphur contain contributions that are not properly evaluated by the electronegativity assessment. This also appears in the correlation of the O(1s) IP with $\Sigma\chi_l$ on sulphur (Figure 6-2b). Here, there are four distinct correlations based upon the coordination number of the sulphur atom: SO_2 (2), SOX_2 (3), SO_2XY (4) and OSF_4 (5). Addition of the literature values for compounds with sulphur coordination number one (CS_2, OCS, $SPCl_3$, $CH_3P(S)Cl_2$) and coordination number two (H_2S, CH_3SH, $(CH_3)_2S$) reveals a smooth correlation between the $S(2p)_{3/2}$ ionization potential and $\Sigma\chi_l$ on sulphur (Figure 6-2c) for each coordination number (dotted lines). The overall correlation (solid line) remains poor. As already discussed, the chemical environment is a local phenomenon. Thus, distance between the ionized atom and each ligand can be expected to influence the interaction between ionized atom and ligand. To account for this, the electronegativity of each ligand was divided by the interatomic distance r between the ligand and the central atom, and the resulting values were added. The overall correlation with the S($2p_{2/3}$) chemical shift (Figure 6-2d, solid line) improves. The correlation for groups of molecules with the same coordination number of the ionized atom remains (Figure 6-2d, dotted lines), however, suggesting a significant contribution to the chemical shift by lone pair electrons.

The electronegativity of the group (SO_nXY) attached to a terminal oxygen atom was calculated using the method of Huheey [150] and the values are listed in Table 6-7. They correlate nicely to the experimental O(1s) binding energy shifts (Figure 6-2e), although there is some scatter..

The inclusion of molecules with a central atom other than sulphur only increases the amount of scatter in the correlation. Especially species with a central carbon atom deviate significantly (Figure 6-2f). Again, this correlation is improved by scaling the group electronegativity with the oxygen—central atom bond distance (Figure 6-2g). In contrast, summing the scaled electronegativities of the individual atoms and CX_3 (X = H,F) groups in the molecule only leads to an uncorrelated scatter of points (Figure 6-2h). These results suggest that second, third, fourth, etc. neighbours influence the ionized atom only indirectly through the chemical bonds. That is, the third neighbour changes the chemical environment of the second neighbour, which causes a change in the chemical environment of the first neighbour. This, in turn, alters the chemical environment of the atom ionized, resulting in a shift in binding energy. Given this indirect action through the bonds, it is expected that changes in second and third neighbours will lead to smaller shifts than changes in first neighbours. This is borne out by the relative $S(2p_{3/2})$ and O(1s) chemical shifts of thionyl and sulphuryl compounds. Other contributions, however, operate, as illustrated by the series CH_3SO_2Cl, CH_3SO_2F, CF_3SO_2Cl, and SO_2Cl. Replacement of the methyl group in CH_3SO_2Cl by CF_3 to give CF_3SO_2Cl—a change in second (sulphur) or third (oxygen) neighbour—produces a greater shift in the $S(2p_{3/2})$ and O(1s) ionization potentials than the replacement of Cl by F to obtain CH_3SO_2F—where we have introduced a change in the first (sulphur) or second (oxygen) neighbour. This behaviour was also observed for the relative chemical shifts of the O(1s) binding energy in CF_3SO_2Cl and SO_2Cl_2, compared to CH_3SO_2Cl (Table 6-5).

6.4.2. Potential at the Nucleus

A simple and successful method applied previously for the calculation of the chemical shifts to part of this system[88-92] is the potential-at-the-nucleus method. The method is of course not an absolute approach, but does apply to the chemical shifts. The differences in potential between the atom in the molecule of interest and an appropriate reference can be equated to the chemical shift of the binding energy of the ionized atom [92]. Section 3.2.1 gives a detailed description of the potential-at-the-nucleus technique.

The charge and potential calculations can be carried out at various levels ranging from simple semiempirical (Hückel and/or CNDO) theories [88, 89] to more elaborate *ab initio* based theories. In the present study we employed Hartree-Fock and Density Functional methods of the Gaussian 94 [94] program package using the experimental bond lengths and angles [95-97] as input for the calculation of the charges q on the atoms in each molecule, as this level of calculation had not been previously applied. Since the resultant charges are highly dependent upon the calculation method employed, several different schemes were used, evaluated by the best fit to the experimental data. The different energy calculation methods were those established in the Gaussian-94 program package [94]: a semi-empirical CNDO method using the Hamiltonian of Segal and Pople [155], which is comparable to the calculation methodology used previously [88, 89, 92], and Hartree-Fock (HF) [79] and Density Functional Theory (DFT) [86], using a 6-311G* basis set. For the latter, the hybrid B3LYP method, a small variation of Becke's 3-parameter hybrid functional [156] was used, equation (6-1).

$$(1-0.20)\,E_x^{LSDA} + 0.20\,E_x^{HF} + 0.72\,\Delta E_x^{Becke} + 0.81\,E_c^{LYP} + (1-0.81)\,E_c^{VWN} \qquad (6\text{-}1)$$

This variation combines the Slater (E_x^{LSDA}) and the Hartree-Fock (E_x^{HF}) exchange with DFT exchange correlation. The exchange function is expressed by Becke's 3-parameter functional [87] with the gradient-corrected correlation functional (E_c^{LYP}) of Lee et al. [157] and the correlation functional (E_c^{VWN}) of Vosko et al. [158] providing non-local and local correlation, respectively. To properly evaluate the ability of the potential at the nucleus model to account for position and movement of valence electrons, the charges were obtained from both Mulliken analysis [138-141] and natural bond orbital analysis [151] in the HF and DFT calculations. Only the Mulliken population analysis was done in the case of the CNDO calculations.

The potentials obtained as well as the calculated O(1s) and S($2p_{3/2}$) chemical shifts relative to SO_2 are listed in Table 6-8 and Table 6-9, respectively. Correlations between these shifts are shown in Figure 6-3 and Figure 6-4. They were evaluated as described in the previous Chapter. A summary of the fit parameters is given in Table 6-10. Only potentials obtained with the transition state or RPM model are presented here, as it has been established that these are most appropriate [88, 89, 92].

As expected, the different calculation methods of the atomic charges result in distinct sets of calculated binding energy shifts. There is fairly good correlation between each set of calculation results and the experimental data (Figure 6-3, Figure 6-4 and Table 6-10). However, some scatter exists. For both binding energies, the best correlation to the experimental results—i.e. the least amount of scatter, or the smallest χ^2 (Table 6-10)—is obtained for the HF Mulliken charges. All four sets of calculated values, however, overestimate the chemical shifts as evidenced by the greater than unity slopes. The least error (slope closest to 1, Table 6-10) in that aspect occurs for the CNDO charges. The calculations perform better for the $S(2p_{3/2})$ level than for the O(1s) level; the slopes of the fit lines are lower for the former (Table 6-10).

Examination of the $S(2p_{3/2})$ chemical shifts reveals several trends. In general a higher sulphur oxidation state corresponds to a more positive chemical shift, both calculated and experimental (Figure 6-3 and Table 6-9). As expected from earlier evaluations [89], there exists an overall linear correlation within all three groups. No trends in the chemical shift are apparent for the six groups of oxygen compounds, other than that the thionyls are consistently below the fit line (Figure 6-4 and Table 6-8). The slopes greater than unity in both correlations represent systematic shortfalls of the potential at the nucleus model. These deficiencies include an inadequate way of dealing with shielding from the nucleus, and the use of point charges to represent the other atoms in the molecule.

6.4.3. Absolute Ionization Potentials

6.4.3.1. The ΔE_{SCF} Method

An absolute method for estimation of the binding energies and therefore chemical shifts of binding energies involves the calculation of the difference in total energy between the initial and final states of the molecule [99] as described in detail in Section 3.2.2 of the thesis. This energy difference (ΔE_{SCF}) between the initial and final states represents the transition energy and the chemical shift is given by the change in ΔE_{SCF} with respect to a reference molecule—SO_2 in this study. As with the potential at the nucleus method the calculations were done using three different energy calculation methods: semiempirical CNDO, Hartree-Fock, and density functional theory (B3LYP). The chemical shifts thus obtained are listed in Table 6-11 and Table 6-12, and the correlation to the experimental data is shown in Figure 6-5 and Figure 6-6.

As was found in an analysis of P(1s) absorption edges [159] (Chapter 5) the ΔE_{SCF} method does not accurately predict the absolute values of the ionization potentials. The CNDO method underestimates the values—for O(1s) by as much as 55%—and the other two methods overestimate. Here, not unexpectedly, the greater error occurs for S($2p_{3/2}$), where the value is overestimated by a factor of 9.5. This failure in calculating the absolute values of the ionization potentials accurately is caused by the use of the equivalent core model to simulate the final state, however, in general, the ΔE_{SCF} model represents the chemical shifts quite nicely. The degree of correlation is highly dependent upon the calculation method used. The semi-empirical CNDO method gives the poorest results—especially for S($2p_{3/2}$)—and the B3LYP method gives the best agreement to experiment with the least amount of scatter (Table 6-10). For the O(1s) data the slope of the B3LYP correlation is 1.00. In general, the slopes for the O(1s) data are closer to 1 than those for the corresponding S($2p_{3/2}$) correlation. This is not surprising, since the equivalent core model used neglects shielding effects by lower lying core orbitals and so it works best for the K shell. Sodhi and Cavell [89] correlated the S(2p) and S(1s) chemical shifts, obtaining an S(1s) vs. S(2p) slope of 1.157 which agrees reasonably well with the present ΔE_{SCF} correlation for S($2p_{3/2}$) using B3LYP (slope = 1.25). The difference in shielding effects between the S-1s and S(2p) orbitals can be expressed by the core-valence-electron interaction integrals (F^0) [88, 89] from the tables compiled by Mann [160]. The ratio of these integrals agrees reasonably well with the slope of the S(1s) *versus* S(2p) binding energy chemical shift correlation [89]. Hence, the differences in shielding between the S(1s) and S(2p) orbitals can be incorporated by multiplying the calculated chemical shifts by the average core-valence-electron interaction integral ratio:

$$\frac{F^0(2p,val)(S) + F^0(2p,val)(Cl)}{F^0(1s,val)(S) + F^0(1s,val)(Cl)} = 0.931 \qquad (6\text{-}2)$$

where $F^0(n,val)(Z) = \frac{1}{4}[F^0(n,3s)(Z) + 3\times F^0(n,3p)(Z)]$. In this work we applied this correction only to the B3LYP data. The resulting calculated chemical shift values are listed in Table 6-11 and the correlation to the experimental data is shown in Figure 6-6d. As expected, inclusion of these shielding effects reduces the slope of the fit line and χ^2 (Table 6-10), thus improving the correlation and the agreement to experiment. The slope, however, is still greater than 1 suggesting some additional relaxation effects operate, which are not accounted for by the ΔE_{SCF} method.

Although the O(1s) data gives better agreement between calculation and experiment, there is also an increased scatter of points (Table 6-10) compared to $S(2p_{3/2})$. In particular, CrO_2Cl_2 deviates significantly for both HF and B3LYP (Table 6-12). This is likely caused by basis set effects.

These results also clearly show that the ΔE_{SCF} model using density functional theory (B3LYP) provides significant improvement in correlation with the experimental data over the potential at the nucleus model.

6.4.3.2. The Xα Method

Our recent success with the Xα method [103] for prediction of chemical shifts [159] (Chapter 5) prompted the use of this method for the present investigation. The Xα method possesses the advantage of allowing direct calculation of the ionization potential by means of the transition state method, removing one-half an electron from the orbital in question (Section 3.5). Unlike Gaussian 94 [94], the Xα program [146] does not reshuffle all occupancies to obtain the lowest energy stable state—the state with the hole in the HOMO. The core level vacancy is allowed to remain.

The experimental molecular geometries [95-97] were used for the calculations. The atomic alpha parameters were the α_{HF} values determined by Schwarz [109] which are incorporated into the computer code [146]. All sphere radii were determined by the program, according to the Norman procedure [112]. To calculate the ionization potentials the transition state method was employed: one-half of an electron was removed from the relevant core orbital. Since the Xα method does not take spin orbit coupling into consideration, the calculated S(2p) ionization potential was assumed to be a weighted average of the two spin-orbit partners. Further, a spin-orbit split energy of 1.20 eV was assumed to determine the calculated $S(2p_{3/2})$ and $S(2p_{1/2})$ binding energies listed in Table 6-13. The correlation of the chemical shifts calculated by Xα with experimental values is shown in Figure 6-7. The $S(2p_{3/2})$ chemical shifts correlate nicely for the most part. The notable exceptions are H_2S and S_2Cl_2. The cause for the deviation of H_2S is at present not understood. However, a similar effect has been observed for the P(1s) ionization potential shift of PH_3 [159] (Chapter 5). Hence, this discrepancy could be caused by an incorrect estimation of the size of the hydrogen atom (Section 12.1.2). The deviation of the value for S_2Cl_2 is caused by symmetry effects and will be discussed below and in Section 12.1.1.

In contrast, the calculated O(1s) ionization energy values do not correlate at all. This can be explained by symmetry effects. Many of the compounds studied have two equivalent oxygen atoms. Upon core ionization of a terminal oxygen atom the overall molecular symmetry is reduced, since the two oxygen atoms are no longer equivalent. In the calculation, however, the Xα program [146] retains the original molecular symmetry of these species. Hence, any relaxation effects caused by symmetry reduction are ignored. It is possible to include these effects by performing the calculations in the reduced symmetry of the ion with an oxygen core hole. This approach was successful for the O(1s) binding energies of the sulphuryl halides and SO_2 as shown in Table 6-14. Unfortunately, the method cannot be applied to all compounds studied, since many have C_s symmetry. Upon O(1s) photoionization the symmetry reduces to C_1, which our version of the Xα program [146] cannot handle. The values calculated for the molecules in Table 6-14 using the ion state C_s symmetry are of similar magnitude as those obtained for molecules whose symmetry does not change upon O(1s) ionization. The correlation with experimental data improves (Figure 6-7c). However, the chemical shifts of the chlorides are consistently over-estimated, a phenomenon which, at present, is not understood.

Table 6-14 further illustrates the accuracy of the absolute values for the O(1s) ionization potential obtained with Xα. The ground state molecular symmetry (C_{2v}) under-estimates the O(1s) binding energy by approximately 8 eV and the oxygen core hole symmetry (C_s) over-estimates by about the same amount. Averaging these values results in an ionization potential corresponding nicely to experiment. This suggests that a molecular symmetry transition state model gives the best description for the O(1s) ionization of the sulphuryl halides.

With the exception of S_2Cl_2 this symmetry problem does not arise for the $S(2p_{3/2})$ binding energy because the central atom is ionized and, hence, the overall molecular symmetry is not altered. S_2Cl_2, however, has two equivalent sulphur atoms. An $S(2p_{3/2})$ photoionization event introduces a symmetry reduction from C_2 to C_1 and the above mentioned symmetry effects operate. An attempt to perform the calculation under the ground state C_2 symmetry did not provide a result, which correlated with the other data.

6.4.3.3. The Application of Koopmans' Theorem

The binding energy of an electron in a molecular orbital *i* can be equated to the negative of the energy of that orbital—Koopmans' theorem [8, 101]—as was common in the early days of photoelectron spectroscopy. These orbital energies can be readily calculated with Gaussian 94 [94]. As expected, the values obtained are dependent upon the calculation method employed: the HF method overestimates and the B3LYP method underestimates the absolute value (Table 6-15 and Table 6-16). The latter is surprising. The use of the Koopmans' ionization energy does not consider any relaxation effects; hence, it often overestimates the absolute value of the ionization potentials. At present, the reason for the unpredicted B3LYP values is not known. It might be caused by an underestimation of the difference in the correlation energy between the initial and final states of the species ionized.

Koopmans' value predicts the $S(2p_{3/2})$ chemical shifts nicely (Figure 6-8 and Table 6-10). It does not, however, perform well for the O(1s) chemical shift. Inclusion of an adiabatic relaxation contribution through the use of the transition state method (equivalent core model) improves the correlation for both ionization potential shifts, especially for O(1s) (Figure 6-9 and Table 6-10). The notable exception from the O(1s) correlation is again CrO_2Cl_2. This might again be caused by basis set effects; *vide supra*. For both edges the B3LYP calculation gives a better prediction of the chemical shifts than HF; the slope of the fit line is closer to 1, the intercept closer to 0 and χ^2 is also smaller (Table 6-10).

Although the correlation improves for the S($2p_{3/2}$) ionization potential shift—there is less scatter of points—the slope of the fit line increases (Table 6-10). The transition state method is overestimating the S($2p_{3/2}$) chemical shift differences which, as before, can be attributed to the use of the equivalent core model. The slope of the fit line for the B3LYP calculation (1.08) is close to value of the inverse of the interaction integral ratio from equation 6-2 (1.074). Inclusion of core shielding effects (Figure 6-9e) as described earlier (Section 3.2.2), significantly improves the correlation (Table 6-10). The slope of the fit line decreases to 1.01, the intercept becomes 0.04 and χ^2 decreases as well.

6.5. Summary

The investigation of the S($2p_{3/2}$) and O(1s) ionization potential shifts of a group of thionyl and sulphuryl compounds revealed comparable behaviour in response to changes in the chemical environment, regardless if the central sulphur or the terminal oxygen atom was ionized. There were, however, significant differences in relaxation following photoionization between the two groups of molecules—thionyls and sulphuryls. The origin of these differences in relaxation effect can be attributed to the lone pair of electrons in the thionyls.

The experimental data were correlated to calculated values obtained by several methods. The simple potential-at-the-nucleus model gave reasonable results; however, due to systematic errors, the chemical shifts were consistently overestimated. The more advanced theoretical methods used improved both correlation (i.e. less scatter of points, a lower χ^2) and agreement with experiment (i.e. the fit line has a slope closer to 1 and an intercept closer to 0). Of these, the shifts predicted by Koopmans' value in the transition state mode give the best agreement with the experimental results. In contrast, the Xα method only performs well for the central sulphur atom. With few exceptions all theoretical models investigated perform better for the S($2p_{3/2}$) orbital than the O(1s) orbital.

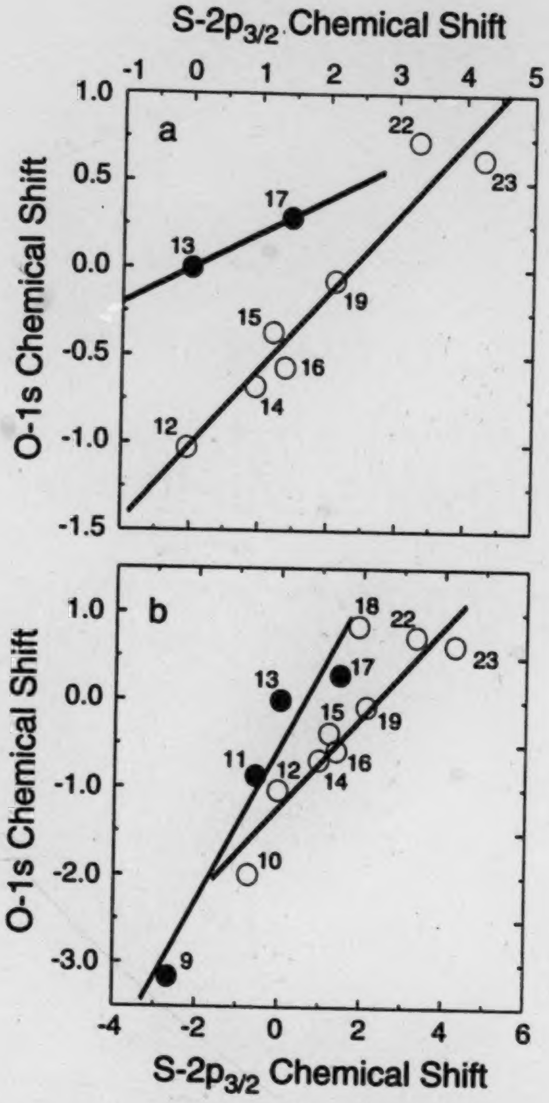

Figure 6-1: Experimental chemical shifts (eV), O(1s) *versus* S(2p$_{3/2}$). Sulphur IV compounds are represented by ●, and sulphur VI compounds by ○. The numbering scheme for molecule identification employed here and in all subsequent figures is given in Table 6-5

a) only data from this work b) includes $(CH_3)_2SO$, $(CH_3)_2SO_2$, $SOCl_2$, and SO_3.

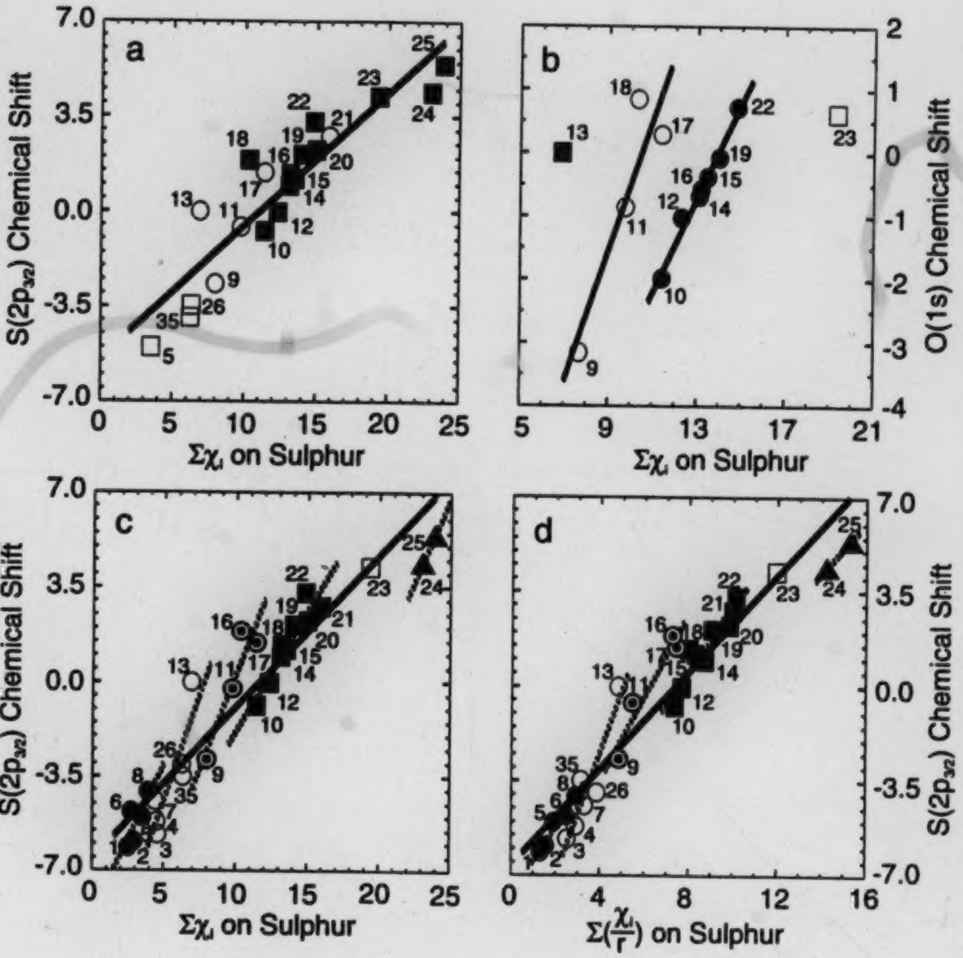

Figure 6-2: Experimental chemical shifts (eV) *versus* ligand electronegativity

a) S(2p$_{3/2}$) *vs.* $\Sigma\chi 1$ on Sulphur b) O(1s) *vs.* $\Sigma\chi 1$ on Sulphur

c) S(2p$_{3/2}$) *vs.* $\Sigma\chi_l$ on Sulphur d) S(2p$_{3/2}$) *vs.* $\Sigma\frac{\chi l}{r}$ on Sulphur.

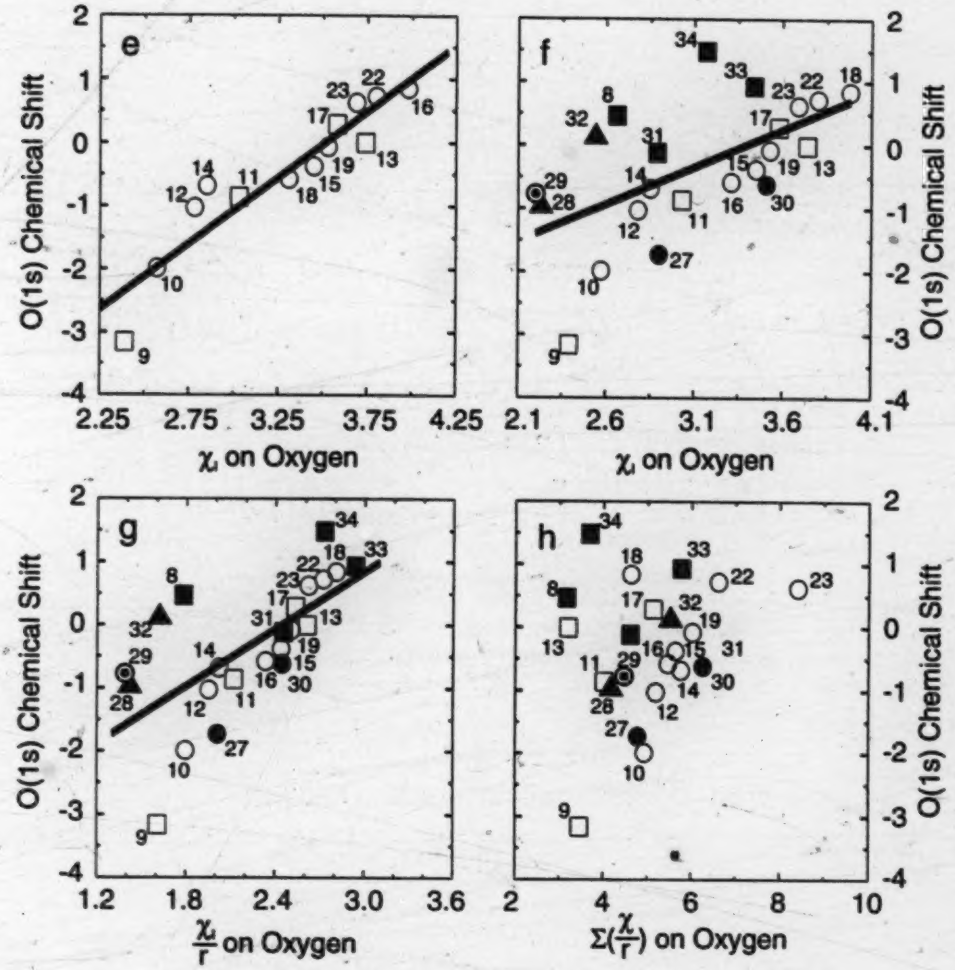

Figure 6-2, continued from the previous page

e) O(1s) vs. χ_l on Oxygen f) O(1s) vs. χ_l on Oxygen

g) O(1s) vs. $\frac{\chi l}{r}$ on Oxygen h) O(1s) vs. $\Sigma\frac{\chi}{r}$ on Oxygen.

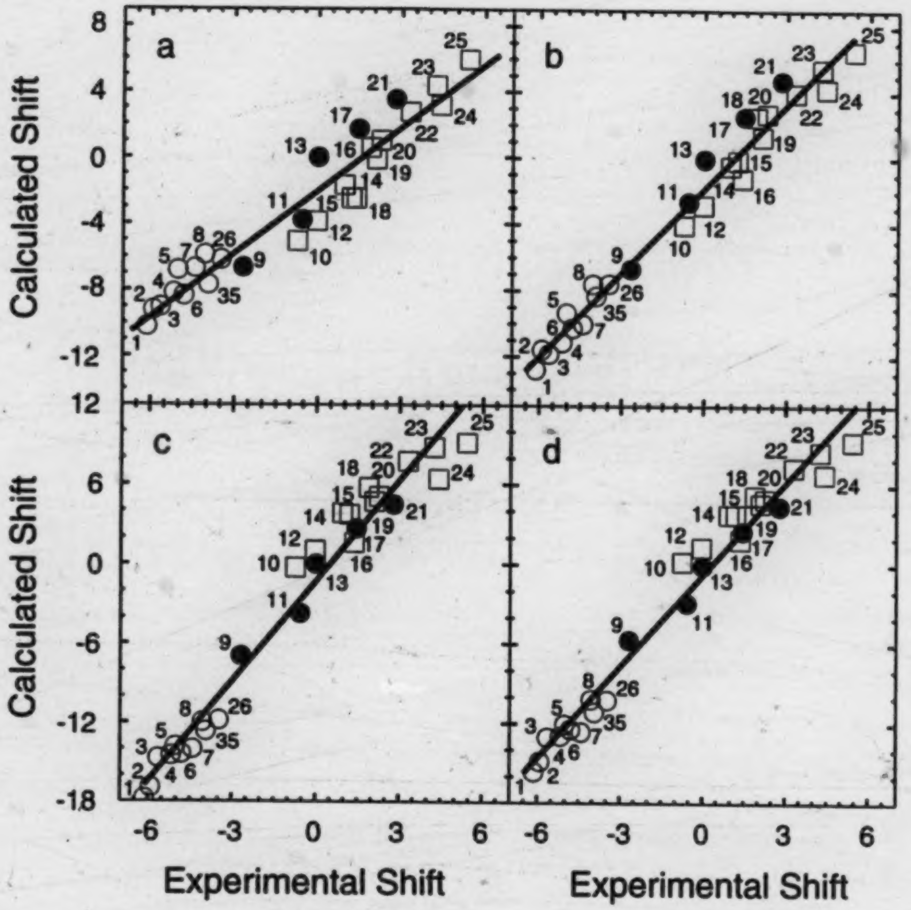

Figure 6-3: $S(2p_{3/2})$ chemical shifts (eV), calculated *versus* experimental: Potential at the Nucleus model [92]. The symbols differentiate between the three different oxidation states of sulphur: sulphur II—○, sulphur IV—●, and sulphur VI—□.

a) CNDO Mulliken Charges

b) HF Mulliken Charges

c) HF Natural Charges

d) B3LYP Natural Charges.

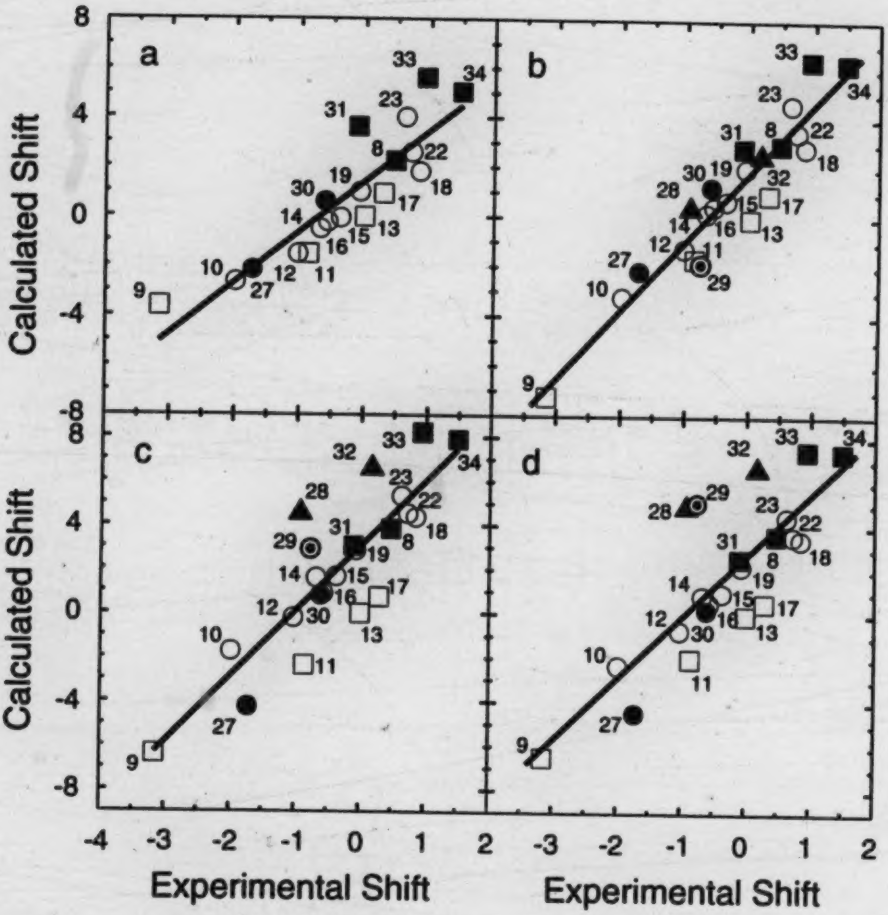

Figure 6-4: O(1s) chemical shifts (eV), calculated *versus* experimental: Potential at the nucleus model [92]. The six groups of oxygen compounds given in Table 6-4 are represented as follows: C-IV by ■, Cr-VI by ⊙, P-V by ●, S-IV by □, S-VI by ○, and V-V by ▲.

a) CNDO Mulliken charges
b) HF Mulliken charges
c) HF Natural Charges
d) B3LYP Natural Charges.

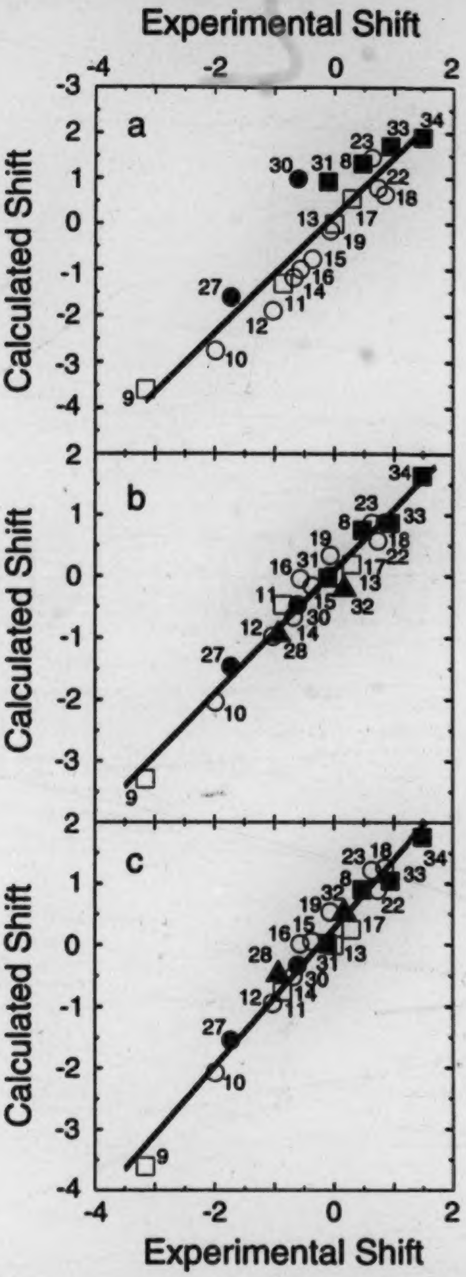

Figure 6-5: O(1s) chemical shifts (eV), calculated *versus* experimental: ΔE_{SCF} model [99]. The six groups of oxygen compounds given in Table 6-4 are represented as follows: C-IV by ■, Cr-VI by ⊙, P-V by ●, S-IV by □, S-VI by ○, and V-V by ▲.

a) CNDO; b) B3LYP; c) HF.

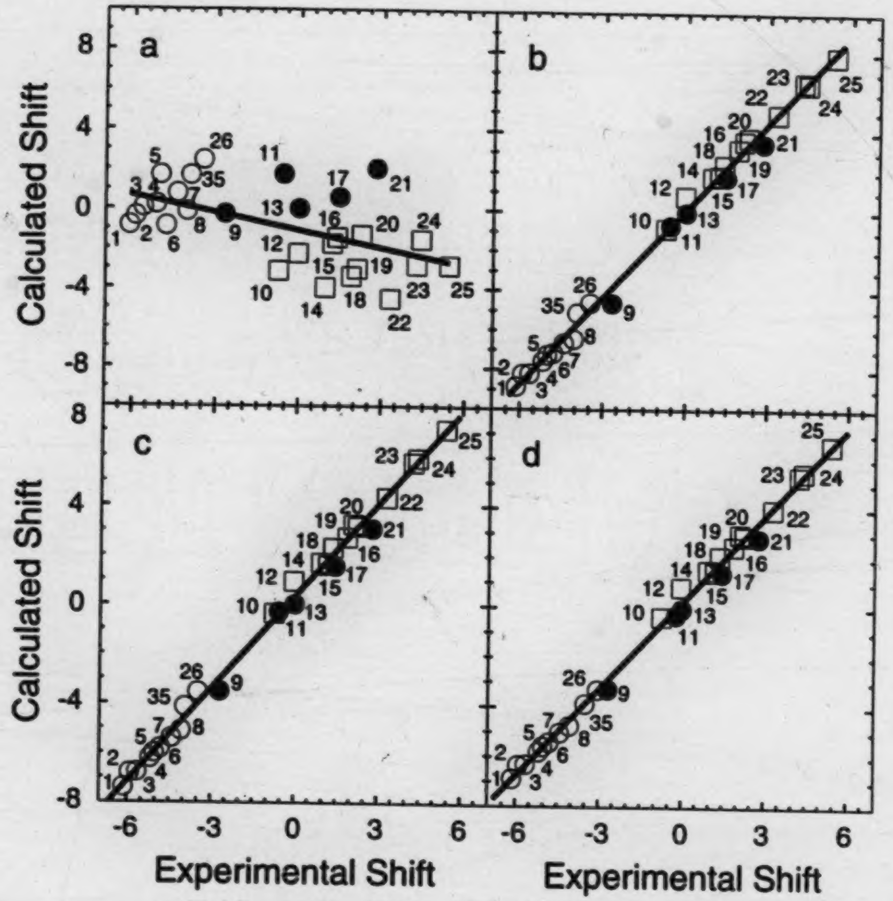

Figure 6-6: S(2p$_{3/2}$) chemical shifts (eV), calculated *versus* experimental: ΔE_{SCF} model [99]. The symbols differentiate between the three different oxidation states of sulphur: sulphur II—○, sulphur IV—●, and sulphur VI—□.

a) CNDO; b) HF; c) B3LYP; d) B3LYP with core shielding.

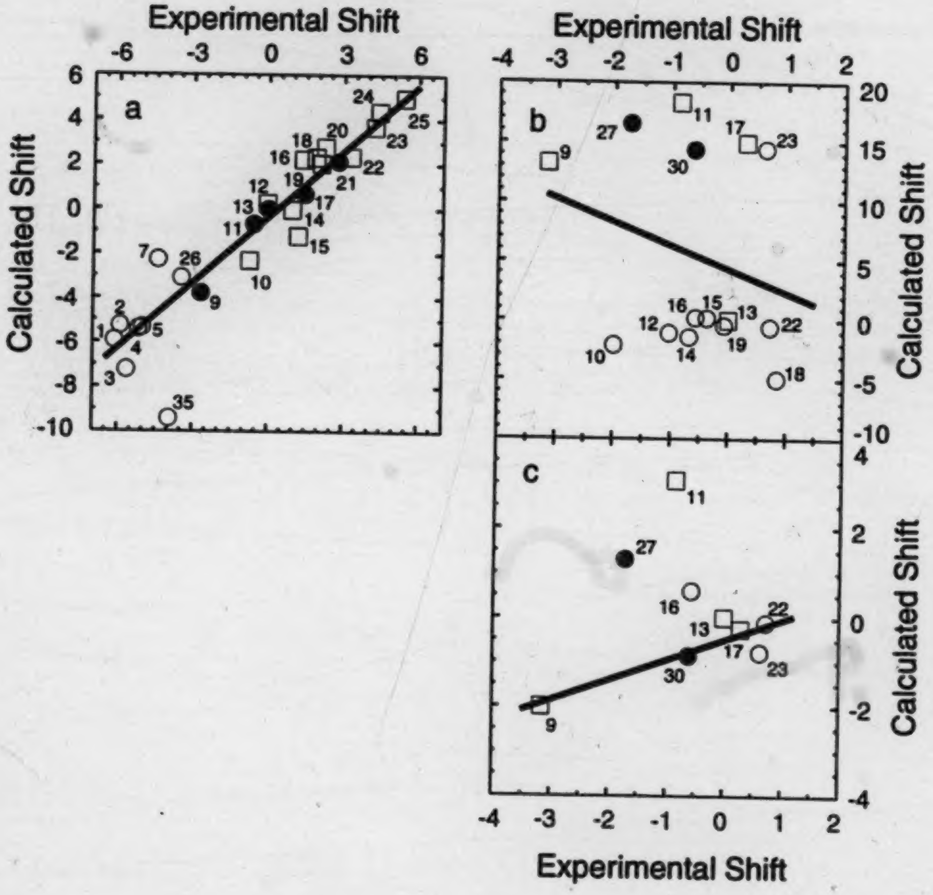

Figure 6-7: Chemical shifts (eV), calculated *versus* experimental: Xα method [103]. The symbols represent the different groups of molecules as defined in Table 6-3 and Table 6-4. $S(2p_{3/2})$: S-II ○, S-IV ●, S-VI □; O(1s): P-V ●, S-IV □, S-VI ○

a) $S(2p_{3/2})$ shift; b) O(1s) shift, ground state symmetry; c) O(1s) shift, ion state symmetry.

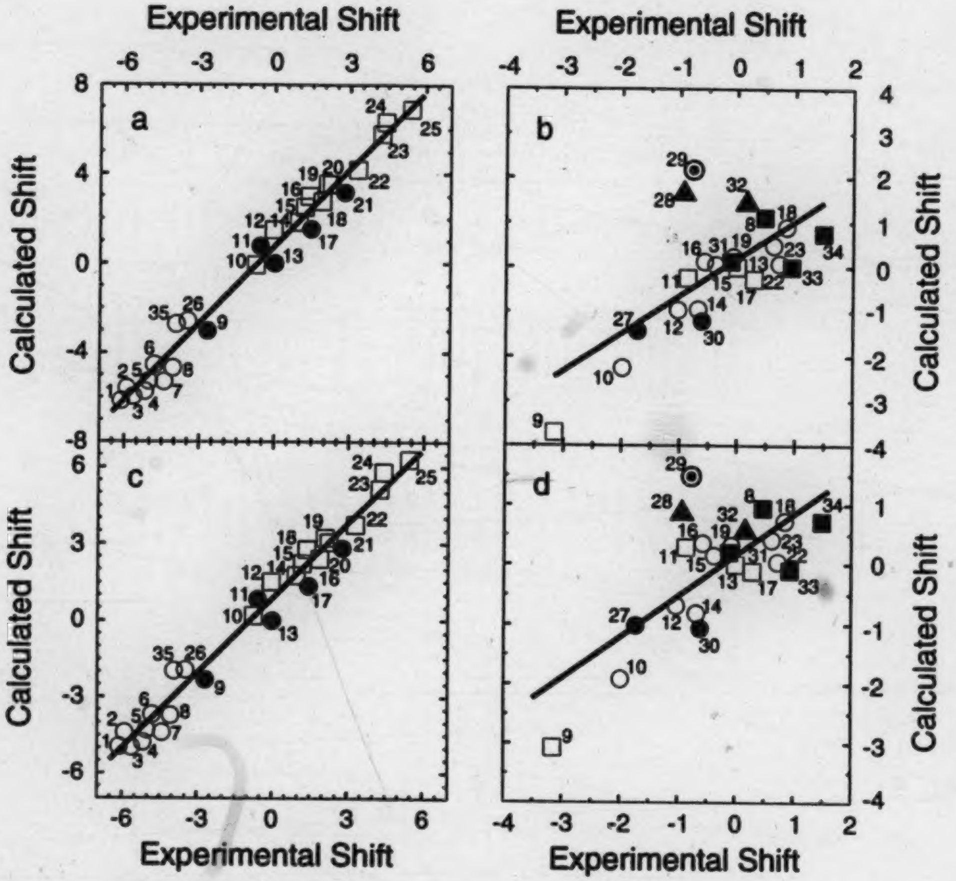

Figure 6-8: Chemical shift (eV), calculated *versus* experimental: Koopmans' value [8], ground state model. The symbols represent the different groups of molecules as defined in Table 6-3 and Table 6-4. S($2p_{3/2}$): S-II ○, S-IV ●, S-VI □

O(1s): C-IV ■, Cr-VI ⊙, P-V ●, S-IV □, S-VI ○, V-V ▲

a) S($2p_{3/2}$), HF; b) O(1s), HF; c) S($2p_{3/2}$), B3LYP; d) O(1s), B3LYP.

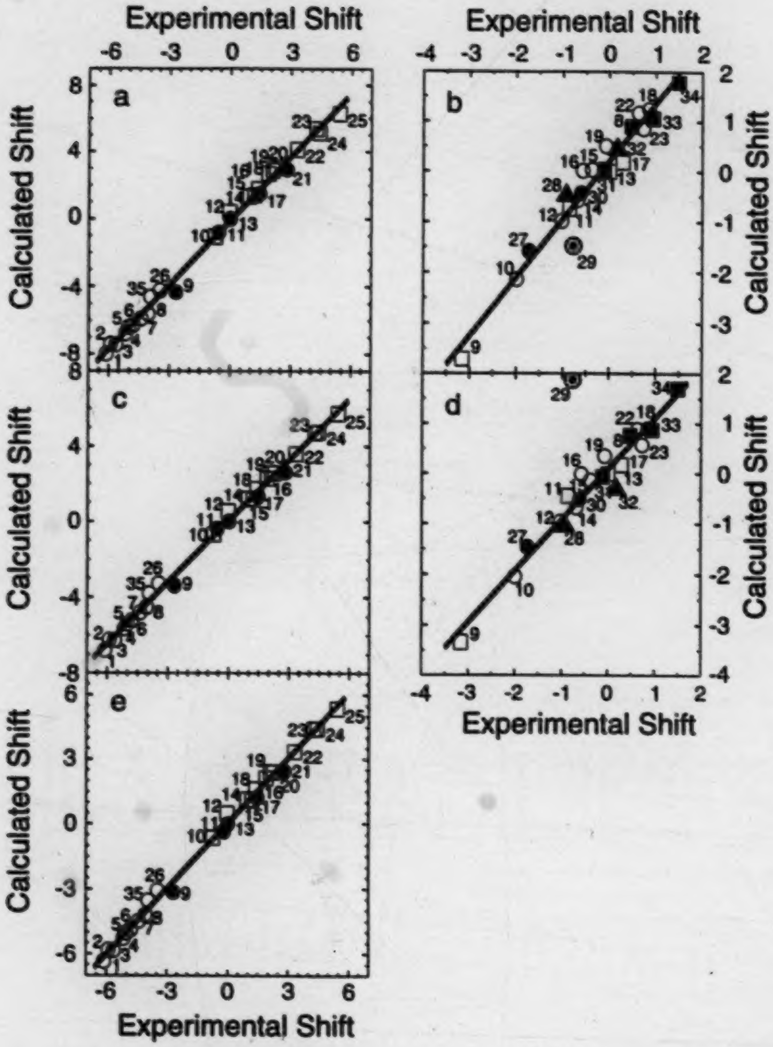

Figure 6-9: Chemical shifts (eV), calculated *versus* experimental: Koopmans' value [8], transition state model. The symbols represent the different groups of molecules as defined in Table 6-3 and Table 6-4. S($2p_{3/2}$): S-II ○, S-IV ●, S-VI □

O(1s): C-IV ■, Cr-VI ⊙, P-V ●, S-IV □, S-VI ○, V-V ▲

a) S($2p_{3/2}$), HF; b) O(1s), HF; c) S($2p_{3/2}$), B3LYP; d) O(1s), B3LYP;

e) S($2p_{3/2}$), B3LYP with core shielding.

Table 6-1: Oxygen 1s ionization potentials (eV).

Compound	Present Work[a]	Literature Values
CH_3SO_2Cl	538.80	
CH_3SO_2F	539.15	
OPF_3	539.22	539.1[b], 539.3[b]
SO_2Cl_2	539.26	539.51[b]
CF_3SO_2Cl	539.46	
SO_2FCl	539.76	
SO_2	539.83	539.84[b]
SOF_2	540.12	539.7[b]
OSF_4	540.46	
SO_2F_2	540.56	540.5[b]

(a) The uncertainty in the O(1s) ionization potentials is ±0.10 eV

(b) reference [154]

Table 6-2: Sulphur 2p ionization potentials (eV).

Compound	Present Work(a)		ΔE(S-O)	Literature Values	
	$2p_{3/2}$	$2p_{1/2}$		$2p_{3/2}$	$2p_{1/2}$
SPF_3	169.76	170.96	1.20	169.76(b)	170.96(b)
S_2Cl_2	170.85	172.02	1.17	171.57(c)	
SCl_2	171.31	172.49	1.18		
$(CH_3)_2SO$	172.10	173.27	1.17	171.91(c)	
$(CH_3)_2SO_2$	174.04	175.30	1.26	173.90(c)	
$SOCl_2$	174.20	175.36	1.16	174.53(c)	
SO_2(d)	174.78	175.93	1.15	174.78(e)	175.99(e)
CH_3SO_2Cl	174.74	175.87	1.13		
CH_3SO_2F	175.73	176.91	1.18		
CF_3SO_2Cl	175.98	177.05	1.07		
SO_2Cl_2	176.16	177.11	0.95	176.05(c)	
SOF_2	176.23	177.44	1.21	176.20(c)	
SO_2FCl	176.88	178.13	1.25		
SF_4	177.57	178.79	1.22	177.58(b)	178.78(b)
NSF_3(f)	177.04	178.23	1.19	176.97(c)	
SO_2F_2	178.08	179.30	1.22	177.67(c)	
OSF_4(f)	179.03	180.20	1.17		
SF_5Cl	179.19	180.43	1.24	179.27(c)	
SF_6	180.20	181.44	1.24	180.20(g)	181.5(g)

(a) the uncertainty in the S(2p) ionization potentials is ±0.05 eV

(b) reference [89], an average S(2p) ionization potential is listed.

(c) reference [154], only S($2p_{3/2}$) is listed.

(d) the S($2p_{3/2}$) IP of SO_2 at 174.78 eV [153] was set as calibration standard

(e) reference [153]

(f) unpublished data from Cavell and Yang.

(g) reference [161]

Table 6-3: Sulphur compound groups.

Group	Oxidation state of Sulphur	Compounds
S-II	2	$(CH_3)_2S$, CH_3SH, CS_2, $SPCl_3$, H_2S, SPF_3, $CH_3P(S)Cl_2$, OCS, SCl_2, S_2Cl_2
S-IV	4	$(CH_3)_2SO$, $SOCl_2$, SO_2, SOF_2, SF_4
S-VI	6	$(CH_3)_2SO_2$, CH_3SO_2Cl, CH_3SO_2F, CF_3SO_2Cl, SO_2Cl_2, SO_2FCl, NSF_3, SO_2F_2, OSF_4, SF_5Cl, SF_6, SO_3

Table 6-4: Oxygen compound groups.

Group	Oxidation State (Central Atom)	Compounds
C-IV	4	$COCl_2$, COF_2, CO_2, OCS
Cr-VI	5	CrO_2Cl_2
P-V	5	$OPCl_3$, OPF_3
S-IV	4	$(CH_3)_2SO$, $SOCl_2$, SO_2, SOF_2
S-VI	6	$(CH_3)_2SO_2$, CH_3SO_2Cl, CH_3SO_2F, SO_2Cl_2, SO_2FCl, SO_2F_2, CF_3SO_2Cl, OSF_4, SO_3
V-V	5	$OVCl_3$, OVF_3

Table 6-5: Experimental ionization potentials and chemical shifts (eV).

No.	Compound	$S(2p_{3/2})$		$O(1s)$	
		IP	Shift(a)	IP	Shift(a)
1	$CH_3\,P(S)Cl_2$	168.25(b)	-6.13	-------	-------
2	$SPCl_3$	168.87[c]	-5.91	-------	-------
3	$(CH_3)_2S$	169.14(b)	-5.64	-------	-------
4	CH_3SH	169.61(b)	-5.17	-------	-------
5	SPF_3	169.76	-5.02	-------	-------
6	CS_2	169.98(d)	-4.80	-------	-------
7	H_2S	170.37(d)	-4.41	-------	-------
8	OCS	170.72(d)	-4.06	540.30(c)	0.47
35	S_2Cl_2	170.85	-3.93	-------	-------
26	SCl_2	171.31	-3.47	-------	-------
9	$(CH_3)_2SO$	172.10	-2.68	536.67(c)	-3.16
10	$(CH_3)_2SO_2$	174.04	-0.74	537.84(c)	-1.99
11	$SOCl_2$	174.20	-0.58	538.97(c)	-0.86
12	CH_3SO_2Cl	174.74	-0.04	538.80	-1.03
13	SO_2	174.78(d)	0	539.83	0.00
14	CH_3SO_2F	175.73	0.95	539.15	-0.68
15	CF_3SO_2Cl	175.98	1.20	539.46	-0.37
16	SO_2Cl_2	176.16	1.38	539.26	-0.57
17	SOF_2	176.23	1.45	540.12	0.29
18	SO_3	176.67(c)	1.89	540.68(c)	0.85
19	SO_2FCl	176.88	2.10	539.76	-0.07

Table 6-5, continued from previous page

No.	Compound	$S(2p_{3/2})$		O(1s)	
		IP	Shift[(a)]	IP	Shift[(a)]
20	NSF_3	177.04	2.26	-------	-------
21	SF_4	177.57	2.79	-------	-------
22	SO_2F_2	178.08	3.30	540.56	0.73
23	OSF_4	179.03	4.25	540.46	0.63
24	SF_5Cl	179.19	4.41	-------	-------
25	SF_6	180.20	5.42	-------	-------
27	$OPCl_3$	-------	-------	538.1(c)	-1.73
28	$OVCl_3$	-------	-------	538.90(c)	-0.93
29	CrO_2Cl_2	-------	-------	539.06(c)	-0.77
30	OPF_3	-------	-------	539.22	-0.61
31	$COCl_2$	-------	-------	539.72(c)	-0.11
32	OVF_3	-------	-------	540.0(c)	0.17
33	COF_2	-------	-------	540.77(c)	0.94
34	CO_2	-------	-------	541.32(c)	1.49

(a) Shift = ΔIP = compound - reference (SO_2); uncertainty is ±0.20 eV or less

(b) reference [89]. An average 2p value was listed. A spin-orbit splitting of 1.2 eV was assumed in order to obtain the $2p_{3/2}$ ionization potential. The uncertainty is ±0.05 eV.

(c) reference [154]. The uncertainty is ±0.10 eV or less

(d) reference [153]. The uncertainty is ±0.03 eV

Table 6-6: Group electronegativities.

Group	electronegativity
P	2.19(a)
H	2.20(a)
$OCrCl_2$	2.20(c)
VCl_3	2.23(c)
CH_3	2.27(b)
CH_3PCl_2	2.48(c)
VF_3	2.54(c)
C	2.55(a)
S	2.58(a)
CS	2.70(c)
CCl_2	2.89(c)
PCl_3	2.90(c)
N	3.04(a)
Cl	3.16(a)
CO	3.17(c)
O	3.44(a)
CF_2	3.44(c)
CF_3	3.46(b)
PF_3	3.51(c)
F	3.98(a)

(a) Pauling values (b) given in [150]

(c) calculated as described in [150]

Table 6-7: Ligand electronegativities.

No.	Compound	$\Sigma\chi_l$ on S	$\Sigma(\chi_l/r)$ on S	χ_l on O	$\Sigma(\chi/r)$ on O	χ_l/r on O
1	$CH_3P(S)Cl_2$	2.48	1.30	-------	-------	-------
2	$SPCl_3$	2.90	1.54	-------	-------	-------
3	$(CH_3)_2S$	4.54	2.51	-------	-------	-------
4	CH_3SH	4.47	2.90	-------	-------	-------
5	SPF_3	3.51	1.90	-------	-------	-------
6	CS_2	2.70	2.47	-------	-------	-------
7	H_2S	4.40	3.29	-------	-------	-------
8	OCS	3.17	2.90	2.70	3.16	1.78
9	$(CH_3)_2SO$	7.98	4.84	2.39	3.46	1.61
10	$(CH_3)_2SO_2$	11.42	7.36	2.57	4.93	1.80
11	$SOCl_2$	9.76	5.47	3.03	4.02	2.12
12	CH_3SO_2Cl	12.31	7.66	2.78	5.19	1.95
13	SO_2	6.88	4.81	3.74	3.20	2.61
14	CH_3SO_2F	13.13	8.72	2.85	5.76	2.02
15	CF_3SO_2Cl	13.50	8.30	3.45	5.64	2.44
16	SO_2Cl_2	13.20	7.99	3.31	5.46	2.33
17	SOF_2	11.40	7.46	3.58	5.13	2.53
18	SO_3	10.32	7.28	3.98	4.62	2.81
19	SO_2FCl	14.02	9.05	3.53	6.03	2.51

Table 6-7, continued from previous page

No.	Compound	$\Sigma\chi_i$ on S	$\Sigma(\chi_i/r)$ on S	χ_i on O	$\Sigma(\chi/r)$ on O	χ_i/r on O
20	NSF_3	14.98	9.84	-------	-------	-------
21	SF_4	15.92	9.99	-------	-------	-------
22	SO_2F_2	14.84	10.13	3.80	6.61	2.72
23	OSF_4	19.36	11.95	3.69	8.41	2.62
24	SF_5Cl	23.06	14.21	-------	-------	-------
25	SF_6	23.88	15.29	-------	-------	-------
26	SCl_2	6.32	3.14	-------	-------	-------
27	$OPCl_3$	-------	-------	2.90	4.78	2.01
28	$OVCl_3$	-------	-------	2.23	4.18	1.42
29	CrO_2Cl_2	-------	-------	2.20	4.48	1.39
30	OPF_3	-------	-------	3.51	6.26	2.45
31	$COCl_2$	-------	-------	2.89	4.61	2.45
32	OVF_3	-------	-------	2.54	5.52	1.62
33	COF_2	-------	-------	3.44	5.76	2.94
34	CO_2	-------	-------	3.17	3.68	2.73
35	S_2Cl_2	6.24	2.49	-------	-------	-------

Table 6-8: Calculated O(1s) ionization potential chemical shifts (ΔIP): Potential at the Nucleus method [92].

#	compound	calculated ΔIP (eV) (a)			
		(A) (b)	(B) (b)	(C) (b)	(D) (b)
9	$(CH_3)_2SO$	-7.21	-6.38	-6.49	-3.63
10	$(CH_3)_2SO_2$	-3.20	-1.73	-2.31	-2.65
27	$OPCl_3$	-2.15	-4.25	-4.46	-2.17
12	CH_3SO_2Cl	-1.23	-0.20	-0.69	-1.53
28	$OVCl_3$	0.52	4.64	5.04	
11	$SOCl_2$	-1.64	-2.37	-1.98	-1.52
29	CrO_2Cl_2	-1.84	2.91	5.12	
14	CH_3SO_2F	0.22	1.61	0.89	-0.51
30	OPF_3	1.28	0.81	0.25	0.61
16	SO_2Cl_2	0.50	0.91	0.55	-0.23
15	CF_3SO_2Cl	0.73	1.68	1.03	-0.06
31	$COCl_2$	2.86	3.06	2.58	3.63
19	SO_2FCl	2.05	2.86	2.24	1.01
13	SO_2	0.00	0.00	0.00	0.00
32	OVF_3	2.65	6.71	6.77	
17	SOF_2	0.99	0.75	0.57	0.94
8	OCS	2.99	3.84	3.64	2.26
23	OSF_4	4.64	5.35	4.50	4.03
22	SO_2F_2	3.51	4.55	3.62	2.61
18	SO_3	2.90	4.38	3.47	1.83
33	COF_2	6.42	8.22	7.50	5.62
34	CO_2	6.30	7.91	7.41	5.05

(a) ΔIP = compound - reference(SO_2).

(b) (A): HF (6-311G*) Mulliken Charges (B): HF (6-311G*) Natural Charges
(C): B3LYP (6-311G*) Natural Charges (D): CNDO Mulliken Charges

Table 6-9: Calculated S($2p_{3/2}$) ionization potential chemical shifts (ΔIP): Potential at the Nucleus method [92].

#	compound	calculated ΔIP (eV)(a)			
		(A)(b)	(B)(b)	(C)(b)	(D)(b)
1	$CH_3P(S)Cl_2$	-12.79	-17.76	-15.64	-10.22
2	$SPCl_3$	-11.56	-16.94	-14.85	-9.21
3	$(CH_3)_2S$	-11.83	-14.71	-13.03	-9.03
4	CH_3SH	-11.13	-14.49	-12.93	-8.18
5	SPF_3	-9.34	-13.81	-12.04	-6.81
6	CS_2	-10.28	-14.37	-12.41	-8.35
7	H_2S	-10.01	-14.01	-12.60	-6.69
8	OCS	-7.60	-11.95	-10.15	-5.87
9	$(CH_3)_2SO$	-6.68	-6.95	-5.65	-6.65
10	$(CH_3)_2SO_2$	-4.01	-0.27	0.26	-5.08
11	$SOCl_2$	-2.60	-3.73	-2.83	-3.79
12	CH_3SO_2Cl	-2.78	0.99	1.37	-3.86
13	SO_2	0.00	0.00	0.00	0.00
14	CH_3SO_2F	-0.41	3.84	3.85	-1.68
15	CF_3SO_2Cl	-0.09	3.73	3.83	-2.46
16	SO_2Cl_2	-1.16	1.61	1.94	-2.47
17	SOF_2	2.59	2.67	2.61	1.71
18	SO_3	2.58	5.75	5.28	0.58
19	SO_2FCl	1.36	4.69	4.67	-0.13

Table 6-9, continued from previous page

#	compound	calculated ΔIP (eV)$^{(a)}$			
		(A)$^{(b)}$	(B)$^{(b)}$	(C)$^{(b)}$	(D)$^{(b)}$
20	NSF_3	2.76	5.08	5.00	1.02
21	SF_4	4.77	4.48	4.46	3.52
22	SO_2F_2	4.02	7.75	7.38	2.75
23	OSF_4	5.49	8.79	8.57	4.38
24	SF_5Cl	4.27	6.41	6.88	3.16
25	SF_6	6.57	9.16	9.37	5.98
26	SCl_2	-7.57	-11.81	-10.20	-6.18
35	S_2Cl_2	-8.31	-12.64	-11.09	-7.70

(a) ΔIP = compound - reference(SO_2)

(b) (A): HF (6-311G*) Mulliken Charges (B): HF (6-311G*) Natural Charges

(C): B3LYP (6-311G*) Natural Charges (D): CNDO Mulliken Charges

Table 6-10: The line of best-fit parameters for the correlation between calculated and experimental chemical shifts

		S($2p_{3/2}$) ionization potential		
Method		slope	intercept	χ^2
Potential at the Nucleus [92]				
CNDO, Mulliken	(Figure 6-3a)	1.27	-2.01	40.90
HF, Mulliken	(Figure 6-3b)	1.70	-1.76	23.78
HF, Natural	(Figure 6-3c)	2.53	-1.29	71.55
B3LYP, Natural	(Figure 6-3d)	2.31	-0.71	50.18
ΔE_{SCF} [99]				
CNDO	(Figure 6-6a)	-0.29	-1.11	70.48
HF	(Figure 6-6b)	1.47	0.14	3.72
B3LYP	(Figure 6-6c)	1.25	0.30	2.67
B3LYP with core shielding	(Figure 6-6d)	1.17	0.23	1.94
$X\alpha$ [103]				
	(Figure 6-7a)	0.99	-0.38	14.42
Koopmans' value [8]				
HF, GSM[(a)]	(Figure 6-8a)	1.15	0.78	7.55
B3LYP, GSM[(a)]	(Figure 6-8c)	0.98	0.87	6.99
HF, TSM[(b)]	(Figure 6-9a)	1.27	-0.10	2.62
B3LYP, TSM[(b)]	(Figure 6-9c)	1.08	0.06	1.62
B3LYP, TSM[(b)] with core shielding	(Figure 6-9e)	1.01	0.04	1.40

Table 6-10, continued from previous page.

O(1s) ionization potential				
Method		slope	intercept	χ^2
Potential at the Nucleus [92]				
CNDO, Mulliken	(Figure 6-4a)	2.05	1.43	23.71
HF, Mulliken	(Figure 6-4b)	2.78	1.89	22.66
HF, Natural	(Figure 6-4c)	2.96	3.04	76.26
B3LYP, Natural	(Figure 6-4d)	2.79	2.71	95.75
ΔE_{SCF} [99]				
CNDO	(Figure 6-5a)	1.28	0.18	6.40
HF	(Figure 6-5c)	1.12	0.27	1.02
B3LYP	(Figure 6-5b)	1.00	0.10	0.91
$X\alpha$ [103]				
	(Figure 6-7b)	-1.97	4.31	946.92
Koopmans' value [8]				
HF, GSM$^{(a)}$	(Figure 6-8b)	0.84	0.20	19.93
B3LYP, GSM$^{(a)}$	(Figure 6-8d)	0.69	0.16	10.88
HF, TSM$^{(b)}$	(Figure 6-9b)	1.16	0.21	1.74
B3LYP, TSM$^{(b)}$	(Figure 6-9d)	1.01	0.09	1.14

(a) Ground State Model

(b) Transition State Model

Table 6-11: Calculated S($2p_{3/2}$) ionization potential chemical shifts (eV): ΔE_{SCF} method [99].

No.	compound	CNDO	HF	B3LYP	B3LYP$^{(a)}$
1	$CH_3P(S)Cl_2$	-0.85	-8.84	-7.40	-6.89
2	$SPCl_3$	-0.38	-8.23	-6.81	-6.34
3	$(CH_3)_2S$	0.05	-8.19	-6.78	-6.31
4	CH_3SH	0.22	-7.56	-6.22	-5.79
5	SPF_3	1.68	-7.25	-6.01	-5.59
6	CS_2	-0.89	-7.16	-5.82	-5.42
7	H_2S	0.77	-6.66	-5.41	-5.03
8	OCS	-0.15	-6.45	-5.10	-4.75
9	$(CH_3)_2SO$	-0.28	-4.63	-3.52	-3.28
10	$(CH_3)_2SO_2$	-3.16	-0.83	-0.38	-0.36
11	$SOCl_2$	1.73	-0.68	-0.30	-0.28
12	CH_3SO_2Cl	-2.27	0.82	0.93	-0.86
13	SO_2	0.00	0.00	0.00	0.00
14	CH_3SO_2F	-4.00	1.81	1.68	1.56
15	CF_3SO_2Cl	-1.77	1.87	1.52	1.48
16	SO_2Cl_2	-1.46	2.42	2.29	2.13
17	SOF_2	0.59	1.78	1.54	1.43
18	SO_3	-3.42	3.22	2.70	2.52
19	SO_2FCl	-3.04	3.62	3.24	3.02
20	NSF_3	-1.34	3.79	3.15	2.93
21	SF_4	2.03	3.49	3.07	2.86
22	SO_2F_2	-4.56	4.96	4.31	4.01
23	OSF_4	-2.85	6.57	5.74	5.34
24	SF_5Cl	-1.55	6.48	5.90	5. 50
25	SF_6	-2.86	7.88	7.08	6.59
26	SCl_2	2.45	-4.60	-3.53	-3.29
35	S_2Cl_2	1.67	-5.12	-4.15	-3.86

(a) with core shielding effects

Table 6-12: Calculated O(1s) ionization potential chemical shifts (eV): ΔE_{SCF} method [99].

#	compound	CNDO	HF	B3LYP
9	$(CH_3)_2SO$	-3.60	-3.61	-3.29
10	$(CH_3)_2SO_2$	-2.76	-2.07	-2.04
27	$OPCl_3$	-1.62	-1.54	-1.47
12	CH_3SO_2Cl	-1.90	-0.94	-0.97
28	$OVCl_3$		-0.43	-0.91
11	$SOCl_2$	-1.31	-0.75	-0.46
29	CrO_2Cl_2		2.21	-22.94
14	CH_3SO_2F	-1.18	-0.50	-0.66
30	OPF_3	1.00	-0.32	-0.46
16	SO_2Cl_2	-0.9932	0.02	-0.04
15	CF_3SO_2Cl	-0.77	0.06	-0.16
31	$COCl_2$	0.93	0.02	-0.02
19	SO_2FCl	-0.15	0.54	0.34
13	SO_2	0.00	0.00	0.00
32	OVF_3		0.57	-0.18
17	SOF_2	0.56	0.26	0.19
8	OCS	1.33	0.91	0.76
23	OSF_4	1.46	1.22	0.87
22	SO_2F_2	0.79	0.90	0.58
18	SO_3	0.65	1.26	0.89
33	COF_2	1.73	1.05	0.88
34	CO_2	1.92	1.77	1.65

Table 6-13: Calculated ionization potentials and chemical shifts (eV): Xα method [103].

#	Compound	Binding Energy			Chemical Shift	
		$S(2p_{3/2})$	$S(2p_{1/2})$	O(1s)	$S(2p_{3/2})$	O(1s)
1	$CH_3P(S)Cl_2$	170.62	171.82	-------	-5.92	-------
2	$SPCl_3$	171.28	172.48	-------	-5.26	-------
3	$(CH_3)_2S$	169.30	170.50	-------	-7.24	-------
4	CH_3SH	171.13	172.33	-------	-5.41	-------
5	SPF_3	171.21	172.41	-------	-5.33	-------
7	H_2S	174.27	175.47	-------	-2.27	-------
9	$(CH_3)_2SO$	172.75	173.95	546.21	-3.79	13.23
10	$(CH_3)_2SO_2$	174.21	175.41	530.85	-2.33	-2.13
11	$SOCl_2$	175.88	177.08	551.28	-0.66	18.30
12	CH_3SO_2Cl	176.79	177.99	531.88	0.25	-1.10
13	SO_2	176.54	177.74	532.98	0.00	0.00
14	CH_3SO_2F	176.50	177.70	531.54	-0.04	-1.44
15	CF_3SO_2Cl	175.32	176.52	533.14	-1.22	0.16
16	SO_2Cl_2	178.76	179.96	533.17	2.22	0.19
17	SOF_2	177.20	178.40	547.95	0.66	14.97
18	SO_3	178.87	180.07	527.71	2.33	-5.27
19	SO_2FCl	178.58	179.78	532.52	2.04	-0.46
20	NSF_3	179.32	180.52	-------	2.78	-------
21	SF_4	178.68	179.88	-------	2.14	-------
22	SO_2F_2	178.88	180.08	532.40	2.34	-0.58
23	OSF_4	180.22	181.42	547.43	3.68	14.45
24	SF_5Cl	180.89	182.09	-------	4.35	-------
25	SF_6	181.51	182.71	-------	4.97	-------
26	SCl_2	173.45	174.65	-------	-3.09	-------
27	$OPCl_3$	-------	-------	549.52	-------	16.54
30	OPF_3	-------	-------	547.35	-------	14.37
35	S_2Cl_2	167.13	168.33	-------	-9.41	-------

Table 6-14: O(1s) ionization potentials (eV), symmetry effects: Xα method [103]

#	Compound	Experiment	Xα Energies		
			C_{2v}	C_s	Ave.
13	SO_2	539.83	532.98	548.21	540.60
16	SO_2Cl_2	539.26	533.17	548.81	540.99
22	SO_2F_2	540.56	532.30	548.10	540.20

Table 6-15: Calculated $S(2p_{3/2})$ chemical shifts (eV): Koopmans' value [8]

No.	compound	ground state method		transition state method		
		(HF)	(B3LYP)	(HF)	(B3LYP)	(B3LYP)[a]
1	$CH_3P(S)Cl_2$	-6.16	-4.94	-8.00	-6.80	-6.31
2	$SPCl_3$	-5.59	-4.39	-7.40	-6.23	-5.77
3	$(CH_3)_2S$	-5.97	-4.97	-7.44	-6.25	-5.79
4	CH_3SH	-5.74	-4.77	-6.80	-5.66	-5.25
5	SPF_3	-5.28	-4.28	-6.42	-5.40	-5.00
6	CS_2	-4.54	-3.68	-6.30	-5.24	-4.85
7	H_2S	-5.30	-4.39	-5.91	-4.82	-4.46
8	OCS	-4.68	-3.72	-5.62	-4.52	-4.19
9	$(CH_3)_2SO$	-3.02	-2.32	-4.32	-3.38	-3.13
10	$(CH_3)_2SO_2$	-0.08	0.19	-1.05	-0.69	-0.64
11	$SOCl_2$	0.77	0.84	-0.81	-0.38	-0.35
12	CH_3SO_2Cl	1.51	1.51	0.41	0.53	0.49
13	SO_2	0.00	0.00	0.00	0.00	0.00
14	CH_3SO_2F	1.85	1.77	1.35	1.22	1.13
15	CF_3SO_2Cl	2.52	2.22	1.42	1.19	1.10
16	SO_2Cl_2	2.99	2.79	1.79	1.73	1.61
17	SOF_2	1.55	1.36	1.53	1.33	1.23
18	SO_3	2.77	2.41	2.71	2.29	2.12
19	SO_2FCl	3.57	3.23	2.90	2.59	2.40
20	NSF_3	3.53	3.05	3.05	2.57	2.39
21	SF_4	3.17	2.82	2.95	2.62	2.43
22	SO_2F_2	4.18	3.74	4.14	3.60	3.34
23	OSF_4	5.79	5.15	5.39	4.73	4.38
24	SF_5Cl	6.32	5.81	5.16	4.75	4.40
25	SF_6	6.91	6.31	6.31	5.75	5.33
26	SCl_2	-2.58	-1.94	-4.23	-3.28	-3.04
35	S_2Cl_2	-2.72	-1.96	-4.63	-3.80	-3.52

(a) with core shielding, previous column divided by 1.079

Table 6-16: Calculated O(1s) chemical shifts (eV): Koopmans' value [8]

No.	compound	ground state method		transition state method	
		HF	B3LYP	HF	B3LYP
9	$(CH_3)_2SO$	-3.71	-3.08	-3.72	-3.34
10	$(CH_3)_2SO_2$	-2.25	-1.92	-2.14	-2.04
27	$OPCl_3$	-1.43	-1.02	-1.58	-1.46
12	CH_3SO_2Cl	-0.96	-0.69	-0.98	-0.95
28	$OVCl_3$	1.69	0.90	-0.45	-1.01
11	$SOCl_2$	-0.24	0.29	-0.74	-0.44
29	CrO_2Cl_2	2.18	1.48	-1.48	1.88
14	CH_3SO_2F	-0.95	-0.81	-0.57	-0.67
30	OPF_3	-1.20	-1.07	-0.43	-0.51
16	SO_2Cl_2	0.13	0.36	0.01	0.00
15	CF_3SO_2Cl	0.06	0.15	0.03	-0.13
31	$COCl_2$	0.14	0.20	0.04	-0.06
19	SO_2FCl	0.24	0.32	0.51	0.36
13	SO_2	0.00	0.00	0.00	0.00
32	OVF_3	1.48	0.60	0.48	-0.27
17	SOF_2	-0.27	-0.11	0.18	0.18
8	OCS	1.11	0.95	0.90	0.77
23	OSF_4	0.49	0.42	1.17	0.89
22	SO_2F_2	0.08	0.04	0.85	0.58
18	SO_3	0.90	0.73	1.25	0.90
33	COF_2	-0.00	-0.09	1.06	0.88
34	CO_2	0.75	0.73	1.79	1.70

7. The Sulphur 2p Photoabsorption Spectrum of NSF_3 [2]

7.1. *Introduction*

Several recent investigations of the phosphorus 2p absorption spectrum of PF_3 have been reported [106, 162-165]. A photoelectron-photoion-coincidence study in the P(2p) ionization region [163] of PF_3 revealed a rather unusual behaviour of the $^1A_1$ state at 136.5 eV; the parent ion yield spectrum showed only one line at 136.5 eV without an apparent spin-orbit partner. This observation has been attributed to the existence of a pure L-S coupled $^1A_1$ state, wherein a large singlet-triplet splitting of 2.4 eV overwhelms the spin-orbit splitting of 0.9 eV [163, 166]. Further investigation of this phenomenon in PF_3 and the overall electronic structure of this class of molecules, pyramidal C_{3v} molecular systems based on phosphorus such as OPF_3 and SPF_3, has been carried out in the phosphorus 2p spectral region [166]. All these systems display evidence of this L-S state, in general to a lesser extent than PF_3. It is now pertinent to evaluate whether this L-S state behaviour may exist in related systems. Herein we investigate the S(2p) photoabsorption spectrum of NSF_3, a molecule of the same structural type, and compare the spectrum to that of OPF_3.

7.2. *Experimental*

Photoabsorption measurements were collected as described in Chapter 2 of the thesis. A double gas cell assembly was used, consisting of two chambers each with a length of 12.4 cm and an inner diameter of 0.4 cm, connected by an intervening chamber of 13.3 cm in length. The cell was isolated from the monochromator chamber with a carbon window and a differential pumping section between the monochromator and the window. Gas pressure in the cells was between 48 and 178 mtorr. The ion current as a function of photon energy was measured for both cells, and the absolute photoabsorption spectrum was determined from the ratio of the two signals [78]. NSF_3 was prepared by Zhenyu Yang and J. S. Thrasher at the University of Alabama.

---

[2] **A version of this chapter has been accepted for publication:**
A. Jürgensen, R. G. Cavell, N. Kosugi; *Chem. Phys.* (1999)

7.3. Calculations

The S(2p) spectrum of NSF_3 was calculated using the GSCF3 computer code [167, 168]. The geometry was optimized by energy minimization using the HF method (Hartree-Fock energy calculation) and the 4-31G* basis set. Agreement of the calculated structure with the experimental values obtained from microwave spectroscopy [169] is quite good (Table 7-1). The calculations tend to underestimate bond lengths and angles. For the bond lengths, the difference between calculated and experimental values was less than 0.04 Å and the F-S-F bond angle was underestimated by 0.5°. However, these differences are substantially larger than the reported uncertainties in the experimental data [169].

The excited molecular states were then calculated using this optimized geometry. The basis set was generated from Gaussian-type functions of Huzinaga et al. [170]: (533/53) for S, and (63/5) for N and F. These were augmented by d-type polarization functions on all atoms (S-3d: $\zeta = 0.659$ and 0.183; N-3d: $\zeta = 1.1$; F-3d: $\zeta = 1.3$) and compact functions on sulphur (s-type: $\zeta = 182.0$ and 16.0; p-type: $\zeta = 33.0$; d-type $\zeta = 6.4$ and 2.1). The latter are required to properly account for the sulphur orbital contraction upon core hole creation [166]. Diffuse functions were not included, as Rydberg states were not the main focus of this work. The contraction scheme of the basis set was $(521211^{+}1^{+}/411111^{+}/1^{+}1^{+}1^{*}1^{*})$ for sulphur and $(621/311/1^{*})$ for nitrogen and fluorine. Since the calculations were non-relativistic, no spin-orbit coupling has been considered. It was added manually using the experimental value of 1.19 eV (Chapter 6) for the S(2p) level of NSF_3 to generate the calculated spectrum. Russell-Saunders coupling—leading to singlet and triplet final states for each electronic transition—was included in the calculation. All triplet excited states are spin-forbidden by the dipole spin selection rule of $\Delta s=0$ (Section 1.2) in photoabsorption transitions, and hence the calculated oscillator strength was zero. Similarly, the orbital selection rule (Section 1.2) dictates a zero oscillator strength for the $^1A_2$ state resulting from the $P(2p\text{-}e) \rightarrow e^*$ transition. The energies for all these states were calculated in order to identify the dominant angular momentum coupling for each excited electronic state, as described in [163, 166]. Table 7-2 lists the calculated excited molecular states obtained without spin-orbit coupling.

The transition energies to Rydberg orbitals were estimated as described in Section 3.7 above. The average values of the quantum defect δ for the Rydberg series were those suggested by Robin [118] for sulphur: 2.02 for ns, 1.60 for np and 0.095 for nd ignoring the molecular field effects. The ionization potentials were obtained from the literature (Chapter 6). The calculated values for the Rydberg transitions are listed in Table 7-3.

The S(2p) ionization cross-sections were calculated with the Xα technique [116] using the experimental molecular geometry [169]. The α parameters [109] were those incorporated into the code and the sphere radii were those determined by the program. Transitions were calculated using the transition state method [113], the molecular potential was calculated with half an electron missing from one of the S(2p) orbitals (a_1 or e). This potential was then used to calculate the post-edge photoabsorption cross-section for excitation from each S(2p) orbital, respectively. Identification of the resonant states was achieved using the method described by Powis [111]: certain members of the angular basis (e.g., sulphur d-waves) were excluded. The spectra thus obtained were then compared to the complete spectrum (no exclusions) to determine the contribution of each type of angular momentum. Spin-orbit coupling was not considered because peak widths are larger than the S-O split energy and splitting is not readily apparent in the post-edge spectrum. Molecular orbital coefficients for the orthonormalized atomic orbital basis set (see Section 3.6) were calculated with Gaussian-94 [94] using the HF method and a 4-31G* basis set at optimized geometry to obtain the atomic orbital compositions (expressed as %) of the molecular orbitals. The contour plots of $1a_1^*$, $1e^*$ and $2a_1^*$ antibonding orbitals were generated from the Gaussian-94 calculation results and visualized with the MOLDEN program [171] using a contour cutoff value of 0.15.

7.4. Results and Discussion

The experimental S(2p) photoabsorption spectrum is shown in Figure 7-1. It has been fitted with a set of mixed Gaussian/Lorentzian curves. A step in the baseline was placed at the approximate position of the ionization edge. The peak energies obtained are listed in Table 7-4. The shape of the first pre-edge peak suggests deconvolution into four relatively broad peaks (average FWHM = 1.41 eV). All are assigned to valence shell antibonding orbitals. The second pre-edge peak results from the overlap of Rydberg transitions as well as transitions to valence shell antibonding orbitals. This is evidenced by the barely resolved features observed on this peak. It has, thus, been deconvoluted into ten peaks with an average FWHM of 0.55 eV. Based upon their shape the two post-edge features have also been deconvoluted into two peaks each. However, in case of the second feature, peak #18 at 192.9 eV is most likely an artifact of the cut-off of the experimental spectrum. Assignment of all these peaks was achieved with the aid of the calculations described earlier. Each region of the spectrum—valence shell antibonding orbitals, Rydberg orbitals and post-edge resonances—shall now be discussed in detail.

7.4.1. Valence shell antibonding orbitals

As described earlier, transitions to these orbitals were calculated using only the Russell-Saunders (LS) coupling scheme, a limiting description which ignores spin-orbit effects—i.e., the singlet-triplet splitting dominates. However, an accurate description of the final electronic states should involve both types of split, that is, some type of intermediate coupling between pure LS (singlet-triplet) and pure jj (spin-orbit). Both LS and jj coupling are limiting descriptions which must connect smoothly [166] over a region of intermediate coupling. Because the nature of the actual coupling for these final states is at present unknown, we have adopted a simple scheme for determination of the dominant type. The calculated singlet-triplet split energy ($\Delta E_{S\text{-}T}$) was compared to the spin-orbit split energy ($\Delta E_{S\text{-}O}$) of 1.19 eV determined from the S(2p) photoelectron spectrum [172]. If $\Delta E_{S\text{-}T} < \Delta E_{S\text{-}O}$ then jj coupling dominates and two spin-orbit peaks are expected. In contrast, if $\Delta E_{S\text{-}T} > \Delta E_{S\text{-}O}$, LS coupling is dominant and only a single peak should be observed, see also [163, 166].

As seen in Table 7-2, for most states $\Delta E_{S\text{-}T} < \Delta E_{S\text{-}O}$, giving rise to the usual spin-orbit pair. However, for both the S(2p-e)→e*(A_1) and the S(2p-a_1)→2a_1*(A_1) transitions $\Delta E_{S\text{-}T} > \Delta E_{S\text{-}O}$. Hence, LS coupling dominates and only a single peak should be observed.

To generate the calculated spectrum shown in Figure 7-2, the peaks in the $2p_{3/2}$ manifold (L_3 edge) were shifted down by 0.4 eV from the corresponding value in Table 7-2 and those in the $2p_{1/2}$ manifold (L_2 edge) were shifted up by 0.8 eV. Peak intensities in these two manifolds have been set equal rather than at a 2:1 ratio. This decision is based upon earlier work involving transition metal systems [173], which showed that multiplet effects differ for the L_3 and L_2 edges. This leads to intensity ratios in these systems of intermediate coupling which differ greatly from those predicted by single particle jj coupling. The two LS states—$^1A_1(e \rightarrow e^*)$ and $^1A_1(a_1 \rightarrow 2a_1^*)$—were placed on a third manifold, since they can be assigned to neither the L_2 nor the L_3 edge. Also, their relative energy has not been shifted from the value in Table 7-2. To facilitate comparison with the experimental results, the calculated spectrum was shifted, so that the first peak—the $^1E(e \rightarrow 1a_1^*)$ transition—aligns with the first experimental peak at 168.81 eV.

As seen in Figure 7-2, the first three experimental peaks result from the spin-orbit pairs of the $S(2p) \rightarrow 1a_1^*$ and $S(2p) \rightarrow e^*(^1E)$ transitions. Peak #4 corresponds to the LS coupled $^1A_1(e \rightarrow e^*)$ state. The peaks resulting from the $S(2p) \rightarrow 2a_1^*$ transitions contribute to the second post-edge peak, overlapping with Rydberg transitions. They have been tentatively assigned to peaks #5, #8 and #9.

7.4.2. Rydberg orbitals

All calculated Rydberg transitions (Table 7-3) fall in the energy region between 173.5 and 177.5 eV, which corresponds to the second pre-edge peak. The barely resolved features on this peak result from various Rydberg transitions. They have been assigned through comparison of the calculated and experimental peak energies and these assignments are listed in Table 7-4. Because of the C_{3v} symmetry of the NSF_3 molecule, $2p \rightarrow 4p$ Rydberg transitions are orbital allowed.

7.4.3. Post-edge resonances

The Xα calculations predict two post-edge resonances, peaking at 182 and 187.5 eV. Most of the cross-section is predicted to originate from the S(2p-e) ionization (Figure 7-3a). The 2p(e) ionization cross-section exceeds the $2p(a_1)$ cross-section by about a factor of 50, far greater than expected from the increased degeneracy. The origin of this phenomenon is, at present, not understood. Calculation of the partial cross-sections reveals both peaks to be due to the e ionization channel. A small broad a_1 ionization channel peak contributes to the tail of the second peak (Figure 7-3b). There is also an a_2 channel, but with a cross-section of the order of 10^{-7} Mbarn it does not contribute to the overall cross-section.

Through examination of the continuum functions in the manner described by Powis [111], it was established that all peaks depend on sulphur d-waves. The second e resonance and the a_1 resonance also depend on sulphur p-waves. Thus, the first peak can be assigned to atomic p→d excitation and the other two to excitations to mixed p/d states. The a_1 channel peak corresponds to a p_z/d_{z^2} shape resonance. The remaining d orbitals all have e symmetry. The d_{xy} and $d_{(x^2-y^2)}$ orbitals are in the xy plane, and the other two—d_{xz} and d_{yz}—are in the xz and yz planes, respectively. There is greater interaction between the latter two orbitals and the ligand atoms. Consequently, they have higher energy. The two e channel peaks are, thus, assigned to d_{xy}, $d_{(x^2-y^2)}$ and $p_x,p_y/d_{xz},d_{yz}$ resonances, respectively. All peaks also depend, to varying degrees, on nitrogen and fluorine s-, p- and d-waves, indicating that they represent semibound outer well states held by the potential well of the molecule. Electrons in these semibound orbitals can tunnel into the ionization continuum. The tunneling probability depends upon the energy of the excited state. Low energy states have a lower tunneling probability and hence a longer lifetime, giving rise to relatively narrow peaks; while higher energy states with a greater tunneling probability have shorter lifetimes, leading to broader peaks.

The experimental spectrum has two post-edge structures peaking at 180.5 and 189.5 eV. The first has been identified as the $d_{xy},d_{(x^2-y^2)}$ - e resonance, and the second as the mixed $p_x,p_y/d_{xz},d_{yz}$ - e resonance. The asymmetric tail of the second peak results from the unresolved low intensity p_z/d_{z^2} - a_1 resonance. The first post-edge peak has been deconvoluted into two, and their energy separation suggests that they form a spin-orbit pair. No splitting is apparent for the second peak, due to line broadening caused by a shorter lifetime of the excited state.

7.4.4. NSF_3 versus OPF_3

NSF_3 is isoelectronic with OPF_3 and has similar molecular structure. It is, thus, not surprising that their central atom 2p photoabsorption spectra also display some similar structure. Both spectra (Figure 7-4) have two pre-edge and two post-edge features (only the first is shown), and the shape of the first pre-edge peak is similar. However, the features are much better resolved in OPF_3. This is especially true for the Rydberg peaks which are well resolved in the spectrum of OPF_3 compared to just barely so in NSF_3. Comparing the valence shell antibonding orbital transitions of these two compounds (Table 7-5) we find that:

1. the order of the observed transitions is the same,
2. the peaks are, in general, closer together in OPF_3 and
3. both compounds have two LS coupled states.

These LS states are the $^1A_1(e \rightarrow e^*)$ and $^1A_1(a_1 \rightarrow 2a_1^*)$ states in both compounds. The predicted S-T split for the former is 0.44 eV larger for NSF_3 while for the latter it is about the same (Table 7-6). The S-T splitting of the excited states has been related to orbital size and degree of overlap between the two open shells in the excited state [166]. For the group of phosphorus compounds studied by Neville et al. [166], the S-T splitting of the $^1A_1(e \rightarrow e^*)$ state was dependent upon the phosphorus p-character of the e* orbital. The S-T splitting of the $^1A_1(a_1 \rightarrow 2a_1^*)$ state depended on both orbital composition and spatial extent of the $2a_1^*$ orbital [166].

Comparison of the contour plots (Figure 7-5) of the relevant antibonding orbitals of OPF_3 and NSF_3 shows that the e* orbital of NSF_3 is slightly more compact around sulphur and noticeably expanded around nitrogen, indicating there is more S-N π^* character than P-O π^* character in the corresponding orbital of OPF_3. The orbital composition analysis predicts decreased central atom p-character for NSF_3, 45.6% compared to 55.6% for OPF_3. The central atom d-character also decreased (9.9% in OPF_3, 5.6% in NSF_3). The nitrogen p-character in NSF_3 (27.9%) is more than twice the oxygen p-character in OPF_3 (12.9%). There is more delocalization onto the nitrogen atom in NSF_3 which leads in turn to increased S-N π^* character. Based on a study of the phosphorus halides [166], a decrease in S-T splitting would be expected for the $^1A_1$ (e→e*) state of NSF_3, contrary to the results suggested by the calculation (Table 7-6).

The $2a_1$* orbital displays significant changes in both orbital shape (Figure 7-5) and orbital contribution, (OPF_3: 1.8% P-s, 47.5% P-p_z, 14.9% P-d_{z^2}, 3.3% O-s, 0.9% O-p_z, 0.01% O-d_{z^2}, 5.0% F-s, 20.0% F-p, 6.6% F-d) compared to (NSF_3: 5.4% S-s, 32.3% S-p_z, 22.9% S-d_{z^2}, 6.5% N-s, 2.6% N-p_z, 0.2% N-d_{z^2}, 2.7% F-s, 18.7% F-p, 8.9% F-d). Notably there is a significant increase in the central atom s- and d_{z^2}-character and a corresponding decrease in the central atom p_z character in NSF_3, which ultimately should lead to a reduced spatial overlap with the central atom $2p_z$ core orbital and hence a lower S-T splitting. The $^1A_1(a_1 \rightarrow 2a_1^*)$ state, however, shows hardly any change in the S-T splitting. These results suggest that significant changes in the spatial extent of the central atom 2p orbitals account for the differences in the predicted S-T splitting of the LS states for NSF_3 and OPF_3.

The two post-edge features in the spectrum of OPF_3 have been assigned to P-3d(e) and P-3d(e, a_1) resonances [166], respectively, with the aid of Ms-Xα calculations reported by Liu et al. [113]. As with NSF_3, the a_1 resonance has comparatively low intensity. It contributes to the asymmetric tail of the second peak. To determine the occurrence of p/d intermixing, the Ms-Xα calculations for OPF_3 were repeated. Indeed, just as in NSF_3, the resonances comprising the second peak (e, a_1) are due to mixed semibound p/d states.

7.5. Summary

The measurement with high resolution of the sulphur 2p photoabsorption spectrum of NSF_3 and subsequent analysis with *ab initio* calculations revealed a number of similarities to isoelectronic OPF_3 and other pyramidal phosphorus compounds. In particular, there are also two LS coupled states corresponding to the e→e* ($^1A_1$) and $a_1 \rightarrow 2a_1$* ($^1A_1$) transitions. Just as for OPF_3, the spectrum of NSF_3 shows two post-edge features corresponding to S-d shape resonances. The semibound states that give rise to the second peak also have a significant amount of p-character. Future investigations should include the measurement of the partial ion yield spectra to further substantiate the assignment of the LS coupled states.

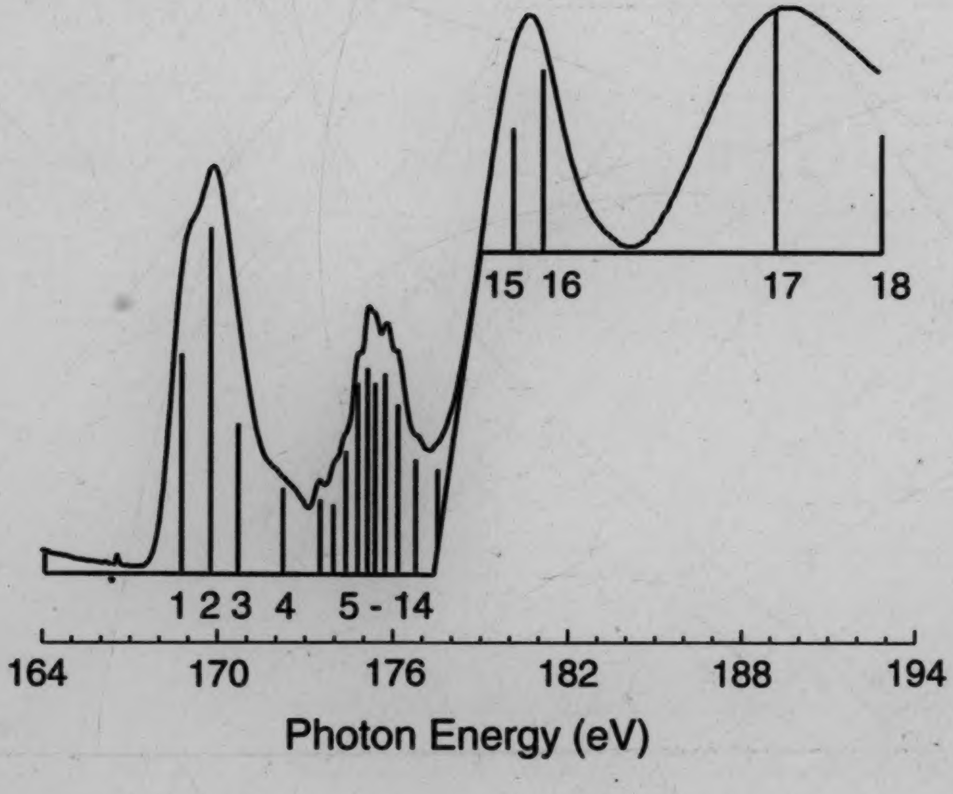

Figure 7-1: The sulphur 2p photoabsorption spectrum of NSF_3.

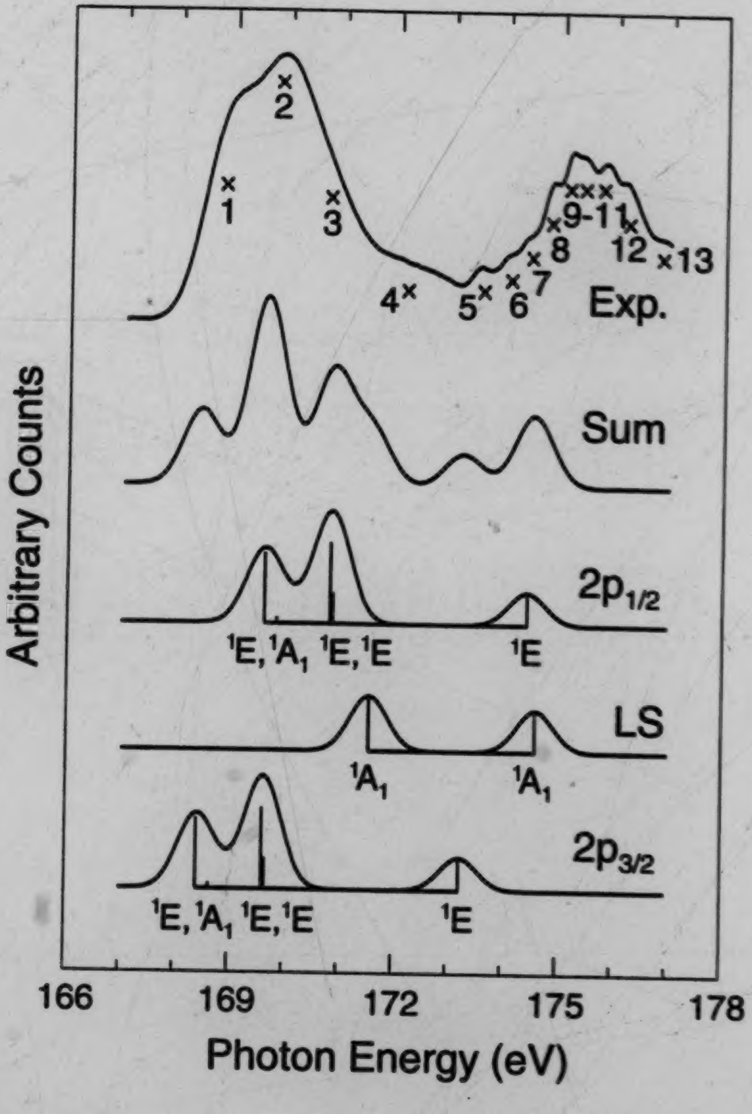

Figure 7-2: Comparison of the experimental S(2p) pre edge spectrum with the results from the GSCF3 calculation [167, 168]. The method used to generate the calculated spectra is explained in the text. The experimental peak positions are indicated by x and numbered as in Table 7-4. The assignment of the experimental peaks is also listed in Table 7-4.

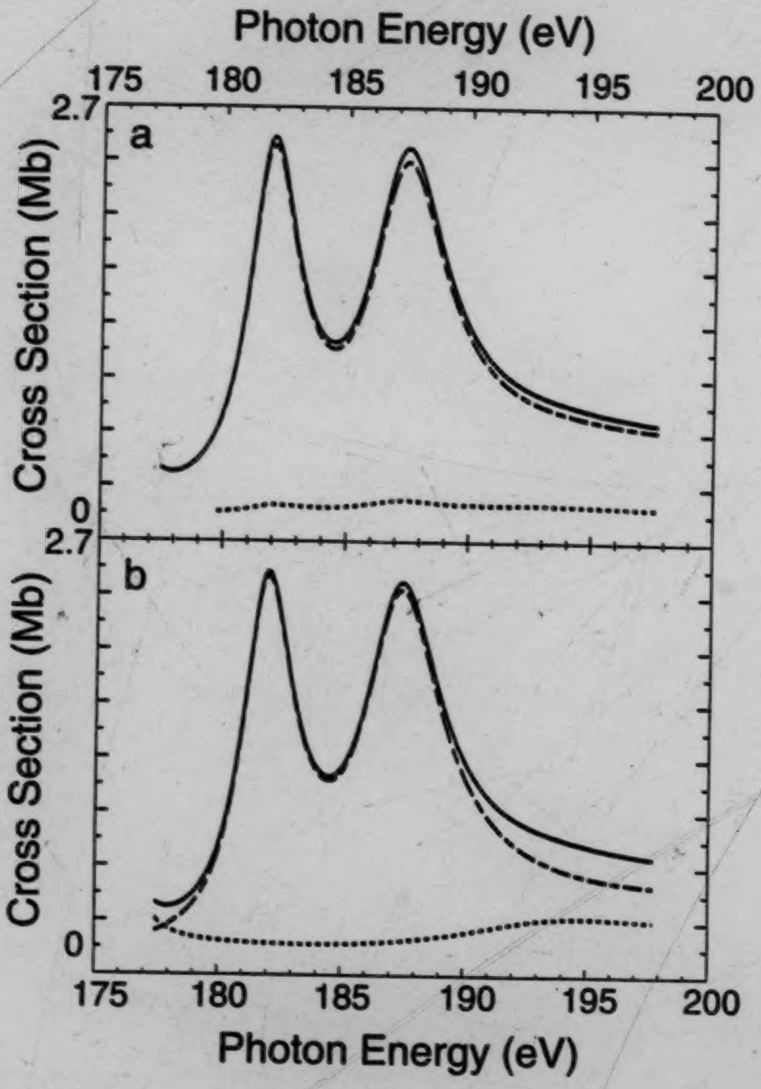

Figure 7-3: The sulphur 2p photoionization cross-section calculated with Xα: a) The total cross-section (——) and partial cross-sections for the ionization from the a_1(·········) and e(–·–·–) orbitals. b) The total cross-section (——) and partial cross-sections for the a_1(·········) and e (–·–·–) ionization channels.

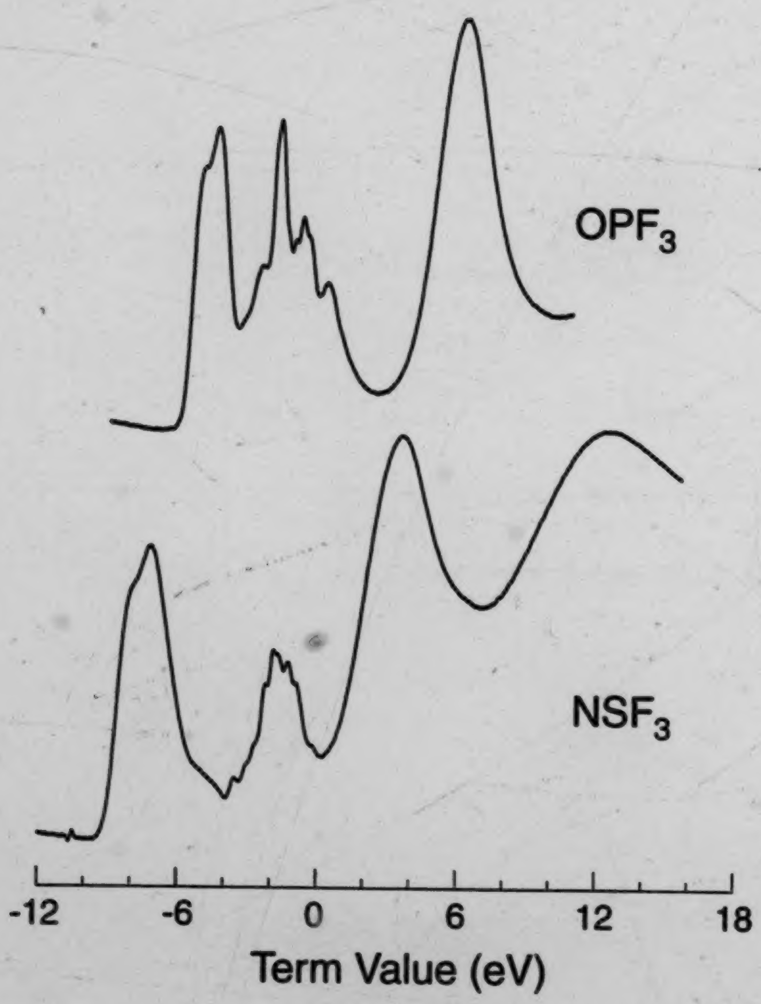

Figure 7-4: Central atom 2p photoabsorption spectra of NSF$_3$ and OPF$_3$ [174]. The two spectra have been aligned at their respective $2p_{3/2}$ ionization potentials so that all term values are relative to the $2p_{3/2}$ ionization potential.

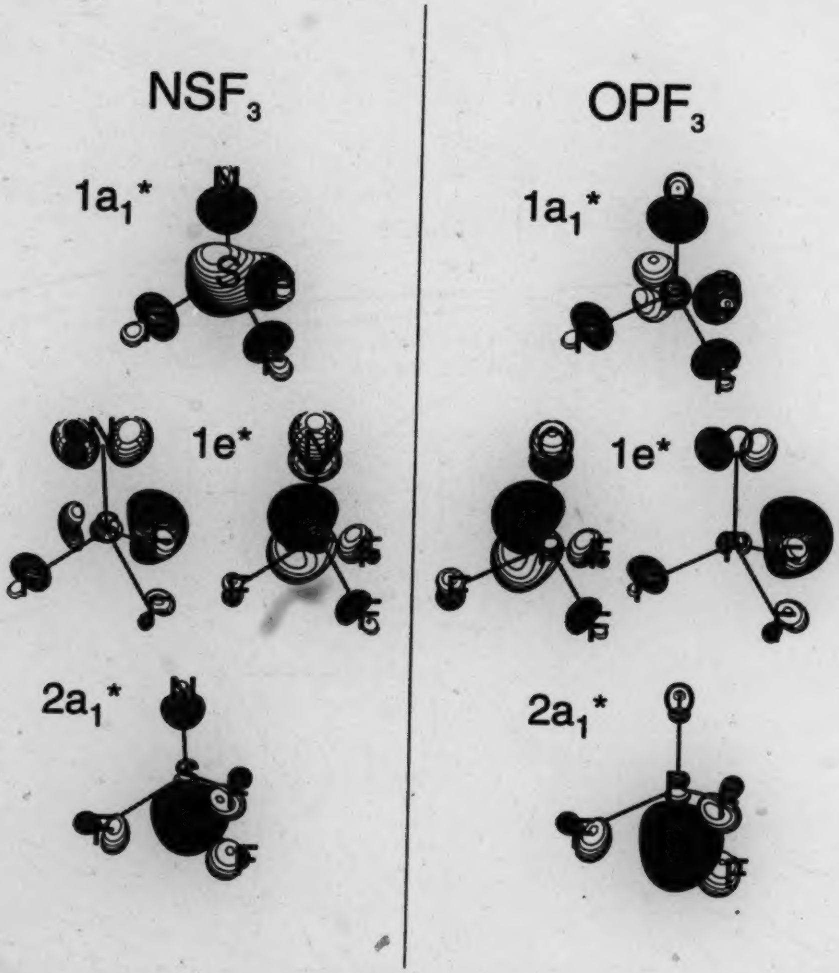
NSF$_3$
OPF$_3$
1a$_1$*
1a$_1$*
1e*
1e*
2a$_1$*
2a$_1$*

Figure 7-5: The contour plots of the valence shell antibonding orbitals for NSF$_3$ and OPF$_3$.

Table 7-1: Molecular geometry of NSF_3

	calculated	experimental [169]
N-S (Å)	1.385	1.4157(8)
S-F (Å)	1.535	1.5515(17)
F-S-F	93.41°	93.92(8)°

Table 7-2: Calculated relative energies (eV) for the electronic transitions from the S(2p) core to the valence shell antibonding orbitals of NSF_3.

transition	final state	triplet	singlet	ΔE(S-T)	singlet osc. strength
S(2p-e)→1a$_1$*	E	-0.419	0.000	0.419	0.0520
S(2p-a$_1$)→1a$_1$*	A$_1$	-0.397	0.227	0.624	0.0043
S(2p-a$_1$)→1e*	E	0.838	1.204	0.366	0.0602
S(2p-e)→1e*	E	1.035	1.254	0.219	0.0230
S(2p-e)→1e*	A$_2$	1.237	1.255	0.018	0.0000
S(2p-e)→1e*	A$_1$	0.424	2.734	2.310	0.0203
S(2p-e)→2a$_1$*	E	4.521	4.807	0.286	0.0240
S(2p-a$_1$)→2a$_1$*	A$_1$	4.050	5.784	1.734	0.0154

Table 7-3: Calculated S(2p)→Rydberg transition energies and term values (eV) of NSF_3.

transition	term value	$2p_{3/2}$ manifold	$2p_{1/2}$ manifold
S(2p)→4s	-3.47	173.57	174.76
S(2p)→4p	-2.36	174.68	175.87
S(2p)→3d	-1.61	175.43	176.62
S(2p)→4d	-0.89	176.15	177.34
S(2p)→5s	-1.53	175.51	176.70
S(2p) IP	0.00	177.04	178.23

Table 7-4: Experimental peak energies and term values (eV) of the $S(2p)$ spectrum of NSF_3.

No	Energy(a)	Term Value(b)		Assignment
		$2p_{3/2}$	$2p_{3/2}$	
1	168.81	-8.23		$^1E(e\rightarrow 1a_1^*)$, $^1A_1(a_1\rightarrow 1a_1^*)$
2	169.82	-7.22	-8.41	$^1E(e\rightarrow 1a_1^*)$, $^1A_1(a_1\rightarrow 1a_1^*)$, $^1E(a_1\rightarrow 1e^*)$, $^1E(e\rightarrow 1e^*)$
3	170.73		-7.50	$^1E(a_1\rightarrow 1e^*)$, $^1E(e\rightarrow 1e^*)$
4	172.16			$^1A_1(e\rightarrow 1e^*)$
5	173.56	-3.48		$^1E(e\rightarrow 2a_1^*)$, $2p\rightarrow 4s$
6	174.05	-2.99	-4.18	
7	174.44	-2.60		$2p\rightarrow 4p$
8	174.80		-3.43	$^1E(e\rightarrow 2a_1^*)$, $2p\rightarrow 4s$
9	175.12			$^1A_1(a_1\rightarrow 2a_1^*)$
10	175.40	-1.64		$2p\rightarrow 3d$, $2p\rightarrow 5s$
11	175.74		-2.49	$2p\rightarrow 4p$
12	176.20	-0.84		$2p\rightarrow 4d$
13	176.84		-1.39	$2p\rightarrow 3d$, $2p\rightarrow 5s$
	177.04			$2p_{3/2}$ IP
14	177.52		-0.71	$2p\rightarrow 4d$
	178.23			$2p_{1/2}$ IP
15	180.06	3.02		$2p_{3/2}\rightarrow d_{xy},d_{(x^2-y^2)}$ resonance
16	181.12		2.89	$2p_{1/2}\rightarrow d_{xy},d_{(x^2-y^2)}$ resonance
17	189.08	12.04	10.85	$2p\rightarrow p_x,p_y/d_{xz},d_{yz}$ resonance tail: $2p\rightarrow p_z/d_{z^2}$ resonance
18	192.92	15.88	14.69	not real

(a) The uncertainty of the transition energies is ±0.06 eV for the pre-edge peaks, ±0.21 eV for the post-edge resonances and ±0.05 eV for the $S(2p_{3/2})$ and $S(2p_{1/2})$ ionization potentials.

(b) The uncertainty in the term values is ±0.11 eV for the pre-edge peaks and ±0.26 eV for the post-edge resonances.

Table 7-5: Transitions to valence shell antibonding orbitals in NSF_3 and OPF_3. The LS coupled states are highlighted in bold type.

Transition	Energy (eV) NSF_3	Energy (eV) OPF_3 [166]
$e(^3/_2)\rightarrow 1a_1^*\ (^1E)$	168.81	137.1
$a_1(^3/_2)\rightarrow 1a_1^*\ (^1A_1)$	168.81	
$e(^1/_2)\rightarrow 1a_1^*\ (^1E)$	169.82	137.8
$a_1(^1/_2)\rightarrow 1a_1^*\ (^1A_1)$	169.82	
$e(^3/_2)\rightarrow e^*\ (^1E)$	169.82	137.8
$a_1(^3/_2)\rightarrow e^*\ (^1E)$	169.82	137.8
$e(^1/_2)\rightarrow e^*\ (^1E)$	170.73	138.9
$a_1(^1/_2)\rightarrow e^*\ (^1E)$	170.73	138.9
$e\rightarrow e^*\ (^1A_1)$	172.16	139.6
$e(^3/_2)\rightarrow 2a_1^*\ (^1E)$	173.56	140.4
$e(^1/_2)\rightarrow 2a_1^*\ (^1E)$	174.80	141.0
$a_1\rightarrow 2a_1^*\ (^1A_1)$	175.12	142.4

Table 7-6: Singlet-Triplet splitting (eV) for the LS states in NSF_3 and OPF_3

state	NSF_3	OPF_3 [166]	difference
$^1A_1$ ($e \rightarrow e^*$)	2.310	1.870	0.440
$^1A_1$ ($a_1 \rightarrow 2a_1^*$)	1.734	1.747	0.013

8. Nitrogen, Oxygen, Phosphorus and Sulfur K-Shell Photoabsorption Spectra of NSF_3 and YPF_3 (Y = O, S, nothing) Molecules

8.1. Introduction

In the previous Chapter the S(2p) photoabsorption spectrum of NSF_3 was investigated. Like the P(2p) spectra of the phosphorus compounds PF_3, OPF_3 and SPF_3 [166] this molecule displays LS coupled states in the S(2p) pre-edge region. In this chapter we continue the study of the electronic structure of these four molecules. The phosphorus, sulphur and oxygen K-edge spectra are presented. Differences in the respective spectra give further insight into how the chemical environment affects the electronic structure and orbital relaxation following K-shell excitation. With the exception of an oxygen K-edge (e 2e) study of OPF_3 [175] and recently an angle-resolved photodissociation study of the P(1s) edge of SPF_3 [176], these regions have not been investigated previously.

8.2. Experimental

All K shell photoabsorption spectra were measured as described earlier in Chapter 2 above. The gas pressure in the cell assembly was uniform throughout and between 0.20 and 0.26 torr. In the S(1s) region the energy scale was calibrated against the $S(1s) \rightarrow \pi^*(1b_1^*)$ transition at 2473.8 eV in the spectrum of SO_2 [177]. The P(1s) spectra were calibrated internally with respect to PF_3, which was in turn referenced to the main peak of the photoabsorption spectrum of solid $Na_4P_2O_7$ at 2152.40 eV [144] in a separate experiment in which both solid samples and the gas cell were assembled as a contiguous unit. The O(1s) spectral region was calibrated against the $O(1s) \rightarrow \pi^*$ transition energy for O_2 at 530.9 eV [72]. All spectra were normalized by taking the ratio of the measured electron currents of the two cells—i_1/i_2.

The N(1s) spectrum of NSF_3 was collected using the new SGM beamline of CSRF. The cell setup was as described above, except that smaller cells were used (length = 12.5

cm, inner diameter = 0.4 cm, absorption length between the cells = 12.5 cm). A carbon foil window isolated the cells from the monochromator. The monochromator exit slit was set at 10 μm to give a photon resolution of 0.06 eV. The gas pressure in the cells was approximately 0.05 torr. The N(1s) spectral region was calibrated with respect to the N(1s)→π^* ($v = 0$ peak) for N_2 at 400.868 eV [178]. The electron yield currents from each cell were added and the total current was normalized with respect to the gas pressure and the electron current in the synchrotron ring.

All relevant 1s ionization potentials, listed in Table 8-1, were obtained from the literature, [88, 89, 154] and Chapter 6. The S(1s) ionization potential of NSF_3, not listed in any of these sources, has been estimated at 2486.35 eV based upon the S(1s) and S(2p) chemical shift correlation determined by Sodhi and Cavell [89] and an average S(2p) ionization potential of 177.44 eV ($E_B(S(2p_{3/2})) + 0.4$ eV) (Chapter 6). The absolute binding energy of H_2S was 2478.43 eV [179].

PF_3 was obtained commercially from Ozark Mahoning and used without further purification. OPF_3 was prepared by Dr. J. Nielson from Los Alamos National Laboratory, NSF_3 by Zhenyu Yang and J. Thrasher at the University of Alabama, and SPF_3 at the University of Alberta by Dr. D. Kennepohl. These gases were used without any on-site purification, the purities having been ascertained by conventional laboratory techniques (IR, NMR) used by the providers.

8.3. Calculations

Assignment of the experimental peaks was supported by means of calculations of all relevant ionization potentials, photoabsorption transition energies and oscillator strengths using the MS-Xa method [103, 114] as outlined in Section 3.5 above.

To calculate the transition energies to antibonding orbitals, a Watson Sphere with a charge of +1.0 was applied to each molecule. The radius of the Watson Sphere was set equal to the radius of the corresponding outer sphere. To generate the calculated pre-edge photoabsorption spectra, Lorentzian curves were used, with the respective oscillator strength as area. The peak width at half-maximum was set to 0.7 eV in the N(1s) and O(1s) spectra, and 1.6 eV in the P(1s) and S(1s) spectra.

Ionization cross-sections as a function of photon energy were calculated for all relevant core orbitals, as described in Section 3.5, in order to assign the post-edge peaks. To identify these peaks, the cross-sections of the a_1 and e ionization channels were calculated separately. Their origin was deduced through comparison of these spectra with those obtained when some components of the basis set were excluded [111]. All cross-sections were obtained using the transition-state method [113]. The calculated pre-edge and post-edge spectra were connected through multiplication of the latter by a constant to obtain equal values for the cross-section at the ionization energy. The calculated K-edge spectra are shown in Figure 8-1 and Figure 8-2. Agreement with the experimental results (Figure 8-3 and Figure 8-4) is satisfactory. The peak structure due to transitions to molecular antibonding orbitals gives a fairly good representation of experiment, but the Rydberg peak intensities are often underestimated. The post-edge shape resonances are also predicted nicely. Their intensity relative to the pre-edge features, however, is generally underestimated.

Molecular orbital compositions were determined with Gaussian 94, using the 6-31G* (five d-functions) basis set and the Hartree-Fock level of theory at the optimized molecular geometry. Atomic orbital contributions (in %) to each molecular orbital were calculated from the normalized molecular orbital coefficients for the orthonormalized atomic orbital basis functions (see Section 3.6). The assignment of the virtual orbitals based on these molecular orbital compositions is listed in Table 8-4.

8.4. Results and Discussion

The group of unoccupied virtual orbitals in a molecule is composed of two main types: the antibonding valence shell molecular orbitals and the atomic like Rydberg orbitals. The former are centered around the atoms in a fashion similar to the occupied molecular orbitals, while the latter are diffuse, but centred on individual atoms. However, because of spatial overlap, orbitals with the same symmetry will intermix producing a set of valence shell-Rydberg hybrid orbitals.

PF_3 has trigonal pyramidal (C_{3v}) geometry and the other three molecules are C_{3v} symmetric tops. None of these compounds has unpaired electrons, hence the ground state for each is ${}^1A_1$. The core→mo* photoabsorption transitions must obey both dipole and spin selection rules. In C_{3v} symmetry, transitions from an ${}^1A_1$ ground state must give rise to ${}^1A_1$ or ${}^1E$ final states, and thus, the allowed transitions are: $a_1 \rightarrow a_1^*, e^*$ and $e \rightarrow a_1^*, a_2^*, e^*$. Since core orbitals are atomic in character, the further restriction of $\Delta l = \pm 1$ applies. Although nominally allowed, transitions to antibonding orbitals, which have little character of the correct angular momentum, tend to have small transition probabilities, and consequently low peak intensities are expected. Peaks in the K-edge spectra thus correspond to antibonding orbitals with relatively high p-character. Another factor affecting the transition probability is the spatial overlap of the two orbitals involved. The core orbital is localized on one particular atom and its spatial extent is inversely proportional to its ionization potential. That is, a 1s orbital of phosphorus will be smaller than a 1s orbital of oxygen. The overlap between a core orbital and Rydberg orbital will not be very great, leading to low transition probability and peak intensity. Only transitions to Rydberg orbitals centred on the atom probed are expected to be observed. In contrast, the valence shell character of the antibonding molecular orbitals leads to increased spatial overlap with the core orbitals, especially if the atom probed gives significant contribution to the virtual orbital, increasing the transition probability and hence peak intensity.

8.4.1. PF_3, OPF_3 and SPF_3

8.4.1.1. P(1s) spectra

The phosphorus K-edge spectra of all three compounds are shown in Figure 8-3. The peak energies, term values and their assignments based upon the Xα results are given in Table 8-5.

All three experimental spectra characteristically display one high intensity peak and a broad shape resonance in the continuum. This shape resonance corresponds to transitions to quasibound states where the electron is temporarily trapped by a potential barrier created by the other atoms. The shape resonance is the most intense in the spectrum of OPF_3. The high intensity pre-edge peak is due to the highly allowed P(1s)→1e* transition. This 1e* orbital corresponds to a P-F σ* orbital centered on phosphorus, it has at least

56% phosphorus p-character. This p-character is largest in PF_3 (74.3%) and decreases in both OPF_3 (66.2%) and SPF_3 (56.6%) as a result of delocalization onto the Group VI atom (OPF_3: 11.7% O-p, 0.8% O-d; SPF_3: 13.3% S-p, 4.4% S-d). The contribution of fluorine to the 1e* orbital is comparable in all three compounds (PF_3: 4.4% F-s, 10.3% F-p, 1.1% F-d; OPF_3: 5.4% F-s, 9.6% F-p, 1.4% F-d; SPF_3: 4.1% F-s, 9.8% F-p, 1.6%F-d).

Following the major 1e* peak, the spectrum of PF_3 has two more prominent and visible low intensity peaks which are then followed by a gradual decline in intensity into the ionization continuum. Transition energies to Rydberg orbitals can be estimated as explained in Section 3.7 above. The average values of the quantum defect δ for the Rydberg series of PF_3 were obtained from the valence→Rydberg transition energies [118]: 2.18 for ns, 1.79 for np and 0.02 for nd, ignoring the molecular field effects. The energies obtained from these values suggest that the second peak in the P(1s) spectrum of PF_3 corresponds to the P(1s)→4s transition, forbidden by the $\Delta l = \pm 1$ selection rule, but orbital allowed in the C_{3v} symmetry of the molecule. The other peak, however, does not fit any of these Rydberg series. Rather, it belongs to a series with $\delta = 1.51$. This shift in δ could represent the molecular field effect on the P(4p) Rydberg orbitals, splitting them into an a_1 and an e orbital. The Xα calculations predict only a single peak due to the P(1s)→$3a_1^*$ and P(1s)→2e* transitions following the main 1e* feature. The two low intensity P(1s)→$1a_1^*$ and P(1s)→$2a_1^*$ transitions fall between these two peaks. Based on their orbital composition $2a_1^*$ and 2e* correspond to the P(4s) and P($4p_{xy}$) Rydberg orbitals, respectively, while $3a_1^*$ is a hybridized P($4p_z$) orbital—it has 9.4% P-s character and 16.7% F-p character—due to spatial overlap with the P-F σ^* orbital of A_1 symmetry, $1a_1^*$. The latter orbital gains P-p character from the hybridization. All of these calculation results lead us to assign the second peak to the P(1s)→$1a_1^*$ and P(1s)→$2a_1^*$ transitions, while the third peak is assigned to the P(1s)→$3a_1^*$ and P(1s)→2e* transitions. Furthermore, the term value of the third peak, -2.20 eV, is comparable to those of the P(2p)→4p(e) transitions, -2.24 eV ($2p_{3/2}$) and -2.27 eV ($2p_{1/2}$) [166]. The tail of peak No. 3 leading to the ionization edge results from overlapping higher order Rydberg peaks of the P(1s)→np series (term values: 5p = -1.36 eV, 6p = -0.79 eV, 7p = -0.51 eV, 8p = -0.36 eV, 9p = -0.24 eV). The broad, low intensity post-edge peak results from the overlap of two shape resonances: the first is due to the a_1 channel and the other due to the e channel (Figure 8-1a). Both arise mainly from phosphorus p- and d-waves, indicating that they are P(1s)→p/d resonances. The a_1 resonance has lower energy, because the p_z and d_{z^2} orbitals of P point along the main C_{3v} axis. This minimizes interaction with the F atoms and leads to greater stabilization of these orbitals. This is also seen by the fluorine contribution to these two peaks. Only d-waves contribute to the a_1-resonance, while the e-resonance is also dependent on fluorine p-waves. The calculated spectrum also displays a sharp intensity decrease at the ionization edge in the a_1-channel. This has been assigned to the tail of the $3a_1$* pre-edge peak.

The P(1s) spectrum of SPF_3 also has several low intensity peaks following the P(1s)→1e* transition. However, in this case not all of the components are resolved. In particular, the first of these is but a shoulder on the second. The last two peaks already lie in the ionization continuum.

According to the Xα calculations peaks corresponding to the P(1s)→$1a_1$* and P(1s)→$2a_1$* transitions overlap with the main 1e* peak. This is then followed by a low intensity peak due to transitions to various Rydberg orbitals (2e*, $3a_1$*, 3e*, $4a_1$* and 4e*). Both $1a_1$* and $2a_1$* are molecular antibonding orbitals, centered on phosphorus and sulphur. The 2e* and 3e* orbitals are the hybridized P($4p_{x,y}$) and S($4p_{x,y}$) Rydberg orbitals, respectively, while 4e* is the P($3d_{xy,x^2-y^2}$) orbital. They are somewhat delocalized due to intermixing. Orbital intermixing occurs to much greater degree among the Rydberg orbitals of phosphorus and sulphur with a_1 symmetry. Based on the Xα results the experimental peak No. 2 has been assigned to the P(1s)→2e*, P(1s)→$3a_1$* and P(1s)→3e* transitions, while peak No. 3 is assigned to the P(1s)→$4a_1$* and P(1s)→4e* transitions.

This assignment disagrees with an earlier study [176] of the P(1s) edge using angle-resolved photodissociation. In that case, peak No. 2 was assigned to the P(1s)→$1a_1$*/P($4p_z$) transition, and peak No. 3 was deconvoluted into two and assigned to the P(1s)→$2a_1$* and P(1s)→P($5p_{x,y}$) transitions, respectively. This assignment was based upon GSCF3 [167, 168] calculations coupled with experimental measurements of the asymmetry parameter β [176]. The experimental partial and total electron yield spectra were measured using the PEPICO spectrometer described elsewhere [176]. Spectra were collected at two different orientations of the detectors with respect to the polarization of the light, 0° and 90° [176], achieved by connecting the spectrometer in two different orientations to the beamline. The β parameter for each transition was obtained from the difference and the sum of the intensity of the spectra collected at these two orientations. The partial ion yield spectra have low intensity and the differences in intensity for the two orientations are, for the most part, small. Also, the spectra for the two orientations were not measured simultaneously, as the spectrometer has only one detector for photoions. All these factors add uncertainty to the experimental values of the asymmetry factor β, which in turn adds uncertainty to the spectral assignment.

So, although the method for spectral assignment used herein is of lesser sophistication than the method employed previously [176], the results obtained cannot be dismissed out of hand. Further analysis of the P(1s) spectrum of SPF_3 is required for an accurate assignment of the pre-edge peak structure. This includes additional experimental PEPICO studies with improved signal-to-noise ratio for the partial ion yield spectra and simultaneous measurement of spectra at both orientations (0° and 90°) of the detector with respect to the polarization of the light. More detailed theoretical calculations of the P(1s) spectrum of SPF_3 are needed as well.

There are three resolved peaks above the ionization edge. The last of these can be deconvoluted into two, giving a total of four post-edge peaks. The first of these, peak #4, is assigned to a P(1s)→e* resonance (Figure 8-1b) corresponding to semibound P(1s)→p_x,p_y transitions. There is some p/d intermixing in the final state as evidenced by the influence of phosphorus d-waves on the peak shape and position. The experimental peak #5, also a P(1s)→e* resonance, is caused by transitions to mixed p/d states; and peak #6 corresponds to the P(1s)→$a_1$resonance, again involving mixed p/d states. The a_1 resonance has the highest energy since the p_z and d_{z^2} orbitals point directly at the sulphur atom. The p and d orbitals with e symmetry do not point directly at any ligand. Hence, they are more stable. As for PF_3 the calculations predict a sharp a_1-channel intensity decrease at the ionization edge. This has been assigned to the tail of the last pre-edge peak, which has some a_1 components.

In contrast to the other two spectra, the P(1s) spectrum of OPF_3 shows only a single peak following the 1e* transition, and even that peak is not fully resolved. Its term value (-2.50 eV) suggests that it corresponds to a P(4p) Rydberg peak with a quantum defect δ of 1.67, below the value of 1.79 proposed by Robin [118] for the P(np) orbitals. The Xα calculations predict two low intensity peaks due to the $P(1s)\rightarrow 1a_1^*$ and $P(1s)\rightarrow 2a_1^*$ transitions, the former preceding, the latter following the main peak. Both virtual orbitals correspond to σ^* antibonding orbitals centred on phosphorus; $1a_1^*$ has mainly P-s character (65.8%) and $2a_1$ mainly P-p character (69.8%). The presence of an unresolved low intensity peak corresponding to the $P(1s)\rightarrow 1a_1^*$ transition is indicated by the shape of the experimental spectrum preceding the main peak. The $P(1s)\rightarrow 2a_1^*$ transition, along with the P(1s)→4p Rydberg transitions, gives rise to the pre-edge feature following the main P(1s)→1e* peak.

The Xα calculation predicts one post-edge shape resonance, comprised of an e-channel and an a_1-channel peak (Figure 8-1c). Both are due to mixed phosphorus-p/d states. The calculated sharp a_1-channel intensity decrease at the ionization edge has been identified as the tail end of the $P(1s)\rightarrow 2a_1^*$ pre-edge peak.

8.4.1.2. O(1s)/S(1s) spectra

The oxygen and sulphur K-edge spectra of OPF_3 and SPF_3 respectively, are shown in Figure 8-4. Peak energies and their assignments based upon the Xα results are listed in Table 8-6.

The O(1s) spectrum of OPF_3 has two well separated peaks at 533.44 and 535.27eV, followed by a third peak at 536.18eV which is a partly resolved shoulder of peak #2. The present spectrum compares favourably with the spectrum obtained by Sodhi and Brion [175] determined by electron energy loss spectroscopy. In particular, the third peak has been resolved in our work, and thus its energy can now be determined accurately. Further, the shape of the spectrum following the third peak suggests the presence of a sequence of low intensity peaks leading up to the oxygen-1s ionization edge at 539.22eV, a feature not observed in the literature spectrum. The first of these appears at 537.13eV as a low intensity shoulder of the third peak. The spectrum also has a single post-edge peak with very low intensity. The second pre-edge absorption peak, having the highest intensity, results from the O(1s)→1e* transition. As already mentioned, the 1e* orbital (a P-F σ^* orbital) gained 11.7% O-p character due to delocalization. The O(1s)→$1a_1$* (σ^* with 4.6% O-p character) transition gives rise to first peak in the experimental spectrum. A transition to the $2a_1$* orbital is not observed as this orbital has very low O-p character (0.02%). The structure following the main O(1s)→1e* peaks results from an O(1s)→np Rydberg series. The first two features, peaks No. 3 and No. 4, have term values of -3.04 eV and -2.04 eV, respectively, leading to quantum defects of 0.88 and 0.42. The value suggested by Robin [118] sandwiches these two. The molecular field of the OPF_3 molecule splits the O(3p) level into an e (p_{xy}, perpendicular to the O-P bond) and an a_1 (p_z, parallel to the O-P bond) orbital, with the latter occurring at higher energy. So peak No. 3 has been assigned as the O(1s)→$3p_{x,y}$(e) transition and peak No. 4 as the O(1s)→$3p_z(a_1)$ transition. Peak No. 5 then results from the O(1s)→4p transition and peak No. 6 represents an overlap of higher order Rydberg transitions.

The experimental O(1s) spectrum of OPF_3 (Figure 8-4b) displays one post-edge peak, having a term value of approximately 4 eV. The Xα calculations (Figure 8-2b) predict three shape resonances with term values 2, 7 and 18 eV respectively; and the third peak has the largest intensity. Based upon the term values, the experimental shape resonance has been assigned as an overlap of the first two calculated peaks. Both correspond to transitions to oxygen p-type states. The former, an a_1-channel peak, is also dependent on phosphorus p- and d-waves and fluorine p-waves, the latter, an e-channel peak, only on fluorine p-waves.

The S(1s) spectrum of SPF_3, in contrast to the oxygen spectrum of OPF_3, has only one high intensity peak. However, this peak displays an inflection, and it may be justifiably deconvoluted into two components. These features are then followed by four low intensity peaks, all located in the ionization continuum. The first component peak of the main pre-edge feature results from the S(1s)→$1a_1$* and S(1s)→$2a_1$* transitions, while the second peak corresponds to the S(1s)→1e* and S(1s)→2e* transitions. The 2e* orbital, a P($4p_{x,y}$) Rydberg orbital, has 16.1% S-p character due to orbital intermixing. The flat section leading to the ionization edge represents various Rydberg peaks, which cannot be readily identified.

For SPF_3, the Xα calculations predict three high intensity resonances above the sulphur K edge, plus a low intensity a_1 resonance right at the edge. This a_1 resonance plus the first high intensity peak—a combined a_1/e resonance—were assigned to the experimental peak #4. The other two peaks—both e resonances—correspond to peaks #5 and #6, respectively. Both arise from phosphorus d-waves. The lower energy peak also depends on phosphorus p-waves and fluorine p-waves, while the higher energy peak depends on fluorine s-waves. Hence, they correspond to transitions to semibound states centred on the phosphorus atom.

8.4.2. The NSF_3 Molecule

The NSF_3 molecule is most interesting, being iso-electronic with OPF_3 and having a comparable molecular structure (Table 8-2). Both molecules are symmetric tops with C_{3v} symmetry. The S-F bond length is slightly longer and the N-S bond length slightly shorter than the corresponding P-F and O-P bond lengths in OPF_3. There is a notable decrease in the F-S-F bond angle compared to the F-P-F bond angle of OPF_3. Considering the close relationship, however these two molecules should have comparable electronic structures. Thus, the S(1s) and N(1s) spectra of NSF_3 should resemble the P(1s) and O(1s) spectra of OPF_3, which is, in fact, observed.

8.4.2.1.S(1s) spectrum

The experimental S(1s) spectrum of NSF_3 (Figure 8-3) displays striking similarities to the P(1s) spectrum of OPF_3. Both have two pre-edge peaks with a third unresolved peak preceding the main peak as indicated by the shape of the spectrum, and both have a broad structure in the ionization continuum. However, in NSF_3, peak #3 is resolved, and it is clear that the shape resonance is composed of, at least, two separate peaks. The assignment of the experimental peaks based upon the Xα calculation is listed in Table 8-5. As with PF_3 and SPF_3 the calculation results are in good agreement with the experimental data.

As with the other three molecules the main peak (#2) stems from the S(1s)→1e* transition. Again, the 1e* is an S-F σ* orbital with high sulphur p-character (46.4%) and there is significant delocalization onto nitrogen (28.3% N-p character). The second resolved experimental peak (No. 3) results from the overlap of several transitions, the most prominent being S(1s)→2e* (S(4$p_{x,y}$) Rydberg orbital) and S(1s)→4a_1* (S(4s)/S(4p_z)/S(3d_{z^2}) Rydberg orbital). The latter is delocalized due to orbital intermixing; it has 8.9% S-s, 40.6% S-p_z, 27.0 S-d_{z^2}, 9.8% N-p_z, 4.9% N-d_{z^2}, 2.9% F-p and 5.5% F-d character. The unresolved experimental peak No. 1 has been assigned to the S(1s)→1a_1* transition. This virtual orbital is a delocalized σ* antibonding orbital with mainly S-s (39.7%) and F-p (25.1%) character, hence the low peak intensity. No separate peak is observed for the S(1s)→2a_1* transition, it overlaps with the main S(1s)→1e* peak.

In the post-edge region, there are two resolved peaks; and the asymmetric tail of the second peak can be deconvoluted into two additional peaks. The Xα calculations predict two post-edge peaks, a relatively narrow e resonance followed by a broad a_1 resonance. These were assigned to experimental peaks #4 and #5, respectively. The a_1 resonance arises from transitions to mixed p/d states centred on sulphur and nitrogen. However, the origin of the e resonance is not clear. The calculations also predict a sharp a_1 channel intensity decrease at the ionization edge. Similar to the phosphorus compounds this has been assigned to the tail of the last pre-edge peak.

8.4.2.2.N(1s) spectrum

The N(1s) spectrum of NSF_3 has three resolved pre-edge peaks followed by a broad structure leading into the ionization continuum. There are also three post-edge shape resonance peaks. The first of these can be deconvoluted into two. As with OPF_3, the main peak (No. 2) corresponds to the N(1s)→1e* transition, however, here it has a high intensity shoulder resulting from the N(1s)→2a_1* (σ* with 0.02% N-p character) transition. The N(1s)→$1a_1$* (σ* with 9.6% N-p character) gives rise to peak No. 1. The remaining pre-edge features result from the N(1s)→np Rydberg series.

The Xα calculations predict two post-edge features, an e channel peak followed by an a_1 channel peak with much higher intensity. There is also a sharp intensity decrease at the ionization edge due to the a_1 channel. The relative peak intensities are reversed compared to the experimental results and the sharp decrease in intensity at the edge is not observed at all in the experimental spectrum. Both post-edge peaks represent transitions to semibound N(p) states; the e channel corresponds to $p_{x,y}$ states and the a_1 channel to p_z states. The experimental peaks No. 8 and No. 9 are assigned to the e channel resonance and peaks No. 10 and No. 11 to the a_1 channel resonance.

8.4.3. NSF_3 versus OPF_3

The comparison of NSF_3 to OPF_3 reveals some significant differences in the experimental photoabsorption spectra, which can be explained in terms of differences in electronic structure between these two molecules. The central atom 1s spectra are similar. Both spectra have three pre-edge peaks. However, they are better resolved in NSF_3 because of greater energy separation, and the relative peak intensities of peaks No. 1 and No. 3 are different. The first peak has slightly greater intensity in NSF_3 while the third peak has more intensity in OPF_3. The spectrum of OPF_3 displays a single, fairly prominent shape resonance in the ionization continuum, while the spectrum of NSF_3 has several resonances with lower intensity.

The spectra of the terminal oxygen or nitrogen atoms also have comparable features: three resolved peaks followed by a series of overlapping Rydberg peaks leading to the ionization continuum. Again the peaks are better resolved in NSF_3, and the N(1s)→$2a_1$* transition appears as a shoulder of the N(1s)→1e* transition. The relative intensity of the $1a_1$* peak is also different and so is the relative intensity of the first Rydberg peak. As with the central atom K shell spectra, there is a single post-edge peak in the O(1s) spectrum of OPF_3, and several peaks in the N(1s) spectrum of NSF_3, but here the peaks in the latter spectrum have higher intensity.

The increased spacing of the final states and the variations in relative peak intensity reflect the differences between the atomic components—i.e. the chemical environment, in part the well recognized electronegativity differences between oxygen and phosphorus in OPF_3 versus nitrogen and sulphur in NSF_3. Calculation of the atomic charges (Table 8-7) using Gaussian 94 [94] revealed comparable charge distributions. In both molecules all bonds are polar, the charge on the central atom is greater than +2.5 and the non-fluorine ligand has the largest negative charge. There are, however, notable differences as well. The charge on the central atom increased by 0.34 in OPF_3 relative to NSF_3. The corresponding increase in negative charge is distributed among the ligand atoms, but not evenly. The charge on each fluorine increased by 0.07 while the charge on oxygen is 0.11 larger than the charge on nitrogen. The polarity of all bonds, in particular O-P, increased. This is reflected by the atomic orbital compositions of the virtual orbitals. The 1e* exhibits greater delocalization onto nitrogen in NSF_3, 21.8% N-p character compared to 11.7% O-p character in OPF_3. Similarly, the $1a_1$* and $2a_1$* orbitals are more delocalized in NSF_3. Both have greater N-p character than the O-p character of their counterparts in OPF_3. Hence, the corresponding peaks have greater intensity in the spectrum of NSF_3. Likewise, $1a_1$* has greater central atom p-character in NSF_3 than OPF_3, and $2a_1$* has greater central atom p-character in OPF_3 than NSF_3, leading to the observed relative peak intensities of the corresponding photoabsorption peaks.

8.5. Summary

The central atom K shell spectra of all four compounds clearly show both the differences and the similarities in electronic structure in this set of related molecules. All have a high intensity pre-edge peak corresponding to the 1s→1e* transition. This is then followed by lower intensity peaks the structure of which is unique for each molecule because of small differences in the orbital character developed in each molecule. The $X\alpha$ calculations give an adequate representation of the experimental spectra allowing the components to be evaluated.

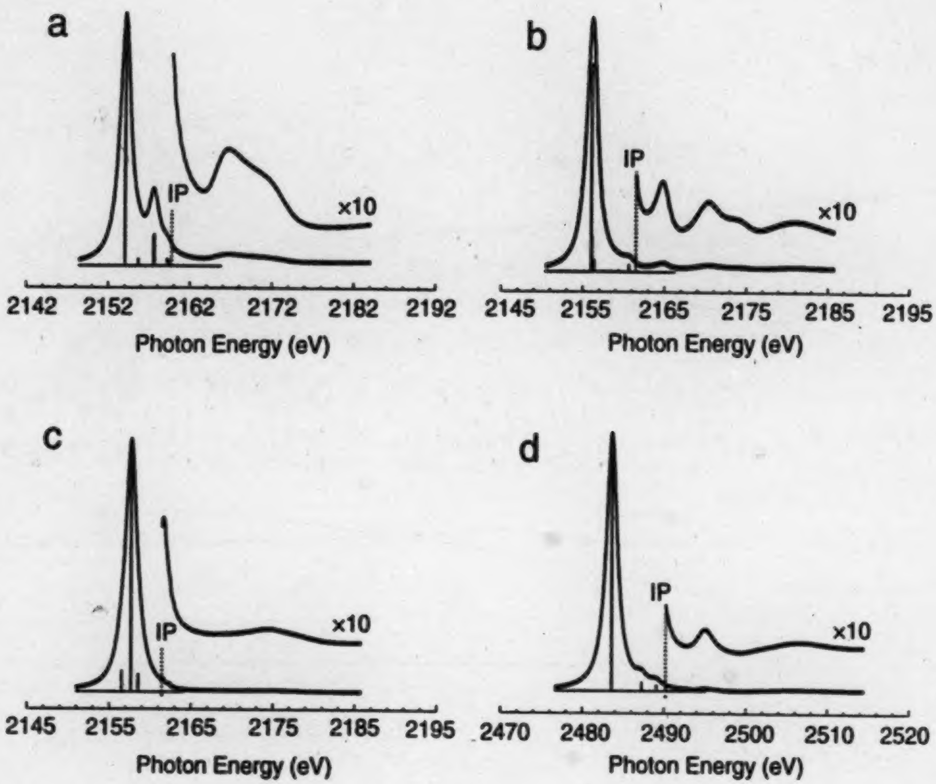

Figure 8-1: Central atom—phosphorus or sulphur—K shell spectra calculated with the Xα technique [103]. (a): PF_3 (b): SPF_3 (c) OPF_3 (d) NPF_3.

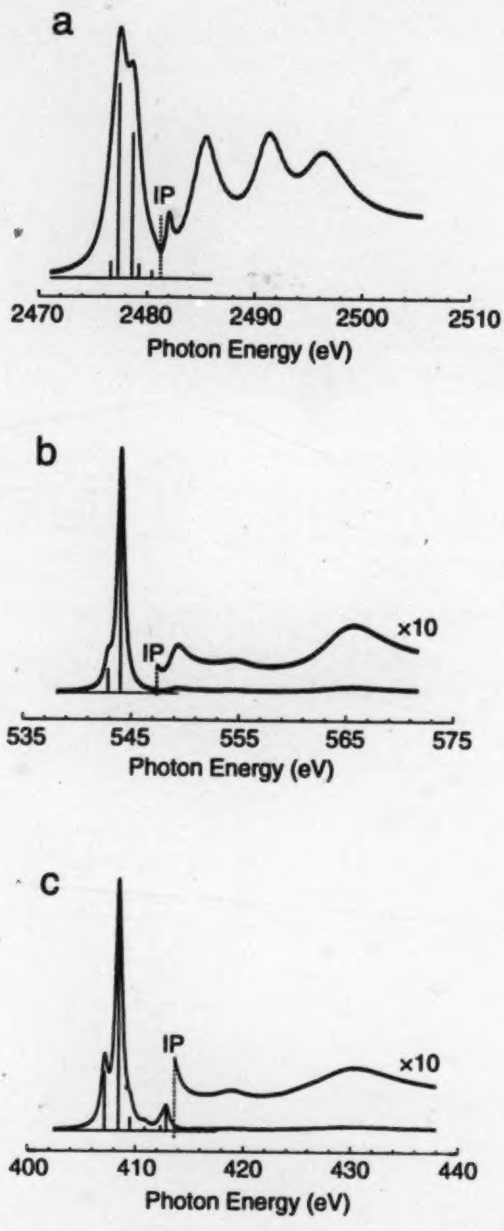

Figure 8-2: Terminal atom—nitrogen, oxygen or sulphur—K shell spectra calculated with the Xα technique [103]. (a): SPF_3 (b):OPF_3 (c): NSF_3.

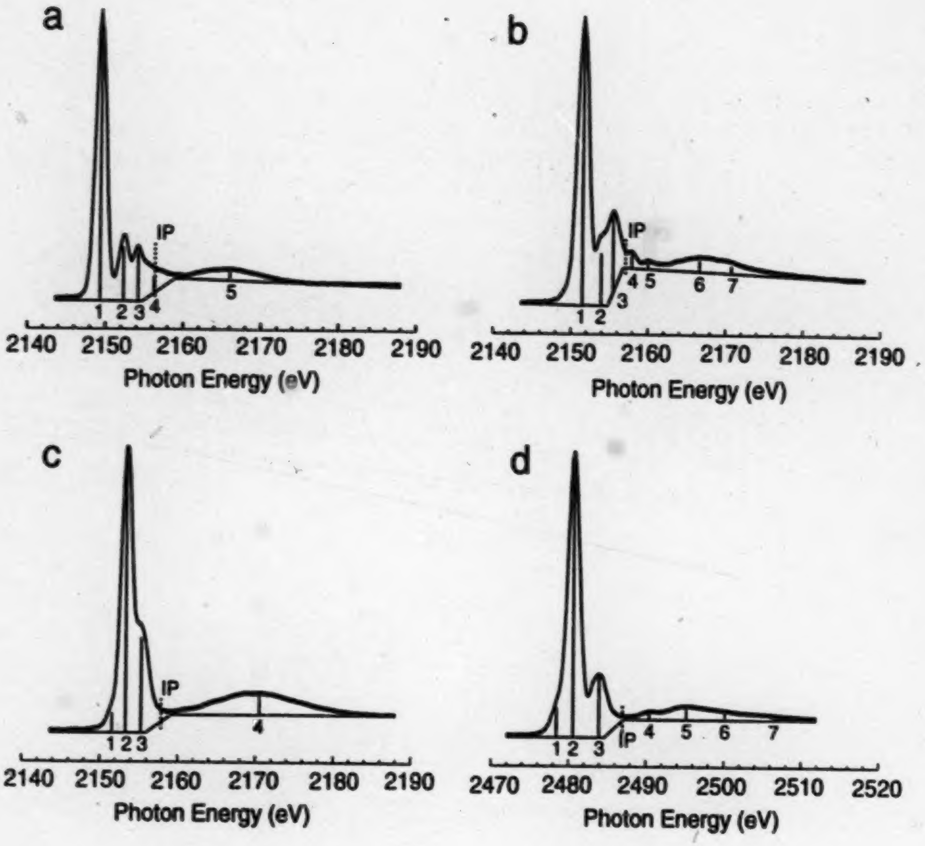

Figure 8-3: Experimental spectra of central atom—phosphorus or sulphur—K shell. The spectra were fitted with mixed Gaussian/Lorentzian curves. Vertical lines indicate the resulting peak positions and intensities. The peak energies, term values and their assignments are listed in Table 8-5. (a): PF_3 (b): SPF_3 (c): OPF_3 (d) NSF_3.

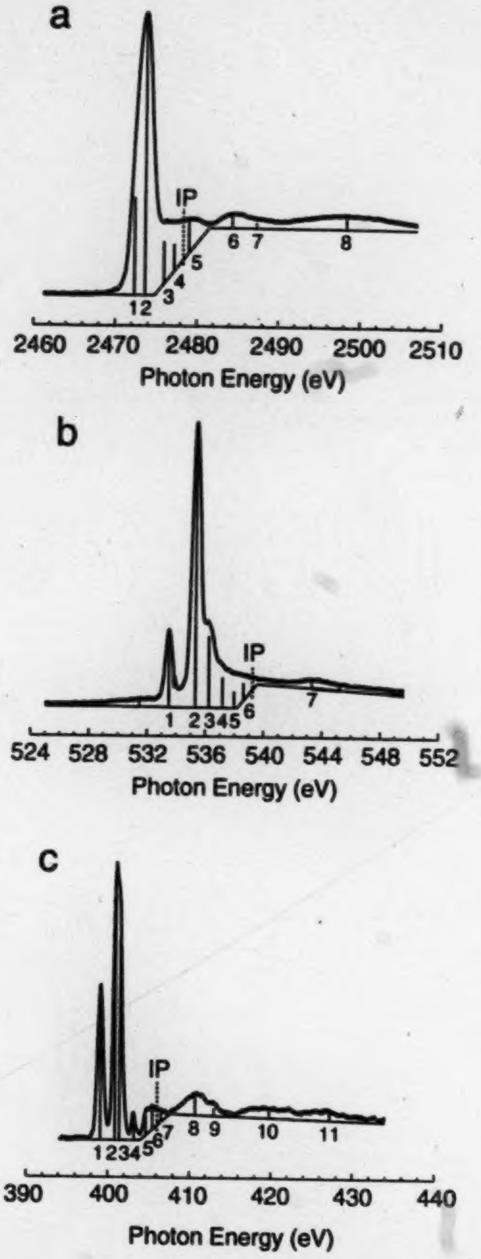

Figure 8-4: Experimental spectra of terminal atom—nitrogen, oxygen or sulphur—K shell. The spectra were fitted with mixed Gaussian/Lorentzian curves. Vertical lines indicate the resulting peak positions and intensities. The peak energies, term values and their assignments are listed in Table 8-6 (a): SPF_3 (b): OPF_3 (c): NSF_3.

Table 8-1: Core ionization potentials (eV)

orbital	PF_3	OPF_3	SPF_3	NSF_3
N(1s)	----	----	----	406.0(a)
O(1s)	----	539.22(b)	----	----
P(1s)	2156.36(c)	2157.84(c)	2157.08(c)	----
S(1s)	----	----	2478.27(d)	2486.35(e)

(a) reference [154]

(b) Chapter 6

(c) Reference [88]

(d) Reference [89]

(e) Estimated from the S(2p) ionization potentials as described in Section 8.2

Table 8-2: Molecular geometry

parameter[(a)]	PF_3	OPF_3	SPF_3	NSF_3
E-F	1.561 Å	1.522 Å	1.538 Å	1.5515 Å
E-T	---------	1.437 Å	1.849 Å	1.4157 Å
∠ F-E-F	97.7°	101.14°	98.5°	93.92

(a) For OPF_3 and SPF_3, E = P and T = O or S respectively,
for NSF_3, E = S, and T = N.

Table 8-3: alpha parameters and sphere radii

	PF_3	OPF_3	SPF_3	NSF_3
α	0.735182	0.736923	0.733226	0.737252
radii (au):				
Out	4.319	4.561	5.115	4.537
P	2.004	1.868	1.933	----
O	----	1.743	----	----
S	----	----	2.435	1.872
F	1.754	1.729	1.738	1.715
N	----	----	----	1.757

Table 8-4: Assignment of the virtual orbitals

PF_3			
$1a_1$*:	P-F σ*	1e*:	P-F σ*
$2a_1$*:	P(4s)	2e*:	P($4p_{xy}$)
$3a_1$*:	P($4p_z$)		
SPF_3			
$1a_1$*:	σ*	1e*:	P-F σ*
$2a_1$*:	σ*	2e*:	P($4p_{xy}$)
$3a_1$*:	P(4s,$4p_z$)	3e*:	S($4p_{xy}$)
$4a_1$*:	P(4s,$4p_z$), S($4p_z$)		
OPF_3			
$1a_1$*:	σ*	1e*:	P-F σ*
$2a_1$*:	σ*	2e*:	P($4p_{xy}$)
$3a_1$*:	P(4s)		
$4a_1$*:	P($4p_z$,$3d_{z^2}$)		
NSF_3			
$1a_1$*:	σ*	1e*:	S-F σ*
$2a_1$*:	σ*	2e*:	S($4p_{xy}$)
$3a_1$*:	S(4s,$4p_z$)	3e*:	S($3d_{xy,x^2-y^2}$)
$4a_1$*:	S(4s,$4p_z$,$3d_{z^2}$)		

Table 8-5: Central atom K shell photoabsorption peaks

PF_3

No.	Energy[a] (eV)	Term Value[b] (eV)	Assignment
1	2149.29	-7.07	1e*
2	2152.29	-4.07	$1a_1$*, $2a_1$*
3	2154.16	-2.20	2e*, $3a_1$*
4	2156.09	-0.27	overlap of P(1s)→np transitions (n}5)
	2156.36	0.00	IP
5	2166.03	9.67	P(1s)→a_1,e resonance

SPF_3

No.	Energy[a] (eV)	Term Value[b] (eV)	Assignment
1	2151.45	-5.63	1e*. $1a_1$*, $2a_1$*
2	2153.95	-3.13	2e*, $3a_1$*, 3e*
3	2155.46	-1.62	$4a_1$*, 4e*
	2157.08	0.00	IP
4	2157.88	0.8	P(1s)→e resonance
5	2159.97	2.89	P(1s)→e resonance
6	2166.64	9.56	P(1s)→a_1 resonance
7	2170.75	13.67	

Table 8-5, continued from previous page

OPF$_3$			
No.	Energy[(a)] (eV)	Term Value[(b)] (eV)	Assignment
1	2151.52	-6.32	1a$_1$*
2	2153.31	-4.53	1e*
3	2155.34	-2.50	2a$_1$*, P(4p)
	2157.84	0.00	IP
4	2170.48	12.64	P(1s)→a$_1$,e resonance

NSF$_3$			
No.	Energy[(a)] (eV)	Term Value[(b)] (eV)	Assignment
1	2478.47	-8.47	1a$_1$*
2	2480.55	-6.39	1e*, 2a$_1$*
3	2483.98	-2.96	2e*, 4a$_1$*
	2486.94	0.00	IP
4	2490.45	3.51	S(1s)→e resonance
5	2495.43	8.49	S(1s)→a$_1$ resonance
6	2500.14	13.20	
7	2506.39	19.45	

(a) The standard deviation in the transition energies is ±0.06 eV for the pre-edge peaks, ±0.38 eV for the post-edge peaks and ±0.05 eV for the ionization potentials.

(b) The standard deviation for the term values is ±0.11 eV for the pre-edge peaks and ±0.43 eV for the post-edge peaks.

Table 8-6: Terminal oxygen or sulphur K shell photoabsorption peaks

OPF_3

No.	Energy[a] (eV)	Term Value[b] (eV)	Assignment
1	533.44	-5.78	$1a_1$*
2	535.26	-3.96	1e*
3	536.18	-3.04	$O(3p_{x,y})$
4	537.18	-2.04	$O(3p_z)$
5	538.00	-1.22	O(4p)
6	538.72	-0.50	O(5p,6p,...)
	539.22	0.00	IP
7	543.32	4.1	O(1s)→e,a_1 resonance

SPF_3

No.	Energy (eV)	Term Value[b] (eV)	Assignment
1	2472.42	-5.62	1e*, $2a_1$*
2	2473.68	-4.45	1e*, 2e*
3	2475.83	-2.44	Rydberg Peaks
4	2477.17	-1.11	
	2478.27	0.00	IP
5	2478.95	0.68	S(1s)→e,a_1 resonance
6	2484.29	6.02	S(1s)→e resonance
7	2487.31	9.04	S(1s)→e resonance
8	2498.31	20.04	

Table 8-6, continued from previous page.

NSF$_3$			
No.	Energy (eV)	Term Value[(b)] (eV)	Assignment
1	399.02	-6.98	1a$_1$*
2	400.81	-5.19	1e*
3	401.35	-4.65	2a$_1$*
4	403.12	-2.88	N(3p)
5	404.59	-1.41	N(4p)
6	405.30	-0.70	N(5p)
	406.00	0.00	
7	406.16	0.16	O(1s)→e,a$_1$ resonance
8	410.88	4.88	N(p$_{xy}$)
9	413.43	7.43	resonance
10	420.06	14.06	N(p$_z$)
11	427.17	21.17	resonance

(a) The standard deviation in the transition energies is ±0.06 eV for the pre-edge peaks, ±0.38 eV for the post-edge peaks and ±0.10 eV for the ionization potentials.

(b) The standard deviation for the term values is ±0.16 eV for the pre-edge peaks and ±0.48 eV for the post-edge peaks.

Table 8-7: Calculated Atomic Charges with Gaussian 94

(HF, D95* basis set, experimental geometry, natural charges [151])

NSF_3	Charge	OPF_3	Charge
S	2.61	P	2.95
N	-1.03	O	-1.14
F	-0.53	F	-0.60

9. Comparative Oxygen 1s Photoabsorption Spectra of SO_2 and NO_2

9.1. *Introduction*

Herein we explore the bonding models for hypervalent molecules with the aid of core photoabsorption spectroscopy and *ab initio* and MS-Xα calculations. SO_2 has been the object of numerous investigations [43, 153, 177, 180-188]. However, most of these studies involved the S(1s), S(2p) and valence shell regions. Relatively little work has been done on the O(1s) edge [180, 181].

The installation of the High Resolution Monochromator (HRMON) beamline at the Synchrotron Radiation Center (SRC) in 1994 provided an opportunity to expand our investigations of hypervalent compounds to the oxygen 1s edge region with high resolution photoabsorption and photoelectron spectroscopy [189-191]. In this Chapter we present the O(1s) photoabsorption spectra of SO_2 and NO_2. The latter compound is not hypervalent, but it has a similar molecular structure, being a bent triatomic molecule with terminal oxygen atoms. However, there are significant differences in electronic structure between the two compounds. The nitrogen valence shell is the L-shell, which does not provide any possibility of d-orbital bonding. In the sulphur compound, however, the valence shell is the M-shell, so the sulphur atom has extra core electrons and unoccupied d-orbitals, which could possibly be involved in bonding. Furthermore, NO_2 with 17 valence electrons is a radical, while SO_2 with 18 valence electrons is a normal diamagnetic molecule. The oxygen 1s spectra of each molecule were examined to explore contrasts in behaviour which would reflect differences in chemical bonding and in particular the question of involvement of d-orbitals in bonding of SO_2.

9.2. *Experimental*

Chapter 2 describes the experimental procedure used to collect the oxygen K shell spectra of these two molecules. The pressure in the cells was approximately 200 mtorr. The position of the $1s \rightarrow \pi^*$ transition of molecular oxygen [72] measured in the same series of experiments was used to calibrate the photon energy scale. The spectra were normalized by taking the ratio i_1/i_2 of the electron currents from each cell.

The chemicals were obtained commercially from Matheson (SO_2: 99.98%; NO_2: 99.5%) and used without further purification. The radical NO_2 molecule dimerizes to N_2O_4 (equilibrium constant $K_p = 1.16 \times 10^{-5}$ $mtorr^{-1}$ at 298.15 K [192]). At the total gas pressure used (200mtorr) 99.54% of the gas is in the form of NO_2. Thus, the experimental oxygen 1s spectrum obtained is dominated by NO_2 with no significant interference from N_2O_4.

The O(1s) ionization potential (IP) of both compounds was obtained from the literature [154] (Chapter 6). Because of the unpaired electron in NO_2, oxygen 1s ionization gives rise to two final states, a singlet and a triplet, and hence two photoelectron peaks. Of these, the lower energy triplet peak (541.3 eV) has greater intensity [154].

9.3. Calculations

The oxygen 1s photoabsorption spectra of both compounds were calculated using the Xα technique [103], described in Section 3.5, in order to assign the experimental peaks. The atom positions based upon the experimental geometry [96, 97] as well as sphere radii and α parameters are listed in Table 9-1.

NO_2 is an open shell molecule with an unpaired electron. So, the calculations necessarily included the electron spins, referred to henceforth as α and β spins. Ionization potentials and transition energies to the symmetry and spin allowed final states were calculated using the transition state method. The oscillator strengths of these transitions were calculated from the transition state potential using the method developed by Noodleman [114]. A Watson sphere [103, 113] was employed to stabilize the final states of the bound transitions. The charge on this sphere was +2.0 and its radius was slightly larger than that of the corresponding outer sphere: 3.50 for NO_2 and 4.26 for SO_2. The ionization cross-section of the oxygen 1s orbitals was obtained according to the method developed by Davenport [116] using the transition state potential [113]. To determine the origins of these features, for example oxygen p-waves, the method developed by Powis [111] was employed.

To obtain the calculated pre-edge spectra, all transitions were assumed to give rise to pure Gaussian peaks with an area given by the oscillator strength. The full width half maximum (FWHM) of the pre-edge peaks was taken to be equal to the FWHM value of the corresponding experimental peak. To match the regions, the calculated pre-edge spectrum was truncated at the ionization edge, and replaced by the calculated post-edge spectrum at higher energies. These two spectra were connected through multiplication by a constant to obtain equal values for the cross-section at the ionization potential. These combined calculated photoabsorption spectra (Figure 9-1), were compared to the experimental results.

The calculated pre-edge spectra include transitions to virtual orbitals whose calculated energy lies slightly above the ionization edge (< 0.5eV), but the corresponding experimental peaks actually lie below the edge. This is an artifact of the Watson Sphere which is required to stabilize the wavefunctions for the high-energy orbitals, a phenomenon discussed in greater detail in Section 12.1.4 of the thesis. The charge chosen in this study was sufficient to calculate all final states with transition energies less than IP + 2.5 eV.

Gaussian 94 [94] was employed to calculate the harmonic vibrational frequencies for both molecules in the electronic ground state and the $B_1(O(1s)\rightarrow 1b_1^*)$ excited state. The geometries were optimized using the Hartree-Fock [79] calculation method and the 6-31G* basis set. To account for anharmonicity and electron correlation contributions the frequencies obtained were scaled by a factor of 0.8953 [193]. For the oxygen core excited states the equivalent core species, simulated by replacement of one oxygen with fluorine, was used. The additional electron introduced by fluorine was placed in the $1b_1^*$ orbital. The use of fluorine (19 amu) rather than oxygen (16 amu) for the excited state will perturb the frequency values. To determine the extent of this mass effect the ground state calculations were performed for the six species: $^{16}ON^{16}O$, $^{16}ON^{17}O$, $^{16}ON^{18}O$, $^{16}OS^{16}O$, $^{16}OS^{17}O$ and $^{16}OS^{18}O$. The increase in mass of a single oxygen consistently led to a decrease in calculated frequency; the maximum was 34 cm^{-1} (0.004 eV), less than the difference between calculations and experimental data [194, 195] (Table 9-4). Considering the results obtained for isotope substitution in the ground state, it is estimated that the difference in a species with ^{19}F and one with ^{16}F would be at most 50 cm^{-1} (0.006 eV), insufficient to significantly affect the calculation results (Table 9-4). Hence, no correction was made for the mass difference between oxygen and fluorine.

To determine the identity of the molecular orbitals the compositions of all valence and virtual orbitals were calculated for the ground state configuration of the molecule. The molecular orbital coefficients (c'_i) for the orthonormalized atomic orbital basis functions (Section 3.6) of the molecular orbitals were obtained at the optimized geometry (Hartree-Fock theory, 6-31G* basis set). From the orthonormalization requirements the contribution in % to the molecular orbital ϕ_j by atomic orbital ψ_i is given by $|c'_i| \times 100$. For NO_2 the reported molecular orbital compositions represent an average value for the two spin orbitals.

9.4. Results and Discussion:

9.4.1. Molecular Structure

The two compounds NO_2 and SO_2 have similar molecular structure. Both are bent molecules with terminal oxygen atoms belonging to the point group C_{2v}. However, the S-O bond length is approximately 0.5Å longer, while the O-S-O bond angle is about 20° smaller than the corresponding values in NO_2. The ground state configurations obtained by Xα are:

SO_2: $(S(1s\text{-}a_1))^2\ (O(1s\text{-}a_1,b_2))^4\ (S(2s\text{-}a_1))^2\ (S(2p\text{-}a_1,b_1,b_2))^6\ /\ (1a_1)^2\ (1b_2)^2\ (2a_1)^2\ (2b_2)^2\ (3a_1)^2\ (1b_1)^2\ (1a_2)^2\ (3b_2)^2\ (4a_1)^2\ /\ (1b_1{*})^0\ (1a_1{*})^0\ (2b_1{*})^0\ (2a_1{*})^0\ (1b_2{*})^0\ (3a_1{*})^0\ (3b_1{*})^0\ (2b_2{*})^0\ (1a_2{*})^0\ (4a_1{*})^0$

NO_2: $(N(1s\text{-}a_1))^2\ (O(1s\text{-}a_1,b_2))^4\ /\ (1a_1)^2\ (1b_2)^2\ (2a_1)^2\ (2b_2)^2\ (3a_1)^2\ (1b_1)^2\ (1a_2)^2\ (4a_1)^2\ (3b_2)^1\ /\ (1b_1{*})^0\ (1a_1{*})^0\ (2b_1{*})^0\ (2a_1{*})^0\ (1b_2{*})^0\ (3a_1{*})^0\ (3b_1{*})^0\ (2b_2{*})^0\ (1a_2{*})^0\ (4a_1{*})^0$

To simplify comparison between the two molecules, the numbering is restarted at one for each virtual orbital set. The orbital composition of the valence shell is similar. $1a_1$ and $1b_2$ are the oxygen 2s orbitals. Both experience significant delocalization onto the central atom, $1a_1$ to greater extent than $1b_2$. The $2b_2$ orbital represents one central atom - oxygen sigma bonding orbital. It is centered on oxygen (SO_2: 13.8% S-p, 13.8% O-s, 71.1% O-p; NO_2: 16.5% N-p, 19.2% O-s, 63.1% O-p). $1a_2$ and $3b_2$ are oxygen 2p orbitals, and $1b_1$ is a π bonding orbital (SO_2: 40.8% S-p, 1.0% S-d, 56.9%O-p, 1.4% O-d; NO_2: 43.1% N-p, 0.4% N-d, 54.5% O-p, 2.0% O-d). The remaining three occupied valence shell orbitals—$2a_1$, $3a_1$ and $4a_1$—are all delocalized and thus cannot be readily identified. The calculations predict the occupied valence shell orbitals to have some d-character, however even S-d character in SO_2 is less than 10% in any given molecular orbital (N-d character is less than 7.0% and O-d character less than 3.0%). So, the sulphur d-orbitals play only a minor rôle in the chemical bonding of SO_2.

The first virtual orbital—$1b_1$*—is a π* molecular antibonding orbital (SO_2: 55.6% S-p, 2.7% S-d, 40.6% O-p, 1.1% O-d; NO_2: 49.5% N-p, 1.0% N-d, 44.4% O-p, 4.6% O-d), and the next two virtual orbitals—$1a_1$* and $1b_2$*—represent σ type molecular antibonding orbitals. In SO_2 both are centered on the central atom ($1a_1$*: 18.6% S-s, 43.8% S-p, 13.7% S-d, 9.6% O-s, 13.4% O-p 0.9% O-d; $1b_2$*: 68.4% S-p, 12.1% S-d, 8.7% O-s, 10.0% O-p, 0.7% O-d), but they are more covalent in NO_2 ($1a_1$*: 21.4% N-s, 15.0 %N-p, 16.4% N-d, 15.2% O-s, 22.3% O-p, 9.7% O-d; $1b_2$*: 53.5% N-p, 8.7% N-d, 19.4% O-s, 14.4% O-p, 4.1% O-d). The remaining virtual orbitals correspond to Rydberg orbitals, most centered on the central atom. The identities of the valence and antibonding orbitals as determined by the Gaussian-94 *ab initio* calculations are summarized in Table 9-2.

The predicted ground state electron configuration by Xα for the NO_2 molecule with a singly occupied $3b_2$ (O-2p) orbital is surprising. A configuration placing the unpaired electron in the delocalized $4a_1$ orbital would be expected to have greater stability (lower energy) and in fact, *ab initio* calculations with Gaussian 94 [94] (HF calculation, 6-31G* basis set) predict precisely such a configuration. It is also the accepted configuration for the ground state NO_2 molecule [196, 197]. The Xα calculations also predict oxygen 1s ionization cross-sections, which differ from the experimental result. The strong line in the experimental spectrum corresponds to the lower energy ionization leading to the triplet state [154]. However, the Xα calculation predicts the higher energy singlet peak to have greater intensity. At present a cause for these deviating Xα results is not known.

An advantage of the Xα method [103] is the ability to perform the calculations for any electronic state of the molecule. Unlike Gaussian 94 [94], for example, our Xα program [146] does not rearrange the electron populations of the molecular orbitals to obtain the lowest energy electronic state. Rather, the originally specified electronic configuration is retained. Hence, the oxygen 1s spectrum of NO_2 could easily be calculated using both the above $^2B_2$ configuration and the $^2A_1$ configuration from the literature [196, 197] as initial state. The total electron energy difference between these two states was calculated (Xα) to be 4.18 eV. The oxygen 1s spectra obtained for each configuration are shown in Figure 9-1. The main difference between them is the relative position and intensity of the peak corresponding to the transition to the singly occupied valence orbital, as expected. The calculated term value increases by 1.6 eV (Table 9-5) and its intensity decreases (Figure 9-1). To a lesser degree this also applies to the $O(1s)\rightarrow 1b_1^*$ transition of the α electron. The relative intensities of the two $1b_1^*$ peaks are reversed as well. The other peaks also shift towards lower energy (Table 9-5), but because the O(1s) ionization potential also decreases, the term values for most of these peaks remain fairly constant. The relative peak intensities alter slightly as well (Figure 9-1).

For analysis of the experimental spectrum, the calculation results employing the $^2A_1$ initial state of NO_2 were used. The ground state of SO_2 is $^1A_1$. The relative energies of the occupied valence and unoccupied virtual orbitals in the initial ground state of the molecules are shown in Figure 9-3. According to the dipole selection rules for the photoabsorption process the final state must be $^1A_1$, $^1B_1$ or $^1B_2$ for SO_2 and $^2A_1$, $^2B_1$ or $^2B_2$ for NO_2. Because of the spin transition restriction $\Delta s = 0$ (Section 1.2), only those final excited states of NO_2 which do not involve the flipping of an electron spin are allowed. Since the oxygen 1s orbitals have a_1 and b_2 symmetry in both compounds, the symmetry allowed transitions are $a_1\rightarrow a_1,b_1,b_2$ and $b_2\rightarrow a_1,a_2,b_2$ for both molecules. The angular momentum selection rule $\Delta l = \pm 1$ (Section 1.2) requires that transitions to antibonding orbitals with large p-character will have greater oscillator strength than those to orbitals with little p-character.

9.4.2. Experimental Spectra and Assignment

The experimental oxygen 1s spectra of SO_2 and NO_2 are shown in Figure 9-2 and the peak assignments based upon the Xα results are shown in Table 9-3. The resolution of both spectra is comparable to that of previous ISEELS work [181, 198]. Both spectra display a high intensity O(1s)→$1b_1$* transition, followed by a group of overlapping lower intensity peaks leading up to the ionization edge. Also both spectra have a broad shape resonance in the ionization continuum, which lies less than 5eV above the ionization edge. The spectrum of NO_2 has one additional peak at lower energy than $1b_1$* due to the O(1s)→$4a_1$ transition, not observed in SO_2 because in this case the $4a_1$ orbital is filled. The shape of the $1b_1$* peak is asymmetric; there is a slight tail towards higher energy. In consequence, an adequate fit could only be obtained if it was deconvoluted into two (NO_2) or three (SO_2) peaks as shown in Figure 9-2. The energy difference between these peaks is 0.32 eV (average value) for SO_2 and 0.56 eV for NO_2.

Because of the spin interaction of the three unpaired electrons in the final state, the O(1s)→$1b_1$* transition in NO_2 leads to two distinct final electronic states depending upon the spin of the excited electron. Peaks No. 2 and No. 3 correspond to these two electronic transitions. In SO_2, on the other hand, the O(1s)→$1b_1$* transition leads only to a single final electronic state, hence only a single peak arises. The three peaks obtained from the deconvolution of the main feature could represent a vibrational progression with $\nu = 2581$ cm^{-1} (0.32 eV). The SO_2 molecule has three vibrational modes (Table 9-4). The largest frequency (1360 cm^{-1} [195]) occurs for the B_2 mode. The vibrational frequencies of the electronically excited final states can have different vibrational frequencies compared to the ground state, but an excited state vibrational frequency twice as large as the corresponding ground state frequency (Table 9-4) is not expected. Given the width of the peaks (Full Width Half Maximum = FWHM = 0.43 eV , average value), they could actually represent the second and fourth vibrationally excited states. In this case the frequency ν would be 1291 cm^{-1}. Considering the experimental frequencies of the ground state (Table 9-4) this value could correspond to the second A_1 (symmetric stretch) or the B_2 (antisymmetric stretch) vibrational mode of the excited electronic state. Comparing the calculated frequencies for the ground and excited state (Table 9-4), a decrease in frequency is observed for all three vibrational modes. This suggests excitation in the B_2 vibrational mode of the excited state. The optimized geometry of the core equivalent model (OSF radical) for the $(O(1s)^3\ 1b_1{*}^1)$ excited state has an increased bond length between sulphur and the core excited oxygen, and a decreased bond angle compared to the ground state. This shift in molecular geometry is similar to the atomic motions in the B_2 vibrational mode, favouring transitions to vibrational excited states of that mode. Vibrational progressions could conceivably be expected for the $O(1s)\rightarrow 1b_1{*}$ transition of NO_2 as well. The calculations predict larger frequencies than for SO_2 (Table 9-4). However, the overlap of two distinct electronic states tends to obscure any indication of vibrational structure.

The $1b_1{*}$ peak occurs further from the ionization edge in NO_2, which is predicted fairly well by the Xα calculations. The $1b_1{*}$ orbital has about 4% more O-p character in NO_2. This likely leads to the lower term value for the $O(1s)\rightarrow 1b_1{*}$ peak in the spectrum of NO_2.

The group of peaks leading up to the ionization edge in both spectra corresponds to transitions to σ type molecular antibonding and Rydberg orbitals. This peak structure is closer to the ionization edge in NO_2, and less well resolved. It also contains fewer peaks in the O(1s) spectrum of NO_2 than in the spectrum of SO_2. Assignment of these peaks is given in Table 9-3. As already mentioned, $1a_1{*}$ and $1b_2{*}$ are the σ type antibonding orbitals. For both compounds these have significantly less O-p character than $1b_1{*}$, and hence lower peak intensity. Again, the orbitals have greater O-p character in NO_2, but they are closer to the ionization edge. This is possibly caused by greater electron-electron repulsion, due to the unpaired electron in the $4a_1$ orbital.

The Rydberg orbitals are all predicted to belong to the central atom, but orbital intermixing in the molecular environment imparts some O-p character on them. Furthermore, they are diffuse, increasing spatial overlap with the O(1s) shell. The Rydberg peaks are further from the ionization edge in SO_2, because the energy difference between the M (n=3) and N (n=4) shells is less in sulphur than the energy difference between the L(n=2) and M shells in nitrogen. Also there is increased electron-electron repulsion between the two unpaired electrons in the Rydberg and the $4a_1$ orbitals in NO_2, increasing the energy of the final state, and hence the transition energy. For SO_2, three bound O(1s)→S(3d) Rydberg transitions are predicted, but they occur very close to the ionization edge. This further indicates that the sulphur 3d orbitals do not participate significantly in the chemical bonding of SO_2.

Both spectra (Figure 9-2) also have a broader peak in the ionization continuum. For NO_2 this peak is well separated from the pre-edge spectrum, peaking about 4 eV above the edge. It is caused by O(1s)→a_1^* transitions and highly dependent upon oxygen p-waves. Thus, it has been assigned as an a_1 type shape resonance caused by transitions to quasibound oxygen p-orbitals with a_1 symmetry. The excited states resulting from these transitions are temporarily stable (with very short lifetimes), because of the potential barrier created by the nuclei [199]. The excited electron needs to tunnel through this barrier to escape from the molecule.

In SO_2 the post-edge peak actually straddles the ionization edge (Figure 9-2). Thus, four peaks (No. 9 to No. 12) were required to obtain a proper fit to experiment for the post-edge structure. It is fairly broad, suggesting a very low potential barrier. The spectrum actually has a second post-edge peak (not shown on Figure 9-2) which is even broader and lower in intensity. The $X\alpha$ calculation results for the post-edge region agree reasonably well with experiment. There are two peaks, but the relative position of the first peak differs from experiment by approximately 5 eV. Both peaks are due to O(1s)→a_1^* transitions. O(1s)→b_2^* transitions also contribute to the second peak. Both are highly dependent upon oxygen p-waves. Considering these calculation results, the first experimental peak has been assigned as an a_1 type shape resonance caused by transitions to quasibound oxygen p-orbitals with a_1 symmetry, just as the peak in the spectrum of NO_2. The second peak has the same origins, but it results from the overlap of an a_1 and a b_2 shape resonance.

9.5. Summary

The oxygen 1s photoabsorption spectra of the triatomic molecules SO_2 and NO_2 were investigated to study their respective electronic structure. Both spectra have a high intensity O(1s)→$1b_1^*(\pi^*)$ transition and a cluster of σ^* and Rydberg peaks leading up to the ionization edge. Major differences in these spectra result from the presence of an unpaired electron in NO_2 leading to the extra O(1s)→4a_1 transition and two peaks for each allowed O(1s)→mo* transition.

There exist a greater number of bound O(1s)→Rydberg transitions in SO_2, because of a lower energy difference between the valence and the first Rydberg shells. Also, electron-electron repulsion between the two unpaired electrons in the 4a_1 and the mo* in the final state leads to an increased transition energy in NO_2 for the O(1s)→σ* and O(1s)→Rydberg transitions.

The a_1 shape resonance of SO_2 occurs closer to the ionization edge, is broader and has less intensity. This results from both the larger size of the SO_2 molecule and the decreased electronegativity of sulphur compared to nitrogen, which reduce the potential barrier seen by the escaping electron.

All observed differences between the two spectra can be explained in terms of differences in the valence shell population and molecular geometry. Sulphur 3d orbitals are not required to explain any features observed in the oxygen 1s spectrum of SO_2. Given its similarity to the spectrum of NO_2, we conclude that the two molecules have comparable electronic structures employing only valence shell s- and p-orbitals of the central atom in the molecular bond formation.

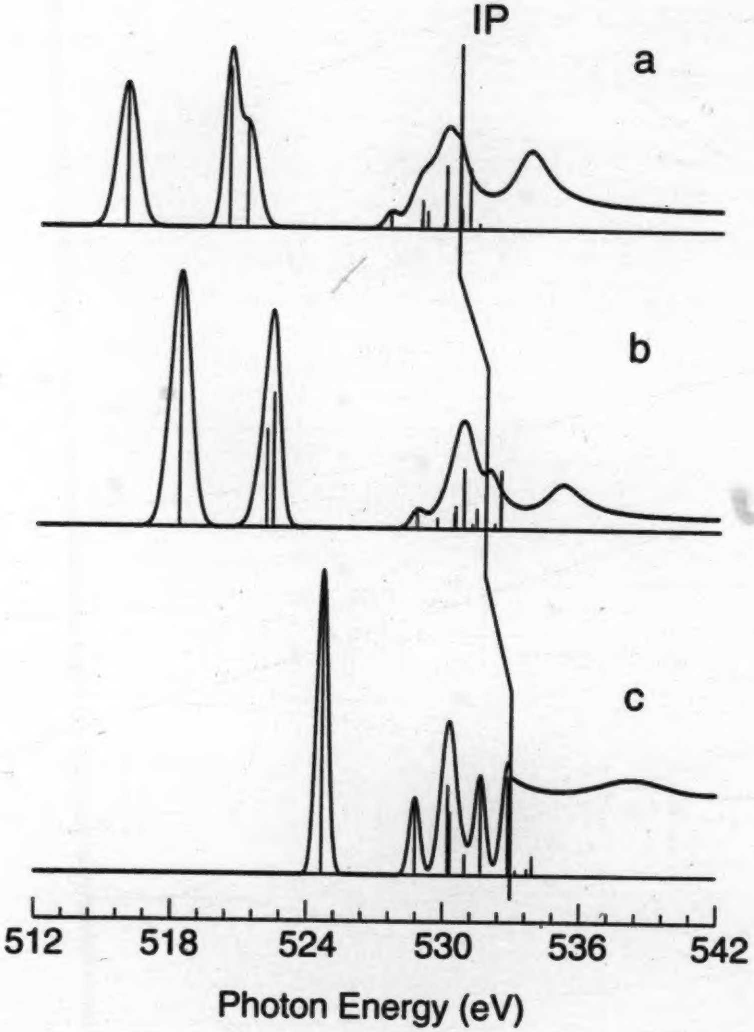

Figure 9-1: The calculated (Xα) oxygen 1s spectra: a. NO_2 with the $^2B_1$ state as initial state, b. NO_2 with the $^2A_1$ state as initial state and c. SO_2.

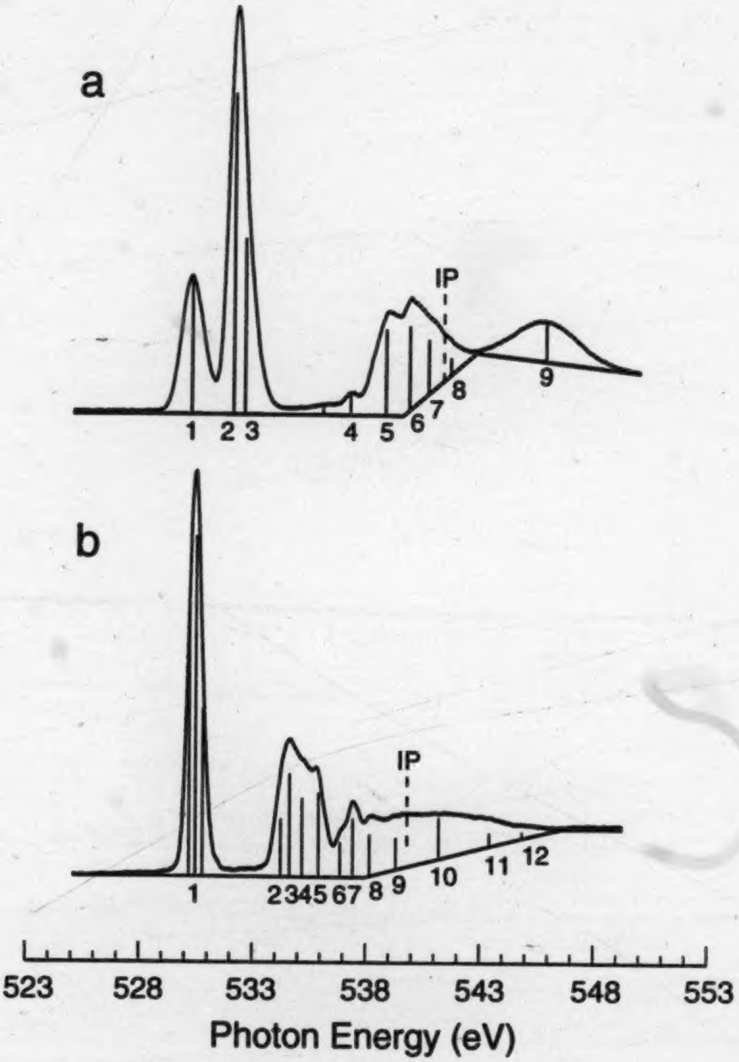

Figure 9-2: The experimental oxygen 1s spectra: a. NO_2 and b. SO_2.

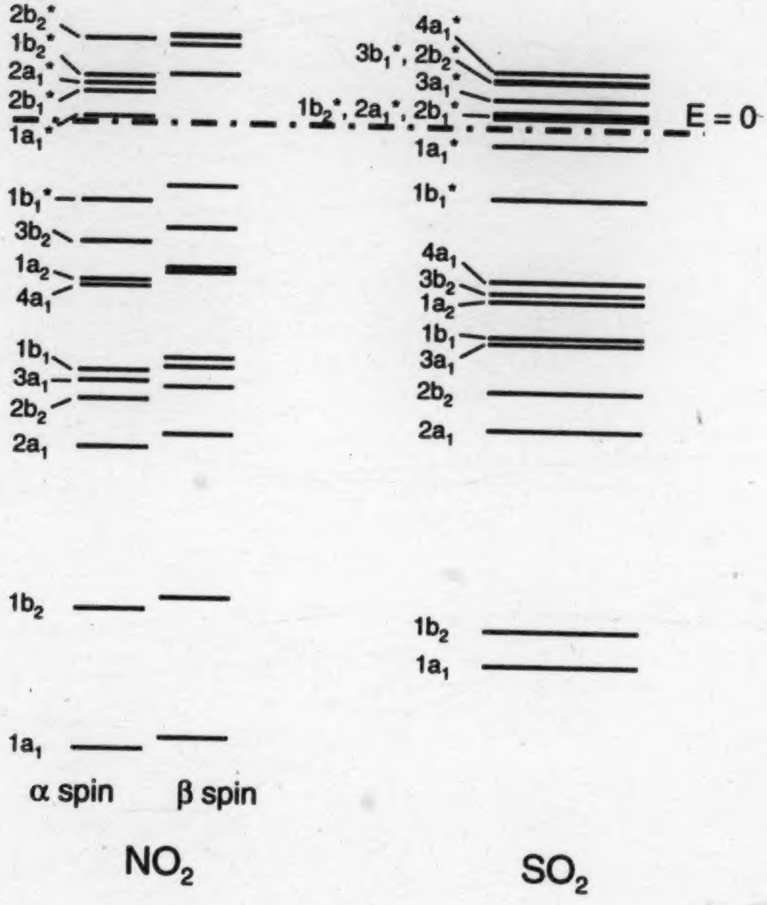
2b2*
1b2*
2a1*
2b1*
1a1*
1b1*
3b2
1a2
4a1
1b1
3a1
2b2
2a1
1b2
1a1
α spin
β spin
NO2
4a1*
3b1*, 2b2*
3a1*
1b2*, 2a1*, 2b1*
E = 0
1a1*
1b1*
4a1
3b2
1a2
1b1
3a1
2b2
2a1
1b2
1a1
SO2

Figure 9-3: The molecular orbital energy diagrams of NO_2 and SO_2, showing the relative positions of the valence and virtual orbitals in the initial electronic state ($^2A_1$ for NO_2 and $^1A_1$ for SO_2).

List of Figures

Figure 1-1: The photoelectron and photoabsorption processes. 12

Figure 1-2: Potential curves for ground state and excited state. 13

Figure 1-3: The valence shell photoelectron spectra of SO_2 and NO_2. 14

Figure 2-1: Diagram of a synchrotron ring. 27

Figure 2-2: A Hemispherical Analyzer. 28

Figure 2-3: Gas cell assembly and illustration of the cell parameters. 29

Figure 3-1: The arrangement of potential spheres in SO_2. 54

Figure 3-2: Muffin tin potential for N_2. 55

Figure 4-1: Resonance structures of PF_5. 71

Figure 4-2: The traditional three-centre-four-electron bonding model (left) and Ángyán's bonding modification [134] involving the central atom d_{z^2} orbital (right). 72

Figure 5-1: P(1s) Photoabsorption Spectra of PH_3, PF_5, $OPCl_3$ and PCl_3. 86

Figure 5-2: The correlation between the P(1s)→ 1e* transition energy shifts and the P(1s) ionization potential (IP) and KL_2L_3 ($^1D_2$) Auger shifts (eV) (relative to PH_3). 87

Figure 5-3: Correlation between the chemical shift (eV) and the sum of the ligand electronegativities, $\Sigma\chi_l$. 88

Figure 5-4: Correlation of the P(1s) Ionization Potential chemical shift (eV) with the Potential at the Nucleus shifts calculated from *ab initio* natural charges (Gaussian 94, D95* basis set). 89

Figure 5-5: Correlation between the calculated charge on the phosphorus atom (Gaussian 94, D95* basis set) and $\Sigma\chi_l$. 90

Figure 5-6: Correlation between the chemical shift (eV) and the calculated charge on the phosphorus atom (Gaussian 94, D95* basis set). 91

Figure 5-7: Correlation between the experimental P(1s)→ 1e* transition energy chemical shift (eV) and the Potential at the Nucleus shifts calculated from *ab initio* charges. 92

Figure 5-8: The correlation between the experimental chemical shifts and calculated values: ΔE_{SCF} method. 93

Figure 5-9: The correlation between the P(1s)→ 1e* experimental transition energy chemical shifts (eV) and the calculated values: CIS method. 94

Table 9-1: The parameters employed for the Xα calculations of NO_2 and SO_2.

	coordinates in au	sphere radius (au)	α
NO_2			
Out[(a)]	0.000, 0.000, -1.563	3.231	0.746676
N	0.000, 0.000, 0.000	1.491	
O	±1.628, 0.000, -1.564	1.603	
SO_2			
Out[(a)]	0.000, 0.000, 1.373	4.035	0.737897
S	0.000, 0.000, 0.000	1.945	
O	0.000, ±2.330, 1.373	1.705	

(a): Out refers to the Outer Sphere.

Table 9-2: The valence shell and virtual molecular orbitals of SO_2 and NO_2 as determined by Gaussian-94 [94].

orbital	SO_2	NO_2 ($^2A_1$)
$1a_1$	O(2s)	O(2s)
$1b_2$	O(2s)	O(2s)
$2a_1$	?	?
$2b_2$	S-O σ	N-O σ
$3a_1$	?	?
$1b_1$	S-O π	N-O π
$1a_2$	O(2p)	O(2p)
$3b_2$	O(2p)	O(2p)
$4a_1$	?	?
$1b_1$*	S-O π*	N-O π*
$1a_1$*	S-O σ*	S-O σ*
$1b_2$*	S-O σ*	S-O σ*
$2a_1$*	S(4s)/S(4p)	N(3p)
$2b_1$*	S(4p)	N(3p)
$3a_1$*	S(4p)/S(4s)	N(3s)
$2b_2$*	S(4p)/S(3d)	N(3p)
$3b_1$*	S(3d)	
$1a_2$*	S(3d)	
$4a_1$*	S(3d)	

Table 9-3: Experimental oxygen 1s photoabsorption peaks and their assignments based upon the Xα calculation results.

a) NO_2

No.	Energy (eV)[a]	Term Value (eV)[b] α spin state	β spin state	Assignment
1	530.15		-11.15	$4a_1(\beta)$ ($^1/_2$ filled)
2	531.99	-10.01		$1b_1^*(\alpha)$
3	532.55		-8.75	$1b_1^*(\beta)$
4	537.18	-4.82		$1a_1^*(\alpha)$
5	538.74	-3.26	-2.56	$1b_2^*(\alpha)$, $2b_1^*(\alpha)$, $1a_1^*(\beta)$
6	539.82	-2.18	-1.48	$2a_1^*(\alpha)$, $1b_2^*(\beta)$
7	540.68	-1.32	-0.62	$2b_1^*(\beta)$, $2b_2^*(\alpha)$
	541.3		0.00	triplet IP (strong line)[c]
8	541.56	-0.44		
	542.0	0.00		singlet IP (weak line)[c]
9	545.68	3.68	4.38	a_1 shape resonance

Table 9-3, continued from previous page

b) SO_2

No.	Energy (eV)(a)	Term Value (eV)(b)	Assignment
1	530.25	-9.58	$1b_1$*
	530.56	-9.27	(d)
	530.88	-8.95	(d)
2	534.20	-5.63	$1a_1$*
3	534.64	-5.19	$2a_1$*,$1b_2$*
4	535.24	-4.59	$2b_1$*
5	535.89	-3.94	$3a_1$*
6	536.89	-2.94	?
7	537.45	-2.38	$2b_2$*
8	538.16	-1.67	$3b_1$*,$4a_1$*, $1a_2$*
9	539.22	-0.61	
	539.83	0.00	IP(c)
10	541.10	1.27	a_1 shape
11	543.43	3.60	resonance
12	544.88	5.05	

(a) the standard deviation in the transition energies is ±0.08 eV.

(b) the standard deviation in the term values is ±0.18 eV.

(c) reference: [154]. The uncertainty is ±0.10 eV or better.

(d) these represent transitions to vibrational excited states (B_2 mode) of the $^1B_1$ (O(1s)→$1b_1$*) electronic state (Section 9.4.2)

(e) Chapter 6, the uncertainty is ±0.10 eV.

Table 9-4: The vibrational modes of SO_2 and NO_2, experiment [194, 195] and Gaussian 94 calculations [94] (optimized geometry, 6-31G* basis set) for the ground state and the $(O(1s)^3\ 1b_1{*}^1)$ excited state.

		Ground State		Excited State [(a)(b)]
	vib. mode	exp. ν (cm^{-1})	calc. ν (cm^{-1})	calc. ν (cm^{-1})
NO_2	A_1	640	746	480(T)
				505(S)
	A_1	1370	1448	968(T)
				865(S)
	B_2	1615	1694	1077(T)
				1073(S)
SO_2	A_1	525	532	395
	A_1	1150	1217	798
	B_2	1360	1404	1102

(a) These are the frequencies calculated for the $(O(1s)^3\ 1b_1{*}^1)$ excited state, using the equivalent core model.

(b) (T) stands for the triplet state and (S) for the singlet state.

Table 9-5: Calculated transition energies (eV) and term values (eV) from the O(1s) core to virtual orbitals, using the MS-Xα method.

orbital	SO_2		NO_2 ($^2B_2$)		NO_2 ($^2A_1$)	
	Energy	Term Value	Energy	Term Value	Energy	Term Value
IP	532.98		531.76(α)		530.43(α)	
			530.97(β)		530.09(β)	
$3b_2/4a_1$	-------	-------	518.24(β)	-12.73	515.77(β)	-14.32
$1b_1$*	524.66	-8.32	522.36(α)	-9.40	520.28(α)	-10.15
			522.08(β)	-8.89	521.07(β)	-9.02
$1a_1$*	528.78	-4.20	528.73(α)	-3.03	527.41(α)	-3.02
			529.61(β)	-1.36	528.76(β)	-1.33
$2a_1$*	530.21	-2.77	531.16(α)	-0.60	529.76(α)	-0.67
			532.15(β)	1.18	531.30(β)	1.21
$1b_2$*	530.31	-2.67	530.42(α)	-1.34	528.79(α)	-1.64
			530.78(β)	-0.19	529.84(β)	-0.25
$2b_1$*	530.96	-2.02	530.36(α)	-1.40	529.03(α)	-1.40
			531.35(β)	0.38	530.52(β)	0.43
$3a_1$*	531.66	-1.32				
$2b_2$*	532.86	-0.12	532.41(α)	1.10	530.88(α)	0.45
$3b_1$*	533.19	0.21				
$1a_2$*	533.91	0.93				
$4a_1$*	533.70	0.72				

10. A Synchrotron Study of the Oxygen 1s Photoabsorption Spectra of Sulphuryl Halides and their Methylated Derivatives SO_2XY ($X, Y = F, Cl, CH_3, CF_3$)

10.1. Introduction

The recent installation of the HRMON beamline at the Aladdin ring has made it possible to measure oxygen 1s edge spectra with high resolution. Thus, we were able to extend our investigation of the electronic structure of hypervalent sulphur compounds to include the K edge of the terminal oxygen atoms. Here, we present the oxygen 1s photoabsorption and photoelectron spectra of several sulphur (VI) oxyhalides and their methylated derivatives. The sulphur K edge of some of these compounds has been studied previously [200, 201]. However, to our knowledge the oxygen K edge of these molecules has not been reported previously.

10.2. Experimental

All experimental photoabsorption spectra were obtained as outlined in Chapter 2 above. The gas pressure in the cells was approximately 250 mtorr. The position of the $1s \rightarrow \pi^*$ transition at 530.9 eV [72] in molecular oxygen was used to calibrate the energy scale. The experimental peak energies were determined by fitting the spectra with Gaussian/Lorentzian (Voigt) curves. A step was put into the baseline at the approximate position of the ionization edge.

The ionization potentials were measured as described previously in Chapters 2 and 6.

All chemicals were obtained commercially, SO_2F_2 and SO_2FCl from the Ozark Mahoning Co., and the others from Aldrich. SO_2Cl_2 was frozen and than degassed in vacuum at liquid nitrogen temperatures to minimize the SO_2 content. The other compounds were used without further purification.

10.3. Calculations

In order to assign the spectra, the transition energies and their oscillator strengths were calculated using the Xα technique [103, 114] as explained in Section 3.5 of the thesis. Molecular geometries were obtained from molecular structure data tables [95-97]. A Watson Sphere [103, 113] was not necessary for stabilization of the virtual orbitals.

To obtain the calculated spectra, all transitions were assumed to give rise to pure Gaussian peaks with the oscillator strength as area. To generate the calculated spectra, the full width half maximum (FWHM) was taken to be equal to the average FWHM value of the peaks below the ionization edge in the corresponding experimental spectrum. These calculated photoabsorption spectra were compared to the experimental results and used in the assignment of the experimental peaks. The experimental peaks were then analyzed in terms of the orbital composition of the antibonding orbitals involved, as assessed from the Xα calculations.

Transition energies to atomic-like Rydberg orbitals were estimated as described earlier in Section 3.7. For the oxygen atom the values of the quantum defect δ, as suggested by Robin [118], are 1.0, 0.65 and 0.1 for the s–, p–, and d–Rydberg series, respectively. Based upon these values the O(1s)→3p Rydberg transition should occur at a photon energy about 2.46 eV below the ionization edge.

The post–edge oxygen 1s photoabsorption cross–section [116] was employed to assign the shape resonances in the ionization continuum. Identification of the resonant states was achieved by the method described by Powis [111] for PF_3. All these cross–sections were calculated in the transition state mode [113]. This cross–section calculation could not be done for SO_2Cl_2 because the program crashed due to non–zero imaginary components of the eigenvalues.

Generally the calculations reproduce the gross features of the experimental spectra. The oscillator strengths, and hence, the peak intensities are, however for the most part, incorrect. Also, some of the term values are underestimated, in particular the O(1s)→LUMO transition in SO_2F_2. The calculations predict an energy difference of 0.43 eV between it and the transition to the next higher lying antibonding orbital. The experimental energy difference between these transitions is, however, 1.06 eV.

The compositions of the molecular antibonding orbitals were determined from the normalized LCAO coefficients calculated with the Gaussian 94 program package [94]. These calculations were performed at the Density Functional level of theory using the hybrid B3LYP method. The exchange potential of the Hartree-Fock equation was approximated by Becke's three-parameter functional [87] with the gradient-corrected correlation functional of Lee et al. [157] and the correlation functional of Vosko et al [158] providing non-local and local correlation respectively. The molecular geometry of each species was optimized and the LCAO coefficients for the orthonormalized basis set (see Section 3.6) were determined at that optimized geometry to determine the molecular orbital compositions.

10.4. Results

The experimental spectra of all six compounds showing the near–edge region (all pre–edge peaks due to discrete transitions plus the first shape resonance in the ionization continuum) are presented in Figure 10-1, and the calculated pre–edge spectra are shown in Figure 10-2. Although the agreement between the experimental and calculated spectra is far from optimal for all six compounds, it is still possible to use the calculation results as a basis for assignment of the peaks in the experimental spectra. These assignments are listed in Table 10-1. In labeling the molecular orbitals, the count was restarted at 1 for the empty orbitals.

10.4.1. SO_2Cl_2

The experimental photoabsorption spectrum displays six pre–edge peaks followed by an intense shape–resonance in the continuum, 0.8 eV above the ionization edge. This compound was the least stable of the whole series and decomposed into SO_2 during the measurements, as illustrated by the marked changes seen in successive spectra of the same gas sample (Figure 10-3). The most notable of these changes is the increase in intensity of the peak at 530.4 eV which corresponds to the $O(1s)\rightarrow\pi^*(1b_1^*)$ transition of SO_2. Also the relative intensity of peaks #3 and #4 changes over time. This decomposition reaction of SO_2Cl_2 could occur by photodissociation or through reactions with the cell walls. The latter pathway seems more likely, because the gas pressure in the cell did not increase during the experiments, suggesting that the chlorine probably binds to cell materials. Further investigations are required to determine the actual reaction pathway.

The four main peaks in the spectrum are caused by transitions to the molecular antibonding orbitals (Table 10-1a). Of these, $1a_1$* and $1b_2$* represent the S–Cl σ* orbitals. Both experience delocalization onto oxygen, $1b_2$* to such an extent that the orbital is better described as Cl–S–O σ* than S–Cl σ*. The other two orbitals, $2a_1$* and $1b_1$*, are S–O σ* orbitals with some delocalization onto chlorine. Peak #5 with a term value of –2.10 eV is caused by the O(1s)→3p Rydberg transition ($\delta = 0.455$), and peak #6 represents an overlap of higher order Rydberg peaks.

10.4.2. SO_2FCl

The experimental spectrum shows three pre–edge peaks and a broad shape resonance above the ionization edge. The broad centre peak was deconvoluted into two, because this resulted in a better fit to the experimental spectrum. All peaks are shifted towards higher energy relative to the SO_2Cl_2 spectrum. This shift is less for peak #3 than for the others. As a result peaks #2 and #3 merge to form the broader centre peak. There was some SO_2 impurity present as evidenced by the small peak at 530.3 eV. However, no decomposition was observed during the experimental measurement.

Again the main peaks result from transitions to molecular antibonding orbitals (Table 10-1b). The 1a′* orbital is the S–Cl σ* orbital, 3a′* and 1a″* are both S–O σ* orbitals, and 2a′* is assigned as an O–S–F σ* orbital. The tail of peak #4 has been deconvoluted into another peak (#5) which corresponds to the O(1s)→3p Rydberg transition ($\delta = 0.557$).

10.4.3. SO_2F_2

This gas did not contain any SO_2 impurity, indicated by the absence of the SO_2 peak at 530.4 eV. No decomposition of the sample was observed during the experiment. The experimental spectrum has four major pre–edge peaks. These are followed by two broader low intensity peaks, one below and the other above the ionization edge. The transition energies of all these peaks are shifted towards higher energy compared to the peaks in the SO_2Cl_2 spectrum.

As with SO_2Cl_2 and SO_2FCl, the four high intensity peaks in the spectrum result from transitions to molecular antibonding orbitals. (Table 10-1c). All four orbitals are highly delocalized over the whole molecule, and are described as O–S–F σ^*. The $1a_1^*$ orbital has greater contribution from fluorine than oxygen, while for the others the contribution from oxygen exceeds the contribution from fluorine. The low intensity pre–edge peak has been deconvoluted into three. The first (#5) corresponds to the O(1s)→3p Rydberg peak (δ = 0.594), the second is the O(1s)→3d peak (δ = 0.018) and the last represents an overlap of higher order Rydberg transitions.

10.4.4. CH_3SO_2F

No decomposition of the sample was observed during the experiment, however, a very low intensity peak was observed at 530.7 eV, which we assigned to a small amount of impurity, possibly O_2. The lower electronegativity of the methyl group changes relaxation contributions and orbital compositions with the result that the antibonding orbital energy spread is compressed. Thus, only two pre–edge peaks are resolved. There is also a broad, low intensity peak above the ionization edge. The first of the pre–edge peaks, the LUMO peak, occurs at the same energy as the corresponding peak in the spectrum of SO_2F_2, while peak #2 falls between the next two main peaks of the SO_2F_2 spectrum, but slightly closer to peak #2 than peak #3. The virtual orbital involved in the transition leading to the first peak is 1a′*, a delocalized O–S–F σ^* orbital. The second main pre–edge peak originates from the overlap of the O(1s)→2a′* (O–S–C σ^*), O(1s)→1a″* (delocalized H–C–S–O σ^*) and O(1s)→3a′* (C–H σ^*) transitions. The shoulder at the high-energy end of peak #2 has been deconvoluted into a third peak. It corresponds to the broader low intensity peak #5 of the SO_2F_2 spectrum, an O(1s)→3p Rydberg transition (δ = 0.624).

10.4.5. CH_3SO_2Cl

There are three main pre–edge peaks. A fourth pre–edge peak appears as a barely resolved shoulder at the high-energy end of peak #3. There is also a broad peak just above the ionization edge. All of the pre–edge peaks are shifted towards higher energy compared to SO_2Cl_2. The intensity pattern is also different. In particular, the relative intensities of peaks #2 and #3 are reversed.

According to the Xα calculation results, the first pre–edge peak arises from the O(1s)→1a′* (S–Cl σ*) transition, and peak #2 from the O(1s)→2a′* (delocalized O–S–C–H σ*) transition. The overlap of the O(1s)→3a′* (delocalized C–S–O σ*), O(1s)→4a′*(C–H σ*) and O(1s)→1a″* (delocalized H–C–S–O σ*) transitions leads to the third main pre–edge peak of the spectrum. Peak #4 corresponds to the O(1s)→3p Rydberg transition ($\delta = 0.599$).

10.4.6. CF_3SO_2Cl

The spectrum displays three pre–edge peaks, the third of these straddles the ionization edge. The second pre–edge peak can be deconvoluted into four: two are barely separated at the top, the third causes the asymmetric tail, and the fourth is the low intensity shoulder. Again, peak #1 results from the O(1s)→1a′* (S–Cl σ*) transition. Peaks #2 and #3 correspond to the O(1s)→2a′* (O–S–C σ*) and O(1s)→3a′* (O–S–C σ*) transitions, respectively. The overlap of the O(1s)→4a′* (C–F σ*) and O(1s)→1a″* (O–S–C–F σ*) transitions gives rise to the asymmetric tail of the second main pre–edge feature. The fifth pre–edge peak has been assigned as the O(1s)→3p Rydberg transition ($\delta = 0.845$).

10.5. Discussion

10.5.1. Pre–edge Peaks

The transition energy to the LUMO is consistently lower for the chlorides than for the fluorides (Table 10-2). The energy difference is approximately 1.5 eV. SO_2Cl_2 has the lowest O(1s)→LUMO transition energy; its value is another 0.5 eV less than those of the other chlorides. Further, the LUMO peak is well separated from the others in the chloride spectra, but this peak lies in with the other transitions in the spectra of the fluorides.

The LUMO corresponds to the $1a_1^*$ or $1a''^*$ orbitals in C_{2v} or C_s compounds, respectively. In the chloride compounds, this orbital has over 70% p-character in total

(Table 10-2); the main contributors are Cl, S, and O. The distribution of atomic contributions to this orbital indicates it is a S–Cl σ^* orbital with delocalization onto oxygen. Across the monochloride series (CH_3SO_2Cl, CF_3SO_2Cl and SO_2FCl) the term value for this peak increases. A decrease in both sulphur and oxygen p-character is observed while the chlorine p-character increases. SO_2Cl_2 follows this established trend between a greater term value and the atomic p-contributions. There are, however, two chlorine atoms in SO_2Cl_2 which contribute equally to the LUMO orbital, leading to a very significant increase in chlorine p-character. The consequence of the increased p-character is that relaxation is substantially increased, and the peak has a larger term value. Clearly, the increased relaxation for the O(1s)→LUMO transition in the chloride compounds is determined by the amount of chlorine p-character in the LUMO ($1a_1^*$, $1a''^*$) orbital.

In contrast, the LUMO orbital of the two fluorides—SO_2F_2 and CH_3SO_2F—has less halogen p-character and slightly increased oxygen p-character (Table 10-2). The sulphur p-character decreases significantly in SO_2F_2, but increases in CH_3SO_2F. The s-character of the LUMO is significantly greater in the SO_2F_2 than in the other compounds. For example, the $1a_1^*$ orbital of SO_2F_2 has 31.8% S-s, 4.9% O-s and 12.8% F-s character, compared to 16.9% S-s, 0.8% O-s and 2.5% Cl-s character of the $1a_1^*$ orbital of SO_2Cl_2. Based upon the atomic contributions, the LUMO orbitals of SO_2F_2 and CH_3SO_2F have been designated as O–S–F σ^* orbitals centred on sulphur.

The second peak in the spectra of the three dihalides corresponds to the other sulphur-halide σ^* orbital transition. In all three cases the virtual orbital involved is delocalized onto oxygen, so that it is best described as an O–S–halogen σ^* orbital (halogen = F in SO_2F_2 and SO_2FCl, Cl in SO_2Cl_2). The term values for this peak are very close in SO_2F_2 and SO_2FCl, but 0.3 eV larger in SO_2Cl_2. Again this result is explained by the p-character of the antibonding orbital involved, $1b_2^*$ in the case of SO_2F_2 and SO_2Cl_2, and $2a'^*$ in SO_2FCl. The $1b_2^*$ orbital has 92.3% p-character in SO_2Cl_2 and 87.9% in SO_2F_2, while the equivalent orbital $2a'^*$ in SO_2FCl has 86.0% p-character. The p-contribution from oxygen to this orbital is slightly larger in SO_2FCl than in SO_2Cl_2 (Table 10-3), but the p-character from sulphur is slightly less. Both sulphur and oxygen p-character are slightly increased in the $1b_2^*$ orbital of SO_2F_2. The $1b_2^*$ orbital of SO_2Cl_2

has significantly greater halogen p-character than the corresponding orbital of the other two molecules. The overall halogen p-character is slightly greater in the 2a′* orbital of SO_2FCl than in $1b_2$* of SO_2F_2, but the fluorine p-character is about the same. The increase in halogen character increases the term value of the O(1s)→$1b_2$* transition in SO_2Cl_2.

In the three remaining molecules (CH_3SO_2F, CH_3SO_2Cl and CF_3SO_2Cl) the corresponding antibonding orbital, O–S–C σ*, has significantly less overall p-character (Table 10-3). This is the 3a′* orbital for CH_3SO_2Cl and 2a′* for CH_3SO_2F with 73.4 and 40.8% overall p-character, respectively. Both sulphur and oxygen p-character decreased compared to the dihalides, hence the lower term value for the transition. In CF_3SO_2Cl the S–C σ* orbital is not readily identifiable. The 2a′* and 3a′* orbitals are both delocalized O–S–C σ* orbitals.

The two S–O σ* orbitals are fairly localized on oxygen and sulphur in the SO_2Cl_2, SO_2FCl and SO_2F_2 molecules (Table 10-4). The total contribution from the halogens is less than 16% (Table 10-4). Both orbitals have over 60% overall p-character with significant contributions from both oxygen and sulphur. The transitions to these orbitals give rise to peaks #3 and #4 in the O(1s) spectra of these two compounds. The term values of these two transitions are nearly identical in SO_2Cl_2 and SO_2FCl, whereas $2a_1$* has a lower term value and $1b_1$* a higher term value in SO_2F_2. Both overall orbital composition and the p-character of the $1b_1$* (1a″*) orbital is essentially the same in the three dihalides, thus this factor does not explain the observed shift in term value for SO_2F_2. For the $2a_1$* orbital the total contribution from oxygen as well as the oxygen p-character decrease in SO_2F_2 compared to the other two molecules. Similarly, the contributions from sulphur and the halogens—both overall and p-character—increase in SO_2F_2. (Table 10-4). These changes in orbital composition could account for the observed term value for the O(1s)→$2a_1$* transition in SO_2F_2 cannot be explained from changes in the orbital composition.

In the two monomethylated compounds both S–O σ* orbitals are significantly delocalized onto the methyl group. For CH_3SO_2F this delocalization occurs to such an extent that it is no longer possible to identify any individual orbital as S–O σ*. The 2a′* and 1a″* orbitals of CH_3SO_2Cl have been assigned as S–O σ*, but both experience at least

25% delocalization onto the methyl group (Table 10-4). Both orbitals have lower p-character compared to those in the dihalides, and especially the sulphur and oxygen p-character is lower. Orbital composition evaluation does not explain the term values, which are comparable to those of SO_2Cl_2 and SO_2FCl. Delocalization of the S-O σ^* orbitals onto the CF_3 ligand group is also observed in CF_3SO_2Cl, but to slightly lesser extent than in CH_3SO_2Cl. Overall p-character is in line with the dihalides for both orbitals, but sulphur p-character is significantly less for the 1a"* orbital.

The O(1s) spectra of all six molecules display a peak corresponding to the O(1s)→3p Rydberg transition. With exception of CF_3SO_2Cl this peak has a term value between -2.1 and -2.4 eV, corresponding to a quantum defect between 0.46 and 0.62. These are all smaller than the value suggested by Robin (0.65) [118] based upon the valence shell→O(3p) term values of alkyl and fluoroalkyl oxy compounds. This likely represents the difference in chemical environment of the oxygen atom in the two sets of molecules. The three dihalides form a pattern of increasing quantum defect with increased fluorination, but the two monomethylated compounds deviate from this trend. Both have a quantum defect greater than that of SO_2F_2. Possibly the greater size of the CH_3 ligand stabilizes the O(3p) Rydberg orbitals through delocalization. The term value of the O(1s)→3p transition is significantly larger in CF_3SO_2Cl compared to the other five molecules (Table 10-2), again possibly due to stabilization of the O(3p) Rydberg shell through delocalization onto the CF_3 ligand group. There is improved stabilization compared to CH_3SO_2F and CH_3SO_2Cl because of the greater size and increased electronegativity of CF_3 compared to CH_3.

10.5.2. Post Edge shape resonances

As already mentioned, the oxygen 1s photoionization cross-section of SO_2Cl_2 could not be calculated, hence this compound has been excluded from the following discussion. Figure 10-4 shows the remaining five spectra extended to 570 eV to display all post-edge structures. With the exception of CF_3SO_2Cl, all have two shape resonances in the ionization continuum. The first lies just above the ionization edge (term value less than +5.0 eV). The second peak occurs at higher energy (term value approximately 15 eV) and it is, consequently, much broader. It also has a high-energy tail. These peaks correspond to shape resonances resulting from transitions to quasibound continuum orbitals, The spectrum of CF_3SO_2Cl has only a single post-edge peak corresponding to the second peak in the spectra of the other four compounds. A peak corresponding to the first resonance in the other spectra is also present, but it occurs 1.03 eV below the edge.

The calculated cross-sections for all five compounds are shown in Figure 10-5. For SO_2F_2 the Xα calculation predicts two post-edge peaks at 539 and 549eV. The former is caused by $O(1s)\rightarrow a_1^*$ and $O(1s)\rightarrow a_2^*$ transitions and the latter by $O(1s)\rightarrow b_1^*$ and $O(1s)\rightarrow a_1^*$. Both peaks depend on oxygen p-waves and the higher energy peak also depends upon sulphur p- and d-waves. Fluorine s-, p- and d-waves influence the position and intensity of both peaks. This suggests that the former corresponds to atomic like oxygen $1s\rightarrow p$ transitions, while the latter is caused by transitions to mixed oxygen-p, sulphur-p and sulphur-d states. Both are stabilized by the potential well established by the other atoms, especially fluorine.

Similarly, two post-edge features are predicted for SO_2FCl and CH_3SO_2F at 535 and 549eV, the former due to $O(1s)\rightarrow a'^*$ ($O(1s)\rightarrow a''^*$ makes a minor contribution in SO_2FCl) and the latter due to both $O(1s)\rightarrow a'^*$ and $O(1s)\rightarrow a''^*$. As for SO_2F_2 both peaks depend on oxygen p-waves and the peak at 549eV depends on sulphur p-and d-waves as well. Hence, they have the same origin as the peaks in the SO_2F_2 spectrum. The sharp intensity decrease at the edge of the spectrum of CH_3SO_2F corresponds to the tail of the last pre-edge peak.

The calculated spectra of CH_3SO_2Cl and CF_3SO_2Cl deviate from this pattern. The former has three peaks at 532 eV ($O(1s)\rightarrow a''$) 541 eV ($O(1s)\rightarrow a1^*$ and $O(1s)\rightarrow a''$) and 555 eV ($O(1s)\rightarrow a''$), and the latter has only a single structure with a peak at 556 eV and two shoulders at 540 eV ($O(1s)\rightarrow a'^*,a''^*$) and 547 eV ($O(1s)\rightarrow a'^*,a''^*$). Investigation of the dependence upon atomic wavefunctions suggests that the first two peaks in the spectrum of CH_3SO_2Cl correspond to the peaks calculated for the spectra of CH_3SO_2F, SO_2FCl and SO_2F_2. The third peak of the CH_3SO_2Cl spectrum and the first two of the CF_3SO_2Cl spectrum are caused by sulphur d-waves, suggesting oxygen-1s$\rightarrow$sulphur-d transitions. The origin of the main peak (556 eV) in the calculated spectrum of CF_3SO_2Cl could not be determined.

The calculations suggest that the first post-edge peak in the spectra of SO_2F_2, SO_2FCl, CH_3SO_2F and CH_3SO_2Cl can be assigned to a oxygen 1s→p resonance and the second peak to a resonance resulting from transitions to mixed oxygen-p, sulphur-p and sulphur-d states. All these states are semibound lying within the potential barrier created by the molecular field.

The post-edge peak of CF_3SO_2Cl has been tentatively assigned as the main peak of the calculated spectrum, a resonance of, at present, unknown origins. The width of the last pre-edge peak (#6) suggests that it is caused by transitions to unstable, and possibly autoionizing, final states. It has been tentatively assigned as the equivalent to the first post-edge peak in the other four spectra, an O(1s)→p* resonance. Further theoretical studies of the O(1s) core excited states of CF_3SO_2Cl should be conducted to properly identify the post-edge structure of the O(1s) photoabsorption spectrum of this molecule.

Further theoretical studies are also needed to assign the post-edge structure of the O(1s) photoabsorption spectrum of SO_2Cl_2. At present, peak #7 (Table 10-1), has been tentatively assigned as an oxygen 1s→p* resonance based upon comparison to SO_2F_2, SO_2FCl, CH_3SO_2F and CH_3SO_2Cl.

10.6. Summary

The O(1s) photoabsorption spectra of sulphuryl halides and their methylated derivatives have comparable peak structure. Several high intensity pre-edge peaks, corresponding to O(1s)→σ* transitions are observed with term values between −7.0 and −3.0 eV. These are then followed by low intensity Rydberg peaks, the most prominent corresponding to the O(1s)→3p transition. All spectra also have two post edge peaks due to O(1s)→O(np) resonances.

The relative positions of the main pre-edge peaks reveal significant differences in the electronic structure and bonding of these six sulphuryl halides. In particular, the position of the LUMO peak can be used to probe the covalency of the sulphur-halide bond. The more covalent S-Cl bond in the chlorides results in a substantially lower O(1s)→LUMO transition energy compared to the rest of the spectrum.

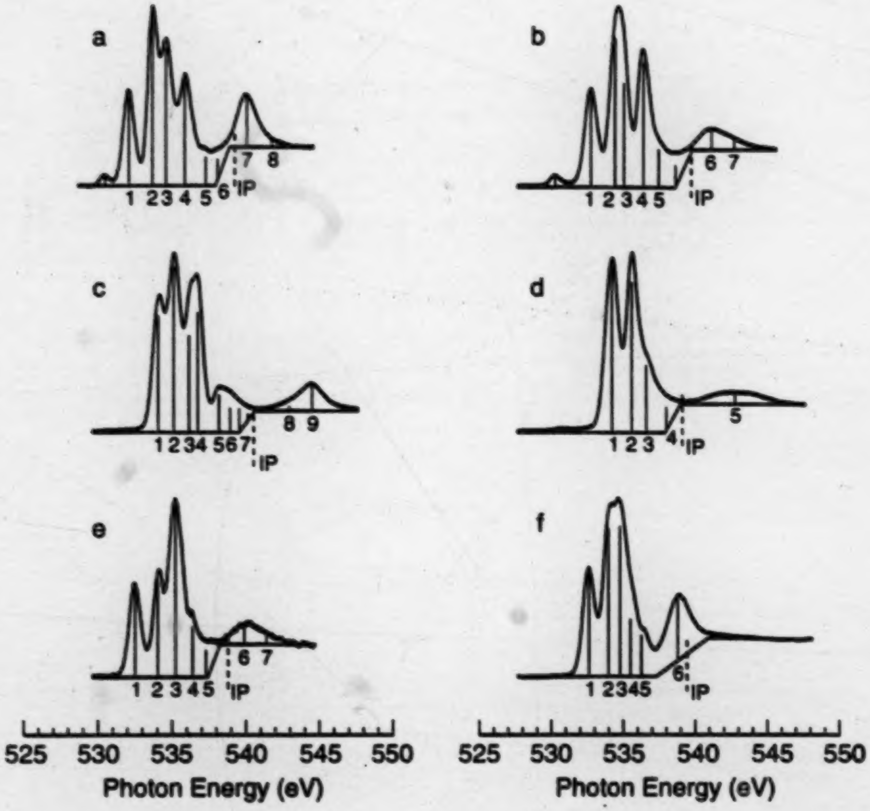

Figure 10-1: Experimental O(1s) photoabsorption spectra, pre-edge peaks.

The numbers of the peaks correspond to Table 10-1:

a) SO_2Cl_2, b) SO_2FCl, c) SO_2F_2, d) CH_3SO_2F, e) CH_3SO_2Cl, f) CF_3SO_2Cl.

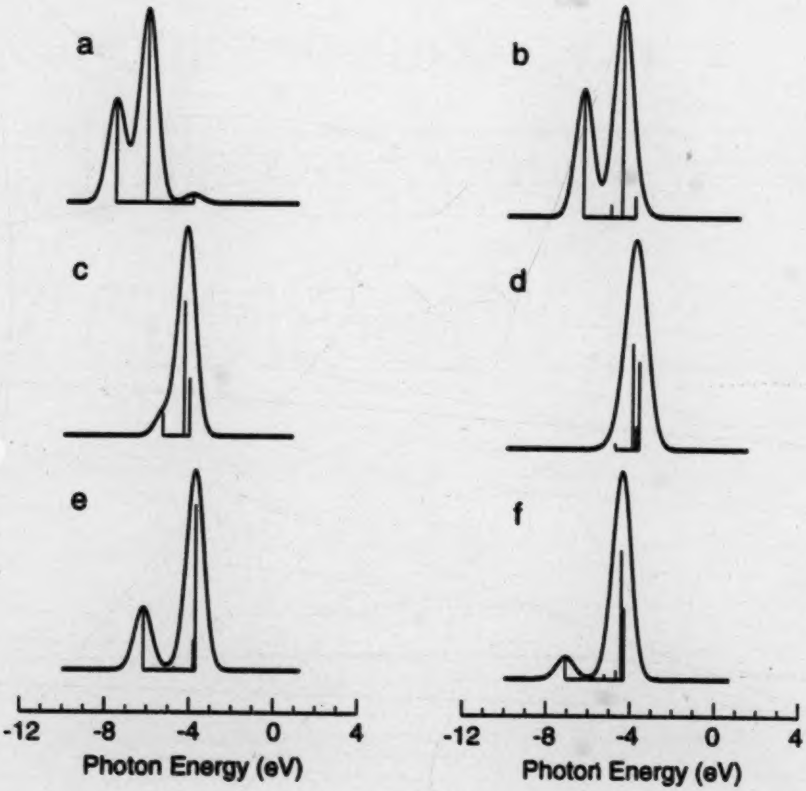

Figure 10-2: Calculated O(1s) spectra, pre-edge peaks:

a) SO_2Cl_2, b) SO_2FCl, c) SO_2F_2, d) CH_3SO_2F, e) CH_3SO_2Cl, f) CF_3SO_2Cl.

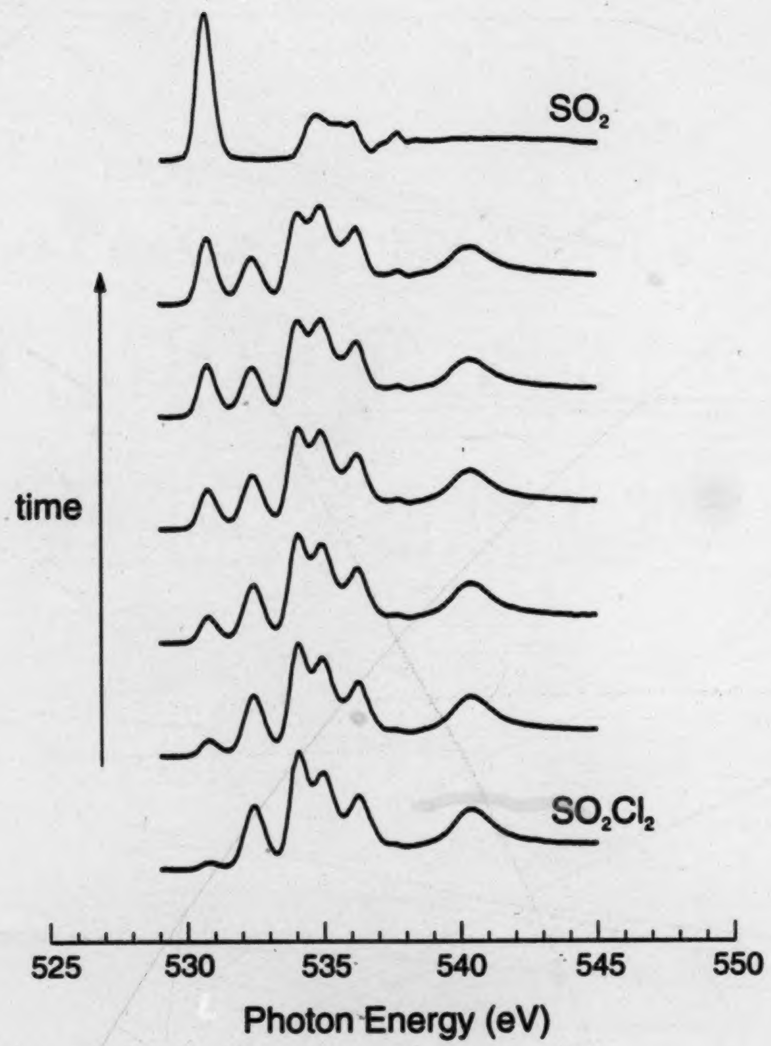

Figure 10-3: Decomposition of SO_2Cl_2 as evidenced from the O(1s) photoabsorption spectrum and the O(1s) spectrum of SO_2, the reaction product.

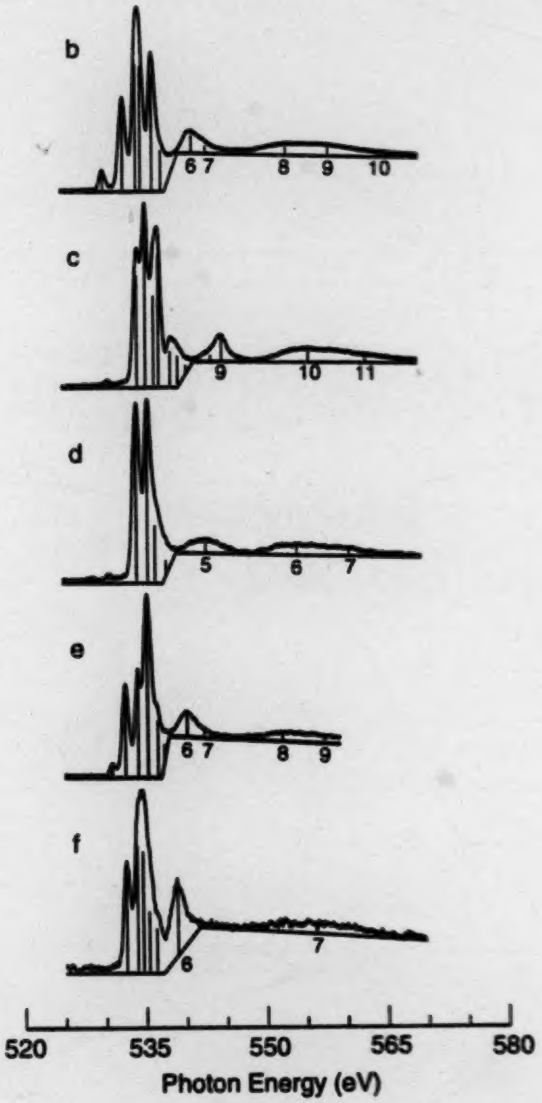

Figure 10-4: Experimental O(1s) Spectra, pre-edge peaks and all post-edge resonances.

b) SO_2FCl, c) SO_2F_2, d) CH_3SO_2F, e) CH_3SO_2Cl, f) CF_3SO_2Cl.

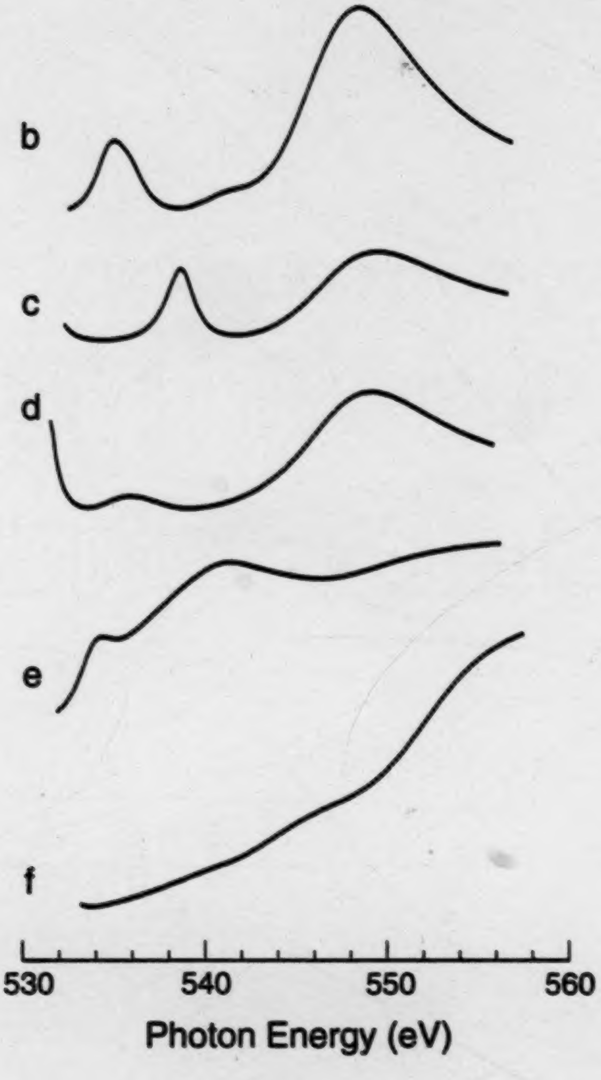

Figure 10-5: Calculated Oxygen 1s Photoionization Cross-Sections:

b) SO_2FCl, c) SO_2F_2, d) CH_3SO_2F, e) CH_3SO_2Cl, f) CF_3SO_2Cl.

Table 10-1: Experimental Transition Energies (eV) and Assignments.

a) SO_2Cl_2

No.	Energy[a]	Term Value[b]	Assignment	
	530.40	–8.84	SO_2 impurity	
1	532.01	–7.23	$1a_1^{*}$	S–Cl σ*
2	533.59	–5.65	$1b_2^{*}$	Cl–S–O σ*
3	534.51	–4.73	$2a_1^{*}$	S–O σ*
4	535.81	–3.43	$1b_1^{*}$	S–O s*
5	537.14	–2.10	O(3p)	Rydberg
6	538.08	–0.84		
IP	539.24[c]			
7	540.00	0.76	O(1s)→O(np)	
8	541.59	2.35	resonance	

b) SO_2FCl

No.	Energy[a]	Term Value[b]	Assignment	
	530.29	–9.45	SO_2 impurity	
1	532.77	–6.97	$1a'^{*}$	S–Cl σ*
2	534.40	–5.34	$2a'^{*}$	O–S–F σ*
3	535.01	–4.73	$3a'^{*}$	S–O σ*
4	536.39	–3.35	$1a''^{*}$	S–O σ*
5	537.46	–2.28	O(3p)	Rydberg
IP	539.74[c]			
6	541.14	1.40	O(1s)→O(np)	
7	542.75	3.01	resonance	
8	552.99	13.25	O(1s)→O(np), S(np), S(nd)	
9	558.26	18.52	resonance	
10	564.63	24.89		

c) SO_2F_2

No.	Energy(a)	Term Value(b)	Assignment	
1	534.11	–6.43	$1a_1^*$	F–S–O σ*
2	535.18	–5.36	$1b_2^*$	O–S–F σ*
3	536.22	–4.32	$2a_1^*$	O–S–F σ*
4	536.81	–3.73	$1b_1^*$	O–S–F σ*
5	538.19	–2.35	O(3p)	Rydberg
6	539.01	–1.53	O(3d)	Rydberg
7	539.62	–0.92		
IP	540.54(c)			
8	542.88	2.34	O(1s)→O(np) resonance	
9	544.55	4.01		
10	555.72	15.18	O(1s)→O(np), S(np), S(nd) resonance	
11	562.90	22.36		

d) CH_3SO_2F

No.	Energy(a)	Term Value(b)	Assignment	
	530.71	–8.42		impurity
1	534.22	–4.91	$1a'^*$	O–S–F σ*
2	535.62	–3.51	$2a'^*$	O–S–C σ*
			$3a'^*$	C–H σ*
			$1a''^*$	H–C–S–O σ*
3	536.72	–2.41	O(3p)	Rydberg
4	538.22	–0.91		
IP	539.13(c)			
5	542.87	3.74	O(1s)→O(np) resonance	
6	554.10	14.97	O(1s)→O(np), S(np), S(nd) resonance	
7	560.56	21.43		

e) CH_3SO_2Cl

No.	Energy(a)	Term Value(b)	Assignment	
1	532.48	−6.30	$1a'^*$	S–Cl σ*
2	534.04	−4.74	$2a'^*$	O–S–C–H σ*
3	535.24	−3.54	$1a''^*$	H–C–S–O σ*
			$3a'^*$	C–S–O σ*
			$4a'^*$	C–H σ*
4	536.42	−2.36	O(3p)	Rydberg
5	537.55	-1.23		
IP	538.78(c)			
6	540.02	1.24	O(1s)→O(np)	
7	541.58	2.80	resonance	
8	552.10	13.32	O(1s)→O(np), S(np), S(nd)	
9	557.29	18.51	resonance	

f) CF_3SO_2Cl

#	Energy(a)	Term Value(b)	Assignment	
1	532.59	−6.85	$1a'^*$	S–Cl σ*
2	534.02	−5.42	$2a'^*$	O–S–C σ*
3	534.79	−4.65	$3a'^*$	O–S–C σ*
4	535.53	−3.91	$4a'^*$	C–F σ*
			$1a''^*$	O–S–C–F σ*
5	536.51	−2.93	O(3p)	Rydberg
6	538.41	−1.03	O(1s)→O(np) resonance	
IP	539.44(c)			
7	556.09	16.65	resonance of unknown origin	

(a) The uncertainty in the transition energies is ±0.08 eV for the pre-edge peaks and ±0.15 eV for the post-edge peaks.

(b) The uncertainty in the term values is ±0.18 eV for the pre-edge peaks and ±0.25 eV for the post-edge peaks.

(c) Chapter 6, the uncertainty is ±0.10 eV.

Table 10-2: O(1s)→LUMO transition and p–character of the LUMO.

	Term Value (eV)	% S–p	% O–p	% Cl–p	% Y–p	Σ %p
SO_2Cl_2	–7.23	14.9	13.6	46.7	----	75.2
CH_3SO_2Cl	–6.29	25.5	19.2	29.4	5.5	79.6
CF_3SO_2Cl	–6.84	22.0	17.5	30.8	8.1	78.4
SO_2FCl	–6.98	17.1	16.3	32.6	6.4	72.4
		% S–p	% O–p	% F–p	% Y–p	Σ % p
CH_3SO_2F	–4.90	32.0	21.7	17.6	3.1	74.4
SO_2F_2	–6.43	5.2	20.5	26.9	----	52.6

Table 10-3: p–character of the other sulphur–"halogen" σ* orbital.

	Term Value (eV)	% S–p	% O–p	% Cl–p	% Y–p	Σ % p
SO_2Cl_2	–5.65	44.4	26.2	21.7	----	92.3
CH_3SO_2Cl	–3.54	35.7	16.0	1.8	19.9	73.4
CF_3SO_2Cl	–5.42	20.7	23.7	0.5	17.7	62.6
SO_2FCl	–5.34	43.3	27.3	2.3	13.1	86.0
		% S–p	% O–p	% F–p	% Y–p	Σ % p
CH_3SO_2F	–4.91	11.5	21.3	0.8	7.2	40.8
SO_2F_2	–5.36	45.8	29.9	12.2	----	87.9

Table 10-4: p–character of the other sulphur–oxygen σ* orbitals.

		Term Value (eV)	% S	% O	% Cl	% Y	Σ %
SO_2Cl_2							
$2a_1^*$	total	–4.73	55.8	36.9	7.3	----	100.0
	p		32.1	28.0	4.4	----	64.5
$1b_1^*$	total	–3.43	61.8	26.4	11.8	----	100.0
	p		44.3	17.2	6.2	----	67.7
CH_3SO_2Cl							
$2a'^*$	total	–4.74	42.1	30.9	1.3	25.8	100.1
	p		19.3	23.3	0.7	4.1	47.4
$1a''^*$	total	–3.54	43.3	20.6	2.5	33.6	100.0
	p		29.5	14.3	1.3	6.8	51.9
CF_3SO_2Cl							
$2a'^*$	total	–5.42	48.7	23.8	4.8	22.8	100.0
	p		35.7	19.7	3.2	15.6	74.2
$1a''^*$	total	–3.91	42.4	21.9	3.5	32.3	100.0
	p		29.0	15.7	2.1	24.9	71.7
SO_2FCl							
$3a'^*$	total	–4.73	55.4	37.1	3.7	3.8	100.0
	p		31.3	27.7	2.3	3.0	64.3
$1a''^*$	total	–3.35	60.4	25.9	7.2	6.5	100.0
	p		43.4	16.1	3.6	5.3	68.3
			% S	% O	% F	% Y	Σ %
SO_2F_2							
$2a_1^*$	total	–4.32	56.8	31.3	11.8		99.9
	p		38.4	24.3	8.6		71.3
$1b_1^*$	total	–3.73	59.0	25.9	15.1		100.0
	p		43.2	15.1	11.9		70.2

11. The Valence Shell Photoionization Energies Cross-Sections of NF_3 and PF_3

11.1. Introduction

The photoelectron process is the interaction between a molecule and a photon leading to the ejection of one of the electrons [8] (Section 1.1). From an energetic viewpoint the electron may be ejected from any molecular orbital as long as the photon energy exceeds the binding energy of the electron. The excess energy is carried off as kinetic energy by the photoelectron. The transition probability is non-zero for all transitions and a peak is observed for each. The peak intensities are different being determined by the transition probability. The area of a photoelectron peak is proportional to the photoionization cross-section [8] $\sigma = P_{if}/F_{ph}$ [24] where F_{ph} represents the incident photon flux and P_{if} the transition probability. Hence, photoelectron spectra can be employed to determine the partial ionization cross-section for each of the molecular orbitals.

The valence shell photoionization potentials and the corresponding ionization cross-sections reveal information about the molecular electronic structure [8], thus they can be used to test the theoretical models employed for the calculation of molecular properties.

Here, we present a comparison of the valence shell photoelectron spectra of the Group V trifluorides PF_3 and NF_3. The experimental spectra were analyzed to determine differences in the electronic structure and the chemical bonding between these two molecules. Ionization potentials and cross-sections were calculated using MS-Xα [103] and various *ab initio* methods. The calculations were compared with experimental values to evaluate the theory.

11.2. Experimental

Valence shell photoelectron spectra of NF_3 and PF_3 were collected at photon energies ranging from 70 to 160 eV, as described in Chapter 2. The binding energy scale was calibrated using the valence shell photoelectron lines of xenon at 12.131 eV ($5p_{3/2}$), 13.438

eV ($5p_{1/2}$) and 23.399 eV (5s) [124]. Peak intensities were normalized with respect to window transmission, analyzer transmission and the electron current in the synchrotron ring. The experimental spectra were fitted with Gaussian/Lorentzian (Voigt) curves to determine the peak energies and areas. To deal with variations in gas pressure and grating reflectivity relative cross-sections or branching ratios were calculated by dividing the area of each peak by the total area of all peaks. The precision of the experimental peak energies is within ±0.06 eV, and the peak areas are precise within ±6 %. Gas samples of NF_3 and PF_3 were obtained commercially from Ozark Mahoning and used without further purification.

11.3. Calculations

Photoionization energies and cross-sections were calculated with the MS-Xα method, in order to assign the experimental spectra. The experimental molecular geometry [95, 96] (Table 11-1) was used for both species. Sphere radii were determined by the Xα program [146] according to the Norman procedure [112], and the atomic α parameters were obtained from the tables compiled by Schwarz [109]. The ionization energies were calculated using the transition state method, wherein a one-half electron was removed form the orbital ionized. The ionization cross-sections were obtained according to the method of Davenport [116] and Dill and Dehmer [115] (Section 3.5) with the molecular potentials of the transition state. The calculated photoelectron spectra at an excitation energy of 87.0 eV were generated using the calculated ionization energies and cross-sections. Since the peak widths were not calculated, the corresponding experimental peak widths were substituted. Pure Gaussian curves were used to generate the calculated spectra.

Gaussian 94 [94] at the Density Functional level of theory (DFT) [86] was used to determine the identities of the valence shell molecular orbitals. The exchange potential of the Hartree-Fock equation was approximated by the B3LYP method: Becke's three-parameter functional [87] with the gradient-corrected correlation functional of Lee et al. [157] and the correlation functional of Vosko et al. [158] providing non-local and local correlation, respectively (see equation 6-1). The molecular geometry was optimized

(Table 11-1). The overlap matrix **S** of the atomic orbital basis functions (Section 3.6) and the molecular orbital coefficients (c_i) were calculated at that optimized geometry. The atomic orbital basis set was then orthonormalized by the symmetric orthogonalization procedure outlined in Section 3.6 of this thesis. From the orthonormalization requirements of the new atomic orbital basis set the % compositions of the molecular orbitals are given by $|c'_i|^2 \times 100$ (Section 3.6).

The ionization potentials were calculated with Gaussian 94 in three different ways, first by employment of Koopmans' theorem [8, 101]. To evaluate the accuracy of the theoretical method, these calculations were performed using the 6-31G* and 6-311+G* basis sets at both the Hartree-Fock (HF) [79] and Density Functional (DFT) [86] level of theory.

Secondly, for the $4a_1$ and $1a_2$ orbitals the ionization potential was computed as the energy difference between the ion with a hole in the relevant orbital (optimized geometry) and the molecular ground state. Again, the 6-31G* and 6-311+G* basis sets were employed. The calculations were done using HF theory—with and without Møller-Plesset (MP2) [82] correlation—and DFT.

The ionization potentials were also calculated using the CIS method of Foresman et al. [102]. For this method the excited states of NF_3^+ and PF_3^+ (optimized geometry) were calculated keeping all virtual orbitals frozen. The ionization potential of the outermost valence shell orbital ($4a_1$) was set equal to the difference in total energy between the ground states of the ion and the neutral molecule. The ionization potentials of the other orbitals equal the sum of this energy difference and the calculated excitation energy of the ground ionic state. These calculations have only been done at the HF level of theory, as the CIS method is not available in the DFT mode. Again, the 6-31G* and 6-311+G* basis sets were used.

11.4. Results and Discussion

11.4.1. Experimental Results

The NF_3 and PF_3 molecules are both pyramidal with C_{3v} symmetry. According to the Lewis-Langmuir bonding pair theory [120, 121], the central Group V atom forms a single bond with each of the three terminal fluorines. There are three lone pairs on each fluorine atom and one lone pair is formally assigned to the central atom. There are, however, differences to the molecular structure. NF_3 has shorter bond lengths and wider bond angles than PF_3 (Table 11-1).

The experimental valence shell photoelectron spectra of the two molecules are shown in Figure 11-1. As expected, they are quite similar. Both have seven main peaks with comparable structure. Of these peaks 2, 3 and 4 occur at the same energy in both spectra (Table 11-2), indicating that the corresponding molecular orbitals have comparable compositions and structures. The remaining peaks (1, 5, 6, and 7) occur at lower energy in the spectrum of PF_3. The peak assignment, based upon the MS-Xα calculation results, is given in Table 2. The numbering scheme employed here excludes the core orbitals to facilitate comparison between the two molecules. The $1a_1$ and 1e orbitals, corresponding to F(2s) lone pair orbitals, were not included in this study. The experimental ionization potentials of the PF_3 valence shell orbitals agree well with earlier results obtained using HeI and HeII radiation [202, 203]. A more recent study [165] using synchrotron radiation reports values that are consistently approximately 0.3 eV lower, possibly due to a calibration error in the earlier work [165]. The experimental ionization potentials of NF_3 measured in the present study also agree well with previous HeI and HeII data [203], for the most part.

11.4.2. Identity of the molecular orbitals

The molecular orbital energy diagrams based upon the experimental ionization energies are shown in Figure 11-2. Calculated molecular orbital compositions are listed in Table 11-3 for all relevant valence shell orbitals. Based upon these Gaussian 94 [94] calculations the $2a_1$ and 2e orbitals represent the sigma bonding framework orbitals of the molecule. Both have higher ionization potentials in NF_3. The two orbitals have greater covalency in NF_3, resulting in increased binding energies. Both orbitals have greater F-s contribution and lesser F-p contribution in NF_3 compared to PF_3. This characteristic is another possible cause for the increased ionization potentials for these two orbitals in NF_3, especially for the $2a_1$ orbital where the F-s character is about 14% greater. The F-s character is likely also responsible for the broad shape of the $2a_1$ photoelectron peak in the NF_3 spectrum.

The next four orbitals ($3a_1$, 3e, 4e and $1a_2$) correspond to fluorine 2p lone pair orbitals. Of these, the $3a_1$ orbital is delocalized onto the central atom. This delocalization is greater in NF_3 than in PF_3, resulting in a higher bonding character of the orbital in the former molecule. In turn, this leads to the higher ionization potential. The other three (3e, 4e and $1a_2$) are pure F(2p) orbitals, hence they have the same ionization potential in both molecules.

The last orbital ($4a_1$) formally represents the lone pair of the central atom. Again, the orbital is delocalized to a greater extent in NF_3 than in PF_3, leading to a higher binding energy in the former molecule. Overall the molecular bonding is more covalent in NF_3 than PF_3, because of the smaller electronegativity difference between nitrogen and fluorine.

Although the greater covalency in NF_3 leads to more tightly bound electrons, this does not translate into stronger bonds. The energy required to cleave one of the bonds is 2.47eV for NF_3 and 5.71 eV for PF_3 [204], thus the chemical bonds are stronger in the latter molecule. Instead, the greater covalency of NF_3 creates an increased potential barrier for electrons in the delocalized $2a_1$, 2e, $3a_1$ and $4a_1$ orbitals.

11.4.3. Comparison of Experiment and Theory

The theoretical valence shell ionization potentials obtained by the MS-Xα calculation method are listed in (Table 11-3). Overall, the agreement with the experimental result is reasonable. The greatest discrepancy occurs for the $3a_1$ orbital in both molecules. The calculations generally underestimate the values, but the predictions are better for NF_3 than PF_3. This is possibly caused by more accurate parameterization of the nitrogen—a first row atom—compared to phosphorus—a second row atom. The calculated spectra shown in Figure 2 illustrate the difficulty of obtaining accurate photoionization cross-sections, however, overall the results are satisfactory. Here, better agreement is observed for PF_3.

The photoionization branching ratios for the energy region of 70 to 170 eV are shown in Figure 11-4 and Figure 11-5. The solid lines represent the MS-Xα calculation and the centered symbols the corresponding experimental data. The values for the 4e and $1a_2$ orbitals are combined to a single data set, because the experimental peaks are not fully resolved. Agreement between the experimental and calculated values varies for different orbitals. For example, the Xα calculation consistently overestimates the $4e+1a_2$ branching ratio and underestimates the $2a_1$ and 2e branching ratios of NF_3. However, in general the agreement is reasonable, and for the most part better for PF_3 than NF_3. Of note is the region around 137 eV corresponding to the energy region of bound P(2p) excitations. Peaks resulting from resonant Auger transitions following the $^1A_1(P(2p)e \rightarrow 1e^*)$ excitation ($h\nu = 136.5$ eV [166]) overlap with the valence shell photoelectron spectrum of PF_3, significantly altering the experimental branching ratios. Details of these Auger peaks are given elsewhere [119, 165] and shall not be discussed here. Otherwise the branching ratios are fairly constant throughout the energy range studied. The behaviour for corresponding orbitals in the two molecules is comparable, both in terms of magnitude and dependence upon photon energy. This is not unexpected at the energies studied here. Orbital specific resonances usually occur close to the ionization edge. Similarly effects due to differences in molecular structure between NF_3 and PF_3 are expected to be prominent at lower excitation energies. The photoionization cross-section of a particular molecular orbital generally rises steeply close to the threshold [8]. The curve displays at least one maximum and then decreases, usually monotonically, with increasing photon energy. The initial maximum in the cross-section occurs at photon energies approximately twice the ionization potential [8]. For the outer valence shell of NF_3 and PF_3 this corresponds to the energy region between approximately 20 and 60 eV.

As expected, the ionization potentials obtained with Gaussian 94 using Koopmans' theorem (Table 11-4) are dependent upon both the theory level and the basis set employed. HF theory overestimates the values and DFT underestimates. The change in the basis set had less effect; the larger 6-311+G* basis set gives higher energy ionization potentials. This effect is more pronounced for DFT than standard HF theory. The absolute values of the Koopmans' ionization potentials do not agree as well with experiment as do the MS-Xα calculations, not surprising, as orbital relaxation following photoionization is not considered here. Relative energies, however, are reproduced quite well by the DFT calculations, but not by the HF calculations. Especially the energy difference between the $4a_1$ and $1a_2$ orbitals is overestimated significantly by HF theory (Table 11-4). Again, the better agreement with experiment for NF_3 in all cases is probably due to better parameterization of the nitrogen compared to phosphorus. Basis set effects on the relative ionization potentials are minimal.

A significant drawback of the Koopmans' theorem is the neglect of relaxation effects. The assumption is made that the overall molecular structure (geometry and electron distribution) does not change upon ionization. In reality this is, however, not the case. The molecular structure can change quite significantly: for example, NH_3 is pyramidal [95], while NH_3^+ is planar [205, 206]. The MS-Xα calculation models the rearrangement of the electron distribution through employment of the transition state method, and as already mentioned gives satisfactory agreement with experiment (Table 11-2). The molecular geometry, however, is kept rigid; thus, cases wherein geometry changes occur will not be done well.

Ideally, the ionization potential should be calculated as the total energy difference between the optimized ion state (in this case NF_3^+ and PF_3^+), with the electron removed from the molecular orbital of interest, and the optimized ground molecular state (NF_3 and PF_3). Geometry optimization can be readily achieved with Gaussian 94 [94], but the calculation method rearranges the electron configuration to minimize the total energy. Even with the use of symmetry constraints only the two lowest electronic states—$^2A_1$ (electron removed from $4a_1$) and $^2A_2$ (electron removed from $1a_2$)—of the ion (NF_3^+ and PF_3^+) can be determined (Table 11-5). HF theory again significantly underestimates the ionization potential of the $4a_1$ orbital, and the ionization potential of the $1a_2$ orbital is overestimated. The energy difference between the two ionization potentials is overestimated significantly as well. The larger basis set (6-311+G*) increases the absolute values slightly but has little effect elsewhere. The use of DFT improves agreement with the experimental data both in terms of relative and absolute value. The higher values of the 6-311+G* basis set are closer to experiment, but otherwise there is little effect. The addition of MP2 correlation to the HF calculation give results comparable to the DFT calculation for NF_3, but for PF_3 the energy difference is again overestimated. As before, basis set effects are minimal.

A way to calculate the electronic excited states of a species is the CIS method developed by Foresman et al. [102]. The ground state of the ion ($^2A_1$, hole in $4a_1$) is optimized, then the excited states are calculated with CIS. The ionization potentials are determined form the CIS excited states as outlined in the previous Section (11.3). To simplify the analysis all antibonding orbitals were frozen. Again the ionization potentials obtained (Table 11-6) do not agree with the experimental values, and the energy difference between the $^2A_1$ (hole in $4a_1$) and $^2A_2$ (hole in $1a_2$) states is overestimated significantly. The relative energies of the excited states agree more favourably with experiment, especially for PF_3. Again, the basis set effects are minor.

11.5. Summary

The valence shell ionization potentials of the NF_3 and PF_3 molecules reflect the differences and similarities in electronic structure between these two species. The electrons in delocalized orbitals are more tightly bound and the overall chemical bonding more covalent in NF_3 because of the smaller electronegativity difference between nitrogen and fluorine. In the energy region studied here the ionization cross-sections of corresponding orbitals in the two species are comparable. Future research should investigate the photoionization cross-sections at lower photon energies to determine orbital specific resonances and structural differences between the two molecules. MS-Xα calculations of the ionization potentials and cross-sections agree reasonably well with the experimental result. For *ab initio* Gaussian 94 [94] calculations the accuracy of the ionization potentials obtained depends on the calculation method used. The basis set effects were minor for the two (6-31G* and 6-311+G*) studied here. The best results were achieved with Koopmans' theorem and Density Functional Theory (B3LYP). Furthermore, photoionization cross-sections could not be obtained with the *ab initio* methods, a significant deficiency of the Gaussian 94 [94] calculation package.

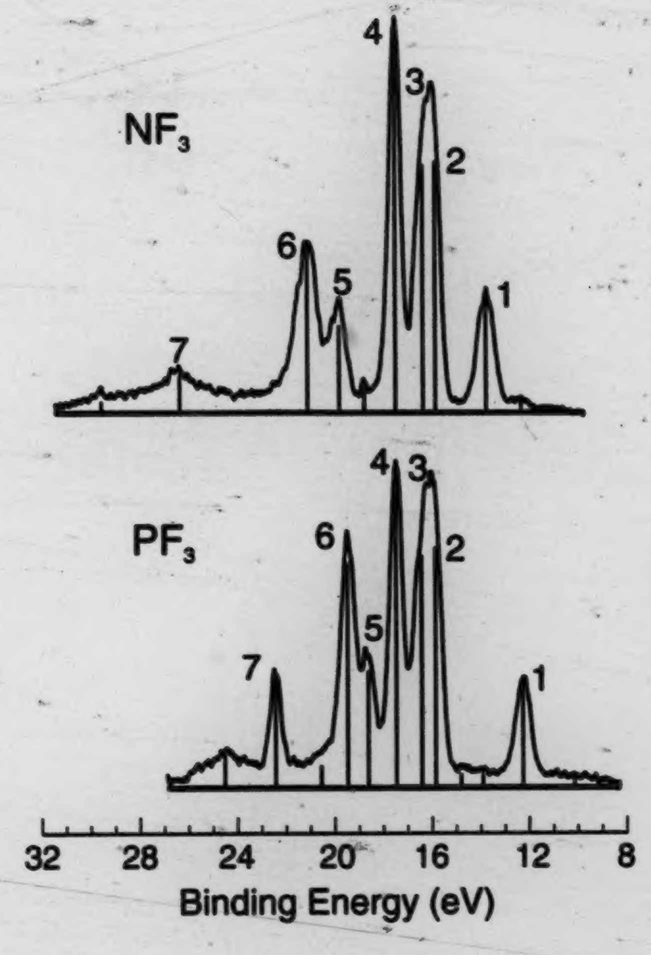

Figure 11-1: The experimental valence shell photoelectron spectra of NF_3 and PF_3.

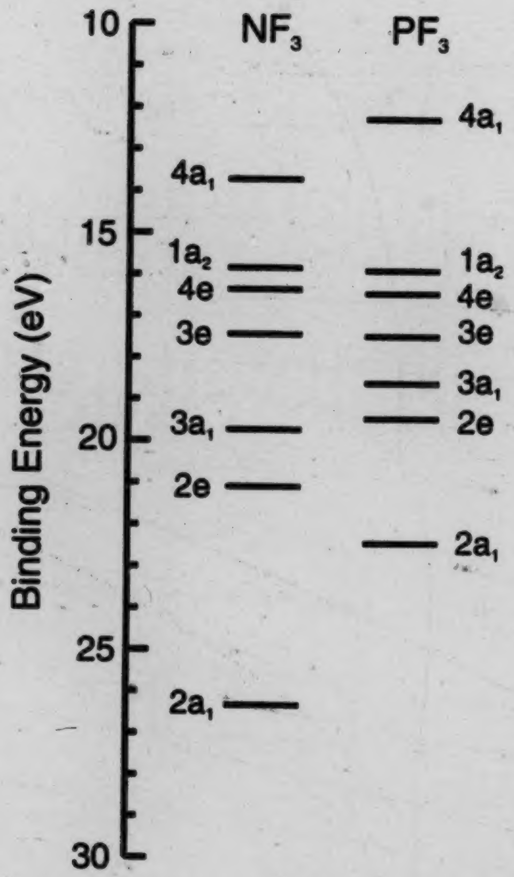

Figure 11-2: The orbital energy diagrams of NF_3 and PF_3.

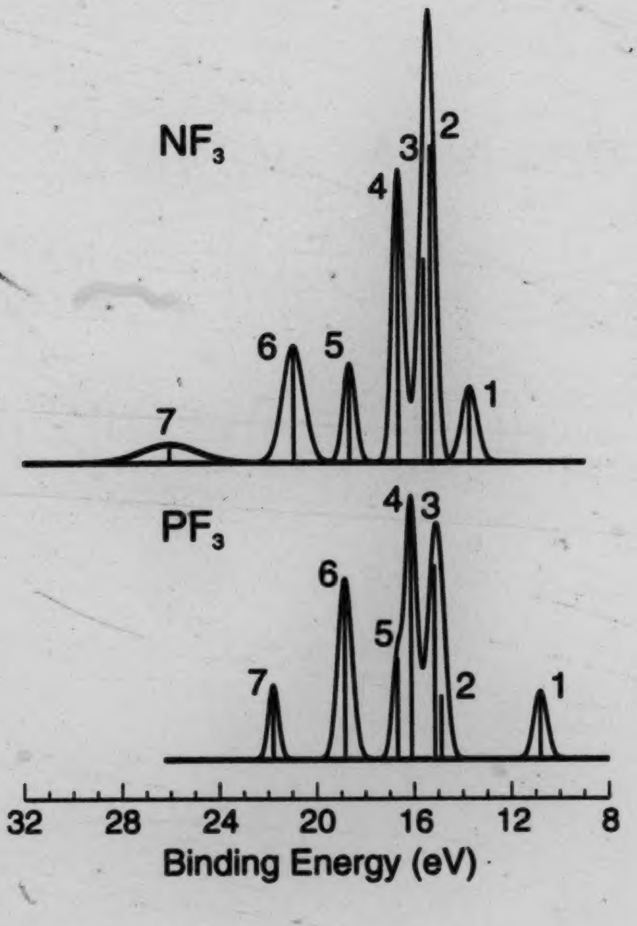

Figure 11-3: The calculated (MS-Xα [103]) valence shell photoelectron spectra of NF_3 and PF_3.

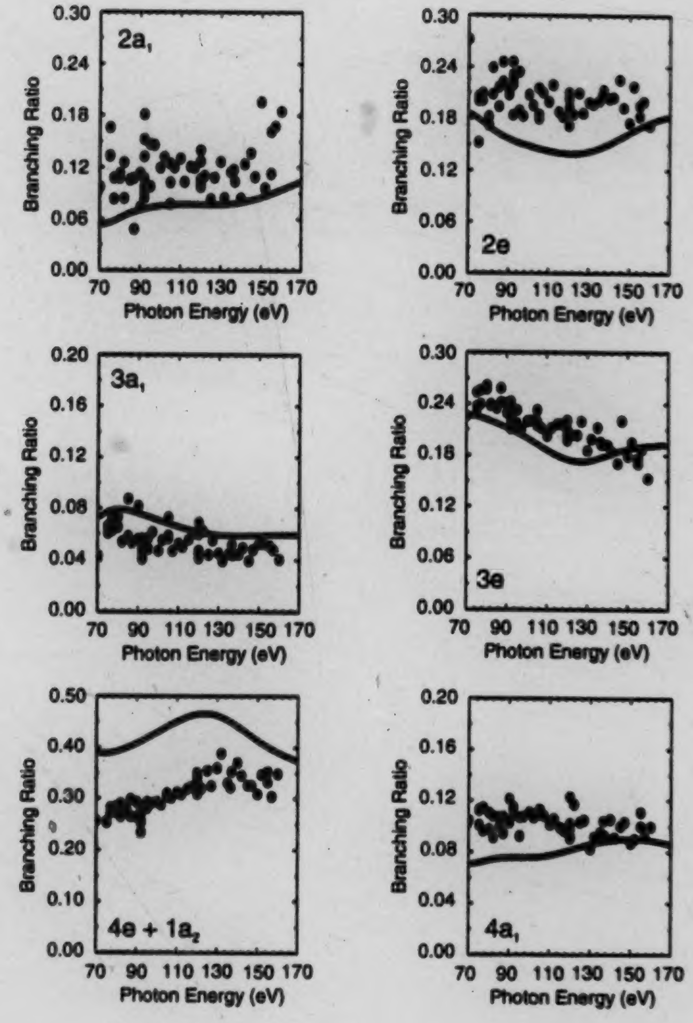

Figure 11-4: The valence shell photoionization branching ratios of NF_3.

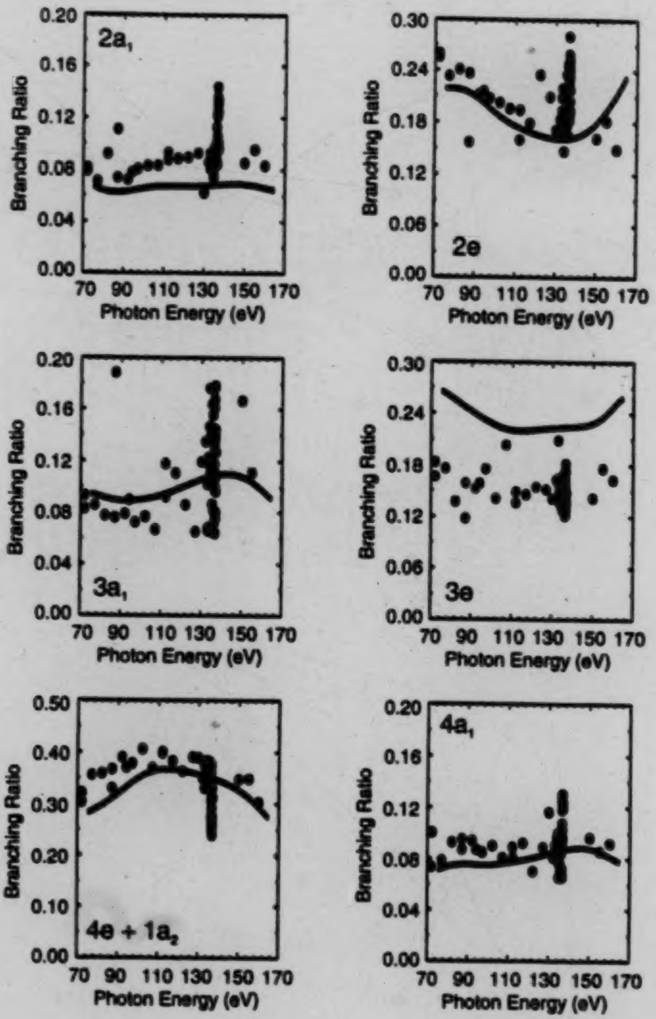

Figure 11-5: The valence shell photoionization branching ratios of PF$_3$.

Table 11-1: The molecular geometries, experiment [95, 96] and theory (Gaussian 94 [94], B3LYP, 6-31G*).

	Experiment	Theory
NF_3		
N-F:	1.3648 Å	1.3826 Å
F-N-F:	102.37	101.96°
PF_3		
P-F:	1.561 Å	1.5969 Å
F-P-F	97.7°	97.55°

Table 11-2: The valence shell ionization potentials (eV) of NF_3 and PF_3 and their assignment.

			This	Literature values			$X\alpha$
	No.	Orbital	Work (a)	[203]	[202]	[165]	calc.
NF_3	1	$4a_1$	13.71	13.73			13.66
	2	$1a_2$	15.81	16.15			15.24
	3	4e	16.32	16.55			15.53
	4	3e	17.44	17.52			16.58
	5	$3a_1$	19.74	19.71			18.60
	6	2e	21.09	21.14			20.90
	7	$2a_1$	26.37				26.01
PF_3	1	$4a_1$	12.27	12.29	12.27	11.97	10.81
	2	$1a_2$	15.89	15.89	16.30	15.61	14.88
	3	4e	16.44	16.31	15.88	16.15	15.14
	4	3e	17.47	17.45	17.46	17.18	16.10
	5	$3a_1$	18.60	18.57	18.60	18.32	16.67
	6	2e	19.46	19.36	19.50	19.16	18.83
	7	$2a_1$	22.44	22.6	22.55	22.18	21.79

(a) The uncertainty in the experimental values is ±0.06 eV.

Table 11-3: The molecular orbital compositions as calculated from the LCAO molecular orbital coefficients (G-94, 6-31G*).

NF$_3$	% N-s	% N-p	% N-d	% F-s	% F-p	% F-d
4a$_1$	16.0	30.8	1.0	0.6	52.0	0.6
1a$_2$	0.0	0.0	0.0	0.0	100.0	0.0
4e	0.0	1.0	1.0	0.0	97.9	0.0
3e	0.0	0.7	2.0	0.0	97.1	0.1
3a$_1$	6.2	31.0	0.6	0.6	61.3	0.9
2e	0.0	24.5	0.3	7.3	66.8	1.1
2a$_1$	29.0	1.5	0.0	27.0	40.4	2.2
PF$_3$	**% P-s**	**% P-p**	**% P-d**	**% F-s**	**% F-p**	**% F-d**
4a$_1$	31.9	28.4	1.4	0.6	37.5	0.2
1a$_2$	0.0	0.0	0.0	0.0	100.0	0.0
4e	0.0	2.6	1.5	0.0	95.9	0.1
3e	0.0	0.9	3.7	0.1	95.1	0.2
3a$_1$	4.3	17.4	1.7	0.2	75.9	0.5
2e	0.0	14.2	1.2	5.0	79.1	0.6
2a$_1$	27.8	1.1	0.0	13.3	56.5	1.2

Table 11-4: The calculated valence shell ionization potentials obtained with Koopmans' theorem (Gaussian 94 [94] *ab initio* calculations) (eV).

	Orbital	Exp.	Theory			
		(a)	(b)	(c)	(d)	(e)
NF_3	$4a_1$	**13.71**	14.54	14.91	9.51	10.40
	$1a_2$	**15.81**	18.27	18.74	11.48	12.40
	4e	**16.32**	18.45	18.96	11.85	12.80
	3e	**17.44**	20.12	20.60	13.03	13.97
	$3a_1$	**19.74**	23.29	23.82	15.53	16.40
	2e	**21.09**	23.51	24.06	16.86	17.77
	$2a_1$	**26.37**	30.16	30.62	22.25	23.13
PF_3	$4a_1$	**12.27**	12.51	12.89	8.79	9.55
	$1a_2$	**15.89**	17.86	18.34	11.46	12.27
	4e	**16.44**	18.21	18.70	11.83	12.62
	3e	**17.47**	19.46	19.97	12.80	13.61
	$3a_1$	**18.60**	20.71	21.25	13.91	14.68
	2e	**19.46**	21.33	21.87	14.87	15.63
	$2a_1$	**22.44**	24.90	25.41	18.10	18.86

(a) The uncertainty in the experimental values is ±0.06 eV.

(b) HF, 6-31G* basis set

(c) HF, 6-311+G* basis set

(d) DFT, 6-31G* basis set

(e) DFT, 6-311+G* basis set

Table 11-5: The calculated valence shell ionization potentials obtained from the difference in total energy between the initial and final sates (eV).

	Orbital	Exp.(a)	(b)	(c)	(d)	(e)	(f)	(g)
NF_3	$4a_1$	**13.71**	11.43	11.65	12.20	12.51	12.08	12.66
	$1a_2$	**15.81**	16.71	17.00	15.02	15.54	15.02	15.68
PF_3	$4a_1$	**12.27**	10.47	10.73	10.93	11.32	11.26	11.81
	$1a_2$	**15.89**	15.90	16.21	14.95	15.42	14.40	15.01

(a) The uncertainty in the experimental values is ±0.06 eV.

(b) HF, 6-31G* basis set

(c) HF, 6-311+G* basis set

(d) MP2, 6-31G* basis set

(e) MP2, 6-311+G* basis set

(f) DFT, 6-31G* basis set

(g) DFT, 6-311+G* basis set

Table 11-6: The calculated valence shell ionization potentials obtained from the CIS [102] excited states of NF_3^+ and PF_3^+ (Gaussian 94 [94] *ab initio* calculations) (eV).

	Orbital	Exp.	Theory	
		(a)	(b)	(c)
NF_3	$4a_1$	**13.71**	11.43	11.65
	$1a_2$	**15.81**	21.43	21.79
	4e	**16.32**	21.92	22.33
	3e	**17.44**	22.67	23.03
	$3a_1$	**19.74**	25.61	26.04
	2e	**21.09**	26.37	26.88
	$2a_1$	**26.37**	31.56	31.98
PF_3	$4a_1$	**12.27**	10.47	10.73
	$1a_2$	**15.89**	20.73	21.16
	4e	**16.44**	21.25	21.68
	3e	**17.47**	22.04	22.56
	$3a_1$	**18.60**	23.08	23.60
	2e	**19.46**	24.00	24.55
	$2a_1$	**22.44**	27.00	27.50

(a) the uncertainty in the experimental data is ±0.06 eV.

(b) 6-31G* basis set

(c) 6-311+G* basis set

12. Overview and General Discussion

A prerequisite for the assignment of x-ray spectra and their use in the determination of molecular electronic structure are theoretical models, which predict the experimental results accurately. In this thesis, MS-Xα [103] and *ab initio* methods were mainly used for the theoretical calculations. These reproduced the experimental data with varying degrees of accuracy.

12.1. The MS-Xα Technique for the Calculation of X-ray Spectra

Under the conditions explained in Section 3.5 for the MS-Xα calculations, the S($2p_{3/2}$) ionization potentials were on average within 1.5% of the experimental value, and the O(1s) ionization potentials within 2.3%. The Xα calculation overestimated the P(1s) ionization potentials and P(1s)→1e* transition energies by less than 0.35%.

12.1.1. The Effect of the Molecular Symmetry on the Ionization Potentials

In general, the calculations tended to overestimate the core ionization potentials. The 1s binding energies of the terminal oxygen atom, however, were a notable exception. For a number of the compounds studied (e.g. SOF_2 and OPF_3) the creation of an oxygen 1s hole does not alter the molecular symmetry. For these molecules the calculated O(1s) ionization potential (Table 6-12) consistently exceeds the experimental value (Table 6-1). Other molecules (e.g. SO_2) have at least two oxygen atoms related by symmetry. Creation of a localized core hole in one of these oxygen atoms breaks the overall molecular symmetry. For these molecules, calculation of the O(1s) ionization potential in the ground state symmetry results in a value about 7 eV (1.3%) less than experiment (Table 12-1), while calculation using the reduced symmetry of the ion yields a value comparable to those of compounds without symmetry reduction, about 7 eV (1.3%) larger than experiment. Averaging these results, thus modeling a symmetry transition state, gives values within 0.5% of the experimental result. These results show:

1. For species with equivalent oxygen atoms the calculation of the O(1s) ionization potential in the reduced symmetry of the ion gives values consistent with those obtained for molecules not experiencing symmetry reduction
2. Symmetry averaging results in the most accurate picture for O(1s) photoionization of molecules with equivalent oxygen atoms.

Although the above demonstrates the necessity of the reduced symmetry for an accurate description of the terminal oxygen 1s binding energies, in practice it cannot be used for many compounds, because their ground state molecular symmetry is C_s. The ion state with an oxygen core hole consequently belongs to the C_1 point group. The basis set for this latter group is too large for our MS-Xα program [146] to handle leading to a situation in which the program fails—that is the program crashes. The calculation of the terminal oxygen 1s spectra of molecules with equivalent oxygen atoms could therefore only be done for the ground state molecular symmetry.

12.1.2. The Chemical Shift of the Hydrides H_2S and PH_3

Although the absolute values of the S(2p) ionization potential of H_2S and the P(1s) ionization potential and P(1s)→$1e^*$ transition energy of PH_3 calculated with the MS-Xα technique agree well with the experimental results, when the chemical shifts (Chapters 5 and 6) were correlated, these particular "representative" molecules consistently deviated from the fit line. This phenomenon is possibly caused by an incorrect parameterization of the hydrogen atom. For the Xα calculations, all atoms were parameterized as described earlier (Section 3.5). In particular the potentials, which derive from the electron-electron interaction, were expressed in terms of the charge density of the electrons in the molecule. Sphere radii were determined based upon the initial atomic charge density for all atoms in the molecule, including hydrogen.

As with all other atoms, the sphere radius for hydrogen is dependent on the chemical environment. Two inequivalent hydrogen atoms in the same molecule can have significantly different sphere radii. Highly electronegative neighbours, for example oxygen and nitrogen, tend to draw electrons towards themselves. The charge density around hydrogen decreases and a small sphere radius is computed. With less electronegative neighbours like phosphorus, there is increased charge density around hydrogen, and thus, the sphere radius increases as well. In water, the sphere radius of hydrogen is 1.11 a.u. (0.59 Å), and in PH_3, 1.46 a.u. (0.77 Å). For methyl groups, the most common occurrence of hydrogen in the compounds studied, the sphere radius of hydrogen varied between 1.30 a.u. (0.69 Å) and 1.34 a.u. (0.71 Å), and for H_2S it was slightly larger: 1.36 a.u. (0.72 Å). Such a large variation in sphere radius is not in itself problematic, because the sphere radii of phosphorus and sulphur vary by 0.6 a.u. (0.3 Å) as the chemical environment is altered. The actual size of the sphere radius is, however, significantly larger than the atomic radius of the hydrogen atom (0.37 Å) [207]. The Xα sphere radii of the halogens, fluorine and chlorine, are also consistently greater than their respective atomic radii, due to the increase in charge density as these highly electronegative atoms gain electrons from their neighbours. In both cases, however, the Xα sphere radius is only about 30% greater than the corresponding atomic radius and it also remains fairly constant over the whole series of molecules studied. For phosphorus and sulphur, the sphere radius varies with the chemical environment. In species with highly electronegative ligand atoms, for example SF_4 or OPF_3, the phosphorus or sulphur sphere radius can be as much as 10% less than the corresponding atomic radius. The terminal sulphur atom in $SPCl_3$ on the other hand has a sphere radius 25% greater than the atomic radius. Similarly, the sphere radius of the central atom in PH_3 and H_2S is about 20% greater than the corresponding atomic radius.

As the above shows, MS-Xα sphere radii exceeding the corresponding atomic radius are not unique to hydrogen. For the latter atom, however, the calculated sphere radius exceeds the atomic radius by almost 60%, even in water, where the highly electronegative oxygen tends to draw most of the electron density away from hydrogen. These results suggest that employment of the atomic charge density to determine the sphere radius is not adequate for hydrogen.

The sphere radii and the molecular potential can also be computed using the radial function rather than the atomic charge density. This method might be preferable for the parameterization of the hydrogen atom. We concentrated on oxides and halides, and so this matter was not pursued. It should, however, be investigated for further evaluation of the MS-Xα technique.

12.1.3. Radicals and the Inclusion of Electron Spin

NO_2 was the only molecule studied which did not have a singlet ground state, hence it required the inclusion of electron spins in the calculation. Overall the MS-Xα method did not perform as well for NO_2 as it did for the other molecules. The calculations predict a $^2B_2$ ground state (Chapter 9) for the molecule with the unpaired electron in the $3b_2$ orbital, an oxygen 2p lone pair orbital, rather than in the $4a_1$ orbital which represents the accepted configuration for the NO_2 molecule [196, 197, 208]. At present, the reason for this discrepancy is not known. The MS-Xα program package [146] used herein retains the electron configuration initially specified. It does not reshuffle the occupancies to attain the lowest overall energy, thus allowing the calculation of any electronic state of the molecule. So the calculations of the ionization potentials and the O(1s)→mo* transition energies and oscillator strengths of NO_2 were performed using both the $^2B_2$ ground state (Chapter 9) predicted by MS-Xα and the accepted $^2A_1$ ground state [196, 197, 208] of the molecule. The results from both calculations were compared with experiment. The energy difference between these two initial electronic states of the molecule is 4.18 eV. This is 0.85 eV more than the value reported in the literature for the $^2A_1 \rightarrow {}^2B_2$ transition (3.33 eV) [196]. The O(1s) photoabsorption spectrum of the NO_2 molecule was discussed in detail in Chapter 9 of the thesis. In general the calculations performed with the $^2A_1$ ground state gave better agreement with experimental results. The ionization potentials for all molecular orbitals are listed in Table 12-2 along with the experimental data [154, 208]. Agreement of the absolute values is as expected for both core levels and valence shell. The MS-Xα method does predict the existence of LS splitting (Section 1.1) between the triplet and singlet states of the ion, but it significantly underestimates its value for the N(1s) core ionization regardless of initial electronic state. The splitting between two O(1s) core hole states was predicted better by the calculations employing the $^2B_2$ initial state. For the valence shell ionization potentials the predicted singlet-triplet splitting also deviates from the experimental result. The energy difference is underestimated for the $2b_2$ and $3b_2$ orbitals and overestimated for the $1a_2$ orbital. The Xα calculations also predict higher binding energies for the $4a_1$ orbital than for the $3b_2$ and, in the case of the $^2A_1$ state, the $1a_2$ orbitals. This is another manifestation of the $^2B_2$ ground state.

Studies with other radicals are required for further evaluation of the calculation method. In particular it must be ascertained whether the discrepancies mentioned above are a general phenomenon or specific to NO_2.

12.1.4. The Role of the Watson Sphere in the Calculation of the Pre-Edge Photoabsorption Peaks

To calculate the pre-edge photoabsorption spectra with the MS-Xα method, a Watson Sphere [103, 113] was applied to the system in order to stabilize the high-energy antibonding orbital. The beneficial effect of the sphere is a lowering of the energy of all molecular orbitals (occupied as well as unoccupied) by a uniform amount, but the relative energies remain fixed [113]. This is, however, not the only effect of the Watson Sphere. Indeed, close examination of the calculation results actually shows a variance of the transition energies with the parameters (charge and radius) of the Watson Sphere.

This is illustrated with the molecular orbital energies and the O(1s)→mo* transitions of SO_2 calculated with several different Watson Spheres. As expected, the energies of all molecular orbitals (occupied as well as unoccupied) are shifted downward by the presence of the Watson Sphere. The magnitude of this energy shift is dependent on the charge of the Watson Sphere, and with the increased charge, more virtual orbitals are stabilized. (Table 12-3). Similarly, the energy shift is inversely proportional to the Watson Sphere radius. A smaller radius leads to greater stabilization of virtual orbitals for the same Sphere charge. It would, thus, seem reasonable to use a sphere with a fairly high charge, e.g. +5.0, to ensure that all bound transitions are computed. Also, a sphere of the same size as the molecule, i.e. the outer sphere, or smaller might be considered appropriate. In the case of the SO_2 molecule, a Watson Sphere radius equal to the outer sphere radius and a charge of +1.0 on the Watson Sphere are sufficient to calculate all bound O(1s)→mo* transitions (Table 12-4). These parameters, however, depend on the individual molecule studied.

The Watson Sphere does achieve its intended goal, namely the stabilization of the virtual orbitals, but there are side effects to its use. The transition energies to virtual orbitals also shift with changes to the Watson Sphere parameters, and these shifts are not uniform. The oscillator strengths are also affected, again not uniformly. This is illustrated by the O(1s)→mo* transitions of SO_2 (Table 12-4). The O(1s)→$1b_1$* transition energy hardly changes as the Watson Sphere charge is increased, but the transition energies to all other virtual orbitals shift upwards by varying amounts. Similarly, a higher value of the Watson Sphere charge tends to increase the oscillator strength, but there are reversals of this general trend. Changes in the Watson Sphere radius also cause shifts in the transition energies and oscillator strengths (Table 12-5). Here, the energies are shifted upwards with the decreasing radius, i.e. increasing charge density. Again, the O(1s)→$1b_1$* transition is relatively unaffected. It does, however, decrease for very small radii (Table 12-5). Oscillator strengths tend to increase with decreasing Watson Sphere radius.

With our Xα program [146] it is possible to calculate the molecular orbital compositions as well. So, to investigate this noticeably different behaviour between the O(1s)→$1b_1$* and the other O(1s)→mo* transitions, the orbital compositions, as calculated with MS-Xα, of the first five antibonding orbitals were examined. Without a Watson Sphere, the $1b_1$* orbital is centered in the atomic and intersphere (IS) regions (34.45% S-p, 28.04% O-p, 23.57% IS). It can best be described as an unoccupied valence shell antibonding orbital. The other four virtual orbitals are all located in the outer sphere (OS) region ($1a_1$: 74.08% OS-s; $2a_1$: 82.21% OS-p; $2b_1$: 91.443% OS-p; $1b_2$: 94.54% OS-p). They are atomic-like Rydberg orbitals. With the addition of a Watson Sphere, all these molecular orbital compositions are altered. These changes are relatively minor for the $1b_1$* orbital. The S-p, O-p and IS character all increase slightly, S-p more so than the other two, with increasing Watson Sphere charge density, but the overall orbital identity remains essentially unchanged.

This is not the case for other orbitals. Here, an increase in the charge density of the Watson Sphere causes substantial changes to the overall orbital character. The contribution from the outer sphere decreases, and contributions from the atoms and the intersphere region increase. The virtual orbitals gain valence shell antibonding orbital character. This significant change in orbital composition is likely the cause of the upward shift of the transition energies as the charge density of the Watson Sphere is increased.

Given these side effects of the Watson Sphere, the calculation of bound photoabsorption transitions should be performed with a low charge density—i.e. a low charge and a large radius—on the Watson Sphere. It would be preferable not to use a Watson Sphere at all; however, this is not always feasible. For example, without a Watson Sphere, only a single antibonding orbital of the OPF_3 molecule is stabilized.

Overall the agreement of the calculated K shell spectra with the experimental results is variable. The Xα calculations for central atom K shell spectra gave results in reasonable agreement with experiment, for example Chapter 8, but for the terminal oxygen K shell spectra the oscillator strengths were often significantly deviant from experiment, leading to little resemblance with the experimental results; see for example Chapter 10.

Two approximations were made [114] in order to calculate the oscillator strength for electronic transitions.

1. H_{SCF} is replaced by an average self-consistent-field Hamiltonian. For this purpose, the one-electron transition-state Hamiltonian is used, appropriate for the configurational average between initial and final state.
2. The ground state density operator ρ_0 is assumed to be diagonal in the basis of this average Hamiltonian, achieved by expansion of ρ_0 in terms of transition state orbitals.

The accuracy of the second approximation depends on the magnitude of the perturbation involved [114]. A possible cause for these unexpected oscillator strengths could arise because the perturbation is too large for the second assumption to be valid. The transition energies and oscillator strengths are also affected by the molecular geometry. For the calculated spectra presented here the ground state molecular geometry [95-97] was used to calculated the transition energies and oscillator strengths (Chapters 8 to 10). It was assumed that the molecular geometry does not change during the excitation process. If this assumption is not correct for the oxygen K shell excitation of sulphuryl halides, for example, it could explain the observed differences between the calculated and experimental K shell spectra (Chapter 10).

Even given this mixed success for the K shell spectra, it seemed worthwhile to employ the Xα technique for the assignment of the peaks observed near the $L_{2,3}$ edge of phosphorus or sulphur, which has been done previously for OPF_3, $OPCl_3$ and PF_5 [113]. This immediately presented challenges due to the interactions between electron spin and orbital angular momentum. While the spin-orbit coupling (Section 1.1) of the 2p level can easily be inserted manually following the calculation, because the energy difference is a constant, this is not possible for the Russell-Saunders coupling (Section 1.1) and the molecular field effect (Section 3.3) which must be calculated directly. The former requires the inclusion of electron spin in the calculation, which can easily be done. To evaluate the molecular field effect, however, the component orbitals of the $L_{2,3}$ shell must be treated individually, in the same manner as the valence shell, rather than combined as a 2p core. The three 2p core orbitals have very similar energies; hence, they can only be computed individually if they have different symmetry. This places severe limits on the number of molecules for which adequate calculations of the $L_{2,3}$ edge can be performed. Molecules with overall C_{2v} symmetry, e.g. SO_2, present no problem, because the central atom 2p orbitals transform as a_1, b_1, and b_2. PF_3 and other molecules with C_{3v} symmetry, however, are more complicated. Here, the central atom 2p orbitals transform as a_1 and e. Although that in itself presents no problem, because the two orbitals have different symmetry, attempts to calculate an e→e excitation, however, will give only one of the four possible final states (A_1, A_2 and E). To obtain all four, the calculation must be done in a lower (e.g. C_s) symmetry to remove the degeneracy of the e orbitals; but then two of the central atom 2p orbitals have the same symmetry and being close in energy will likely mix. For example, in C_s symmetry the central atom 2p orbitals transform as a′, a′ and a″. The calculations are therefore extremely difficult, if not impossible. The same problem also arises for molecules with overall C_s symmetry.

12.2. Ab initio Gaussian 94 Methods for the Calculation of Ionization Potentials and X-ray Spectra.

Ionization potentials have been obtained with the Gaussian 94 program package [94] through application of Koopmans' theorem [8, 101] (Chapters 6 and 11). This method neglects all effects due to orbital relaxation in the final core hole state [8]. Theoretical values obtained at the Hartree-Fock (HF) [79] level tend to overestimate, while those obtained using Density Functional Theory (DFT) [86] underestimate the experimental result, see Chapters 6 and 11.

Ideally the transition energies to electronically excited states should be calculated as the total energy difference between the optimized excited state and the optimized ground state of the molecule to account for any relaxation effects and possibly changes in the molecular geometry resulting from the change in electron configuration. While geometry optimization can be achieved easily for most molecular systems with the Gaussian 94 package [94], the method cannot be readily employed to optimize electronically excited states (Chapter 11). The electron configuration is rearranged to minimize the total energy. Even with the use of symmetry constraints only the two, three or four lowest energy electronic states of an ion or molecule can be computed, a significant drawback of the method. Furthermore, there is no method for the calculation of the transition probabilities, see Chapter 11.

12.2.1. Molecular excited states with CIS

Transition energies to electronically excited states of a molecule can be calculated with Gaussian 94 [94] using the configuration interaction singles (CIS) method developed by Foresman et al. [102]. For a closed-shell molecule, all singly excited singlet and triplet states can be calculated. This method can thus be used to determine the Russell-Saunders coupling and the molecular field splitting. The accuracy of the CIS method is comparable to the MS-Xα technique. As expected, there are basis set effects to the calculated transition energies (Chapter 5). The value of the P(1s)$\rightarrow$1e* transition energy of various phosphorus compounds was calculated with CIS at the experimental geometry using the STO-3G and STO-3G* basis sets. Agreement with experiment is within 0.25% for the former and 0.16% for the latter basis set (Table 5-2 and Table 5-7). A somewhat surprising find was that the O(1s) core excited states of SO_2 calculated using the STO-3G basis set gives absolute values which were in better agreement with experiment than those given by the much larger 6-311+G* basis set (Table 12-6), the opposite to what would be expected. The larger basis set, however, gives better agreement with experiment for the relative peak energies, except for the energy difference between the first two peaks (Table

12-6). Geometry optimization has little effect on the calculated transition energies (Table 12-6). As with the MS-Xα technique, however, the spin-orbit coupling has to be added manually to the 2p core hole states.

There exists, however, a serious limitation to the CIS method in the Gaussian 94 [94] (and subsequent) packages. The Davidson Matrix used in the calculation of the excited states has a built-in maximum of 2000 diagonal elements. This places an upper limit on the number of excited states that can be calculated. For most polyatomic molecules this is 125; however, for molecules with very high symmetry—e.g. SF_6 (O_h) or CO_2 ($D_{\infty h}$)—only about 60 excited states can be computed. The excited states are calculated in order of increasing energy starting with the excitation of an electron from the HOMO into the LUMO. If large basis sets are used there are many virtual orbitals, and consequently a large number of excited states, resulting from the valence shell to virtual orbital electronic transitions. These can easily exceed the maximum number of states that can be computed. To compute the core excited molecular states, this must be overcome, and so most virtual orbitals must be frozen in the CIS calculation—i.e. they are not considered in the configuration interaction. The required orbital freezing is determined by both the core level investigated and the number of higher energy occupied orbitals in the molecule. For example, the O(1s)→mo* excited states of SO_2 can be determined with eight active virtual orbitals, while for SO_2F_2 all but the first five must be frozen, and for CF_3SO_2Cl only three can be left active. This severely limits the number and type of molecule for which core excited states can be calculated with the CIS method. In consequence the CIS method was not used extensively for the theoretical analysis of the data presented here.

The theoretical S(2p) spectrum of NSF_3 presented here (Chapter 7) was calculated using the GSCF3 computer code [163, 168]. The calculations were done by Dr. N. Kosugi at the Institute for Molecular Sciences in Okazaki, Japan. For this spectrum (see Chapter 7) and the P(2p) and P(1s) spectra of phosphorus halides [166, 176] the theoretical spectra obtained agree reasonably well with experiment. To make a proper evaluation of this code, however, further studies into the capabilities and limitations of the method are required.

12.3. The Occurrence of LS states. Is this a General Phenomenon?

Recent studies of the $L_{2,3}$ edges of phosphorus and sulphur halides [163] led to the proposal of the existence of a final electronic state (e→e $^1A_1$) which displays LS coupling rather than the usual jj coupling. Further studies of this molecule and other phosphorus halides [166] showed that this LS coupled electronic state is not unique to PF_3. It does, however, have much lower intensity in the other molecules. It is also not unique to phosphorus halides as a study of the $L_{2,3}$ edge of NSF_3 [209] (Chapter 7) has shown. Several question now arise:

1. How common is this LS coupled state?
2. Under what circumstances is it observed?
3. Why does it occur?

To try to answer the first question, the excited states immediately preceding the $L_{2,3}$ edge for a variety of phosphorus and sulphur molecules were calculated. These calculations were done with the CIS method [102] in the Gaussian 94 program package [94]. The 6-311G* basis set was used. All molecular geometries were optimized at the Hartree-Fock level of theory before calculation of the excited states. Only the first four virtual orbitals were considered in the calculation of the excited states for most molecules, but there were some cases, where, out of necessity three or five virtual orbitals had to be considered. The transition energies were obtained for both the singlet and triplet states and the split energy ($\Delta E_{S\text{-}T}$) for each pair was compared to the spin-orbit split energy ($\Delta E_{S\text{-}O}$) (0.9 eV for P and 1.2 eV for S). States with $\Delta E_{S\text{-}T}$ exceeding $\Delta E_{S\text{-}O}$ were considered to be L-S coupled.

Table 12-7 lists those molecules investigated where the calculations predict the existence of an LS coupled final state following $L_{2,3}$ core excitation of the central atom. The absence of OPF_3 from this list is surprising. A recent study of the phosphorus $L_{2,3}$ photoabsorption spectrum of this molecule indicated the presence of two such states, $^1A_1$ ($e \rightarrow 1e^*$) at 139.6 eV and $^1A_1$ ($a_1 \rightarrow 2a_1^*$) at 142.4 eV [166]. Similarly two such LS coupled states were reported for SPF_3 [166] and NSF_3 [209] (Chapter 7). The conflicting result in the present calculation could be a basis set effect. Two LS states are predicted for

OPF_3 if the 4-31G* basis set is used rather than 6-311G*. Clearly, further investigation into the reliability of the CIS method is required.

Nevertheless, these calculation results can be used for a preliminary study of LS states in the photoabsorption spectra. They suggest an L-S coupled final state in the central atom $L_{2,3}$ pre-edge region is a fairly general phenomenon. It is most prominent in species with highly electronegative ligands such as Cl, O and F and with a non-bonding electron pair nominally centred on the central atom, as is the case in PF_3, SCl_2 and SF_4, for example. In all instances the electronic state is fully symmetric with respect to the molecular symmetry.

It has been proposed [166] that the magnitude of $\Delta E_{S\text{-}T}$ is related to the size of the two open-shell orbitals and the degree of overlap between them. Of particular importance are the central atom p-character of the virtual orbital, the amount of localization of the virtual orbital and the spatial extent of the central atom 2p orbitals. The present calculations indicate that the interaction between the two unpaired electrons and lone pair electrons in the valence shell of the central atom is also of importance in the determination of the $\Delta E_{S\text{-}T}$ for the excited state. Further detailed calculations are required to ascertain the origin of the LS coupled states in the $L_{2,3}$ pre-edge region.

The jj and LS coupling schemes traditionally employed in the assignment of photoabsorption spectra represent two extreme cases which must connect smoothly through a region of intermediate coupling [163, 166]. A form of intermediate coupling would give the best description of the final electronic states of the molecule. So, a proper theoretical calculation should ideally be done with an intermediate-coupling scheme. This extra level of complexity to the calculation is, to our knowledge, at present not available.

In addition to the theory development further experimental studies should be done. This includes the investigation of the sulphur $L_{2,3}$ edge of molecules such as SCl_2, SO_2 and SF_4 for evidence of L-S coupled states, and ISEELS measurements should be done to determine the energies of the triplet states. The electronic structure of the LS state should also be studied through investigation of the decay mechanisms. The PF_3 molecule is so far the best species for such studies, as the LS coupled $^1A_1$ $(e \rightarrow 1e^*)$ state gives rise to a very prominent peak in the P(2p) photoabsorption spectrum [166]. A resonant Auger spectrum

[119, 165] has been observed corresponding to this state of the molecule, and this should receive further investigation.

12.4. Bond Covalency deduced from the p-character of molecular antibonding orbitals

An important aspect of x-ray spectroscopy is the ability to make an accurate determination of photoionization cross-section as a function of energy. As this value is dependent upon the transition probability, it should then be possible to deduce information about the final electronic state from the peak intensity. This includes the composition of the antibonding orbitals. The pre-edge feature in the Cl 1s spectrum of $CuCl_4^{2-}$ salts has been used to evaluate the covalency of the $Cu(3d_{x^2-y^2})$-Cl(3p) antibonding orbital [210].

For an electronic transition from an atomic core orbital $\psi_i(A)$ on atom A to a valence shell molecular antibonding orbital $\phi_f = \sum a_j\psi_j$, where (ψ_j) is the set of orthonormalized atomic orbital basis functions (see Section 3.6), the photoabsorption cross-section is given by equation (12-1), where c is a constant [210]:

$$I(\psi_i(A)\rightarrow\varphi_f) = c \mid \langle\psi_i(A)| \, \mathbf{r} \, |\phi_f\rangle \mid^2 = c \sum_j |a_j|^2 \mid \langle\psi_i(A)| \, \mathbf{r} \, |\psi_j\rangle \mid^2 \qquad (12\text{-}1)$$

Due to the localized nature of ψ_i only the terms corresponding to dipole allowed transitions within atom A are non-zero. In particular if $\psi_i(A)$ is the 1s orbital then the surviving terms all correspond to np orbitals on A, where n is the principal quantum number of the valence shell of atom A [210].

$$\begin{aligned} I(A(1s)\rightarrow\varphi_f) &= c \mid \langle A(1s)| \, \mathbf{r} \, |\phi_f\rangle \mid^2 \\ &= c \sum_j |a_j|^2 \mid \langle A(1s)| \, \mathbf{r} \, |\psi_j\rangle \mid^2 \\ &= |a_{A(np)}|^2 \, [c \mid \langle A(1s)| \, \mathbf{r} \, |A(np)\rangle \mid^2] \end{aligned} \qquad (12\text{-}2)$$

The term $[c \mid \langle A(1s)| \; \mathbf{r} \; |A(np)\rangle \mid^2]$ represents the 1s→np peak intensity in the spectrum of an isolated A atom. From the normalization condition

$$\phi_j = \langle\phi_j|\phi_j\rangle = \sum_j |a_j|^2 = 1, \tag{12-3}$$

the parameter $|a_{A(np)}|^2$ represents the % contribution of the A(np) atomic orbitals to ϕ_j. So, the observed $A(1s)\rightarrow\phi_f$ transition peak intensity in a molecular spectrum is scaled to the corresponding A(1s)→np peak intensity in the spectrum of the isolated atom by the delocalization of ϕ_f [210].

A preliminary study of the covalency based upon peak intensity is presented here for A=O π^* and P–X σ^* bonds. Oxygen 1s and Phosphorus 1s spectra were obtained as described previously (Chapters 5 and 6). They were normalized by taking the ratio of the two cell currents (i_1/i_2). The absorption cross-section σ was calculated according to equation 2-10. The number density N = n/V was obtained from the ideal gas equation and experimental gas pressures in the cells. The phosphorus compounds investigated are a subset of those studied in Chapter 5 and the oxygen spectra include O_2, CO, CO_2, NO_2, NO and SO_2, see Table 12-8 and Table 12-9.

As already discussed (Chapter 5) the phosphorus 1s spectra display a high intensity pre-edge peak resulting from the P(1s)→1e* (P-X σ^*) transition. Chemical shift effects of the transition energy of this feature were investigated in detail. Similarly, all of the oxygen 1s spectra possessed a high intensity peak corresponding to the O(1s)→π^* transition demonstrating chemical shift effects as well (Table 12-8).

The spectra were collected during several different experimental sessions. At the time quantitative determination of the photoabsorption cross-section was not a goal of the experiment. Interest focused mainly on spectral resolution, chemical shifts and overall spectral appearance (features observed and relative peak intensities within a spectrum). So, the pressure gauge was not absolutely calibrated, and in consequence, the experimental cross-sections are not accurate absolute values. They can only be compared for molecules whose spectra were run during the same experimental session. The resultant covalencies, however, can be compared for all molecules.

The 1s absorption spectra of isolated P and O atoms could not be measured, so it was necessary to determine the intensity of the O(1s)→2p and P(1s)→3p peaks by other means. In the case of oxygen this was easily achieved using the experimental spectrum of O_2, where the O-O π bond is purely covalent. The contribution from each oxygen atom to the π and π* orbitals is 50% O(2p). The term $|a_{A(np)}|^2$ equals 0.5 and the O(1s)π* peak intensity in the spectrum of O_2 is half that of the 1s→2p peak in the oxygen atom. For phosphorus the situation is more complex, because a corresponding gaseous P_2 molecule is not readily available under the experimental constraints which prevailed. The normal state of elemental phosphorus is P_4, a solid, which volatizes at relatively high temperature (280 °C [211]).

The P_2 molecule can be formed in the gas phase, but exists in equilibrium with P_4 only at temperatures above 800 °C [30]. A gas cell system at such extreme temperatures is impractical, so the total ion yield spectrum needs to be measured under constant flow conditions similar to gas phase PEPICO spectra with a heated gas inlet system. Spectra must be collected at several different temperatures above and below 800 °C to evaluate temperature effects and to separate the P_2 spectrum from the P_4 spectrum. Alternatively P atoms could be created from gaseous P_4 with the aid of a microwave discharge attached to the gas inlet system as was used for the measurement of the K shell spectrum of the oxygen atom [212, 213]. The photoabsorption cross-section can be obtained from a constant flow system as described elsewhere [214]. A calibrated photodiode is required to measure the incident photon flux I_0, and care must be taken to keep the gas flow constant in order to be able to estimate the pressure in the ionization region accurately.

Of the compounds studied here, the PH_3 molecule is the best choice for a standard. Phosphorus and hydrogen have nearly identical electronegativity (2.19 and 2.20, respectively on the Pauling scale), so the P-H bond is expected to be essentially covalent (50% H-1s, 50% P), and 1e*—a valence shell antibonding orbital—is expected to have 50% H-s character and 50% P-p character. Because the spectrum of PH_3 was not measured at each session, the covalency of PF_3 obtained from one data set vs. PH_3 was used as standard for the other two sessions. Similarly CO_2 was used as standard in another session of measurement, because of suspected contamination of the O_2 sample with air.

Table 12-8 and Table 12-9 list the transition energies and the photoabsorption cross-section of the O(1s)→π* and P(1s)→1e* transitions, respectively. The oxygen or phosphorus p-character of the antibonding orbital determined from the experimental cross-section is listed in the Tables as well. The molecules are grouped according to the experimental session. As already explained, the cross-sections differ significantly from session to session, because they are not absolute nor correctly calibrated values. The p-character, however, was fairly reproducible (within 2% for N_2O and within 8% for OPF_3, SPF_3 and PF_5). Given these results the overall uncertainty of the experimentally determined p-character is estimated at 10%.

Quantitative analysis of gas phase photoabsorption spectra to determine ionization cross-section and molecular orbital composition is possible, provided an accurate method for pressure determination is available. The gauge employed must be calibrated, and the pressure must be measured for each data point of the spectrum, to properly account for slight pressure variations, which may occur during each acquisition sequence.

The gas pressure is also affected by any gaseous impurities present in the cell. These impurities include nitrogen and oxygen, which may be introduced through small air leaks in the gas inlet system. Their presence may only be detected if the N(1s) or O(1s) energy regions are probed, and the 1s→π*peak of N_2 and O_2 does not overlap with a photoabsorption peak of the compound studied. Also, gaseous photodecomposition products of the compound may accumulate in the cell, affecting the overall gas pressure. These might be detected by accurate measurement of the pressure and the absorption spectrum with time, as illustrated in Chapter 10 for SO_2Cl_2.

Theoretical values for the p-character of the antibonding orbital were calculated with Gaussian 94 [94] at the Hartree-Fock level of theory, using the 6-311G* basis set. The molecular geometry was optimized. The molecular orbital compositions were determined from the orthonormalized LCAO molecular orbital coefficients (Section 3.6). Natural Bond Orbital (NBO) Analysis [151] was also used to determine the composition of the antibonding orbital of interest. The results of these calculations are listed in Table 12-8 and Table 12-9 as well.

Agreement between the two calculation methods is variable. In general, it is better for the π* orbital in the oxides than for the 1e* orbital in the phosphorus halides. The phosphorus p-character of the three hypervalent molecules—SPF_3, OPF_3, and PF_5—differs significantly (Table 12-9), with the NBO method predicting much lower p-character. The NBO method also predicts significant phosphorus d-character for the 1e* orbital in the hypervalent species, but the LCAO method does not.

According to both calculation methods, the chemical bonds in all molecules except O_2 are polar. The degree of polarity depends on the ligands involved. P-F bonds are significantly more polar than P-H or P-Cl bonds, for example. The NBO analysis method, however, does suggest some unusual bonding patterns, for example $O{-}C{\equiv}O$, $S{-}C{\equiv}O$, $O{\equiv}PF_3$, and $S{\equiv}PF_3$.

Agreement between the calculated p-character of the antibonding orbital and experimental value is also variable (Table 12-8 and Table 12-9). In general, the experimental P(3p) character exceeds the calculated results, suggesting greater polarity of the chemical bonds than predicted by theory. Similarly, the experimental O(2p) character is greater than the theoretical value for most molecules.

For the O(1s)→π* data there is no overall trend to which calculation method (LCAO or NBO) gives better agreement with experiment. The O(2p) character of the π* orbital of N_2O calculated by the NBO method illustrates another example of an incorrectly predicted molecular structure ($N{\equiv}N{-}O$). The π* orbital is given as an N-N antibonding orbital without any O(2p) character by the NBO method.

For the P(1s)→1e* data, however, the LCAO method gives better agreement with the experimental result. Especially, for the hypervalent molecules the P(3p) character of the 1e* orbital calculated by the NBO method differs significantly from the experimental result. As the Tables show, the theoretical values of the oxygen or phosphorus p-character of the π* or 1e* orbitals, respectively, often differs from the experimental result by amounts exceeding the experimental uncertainty, regardless of the calculation method used. This preliminary study suggests that further development of the theory is required.

12.5. Conclusion

The above discussions show that at present there are serious shortfalls to the theoretical methods for the study of core level photoabsorption spectra. As the use of x-ray spectroscopy becomes increasingly important in the study of the electronic structure of both gas phase and solid state molecular systems, good theoretical models are required. The development of such models is thus an important focus for future research in this area.

Table 12-1: The effects of molecular point group on the O(1s) ionization potentials calculated with Xα.

Compound	C_{2v}	C_s	Ave.	Exp.$^{(a)}$	% Diff
SO_2	532.98	548.21	540.60	539.83	+0.14
SO_2F_2	532.30	548.10	540.20	540.56	-0.07
SO_2Cl_2	533.17	548.81	540.99	539.26	+0.32
NO_2 str.	531.76	540.64	536.20	541.3$^{(b)}$	-0.94
wk.	530.97	540.46	535.72	540.0$^{(b)}$	-0.79
	D_{3h}	C_{2v}			
SO_3	528.02	548.70	538.36	540.68$^{(b)}$	-0.43

(a) The uncertainty in the experimental data is estimated at ±0.10 eV.

(b) Reference [154].

Table 12-2: The Ionization Potentials (eV) of the NO_2 Molecule.

orbital		Exp.$^{(a)}$	MS-Xα		G-94
			$^2B_2$	$^2A_1$	
O(1s)	S	542.0	531.76	530.43	563.44
	T	541.3	530.97	530.09	563.03
N(1s)	S	413.3	411.27	412.28	432.64
	T	412.6	411.48	412.16	432.01
$1a_1$	S		41.14	41.31	46.86
	T		40.42	40.52	45.63
$1b_2$	S		33.32	33.12	41.65
	T		32.30	32.30	40.48
$2a_1$	S		23.53	23.24	26.48
	T	21.26	22.55	22.47	24.07
$2b_2$	S	21.0	20.97	20.67	21.92
	T	18.86	19.94	19.88	20.42
$1b_1$	S		18.58	18.63	21.31
	T	17.64	17.91	17.88	20.69
$3a_1$	S		19.04	19.27	23.14
	T	17.45	18.50	18.52	19.71
$1a_2$	S	14.06	14.20	13.43	14.43
	T	13.60	12.90	12.71	14.27
$3b_2$	S	14.51	12.13	11.29	16.50
	T	13.01		10.55	13.65
$4a_1$	S	11.23	13.73	13.72	13.94
	T		12.99		

(a) the core ionization potentials were obtained from [154] and the valence shell ionization potentials were obtained from [208].

Table 12-3: The stabilization effect by the Watson Sphere on the virtual orbitals of SO_2. At a constant sphere radius (R = 4.035 a.u.) an increased Sphere charge Q leads to increased stabilization.

orbital	orbital energy (Rydberg)		
	no Sphere	Q = 0.5	Q = 1.0
$1b_1^*$	-0.3039	-0.5389	-0.7743
$1a_1^*$	-0.2174	-0.3934	-0.5875
$2b_1^*$	-0.1649	-0.3204	-0.4947
$2a_1^*$	-0.1576	-0.3049	-0.4735
$1b_2^*$	-0.1512	-0.2986	-0.4679
$3a_1^*$	-------	-0.2502	-0.4273
$3b_1^*$	-------	--------	-0.3738
$2b_1^*$	-------	-------	-0.3636
$4a_1^*$	-------	-------	-0.3515
$1a_2^*$	-------	-------	-0.3542
$5a_1^*$	-------	-------	-0.3107
$3b_1^*$	-------	-------	-0.3019

Table 12-4: The effect of the Watson Sphere charge Q on the calculated O(1s)→mo* transition energies (E) and oscillator strengths (f) of SO_2 at a constant Sphere radius (R = 4.035 a.u.).

The calculated O(1s) ionization potential is 532.98 eV.

transition	no Sphere		Q = 0.5		Q = 1.0	
	E (eV)	f($\times 10^8$)	E (eV)	f($\times 10^8$)	E (eV)	f($\times 10^8$)
$O(1s)\rightarrow 1b_1^*$	524.69	1964592	524.68	1991078	524.66	2004174
$O(1s)\rightarrow 1a_1^*$	527.72	151923	528.19	246536	528.51	347276
$O(1s)\rightarrow 2b_1^*$	528.90	34521	529.72	76363	530.36	122784
$O(1s)\rightarrow 1b_2^*$	529.04	80737	529.69	204087	530.03	378280
$O(1s)\rightarrow 2a_1^*$	529.13	47110	529.93	41743	530.04	122135
$O(1s)\rightarrow 3a_1^*$	-------	-------	529.76	743923	530.81	556665
$O(1s)\rightarrow 2b_2^*$	-------	-------	-------	-------	531.80	651038
$O(1s)\rightarrow 3b_1^*$	-------	--------	-------	-------	532.25	68263
$O(1s)\rightarrow 4a_1^*$	-------	-------	-------	-------	532.56	94509
$O(1s)\rightarrow 1a_2^*$	--------	--------	-------	-------	532.74	204372
$O(1s)\rightarrow 3b_2^*$	-------	-------	-------	-------	532.91	133934
$O(1s)\rightarrow 5a_1^*$	-------	-------	-------	-------	532.95	300067

Table 12-5: The effect of the Watson Sphere radius on the calculated O(1s)→mo* transition energies (E) and oscillator strengths (f) of SO_2 at a constant Sphere charge (Q = 0.5).

The calculated O(1s) ionization potential is 532.98 eV.

transition	R = 10.0 a.u.		R = 4.035 a.u.		R = 1.0 a.u.	
	E (eV)	f(×10^8)	E (eV)	f(×10^8)	E (eV)	f(×10^8)
O(1s)→$1b_1$*	524.69	1969825	524.68	1991078	524.24	2129388
O(1s)→$1a_1$*	527.72	154415	528.19	246536	529.33	1497049
O(1s)→$2b_1$*	528.91	36219	529.72	76363	533.59	413764
O(1s)→$1b_2$*	529.04	84906	529.69	204087	530.84	1167429
O(1s)→$2a_1$*	529.13	48534	529.93	41743	531.81	622229
O(1s)→$3a_1$*	-------	-------	529.76	743923	534.78	817743
O(1s)→$2b_2$*	-------	-------	-------	-------	537.17	352056
O(1s)→$1a_2$*	--------	--------	-------	-------	537.36	953415
O(1s)→$3b_1$*	-------	--------	-------	-------	536.79	22516
O(1s)→$4a_1$*	-------	-------	-------	-------	537.86	84953
O(1s)→$5a_1$*	-------	-------	-------	-------	538.99	71949
O(1s)→$3b_2$*	-------	-------	-------	-------	539.24	167399

Table 12-6: The O(1s)→mo* transitions of SO_2, calculated with the CIS [102] method of Gaussian 94 [94].

#	Experiment	Calculation			
	(Chapter 9)(a)	(b)	(c)	(d)	(e)
1	$^1B_1$	$^1A_2$ 539.63	$^1A_2$ 550.27	$^1A_2$ 550.27	$^1A_2$ 550.45
	530.25	$^1B_1$ 539.64	$^1B_1$ 550.27	$^1B_1$ 550.27	$^1B_1$ 550.45
2	$^1A_1$, $^1B_2$	$^1B_2$ 544.24		$^1A_1$ 557.30	$^1A_1$ 557.43
	534.20	$^1A_1$ 544.25		$^1B_2$ 557.30	$^1B_2$ 557.43
3	$^1A_1$, $^1B_2$	$^1B_2$ 557.13		$^1B_2$ 558.35	$^1B_2$ 558.33
	534.64	$^1A_1$ 557.13		$^1A_1$ 558.35	$^1A_1$ 558.33
4	$^1B_1$		$^1B_2$ 558.72	$^1B_2$ 558.85	$^1B_2$ 558.91
	535.24		$^1A_1$ 558.72	$^1A_1$ 558.85	$^1A_1$ 558.91
5	$^1A_1$, $^1B_2$		$^1B_1$ 559.46	$^1B_1$ 559.46	$^1B_1$ 559.33
	535.89		$^1A_2$ 559.46	$^1A_2$ 559.46	$^1A_2$ 559.33
6	?			$^1A_1$ 560.06	$^1A_1$ 560.07
	536.89			$^1B_2$ 560.06	$^1B_2$ 560.07
7	$^1A_1$, $^1B_2$			$^1B_2$ 561.10	$^1B_2$ 561.05
	537.45			$^1A_1$ 561.10	$^1A_1$ 561.05
8	$^1A_1$, $^1B_1$, $^1B_2$			$^1A_1$ 562.97	$^1A_1$ 562.85
	538.16			$^1B_2$ 562.97	$^1B_2$ 562.85

(a) Table 9-3b lists the antibonding orbitals involved. The O(1s) orbitals have a_1 and b_2 symmetry, respectively. The uncertainty in the experimental values is ±0.08 eV.

(b) STO-3G basis set, three (all) antibonding orbitals used in the calculation. Experimental geometry [97]

(c) 6-311+G* basis set, three antibonding orbitals used in the calculation. Experimental geometry [97]

(d) 6-311+G* basis set, eight antibonding orbitals used in the calculation. Experimental geometry [97]

(e) 6-311+G* basis set, eight antibonding orbitals used in the calculation. Optimized geometry.

Table 12-7: The central atom $L_{2,3}$ shell excited state, which displays LS coupling. Listed are the compound, the identity of the state and the calculated split energy between the singlet and the triplet states.

Compound	State	ΔE_{S-T} (eV)
PF_3	A_1 (e→1e*)	2.53
PCl_3	A_1 (e→1e*)	1.86
PBr_3	A_1 (e→1e*)	1.83
$SPCl_3$	A_1 (e→1e*)	1.81
$OPCl_3$	A_1 (e→1e*)	1.38
SPF_3	A_1 (e→1e*)	1.22
$CH_3P(S)Cl_2$	A′ (a″→1a″*)	1.17
CH_3PCl_2	A′ (a″→1a″*)	1.08
CF_3PCl_2	A′ (a″→1a″*)	1.00
CH_3OPCl_2	A′ (a″→1a″*)	1.00
$CH_3P(O)Cl_2$	A′ (a″→1a″*)	0.91
SCl_2	A_1 (b_2→1b_2*)	2.29
SF_4	A_1 (a_1→1a_1*)	1.79
SOF_2	A_1 (a″→1a″*)	1.64
SO_2Cl_2	A_1 (b_1→1b_1*)	1.55
$SOCl_2$	A_1 (a″→1a″*)	1.49
SO_2	A_1 (b_1→1b_1*)	1.48
NSF_3	A_1 (e→1e*)	1.34

Table 12-8: The $O(1s)\rightarrow\pi^*$ transition energies and cross-sections, and the experimental and calculated O(2p) character of the π^* orbital.

Compound	Peak Energy (eV)(a)	cross-section (MB)	%O(2p) character		
			Exp.(b)	LCAO	NBO
Sept. 94 data					
O_2	530.90	11.5	50.0	49.5	49.8
CO_2	534.96	7.89	34.3	19.0	20.1
N_2O	534.46	4.73	20.1	13.1	0.00
Jun. 95 data					
CO_2	535.01	3.54	34.3	19.0	20.1
CO	533.78	3.93	38.1	22.8	21.2
Aug. 95 data					
O_2	530.90	8.77	50.0	49.5	49.8
N_2O	534.36	3.60	20.5	13.1	0.00
NO	532.46	2.43	13.9	32.6	31.9
NO_2	532.15	3.73	21.3	22.8	-------
SO_2	530.36	5.10	29.1	20.3	24.5
COF_2	532.47	2.78	15.8	26.1	28.1
OCS	533.13	4.22	24.1	18.2	24.5

(a) The uncertainty in the $O(1s)\rightarrow\pi^*$ transition energy is ±0.08 eV.

(b) The uncertainty in the experimental p-character is estimated as ±10%.

Table 12-9: The P(1s)→1e* transition energies and cross-sections, and the experimental and calculated P(3p) character of the 1e* orbital.

Compound	Peak Energy (eV)[a]	cross-section (MB)	%P(3p) character Exp.[b]	LCAO	NBO
May 94 data					
PF_3	2149.27	0.470	91.6	80.8	70.6
PF_5	2154.98	0.361	70.4	81.4	53.4
OPF_3	2153.29	0.435	84.8	82.2	40.7
SPF_3	2151.43	0.365	71.2	62.7	40.4
Aug. 94 data					
OPF_3	2153.29	0.856	78.4	82.2	40.7
SPF_3	2151.43	0.852	78.0	62.7	40.4
PF_3	2149.27	1.000	91.6	80.8	70.6
PCl_3	2147.31	1.041	95.3	65.1	58.4
PH_3	2145.84	0.546	50.0	64.9	43.6
PBr_3	2146.46	0.493	45.1		
PF_5	2154.98	0.802	73.4	81.4	53.4
Apr. 98 data					
PF_3	2149.27	1.142	91.6	80.8	70.6
SPF_3	2151.43	1.004	80.5	62.7	40.4

(a) The uncertainty in the P(1s)→1e* transition energy is ±0.04 eV.

(b) The uncertainty in the experimental p-character is estimated as ±10%.

13. References

[1] B.M. Gimarc. *Molecular Structure and Bonding. The Qualitative Molecular Orbital Approach* Academic Press, New York, 1979.

[2] F. Herman. in *Encyclopedia of Physics. 2nd Edition* (Ed. R.G. Lerner & G.L. Trigg) 72-76, VCH Publishers Inc., New York, 1991.

[3] R.K. Nesbet. in *Encyclopedia of Physics. 2nd Edition* (Ed. R.G. Lerner & G.L. Trigg) 70-72, VCH Publishers Inc., New York, 1991.

[4] J.T. Waber. in *Encyclopedia of Physics. 2nd Edition* (Ed. R.G. Lerner & G.L. Trigg) 76-80, VCH Publishers Inc., New York, 1991.

[5] H.F. Schaefer III. in *McGraw-Hill Encyclopedia of Chemistry. 2nd Edition* (Ed. S.P. Parker) 904-908, McGraw-Hill Inc., New York, 1993.

[6] J.K. Burdett. in *McGraw-Hill Encyclopedia of Chemistry. 2nd Edition* (Ed. S.P. Parker) 649-655, McGraw-Hill, New York, 1993.

[7] R. McWeeny. *Methods of Molecular Quantum Mechanics, 2nd Edition* 1-517, Academic Press, London, 1989.

[8] J.W. Rabalais. *Principles of Ultraviolet Photoelectron Spectroscopy* 1-454, John Wiley & Sons, New York, 1977.

[9] R. Tertian and F. Claisse. *Principles of Quantitative X-Ray Fluorescence Analysis* 1-385, Heyden, London, 1982.

[10] H. Aksela, S. Aksela and N. Kabachnik. in *VUV and Soft X-Ray Photoiionization* (Ed. U. Becker & D. A. Shirley) 401-440, Plenum Press, New York, 1996.

[11] I. Nenner and P. Morin. in *VUV and Soft X-Ray Photoionization* (Ed. U. Becker & D.A. Shirley) Plenum Press, New York, 1996.

[12] J.H.D. Eland and V. Schmidt. in *VUV and Soft X-Ray Photoionization* (Ed. U. Becker & D.A. Shirley) 495-520, Plenum Press, New York, 1996.

[13] H. Winick. in *Synchrotron Radiation Research* (Ed. H. Winick & S. Doniach) 754, Plenum Press, New York, 1980.

[14] A.E. Reed and P. von Ragué Schleyer, J. Am. Chem. Soc. 112 (1990) 1434-1445.

[15] J.I. Musher, Angew. Chem. Internat. Edit. 8 (1969) 54-68.

[16] T.A. Carlson. *Photoelectron and Auger Spectroscopy* 1-417, Plenum Press, New York, 1975.

[17] J.D. Bozek, J.N. Cutler, G.M. Bancroft, L.L. Coatsworth, K.H. Tan, D.S. Yang and R.G. Cavell, Chem. Phys. Lett. 165 (1990) 1-5.

[18] R.G. Cavell and K.H. Tan, Chem. Phys. Lett. 197 (1992) 161.

[19] Z.F. Liu, G.M. Bancroft, J.N. Cutler, D.G. Sutherland, K.H. Tan, J.S. Tse and R.G. Cavell, Phys. Rev. A 46 (1992) 1688-1691.

[20] G.M. Bancroft, Canadian Chemical News June 1992 (1992) 15-22.

[21] G. Öhrwall, P. Baltzer and J. Bozek, Phys. Rev. Lett. 81 (1998) 546-549.

[22] P. Baltzer, L. Karlsson and B. Wannberg, Phys. Rev. A 46 (1992) 315-317.

[23] G. Öhrwall, P. Baltzer and J. Bozek, J. Phys. B: At. Mol. Opt. Phys. 32 (1999) L51-L56.

[24] J. Stöhr. *NEXAFS Spectroscopy* 1-403, Springer-Verlag, Berlin, 1992.

[25] L. Pauling and E.B.W. Jr. *Introduction to Quantum Mechanics With Applications to Chemistry* 1-468, Dover Publications, Inc., New York, 1935.

[26] C. Cohen-Tannoudji, B. Diu and F. Laloë. *Quantum Mechanics, Volume 2* John Wiley & Sons, New York, 1977.

[27] P.W. Atkins. *Physical Chemistry, 4th edition* W.H. Freeman and Company, New York, 1990.

[28] D.C. Harris and M.D. Bertolucci. *Symmetry and Spectroscopy* Dover Publications Inc., New York, 1978.

[29] M. Karplus and R.N. Porter. *Atoms & Molecules: An Introduction for Students in Physical Chemistry* 1-620, W.A. Benjamin Inc., Menlo Park, California, 1970.

[30] D.F. Shriver, P.W. Atkins and C.H. Langford. *Inorganic Chemistry* W.H. Freeman and Company, New York, 1990.

[31] R.H. Sands. in *Encyclopedia of Physics. 2nd Edition* (Ed. R.G. Lerner & G.L. Trigg) 1162-1165, VCH Publishers Inc., New York, 1991.

[32] G.A. Somorjai. *Principles of Surface Chemistry* Prentice-Hall Inc., Englewood Cliffs, New Jersey, 1972.

[33] J.A. Bearden and A.F. Burr, Rev. Mod. Phys. 39 (1967) 125.

[34] D. Chattarji. *The Theory of Auger Transitions* 1-265, Academic Press, London, 1976.

[35] M. Richter, M. Meyer, M. Pahler, T. Prescher, E. v. Raven, B. Sonntag and H.E. Wetzel, Phys. Rev. A 39 (1989) 5666.

[36] T. Ibuki, T. Imamura, I. Koyano, T. Masuoka and C.E. Brion, J. Chem. Phys. 98 (1993) 2908-2915.

[37] R. Thissen, J. Delwiche, J.M. Robbe, D. Duflot, J.P. Flament and J.H.D. Eland, J. Chem. Phys. 99 (1993) 6590-6599.

[38] C. Servais and R. Locht, Chem. Phys. Lett. 236 (1995) 96-102.

[39] I. Powis, J. Chem. Phys. 99 (1993) 3436-3443.

[40] J.C. Creasey, H.M. Jones, D.M. Smith, R.P. Tuckett, P.A. Hatherly, K. Codling and I. Powis, Chem. Phys. 174 (1993) 441-452.

[41] J.C. Creasey, D.M. Smith, R.P. Tuckett, K.R. Yoxall, K. Codling and P.A. Hatherly, J. Phys. Chem. 100 (1996) 4350-4360.

[42] M.-J. Hubin-Franskin, J. Delwiche, P.-M. Guyon, M. Richard-Viard, M. Lavollée, O.Dutuit, J.-M. Robbe and J.-P. Flament, Chem. Phys. 209 (1996) 143-157.

[43] C. Cornaggia, F. Salin and C.L. Blanc, J. Phys. B: At. Mol. Opt. Phys 29 (1996) L749-L754.

[44] R.L. Johnson and M. Cardona. in *Encyclopedia of Physics. 2nd Edition* (Ed. R.G. Lerner & G.L. Trigg) 1235-1241, VCH Publishers Inc., New York, 1991.

[45] I.H. Munro and A.P. Sabersky. in *Synchrotron Radiation Research* (Ed. H. Winick & S. Doniach) 323-352, Plenum Press, New York, 1980.

[46] E.M. McMillan and J.M. Peterson. in *Encyclopedia of Physics. 2nd Edition* (Ed. R.G. Lerner & G.L. Trigg) 1235-1241, VCH Publishers Inc., New York, 1991.

[47] Synchrotron Radiation Center. *1 GeV Ring Parameters* [online]. Accessed: 19. August. 1999. Available at http://www.src.wisc.edu/currentusers/beamlineinformation/parameters.html.

[48] Synchrotron Radiation Center. *SRC Homepage* [online]. Accessed: 19. August. 1999. Available at http://www.src.wisc.edu.

[49] H. Winick. in *Synchrotron Radiation Research* (Ed. H. Winick & S. Doniach) 27-60, Plenum Press, New York, 1980.

[50] E.W. Nuffield. *X-Ray Diffraction Methods* 1-409, John Wiley & Sons, Inc., New York, 1966.

[51] Synchrotron Radiation Center. *Port 093, The Canadian Double Crystal Monochromator* [online]. Accessed: 19. August. 1999. Available at http://www.src.wisc.edu/currentusers/beamlineinformation/beamline_list/093.html.

[52] Advanced Light Source. *Beamline 5.0.1. Monochromatic Protein Crystallography* [online]. Accessed: 20. August. 1999. Available at http://www-als.lbl.gov/als/quickguide/bl5.0.1.html.

[53] Advanced Light Source. *Beamline 5.0.2. Multiple-Wavelength Anomalous Diffraction (MAD) and Monochromatic Protein Crystallography* [online]. Accessed: 20. August. 1999. Available at http://www-als.lbl.gov/als/quickguide/bl5.0.2.html.

[54] Advanced Light Source. *Beamline 9.3.1: Atomic, Molecular and Materials Science* [online]. Accessed: 20. August. 1999. Available at http://www-als.lbl.gov/als/quickguide/bl9.3.1.html.

[55] Advanced Photon Source. *Beamline 5-ID/DND-CAT* [online: .pdf file]. Accessed: 20. August. 1999. Available at http://www.aps.anl.gov/xfd/communicator/useroffice/catguide/05_id.pdf.

[56] Advanced Photon Source. *Beamline 22-BM/SER-CAT* [online: .pdf file]. Accessed: 20. August. 1999. Available at http://www.aps.anl.gov/xfd/communicator/useroffice/catguide/22_bm.pdf.

[57] Advanced Photon Source. *Beamline 33-BM/UNI-CAT* [online: .pdf file]. Accessed: 20. August. 1999. Available at http://www.aps.anl.gov/xfd/communicator/useroffice/catguide/33_bm.pdf.

[58] Advanced Light Source. *Beamline 6.3.1: Calibration and Standards, EUV/Soft X-Ray Optics Testing, Solid State Chemistry* [online]. Accessed: 20. August. 1999. Available at http://www-als.lbl.gov/als/quickguide/bl6.3.1.html.

[59] Advanced Light Source. *Beamline 7.0.1: Surface and Materials Science, Spectromicroscopy, Spin Resolution, Photon-Polarization Dichroism.* [online]. Accessed: 20. August.1999. Available at http://www-als.lbl.gov/als/quickguide/bl7.0.1.html.

[60] Advanced Light Source. *Beamline 7.3.1.1: Magnetic Microscopy, Spectromicroscopy* [online]. Accessed: 20. August. 1999. Available at http://www-als.lbl.gov/als/quickguide/bl7.3.1.1.html.

[61] Advanced Light Source. *Beamline 7.3.1.2: Surface and Materials Science, Micro X-Ray Photoelectron Spectroscopy* [online]. Accessed: 20. August. 1999. Available at http://www-als.lbl.gov/als/quickguide/bl7.3.1.2.html.

[62] Advanced Light Source. *Beamline 4.0.1-2. Magnetic Spectroscopy* [online]. Accessed: 20. August.1999. Available at http://www-als.lbl.gov/als/quickguide/bl4.0.1-2.html.

[63] Advanced Light Source. *Beamline 6.3.2: Calibration and Standards; EUV Optics; Testing; Atomic, Molecular and Materials Science* [online]. Accessed: 20. August. 1999. Available at http://www-als.lbl.gov/als/quickguide/bl6.3.2.html.

[64] Synchrotron Radiation Center. *Plane-Grating Monochromator Beamline. Port 071* [online]. Accessed: 20. August. 1999. Available at http://www.src.wisc.edu/currentusers/beamlineinformation/beamline_list/071.html.

[65] Synchrotron Radiation Center. *Four Meter Normal Incidence Monochromator. Port 081* [online]. Accessed: 20. August. 1999. Available at http://www.src.wisc.edu/currentusers/beamlineinformation/beamline_list/081.html.

[66] Synchrotron Radiation Center. *Six Meter Toroidal Grating Monochromators. Ports 062 and 042* [online]. Accessed: 20. August. 1999. Available at http://www.src.wisc.edu/currentusers/beamlineinformation/beamline_list/ 6m_tgm_062042/default.html.

[67] J. Kirz and D. Sayre. in *Synchrotron Radiation Research* (Ed. H. Winick & S. Doniach) 277-322, Plenum Press, New York, 1980.

[68] Advanced Light Source. *Beamline 6.1.2: High-Resolution Zone-Plate Microscopy* [online]. Accessed: 20. August. 1999. Available at http://www-als.lbl.gov/als/quickguide/bl6.1.2.html.

[69] K.H. Tan, G.M. Bancroft, L.L. Coatsworth and B.W. Yates, Can. J. Phys. 60 (1982) 131-136.

[70] J.A.R. Samson. *Techniques of Vacuum Ultraviolet Spectroscopy* John Wiley & Sons, Inc., New York, 1967.

[71] Synchrotron Radiation Center. *Port 091, The Canadian Mark IV Grasshopper* [online]. Accessed: 19. August. 1999. Available at http://www.src.wisc.edu/currentusers/beamlineinformation/beamline_list/091.html.

[72] M. Bissen, M. Fisher, G. Rogers, D. Eisert, K. Klemen, T. Nelson, B. Mason, F. Middleton and H. Höchst, Rev. Sci. Instrum. 66 (1995) 2072-2074.

[73] M.C. Hettrick, Appl. Opt. 29 (1990) 4531-4535.

[74] Synchrotron Radiation Center. *High Energy and High Resolution Beamline, Port 033* [online]. Accessed: 19. August. 1999. Available at http://www.src.wisc.edu/currentusers/beamlineinformation/beamline_list/033.html.

[75] B.X. Yang, F.H. Middleton, B.G. Olsson, G.M. Bancroft, J.M. Chen, T.K. Sham, K. Tan and D.J. Wallace, Nucl. Instr. Methods A316 (1992) 422-436.

[76] B.X. Yang, F.H. Middleton, B.G. Olsson, G.M. Bancroft, J.M. Chen, T.K. Sham, K. Tan and D.J. Wallace, Rev. Sci. Instrum. 63 (1992) 1355-1358.

[77] J. Berkowitz. *Photoabsorption, Photoionization and Photoelectron Spectroscopy* Academic Press, New York, 1979.

[78] J.A.R. Samson, J. Opt. Soc. Am. 54 (1964) 6-15.

[79] I.N. Levine. *Quantum Chemistry. Volume I: Quantum Mechanics and Molecular Electronic Structure* 1-591, Allyn and Bacon, Inc., Boston, 1970.

[80] A. Szabo and N.S. Ostlund. *Modern Quantum Chemistry* McGraw-Hill Publishing Company, New York, 1989.

[81] R.G. Parr. *The Quantum Theory of Molecular Electronic Structure* W.A. Benjamin, inc., New York, 1963.

[82] C. Møller and M.S. Plesset, Phys. Rev. 46 (1934) 618.

[83] R. Krishnan, M.J. Frisch and J.A. Pople, J. Chem. Phys. 72 (1980) 4244-4245.

[84] J.A. Pople, Int. J. Quant. Chem. Symp. 11 (1977) 149-163.

[85] J.A. Pople, M. Head-Gordon and K. Raghavachari, J. Chem. Phys. 87 (1987) 5968-5975.

[86] R.M. Dreizler and E.K.U. Gross. *Density Functional Theory* Springer-Verlag, Berlin, 1990.

[87] A.D. Becke, Phys. Rev. A 38 (1988) 3098-3100.

[88] R.N. Sodhi and R.G. Cavell, J. Elec. Spec. 32 (1983) 283-312.

[89] R.N.S. Sodhi and R.G. Cavell, J. Elec. Spec. 41 (1986) 1-24.

[90] R.G. Cavell and R.N.S. Sodhi, J. Elec. Spec. 41 (1986) 25-35.

[91] C.X. Yan and R.G. Cavell, J. Elec. Spec. 42 (1987) 49-60.

[92] D.W. Davis and D.A. Shirley, J. Elec. Spec. 3 (1974) 137-163.

[93] E. Clementi and D.L. Raimondi, J. Chem. Phys. 38 (1963) 2686-2689.

[94] M.J. Frisch, G.W. Trucks, H.B. Schlegel, P. M. W. Gill, B.G. Johnson, M.A. Robb, J.R. Cheeseman, T. Keith, G.A. Petersson, J.A. Montgomery, K. Raghavachari, M.A. Al-Laham, V.G. Zakrzewski, J.V. Ortiz, J.B. Foresman, J. Cioslowski, B.B. Stefanov, A. Nanayakkara, M. Challacombe, C.Y. Peng, P.Y. Ayala, W. Chen, M.W. Wong, J. L. Andres, E.S. Replogle, R. Gomperts, R.L. Martin, D. J. Fox, J.S. Binkley, D.J. Defrees, J. Baker, J. P. Stewart, M. Head-Gordon, C. Gonzalez and J.A. Pople, (Gaussian, Inc., Pittsburgh PA, 1995).

[95] J.H. Callomon, E. Hirota, K. Kuchitsu, W.L. Lafferty, A.G. Maki and C.S. Pote. *Landolt-Börnstein: Structure Data of Free Polyatomic Molecules* 1-395, Springer-Verlag, Berlin, 1976.

[96] J.H. Callomon, E. Hirota, T. Iijima, K. Kuchitsu and W.L. Lafferty. *Landolt-Börnstein: Structure Data of Free Polyatomic Molecules: supplement to volume II/7* 1-608, Springer-Verlag, Berlin, 1987.

[97] E. Hirota, T. Iijima, K. Kuchitsu, W.L. Lafferty, D.A. Ramsay and J. Vogt. *Landolt-Börnstein: Structure Data of Free Polyatomic Molecules: supplement to volume II/7 and II/15* 1-484, Springer-Verlag, Berlin, 1992.

[98] L.J. Sæthre, O. Sværen, S. Svensson, S. Osborne, T.D. Thomas, J. Jauhiainen and S. Aksela, Phys. Rev. A 55 (1997) 2748-2756.

[99] L.J. Sæthre, T.D. Thomas and S. Svensson, J. Chem. Soc., Perkin Trans. 2 (1997) 749-755.

[100] L.J. Sæthre, O. Sværen, S.Svensson, S. Sundin and S. Aksela, (San Francisco, California, USA. August 3-7, 1998, 1998).

[101] T.A. Koopmans, Physica 1 (1933) 104.

[102] J.B. Foresman, M. Head-Gordon, J.A. Pople and M.J. Frisch, J. Phys. Chem. 96 (1992) 135-149.

[103] K.H. Johnson, Advances in Quantum Chemistry 7 (1973) 143-185.

[104] S. Svensson, A. Ausmees, S.J. Osborne, G. Bray, F. Gel'mukhanov, H. Ågren, A.N.d. Brito, O.-P. Sairanen, A. Kivimäki, E. Nõmmiste, H. Aksela and S. Aksela, Phys. Rev. Lett. 72 (1994) 3021-3024.

[105] W.J. Moore. *Physical Chemistry. 4th Edition* Prentice-Hall, Inc., Englewood Cliffs, New Jersey, 1972.

[106] E. Ishiguro, S. Iwata, A. Mikuni, Y. Suzuki, H. Kanamori and T. Sasaki, J. Phys. B: At. Mol. Opt. Phys. 20 (1987) 4725-4739.

[107] M. Tinkham. *Group theory and quantum mechanics* 1-340, McGraw-Hill, New York, 1964.

[108] F.A. Cotton. *Chemical Applications of Group Theory, 2nd edition* 1-386, Wiley-Interscience, New York, 1971.

[109] K. Schwarz, Phys. Rev. B 5 (1972) 2466-2468.

[110] K. Schwarz, Theoret. Chim. Acta (Berl.) 34 (1974) 225-231.

[111] I. Powis, Chem. Phys. Lett. 215 (1993) 269-274.

[112] J.G. Norman Jr., Mol. Phys. 31 (1976) 1191-1198.

[113] Z.F. Liu, J.N. Cutler, G.M. Bancroft, K.H. Tan, R.G. Cavell and J.S. Tse, Chem. Phys. 168 (1992) 133-144.

[114] L. Noodleman, J. Chem. Phys. 64 (1976) 2343-2349.

[115] D. Dill and J.L. Dehmer, J. Chem. Phys. 61 (1976) 692-699.

[116] J.W. Davenport, Phys. Rev. Lett. 36 (1976) 945-949.

[117] P.-O. Löwdin, J. Chem. Phys. 18 (1950) 365-375.

[118] M.B. Robin. *Higher Excited States of Polyatomic Molecules, Volume I* 1-374, Academic Press, New York, 1974.

[119] A. Jürgensen and R.G. Cavell, Manuscript in preparation (1999) .

[120] G.N. Lewis, J. Am. Chem. Soc. 38 (1916) 762-785.

[121] J. Langmuir, J. Am. Chem. Soc. 41 (1919) 868-934.

[122] E.A. Robinson, J. Molec. Struc. (Theochem) 186 (1989) 9-28.

[123] J.H. Huheey. *Inorganic Chemistry. Principles of structure and reactivity* Harper & Row, Publishers, New York, 1978.

[124] C.E. Moore. *Atomic energy levels: as derived from the analysis of optical spectra* US National Bureau of Standards, 1971.

[125] R.E. Rundle, J. Am. Chem. Soc. 85 (1963) 112-113.

[126] G.C.J. Pimentel, J. Chem. Phys. 19 (1951) 446-448.

[127] R.J. Hach and R.E. Rundle, J. Am. Chem. Soc. 73 (1951) 4321-4324.

[128] W.H. Kirchhoff and D.R. Johnson, J. Mol. Spectrosc. 48 (1973) 157-164.

[129] L. Pauling. *The Nature of the Chemical Bond* Cornell, Ithaca, NY, 1940.

[130] A.E. Reed and F. Weinhold, J. Am. Chem. Soc. 108 (1986) 3586-3593.

[131] E. Steiner. *The determination and interpretation of molecular wave functions* 1-205, Cambridge University Press, Cambridge, 1976.

[132] I. Mayer, J. Mol. Struc. (Theochem) 149 (1987) 81-89.

[133] I. Mayer, J. Mol. Struct. (Theochem) 186 (1989) 43-52.

[134] J.G. Ángyán, J. Mol. Struc. (Theochem) 186 (1989) 61-67.

[135] I. Mayer, Chem. Phys. Lett. 97 (1983) 270-274.

[136] J. Baker, Theor. Chim. Acta. 68 (1985) 221-229.

[137] M.A. Natiello and J. Medrano, Chem. Phys. Lett. 105 (1984) 180-182.

[138] R.S. Mulliken, J. Chem. Phys. 23 (1955) 1833-1840.

[139] R.S. Mulliken, J. Chem. Phys. 23 (1955) 1841-1846.

[140] R.S. Mulliken, J. Chem. Phys. 23 (1955) 2338-2342.

[141] R.S. Mulliken, J. Chem. Phys. 23 (1955) 2343-2346.

[142] A.E. Reed and F. Weinhold, J. Chem. Phys. 78 (1983) 4066-4073.

[143] P.O. Löwdin, Phys. Rev. 97 (1955) 1474.

[144] C. Engemann, G. Kohring, A. Pantelouris, J. Hormes, S. Grimme, S.D. Peyerimhoff, J. Clade, F. Frick and M. Jansen, Chem. Phys. 221 (1997) 189-198.

[145] A. Jürgensen and R.G. Cavell, unpublished data (1998) .

[146] M. Cook and D. Case, (1978).

[147] T.D. Thomas, J. Electron Spectrosc. 20 (1980) 117-125.

[148] E.J. Aitken, M.K. Bahl, K.D. Bomben, J.K. Gimzewski, G.S. Nolan and T.D. Thomas, J. Am. Chem. Soc. 102 (1980) 4873-4879.

[149] A. Jürgensen and R.G. Cavell, unpublished data (1995) .

[150] J.E. Huheey, J. Phys. Chem. 69 (1965) 3284-3291.

[151] A.E. Reed, A.B. Weinstock and F. Weinhold, J. Chem. Phys. 83 (1985) 735-746.

[152] T.D. Thomas and J. R.W. Shaw, J. Elec. Spec. 5 (1974) 1081-1094.

[153] M. Coville and T.D. Thomas, J. Elec. Spec. 71 (1995) 21-23.

[154] W.L. Jolly, K.D. Bomben and C.J. Eyermann, At. Data and Nuc. Data Tables 31 (1984) 433-493.

[155] J.A. Pople and G.A. Segal, J. Chem. Phys. 44 (1966) 3289-3296.

[156] A.D. Becke, J. Chem. Phys. 98 (1993) 5648-5652.

[157] C. Lee, W. Yang and R.G. Parr, Phys. Rev. B 37 (1988) 785-789.

[158] S.H. Vosko, L. Wilk and M. Nusair, Can. J. Phys. 58 (1980) 1200-1211.

[159] A. Jürgensen and R.G. Cavell, J. Elec. Spec. 100-103 (1999) 125-129.

[160] J.B. Mann. *Atomic Structure Calculations I. Hartree-Fock Energy Results for the Elements Hydrogen to Lawrencium*. Los Alamos Scientific Laboratory of the University of California, 1967. (LA-3690; UC-34, Physics; TID-4500)

[161] L. Pettersson, J. Nordgren, C. Nordling and K. Siegbahn, J. Elec. Spec. 27 (1982) 29-37.

[162] J.W. Au, G. Cooper and C.E. Brion, Chem. Phys. 215 (1997) 397-418.

[163] N. Kosugi, R.G. Cavell and A.P. Hitchcock, Chem. Phys. Lett. 265 (1997) 490-496.

[164] R.N.S. Sodhi and C.E. Brion, J. Elec. Spec. 37 (1985) 97-123.

[165] I.J. Väyrynen, T.A. Kaurila, R.G. Cavell and K.H. Tan, J. Elec. Spec. 61 (1992) 55-64.

[166] J.J. Neville, A. Jürgensen, R.G. Cavell, N. Kosugi and A.P. Hitchcock, Chem. Phys. 238 (1998) 201-220.

[167] N. Kosugi and H. Kuroda, Chem. Phys. Lett. 74 (1980) 490-493.

[168] N. Kosugi, Theor. Chim. Acta 72 (1987) 149-173.

[169] C.E. Small and J.G. Smith, Molecular Physics 37 (1979) 665-679.

[170] S. Huzinaga, J. Andzelm, M. Klobukowski, E. Radzio-Andzelm, Y. Sasaki and H. Tatewaki. *Gaussian Basis Sets for Molecular Calculations* Elsevier, Amsterdam, 1984.

[171] G. Schaftenaar, (QCPE Bulletin, 12,3, 1992).

[172] A. Jürgensen and R.G. Cavell, Manuscript in preparation (1999).

[173] F.M.F. de Groot, Z.W. Hu, M.F. Lopez, G. Kaindl, F. Guillot and M. Tronc, J. Chem. Phys. 101 (1994) 6570-6576.

[174] A. Jürgensen and R.G. Cavell, unpublished data.

[175] R.N.S. Sodhi and C.E. Brion, J. Elec. Spec. 37 (1985) 125-144.

[176] J.J. Neville, T. Tyliszczak, A.P. Hitchcock, A. Jürgensen and R.G. Cavell, Chem. Phys. Lett. 300 (1999) 451-459.

[177] S. Bodeur and J.M. Esteva, Chem. Phys. 100 (1985) 415-427.

[178] C.T. Chen, Y. Ma and F. Sette, Phys. Rev. A 40 (1989) 6737-6740.

[179] R.G. Cavell and R.N.S. Sodhi, J. Elec. Spec. 43 (1987) 215-223.

[180] V.N. Akimov, A.S. Vinogradov and T.M. Zimkina, Opt. Spectrosc. 53 (1982) 548-550.

[181] K.-H. Sze, C.E. Brion, X.-M. Tong and J.-M. Li, Chem. Phys. 115 (1987) 433-451.

[182] D.M.P. Holland, M.A. MacDonald, M.A. Hayes, P. Baltzer, L. Karlsson, M. Lundqvist, B. Wannberg and W.v. Niessen, Chem. Phys. 188 (1994) 317-337.

[183] I.W. Fomunung, Z. Chen and A.Z. Msezane, Phys. Rev. A 53 (1996) 806-817.

[184] C. Reynaud, M.A. Gaveau, P. Millié, S. Bodeur, P. Archirel, B. Lévy and I. Nenner, J. Elec. Spec. 79 (1996) 357-360.

[185] C. Reynaud, M.-A. Gaveau, K. Bisson, P. Millié, I. Nenner, S. Bodeur, P. Archirel and B. Lévy, J. Phys. B: At. Mol. Opt. Phys. 29 (1996) 5403-5419.

[186] J. Adachi, Y. Takata, N. Kosugi, E. Shigemasa, A. Yagishita and Y. Kitajima, Chem. Phys. Lett. 294 (1998) 559-564.

[187] E. Gedat, R. Püttner, M. Domke and G. Kaindl, J. Chem. Phys. 109 (1998) 4471-4477.

[188] T. Masuoka, Y. Chung, E.-M. Lee and J.A.R. Samson, J. Chem. Phys. 109 (1998) 2246-2253.

[189] A. Jürgensen, R.G. Cavell, H. Höchst and M. Bissen, (Windsor, Ontario, Canada, June 1-4, 1997, 1997).

[190] A. Jürgensen and R.G. Cavell, Manuscript in preparation (1999).

[191] A. Jürgensen and R.G. Cavell, Manuscript in preparation (1999).

[192] J. McMurry and R.C. Fay. *Chemistry* Prentice Hall, Englewood Cliffs, New Jersey, 1995.

[193] J.A. Pople, A.P. Scott, M.W. Wong and L. Radom, Isr. J. Chem. 33 (1993) 345-350.

[194] *Gmelins Handbuch der Anorganischen Chemie 8. Auflage; System - Nummer 4, Stickstoff, Lieferung 3, Verbindungen des Stickstoffs mit Sauerstoff* Verlag Chemie, Gmbh, Weinheim/Bergstr., 1936 (Nachdruck 1955).

[195] *Gmelins Handbuch der Anorganischen Chemie 8. Auflage; System - Nummer 9, Schwefel, Teil B - Lieferung 3, Hydride und Oxyde des Schwefels* Verlag Chemie, Gmbh, Weinheim/Bergstr., 1953.

[196] J.W. Au and C.E. Brion, Chem. Phys. 218 (1997) 109-126.

[197] P. Baltzer, L. Karlsson, B. Wannberg, D.M.P. Holland, M.A. MacDonald, M.A. Hayes and J.H.D. Eland, Chem. Phys. 237 (1998) 451-470.

[198] W. Zhang, K.H. Sze, C.E. Brion, X.M. Tong and J.M. Li, Chem. Phys. 140 (1990) 265-279.

[199] J.L. Dehmer, J. Chem. Phys. 56 (1972) 4496-4504.

[200] A.P. Hitchcock, S. Bodeur and M. Tronc, Chem. Phys. 115 (1987) 93-101.

[201] A.P. Hitchcock and M. Tronc, Chem. Phys. 121 (1988) 265-277.

[202] J.P. Maier and D.W. Turner, J. Chem. Soc. Faraday Trans. 2 68 (1972) 711-719.

[203] P.J. Bassett and D.R. Lloyd, J. Chem. Soc. Dalton Trans. (1972) 248-254.

[204] J. Berkowitz, J.P. Greene, J.F. Jr. and O.M. Neskovic, J. Chem. Phys. 81 (1984) 6166-6175.

[205] C. Krier, M.T. Praet and J.C. Lorquet, J. Chem. Phys. 82 (1985) 4073-4075.

[206] A.R. Rossi and P. Avouris, J. Chem. Phys. 79 (1983) 3413-3420.

[207] R.L. DeKock and H.B. Gray. *Chemical Structure and Bonding* 1-73, University Science Books, Mill Valley, California, 1989.

[208] C.R. Brundle, D. Neumann, W.C. Price, D. Evans, A.W. Potts and D.G. Streets, J. Chem. Phys. 53 (1970) 705-715.

[209] A. Jürgensen, R.G. Cavell and N. Kosugi, accepted by Chem. Phys. (1999) .

[210] B. Hedman, K.O. Hodgson and E.I. Solomon, J. Am. Chem. Soc. 112 (1990) 1643-1645.

[211] R.C. Weast, M.J. Astle and W.H. Beyer, (CRC Press, Boca Raton, Florida, 1984).

[212] A. Menzel, S. Benzaid, M.O. Krause, C.D. Caldwell, U. Hergenhahn and M. Bissen, Phys. Rev. A 54 (1996) R991-R994.

[213] W.C. Stolte, Y. Lu, J.A.R. Samson, O. Hemmers, D.L. Hanson, S.B. Whitfield, H. Wang, P. Glans and D.W. Lindle, J. Phys. B: At. Mol. Opt. Phys. 30 (1997) 4489-4497.

[214] G.C. Angel and J.A.R. Samson, Phys. Rev. A 38 (1988) 5578-5585.

CURRICULUM VITAE

PERSONAL DATA

Name:	Astrid Jürgensen	
Address:	*Home:* 1304 Galbraith House 12020 - 49th Ave. Edmonton, Alberta, Canada T6H 5B5	*Business:* Dept. of Chemistry University of Alberta Edmonton, Alberta, Canada T6G 2G2
Telephone:	*Home:* (780) 436-7296	*Business:* (780) 492-2194
e-mail:	ajurgens@gpu.srv.ualberta.ca	

Date of Birth:	01. March. 1971
Place of Birth:	Kiel, West Germany
Citizenship:	Canadian and German
Languages:	English, French, German

DEGREES

Ph.D.:	University of Alberta in progress, estimated date of completion summer 1999 Physical Chemistry
B.Sc.:	University of Waterloo, May 1993 Honours Chemical Physics

OTHER POST-SECONDARY EDUCATION

Jan. 1992 to Mar. 1992	University of Sussex, Brighton UK Exchange Student

RELATED EXPERIENCE

Research:

Sept. 1993 to present:	Graduate Student at the University of Alberta (photoabsorption and photoelectron spectroscopy) Supervisor: Dr. R.G. Cavell
May to Aug. 1993:	Natural Sciences and Engineering Research Council of Canada (NSERC) Summer Student (Catalysis) Supervisor: Dr. J.B. Moffat
Sept. 1992 to Apr.1993:	Undergraduate Student, 4th year research project (Catalysis) Supervisor: Dr. J.B. Moffat
May to Aug. 1991:	NSERC Summer Student (Catalysis) Supervisor: Dr. J.B. Moffat
May to Aug. 1990:	NSERC Summer Student (X-ray diffraction) Supervisor: Dr. L.F. Nazar

Teaching:

Sept. 1997 to Apr. 1998:	Lecture Help for the first year inorganic chemistry course (Teaching Assistant).
Sept. 1996 to Apr. 1997:	Lecture Help for the first year inorganic chemistry course (Teaching Assistant).
Sept. 1995 to Apr. 1996:	Lecture Help for the first year inorganic chemistry course (Teaching Assistant).
Sept. 1994 to Apr. 1995:	Laboratory Instructor for the first year inorganic chemistry course (Teaching Assistant).
Sept. 1993 to Apr. 1994:	Laboratory Instructor for the first year inorganic chemistry course (Teaching Assistant).

Other Skills:

Data analysis of the experimental spectra collected as part of Ph.D. research was accomplished with the aid of a curve fitting program written by a former summer student of Dr. R.G. Cavell. I expanded the code of this program, originally written for only the analysis of photoelectron spectra, considerably to allow analysis of photoabsorption and Auger spectra as well. In the process I acquired extensive programming experience with the C language in the Windows environment.

During my last two years (1987/88, 1988/89) in high school (South Secondary School in London, Ont.) I was one of the co.-editors of the school's yearbook.

POST-SECONDARY SCHOLARSHIPS AND AWARDS HELD

Name	From	To	Name of institution and location
NSERC PGS A	1993/09	1995/09	University of Alberta, Edmonton, Alta.
Walter H Johns Graduate Fellowship	1993/09	1994/05	University of Alberta, Edmonton, Alta.
University of Alberta Ph.D. Scholarship	1993/09	1994/05	University of Alberta, Edmonton, Alta.
Graduate Entrance Scholarship	1993/09	1994/05	University of Alberta, Edmonton, Alta.
Canada Scholarship	1989/09	1993/05	University of Waterloo, Waterloo, Ont.
NSERC Summer Student	1993/05 1991/05 1990/05	1993/08 1991/08 1990/08	University of Waterloo, Waterloo, Ont.
Sony Scholarship	1992/09	1993/05	University of Waterloo, Waterloo, Ont.
Science Faculty Chemistry Upper Year Scholarship	1991/09	1992/05	University of Waterloo, Waterloo, Ont.
Jerome T. Miller Memorial Prize	1991/09	1992/05	University of Waterloo, Waterloo, Ont.
Bruker Chemistry Scholarship	1990/09	1991/05	University of Waterloo, Waterloo, Ont.
Hewlett-Packard (Canada) Ltd. Award	1990/09	1991/05	University of Waterloo, Waterloo, Ont.
Science Faculty Entrance Scholarship	1989/09	1990/05	University of Waterloo, Waterloo, Ont.
Ontario Scholarship	1989/09	1990/05	University of Waterloo, Waterloo, Ont.
Shad Valley Summer Program (en français)	1988/06	1988/07	Université de Sherbrooke, Sherbrooke, Que.

PUBLICATIONS

Refereed Publications

1. The Sulphur 2p Photoabsorption Spectrum of NSF_3
   Astrid Jürgensen, Ronald G. Cavell, Nobuhiro Kosugi
   Chem. Phys. (1999) Accepted for publication

2. P 1s spectroscopy of SPF_3: spectral assignments aided by angle-resolved photodissociation
   J.J. Neville, T. Tyliszczak, A.P. Hitchcock, A. Jürgensen, R.G. Cavell
   Chem. Phys. Lett. **300** (1999) 451-459

3. Chemical Shifts in P 1s Photoabsorption Spectra of Gaseous Phosphorus Compounds
   A. Jürgensen, R.G. Cavell
   J. Elec. Spec. **101-103** (1999) 125-129 (VUV XII proceedings)

4. Inner shell excitation of PF_3, PCl_3, PCl_2CF_3, OPF_3 and SPF_3: Part I. Spectroscopy
   J.J. Neville, A. Jürgensen, R.G. Cavell, N. Kosugi, A.P. Hitchcock
   Chem. Phys. **238** (1998) 201-220

5. Ionic Fragmentation of inner-shell excited molecules
   A.P. Hitchcock, J.J. Neville, A. Jürgensen, R.G. Cavell
   J. Elec. Spec. **88-91** (1998) 71-75

6. The stability of 12-molybdosilicic, 12-tungstosilicic, 12-molybdophosphoric and 12-tungstophosphoric acids in aqueous solution at various pH
   A. Jürgensen, J.B. Moffat
   Catalysis Letters **34** (1995) 237-244

7. Ion chromatographic analysis of inorganic molecular metal-oxygen cluster compounds
   A. Jürgensen, J.B. Moffat
   Journal of Chromatography **602** (1992) 173-178

Conference Presentations

8. The valence shell photoionization cross-sections of NF_3 and PF_3, a comparison
A. Jürgensen, R.G. Cavell
Canadian Society of Chemistry Conference, Toronto, Ont., May 30-June 2, 1999

9. The role of LS-coupling in the P 2p spectroscopy of phosphorus halides
John J. Neville, Astrid Jürgensen, Ronald G. Cavell, Nobuhiro Kosugi,
Adam P. Hitchcock
The 12th International Conference on Vacuum Ultraviolet Radiation Physics,
San Francisco, California, USA, Aug. 3-7, 1998

10. Photofragmentation of OCS and SPF_3 at the S 1s and P 1s edges
John J. Neville, Tolek Tyliszczak, Astrid Jürgensen, Ronald G. Cavell, Adam P. Hitchcock
The 12th International Conference on Vacuum Ultraviolet Radiation Physics,
San Francisco, California, USA, Aug. 3-7, 1998

11. The Valence Shell Spectrum of Core Ionized PF_3
Ronald G. Cavell, Astrid Jürgensen, Juhani Väyrynen
The 12th International Conference on Vacuum Ultraviolet Radiation Physics,
San Francisco, California, USA, Aug. 3-7, 1998

12. High resolution oxygen 1s photoabsorption and photoelectron spectra of sulfur (IV) oxyhalides and their derivatives
A. Jürgensen, R.G. Cavell, H. Höchst, M. Bissen
Canadian Society of Chemistry Conference, Windsor, Ont., June 1-4, 1997

13. K and L shell photoabsorption spectroscopy of solid and gaseous inorganic species
R.G. Cavell and A. Jürgensen
Pacifichem 1995, Honolulu, HI, Dec. 17-22, 1995

Manuscripts in Preparation:

14. A Synchrotron Photoelectron Study of the O-1s and S-2p Ionization Potentials of Volatile Sulphur Compounds (32 pages)
    Astrid Jürgensen, Ronald G. Cavell

15. K-Shell Photoabsorption spectra of YPF_3 molecules and NSF_3 (19 pages)
    Astrid Jürgensen, Ronald G. Cavell

16. O-1s Photoabsorption of SO_2XY (X,Y = F, Cl, CH_3, CF_3) (24 pages)
    Astrid Jürgensen, Ronald G. Cavell

17. The Chemical Shift Trends Revealed by P(1s) Photoabsorption Spectra of Gaseous Phosphorus Compounds (49 pages)
    A. Jürgensen, R.G. Cavell

18. Inner shell excitation of PF_3, PCl_3 and PCl_2CF_3: Part II. Fragmentation
    J.J. Neville, A Jürgensen, R.G. Cavell, N. Kosugi, A.P. Hitchcock

19. The Oxygen 1s Spectra of SO_2 and NO_2 (13 pages)
    A. Jürgensen, R.G. Cavell